UNIVERSITY OF OKLAHOMA

GRADUATE COLLEGE

FULL WAVE-EQUATION BASED PASSIVE SEISMIC IMAGING AND MULTISPECTRAL SEISMIC GEOMETRIC ATTRIBUTES

A DISSERTATION

SUBMITTED TO THE GRADUATE FACULTY

in partial fulfillment of the requirements for the

Degree of

DOCTOR OF PHILOSOPHY

By

BIN LYU

Norman, Oklahoma

2020

FULL WAVE-EQUATION BASED PASSIVE SEISMIC IMAGING AND MULTISPECTRAL SEISMIC GEOMETRIC ATTRIBUTES

A DISSERTATION APPROVED FOR THE

SCHOOL OF GEOSCIENCES

BY THE COMMITTEE CONSISTING OF

Dr. Kurt J. Marfurt, Chair

Dr. Xingru Wu

Dr. Nori Nakata

Dr. Michael Behm

Dr. Heather Bedle

ACKNOWLEDGEMENTS

My PhD journey would not have been possible without the support from my advisor, my committee members, my family, colleagues, and friends.

I would like to express my deepest appreciation to Dr. Kurt Marfurt, who is my PhD advisor and the committee chair. Without his support, my PhD career would be impossible. Dr. Marfurt has been always supportive, encouraging, and patient for my research. I really appreciate the opportunity to be advised by Dr. Marfurt, not only for his profound knowledge in seismic exploration, but also his passion for research, his humor, and his optimistic spirit. It is my great honor to be his student, and he will always be an idol for my future life.

I would like to show my greatest gratitude to my committee members: Dr. Nori Nakata, Dr. Xingru Wu, Dr. Michael Behm, and Dr. Heather Bedle for their guidance, insights, and encouragement. I will thank Dr. Nakata for the cooperation on the research and publication of passive seismic imaging in Chapter 2. I would like to thank Dr. Wu for his insightful suggestion for my PhD study and career development. I will thank Dr. Behm for the support of my PhD research and insights of seismic processing. I would like to thank Dr. Bedle for her insightful knowledge of seismic attributes. It is my great honor to have them on my committee.

I want to show my great thanks to the support and collaboration from my current teammates in the AASPI consortium: Thang Ha, Saurabh Sinha, David Lubo Robles, Karelia LaMarca-Molina, Carl Buist, Alexandro Vera-Arroyo, and former teammates: Jie Qi, Fangyu Li, Tao Zhao, Bo Zhang, Sumit Verma, Bradley Wallet, Abdulmohsen AlAli, Gabriel Machado, Lennon Infante, Xuan Qi, Yuji Kim, Swetal Patel, and Rafael Pires de

Lima. I would like to thank my friends: Yichuan Wang, Jianjun Li, Hui Chen, Ying Hu, Emilio J. Torres, Raymond Ng, and Kui Zhang for support and helpful discussions.

I would show my great thanks to the staff of School of Geosciences: Rebecca Fay, Ginger Leivas, Leah Moser, Ashley Tullius, and Robert L. Turner for their help and supports.

I would like to express my deepest thanks to my family for everything they have done for me. Without their continued love, support, and understanding, it is impossible for me to finish my PhD journey. I would like to express my special thanks to my wife Yanju Chen. During my PhD study and my entire life, she has always been supportive and encouraging.

TABLE OF CONTENTS

LIST OF FIGURES

ABSTRACT

Both passive (e.g., microseismic) and active seismic methods are used for the hydrocarbon exploration. For example, microseismic data analysis provides helpful information in not only mapping hydraulic fracture initiation, but also reservoir monitoring and even structural imaging. In 3D seismic interpretation, geometric attributes provide effective tools to map structure and stratigraphy. However, current microseismic events locating method faces challenge due to the poor resolution of passive-seismic imaging result and the dependency of the subsurface velocity model. Further, some stratigraphic features are buried in the conventional seismic geometric attributes. Focusing on these challenges, I develop new passive seismic imaging method and multispectral geometric attributes in this dissertation to provide more effective tools for hydrocarbon exploration.

To improve the quality of passive seismic imaging, I have constructed an iterative approach to locate the passive source locations and estimate the background overburden velocity based on full wave-equation methods. Specifically, I use a high-resolution geometric-mean reverse-time migration (GmRTM) to provide source locations that are better focused compared to conventional time-reversal imaging method. I also use the passive-source full-waveform inversion (FWI) to optimize the overburden velocity model. Given this accurate velocity, I use passive-source reverse-time migration to provide a structural image. Numerical experiments on the Marmousi model dataset indicate that the proposed approach can handle complicated structures and noisy seismic recordings.

Recent developments in multispectral coherence based on simple band-pass filters show improvements in fault and stratigraphic edge delineation. To further improve this technology, I evaluate several different spectral decomposition algorithms to determine

which, if any provide superior coherence images, I find that exponentially-spaced spectral voices provide better coherence images than linearly-spaced spectral components for the same computation cost. I also find that multispectral coherence computed from generated using the high-resolution maximum entropy algorithm provides reduced noise and better resolution of thinner channels than the other spectral decomposition algorithms.

Equally important, I analyze why multispectral coherence provides more continuous fault images where conventional coherence images often exhibit gaps in areas where a human interpreter would draw a single, unbroken fault. These coherence fault occur when the displacement across the fault aligns different stratigraphic reflectors, resulting in what appears to be a continuous reflector. This same alignment also confounds auto-pickers. Although two different broadband seismic reflectors may be aligned across faults, in general, the corresponding spectral voices are not, thereby reducing their cross-correlation, and for multispectral coherence, elements in their covariance matrices, across the fault.

Considering that multispectral coherence provides a better delineation of the seismic discontinuities due to data quality, thin-bed tuning, or non-stratigraphic alignments, I further investigate multispectral dip attributes, which try to combine the benefits from different spectral voices. I illustrate the multispectral gradient structure tensor (GST) dip method, which helps improve the quality of dip attributes in the conventional broadband dips. Multispectral GST dip is performed by computing the eigenvectors and eigenvalues from the multispectral gradient structure tensor matrix. I use two 3D seismic surveys to indicate the improvement using the multispectral GST dip over conventional broadband dip attributes.

CHAPTER 1: INTRODUCTION

Both passive (typically microseismic) and active seismic methods are used for the hydrocarbon exploration. Locating microseismic events is routinely used to monitor hydraulic fracturing completion processes (e.g., Maxwell, 2014), understand the reservoir depletion (e.g., Dohmen et al., 2014), and monitor seismically active faults (e.g., Wessels et al., 2011). Seismic geometric attributes (such as volumetric dip, coherence, curvature, and aberrancy) computed from the active source 3D seismic volumes provide effective tools to delineate structural and stratigraphic features in the subsurface such as faults, channels, karst collapse, and other subtle tectonic and sedimentary features which might be overlooked on the conventional seismic amplitude volumes (e.g., Chopra and Marfurt, 2007).

However, current microseismic events locating faces challenge due to the poor resolution and noise of the passive-seismic imaging result (Nakata and Beroza, 2016), and dependency of the subsurface velocity model. Seismic geometric attributes are generally computed using full-bandwidth seismic amplitude volume. First, due to the thin-bed tuning phenomena, the discontinuities in a stratigraphic feature with a specific thickness could be tuned and illuminated at a specific frequency (Marfurt and Kirlin, 2001). Further, whether due to the seismic data quality or the subsurface geology, certain spectral components exhibit higher S/N (signal-to-noise ratio), which will result in correspondingly higher quality attribute images. Especially, when we use full-bandwidth coherence attribute to detect faults, the non-stratigraphic alignments of similar reflections juxtaposing across the faults will result in pseudo fault breakpoints, challenging accurate fault delineation.

In this dissertation, I focus on two primary research topics, which are relatively independent but both are centered to develop effective tools for hydrocarbon exploration. Focusing the challenges of passive seismic imaging, I proposed an iterative passive-source estimation and velocity inversion method using geometric-mean reverse-time migration (GmRTM) and passive-source full-waveform inversion (FWI). To further improve the quality of seismic attribute, I optimized the multispectral seismic geometric attributes workflow by evaluating which spectral voices to choose and which spectral decomposition algorithm works best.

This dissertation is organized as follows:

In Chapter 2, I first illustrate the proposed iterative passive-source estimation and velocity inversion method using GmRTM (Nakata and Beroza, 2016) and FWI. In each iteration, I first estimate the source location using the high-resolution GmRTM method, which provides better focusing of passive-source imaging compared to conventional time-reversal imaging results. Next, I use the passive-source FWI to optimize the velocity model with the estimated source location. Then I construct a subsurface structural imaging using the passive-source RTM with the optimized source locations and velocity model. Numerical experiments on the Marmousi model, indicate that the proposed approach can handle not only complex structures but also noisy seismic recordings. This chapter has been published in Geophysical Journal International as Lyu and Nakata (2020).

In Chapter 3, I expand earlier work on multispectral coherence originated by Li et al. (2018) who combined the information content of bandpass-filtered versions of the seismic amplitude data using a simple short time window Fourier transform (STFT). I evaluate the multispectral response of spectral voices computing using the continuous wavelet

transform (CWT), maximum pursuit, maximum entropy, amplitude volume technique (AVT), and spectral probes to determine if any provide superior images of the TUI-3D seismic data volume from the Taranaki Basin, New Zealand. The CWT experiments indicate that the exponentially-spaced components provide sharper coherence images than linearly-spaced components in multispectral coherence for the same computation cost. My experiments further indicate that the coherence from AVT dataset provides continuous images of thicker channel boundaries, but poor images of the small-scale architectural elements inside the thicker channels. Spectral probes are defined by their period rather than by their frequency. Multispectral coherence computed using spectral probes exhibits more balanced and reveals clear small-scale geologic features inside the thicker channel, but appears much noisier than other spectral decomposition algorithms due to the equal weights for all components. The multispectral coherence computed using maximum entropy spectral voices provides the best imaging quality among these spectral decomposition algorithms with improved resolution of the thinner channels and other small-scale features. This chapter has been published in the AAPG-SEG journal Interpretation as Lyu et al. (2020a).

In Chapter 4, I address the limitation of fault delineation using coherence attributes when the offset across a fault aligns two similar looking but stratigraphically different reflectors. As with autopicking of reflector horizons, such alignment of different stratigraphic reflectors with similar waveforms across a fault will algorithmically appear to be continuous. In this situation, an autopicker will start to track the wrong stratigraphic horizon and the fault will appear as high coherence, resulting in a broken fault image. These coherence gaps provide an inaccurate fault images and negatively impact subsequent

processes such as edge-preserving structure-oriented smoothing/ Building on the findings of Chapter 3 that examined a complex turbidites, I use maximum entropy spectral voices as input to only multispectral coherence. Because the aligned by stratigraphically independent horizons occur for only a few spectral components, multispectral coherence fills most of the previously identified “fault gaps”. I also note and analyze the increased lateral smearing when using multispectral coherence and find that part of the cause is the different spectral response to stairstep anomalies (Lin and Marfurt, 2017) seen on the vertical seismic data. I address this smearing issue using a fault enhancement workflow described by Qi et al. (2019) and obtain improved results of minor faults and reduced stair-step artifacts on the larger faults. I show the effectiveness of the proposed workflow using the highly faulted Opunake 3D seismic dataset from the offshore Taranaki Basin, New Zealand. This chapter has been published in the AAPG-SEG journal Interpretation as Lyu et al. (2020b).

In Chapter 5, I generalize the concept of multispectral coherence that stacks the covariance matrices computed from each spectral voice to multispectral dip that stacks the gradient structure tensor (GST) for each spectral voice. After applying the structure-oriented filtering (SOF) and spectral balancing to improve the data quality of the original full-bandwidth seismic amplitude volume, we compute the multispectral GST dip attribute. I first built the multispectral covariance matrix using the decomposed spectral voices. Then I compute the eigenvectors and eigenvalues from the multispectral gradient structure tensor matrix, followed by the generation of inline and crossline dip volumes. I indicate the quality improvement of the multispectral GST dip over conventional broadband dip using 3D seismic surveys acquired over the Barnett Shale gas reservoir of the Fort Worth Basin,

Texas, and the offshore Taranaki Basin, New Zealand. This chapter will be submitted for journal publication at the end of 2020.

In Chapter 6, I show brief conclusions by summarizing my research work from Chapter 2 to Chapter 5. Finally, I provide an appendix Chapter focusing on tomographic velocity analysis and wave equation depth migration in overthrust terrain. In this chapter, after analyzing the seismic imaging challenges in the overthrust plays, I have developed the workflow to improve the seismic imaging quality for the overthrust terrain, especially the application of tomographic velocity analysis and optimized one-way wave equation depth migration. This chapter has been published in the AAPG-SEG journal Interpretation as Lyu et al. (2018).

References

Chopra, S., and K. J. Marfurt, 2007, Seismic attributes for prospect identification and reservoir characterization: SEG.

Dohmen, T., J.-P. Blangy, and J. Zhang, 2014, Microseismic depletion delineation: Interpretation, **2**, SG1–SG13.

Li, F., J. Qi, B. Lyu, and K. J. Marfurt, 2018, Multispectral coherence: Interpretation, **6**, T61–T69.

Lin, T., and K. J. Marfurt, 2017, What causes those annoying stair step artifacts on coherence volumes?: AAPG Explorer Geophysical Corner, March, Article 37830.

Lyu, B., Q. Su, and K. J. Marfurt, 2018, Tomographic velocity analysis and wave equation depth migration in an overthrust terrain: A case study from the Tuha Basin, China: Interpretation, **6**, T1-T13.

Lyu, B., and N. Nakata, 2020, Iterative passive-source location estimation and velocity

inversion using geometric-mean reverse-time migration and full-waveform inversion: Geophysical Journal International, **223**, 1935-1947.

Lyu, B., J. Qi, F. Li, Y. Hu, T. Zhao, S. Verma, and K. J. Marfurt, 2020a, Multispectral coherence: Which decomposition should we use?: Interpretation, **8**, T115-T129.

Lyu, B., J. Qi, S. Sinha, J. Li, and K. J. Marfurt, 2020b, Improving fault delineation using maximum entropy multispectral coherence: Interpretation, **8**, T835-T850.

Marfurt, K. J., and R. Kirlin, 2001, Narrow-band spectral analysis and thin-bed tuning: Geophysics, **66**, 1274–1283.

Maxwell, S., 2014, Microseismic imaging of hydraulic fracturing: Improved engineering of unconventional reservoirs: SEG.

Nakata, N., and G. C. Beroza, 2016, Reverse time migration for microseismic sources using the geometric mean as an imaging condition: Geophysics, **81**, no. 2, KS51–KS60.

Qi, J., B. Lyu, A. AlAli, G. Machado, Y. Hu, and K. J. Marfurt, 2019, Image processing of seismic attributes for automatic fault extraction: Geophysics, **84**, R1-R13.

Wessels, S. A., A. De La Pena, M. Kratz, S. Williams-Stroud, and T. Jbeili, 2011, Identifying faults and fractures in unconventional reservoirs through microseismic monitoring: First Break, **29**, 99–104.

CHAPTER 2: ITERATIVE PASSIVE-SOURCE LOCATION ESTIMATION AND VELOCITY INVERSION USING GEOMETRIC-MEAN REVERSE-TIME MIGRATION AND FULL-WAVEFORM INVERSION

Abstract

Passive-seismic provides useful information for reservoir monitoring and structural imaging; for example, the locations of microseismic events are helpful to understand the extension of the hydraulic fracturing. However, passive-seismic imaging still faces some challenges. First, it is not easy to know where the passive-seismic events happened, which is known as passive-source locating. Additionally, the accuracy of the subsurface velocity model will influence the accuracy of the estimated passive-source locations and the quality of the structural imaging obtained from the passive-seismic data. Therefore the velocity inversion using the passive-seismic data is required to provide the velocity with higher accuracy. Focusing on these challenges, we develop an iterative passive-source location estimation and velocity inversion method using geometric-mean reverse-time migration (GmRTM) and full-waveform inversion (FWI). In each iteration, the source location is estimated using a high-resolution geometric-mean reverse-time migration method, which provides a better focusing of passive-source imaging compared to conventional wavefield scanning method. The passive-source full-waveform inversion is then followed to optimize the velocity model using the estimated source location provided by GmRTM. The source location estimation and velocity inversion are implemented sequentially. We evaluate this iterative method using the Marmousi model dataset. The experiment result and sensitivity analysis indicate that the proposed method is effective to locate the sources and optimize velocity model in the areas with complicated subsurface structures and noisy recordings.

Introduction

The subsurface reservoir properties could be identified using both the active and/or passive-seismic methods. A proven application of the passive-seismic method for oil and gas exploration is the microseismic due to hydraulic fracturing (e.g., Maxwell, 2014; Witten & Shragge, 2017). We generally use fracturing to extract the oil and gas from the subsurface rocks with low permeability such as shale (Maxwell, 2014). To make the oil and gas flow more freely, a high-pressure liquid is then injected into the well to create fracture openings, which will result in microseismic events. We can use the locations of these seismic events to help understand the hydraulic fracturing. Locating microseismic events has also been used in understanding reservoir depletion (e.g., Dohmen et al., 2014) and monitoring seismically active faults (e.g., Wessels et al., 2011). Additionally, passive seismic provides useful information for subsurface structural imaging. For example, Dueker & Sheehan (1997) used a common conversion point (CCP) stacking technique to image the interfaces in the crust and mantle. Shang et al. (2012) decoupled the multi-component recorded data and then extrapolated the P- and S-wavefields for passive-source imaging.

However, we still face several challenges in the passive-seismic. The first one is how to accurately locate these passive-seismic events, which is known as passive-seismic source imaging. We can use the arrival-time differences between pairs of the events to estimate the passive-source-location, which is known as double-difference technique (Waldhauser & Ellsworth, 2000). Later, waveform information is used for source-location estimation (Kao & Shan, 2004), instead of simple the arrival times. Receiver wavefields are extrapolated in the reverse-time direction (McMechan, 1982; Rietbrock &

Scherbaum,1994; Gajewski & Tessmer, 2005; Steiner et al., 2008; Duncan & Eisner, 2010; Li et al., 2019, 2020), which generate a 4D wavefield volume. Then scanning or threshold methods are used to find the focusing and estimate the source location. P- and S-waves could be simultaneously extrapolated using this time-reverse wave propagation method to locate passive sources (e.g., Artman et al., 2010; Yang & Zhu, 2019). Zhu (2014) further improved the imaging quality by compensating for attenuation. To collapse the time axis and improve the resolution of the passive-source imaging, Sun et al. (2015) and Nakata & Beroza (2015, 2016) developed a geometric-mean reverse-time migration (GmRTM) method, which is implemented by a zero-lag cross-correlation among all the independently back-propagated receiver wavefields.

Further, the precision of the subsurface velocity model is a key factor which will affect the estimation of the passive-source location. A velocity model with high precision and resolution is expected for the passive-seismic source imaging. The velocity model is also critical for the seismic structural imaging. Traveltime tomography (Aki et al., 1977; Pratt & Chapman, 1992; Williamson & Worthington, 1993) is commonly employed to estimate the subsurface velocity model but usually provides results with low resolution due to the limitation of the ray theory, which is based on the high-frequency assumption. To improve the resolution, wave-equation based velocity inversion approaches have been developed, which involve full-waveform information, not only the traveltime. Full-waveform inversion (FWI) (Tarantola, 1984) provides a powerful tool to estimate the subsurface model with much higher spatial resolution over the traveltime tomography. FWI represents a series of methods to search for a model which best fits the observed waveforms (e.g., Virieux & Operto, 2009).

FWI has been used in both active-seismic data (Virieux & Operto, 2009; Xu et al., 2012; Warner et al., 2013) and passive-seismic data (Kamei & Lumley, 2014, 2017; Zhu et al., 2015). For the active-seismic FWI, we usually know the source-locations and only need to estimate their signatures. But for the passive-seismic FWI, the unknown source information makes the FWI more challenging. A natural approach of passive FWI is to update the velocity model and source parameters simultaneously (Sun et al., 2016; Igonin & Innanen, 2018; Wang & Alkhalifah, 2018). However, the cross-talk between the velocity model and the source properties challenges the inversion, which is a common difficulty in all multi-parameter FWI algorithms (Brossier et al., 2010; Operto et al., 2013; Innanen, 2014; Pan et al., 2016; Wang et al., 2016).

In this paper, we develop an iterative passive-source estimation and velocity inversion method using GmRTM and FWI. In each iteration, we first estimate the source location using the high-resolution GmRTM method, which provides a better focusing of passive-source imaging compared to conventional wavefield scanning method. Next, the passive-source FWI is followed to optimize the velocity model using the estimated source location provided by GmRTM. The iterations are repeated until convergence, providing the optimized source imaging and velocity model. In this proposed method, the source location estimation and velocity inversion are implemented sequentially, which could partly relax the cross-talk limitation in the simultaneous FWI inversion.

This paper is organized as follows. We begin with this introduction. Next, we illustrate the detailed theory and method of the iterative passive-source estimation and velocity inversion. We then show the numerical results of the Marmousi model. Finally, we provide discussions and conclusions.

Methodology

Focusing on the above three challenges in passive-seismic, we develop an iterative passive-source estimation and velocity inversion method using GmRTM and FWI, which is shown in Figure 2.1. We first input the observed passive-seismic data, and the initial background velocity model, which could be provided by the ray-based tomography methods.

Next, we optimize the passive-source locations and velocity model in an iterative way. In each iteration, we first numerically propagate all the independent receiver or receiver-group wavefields in the reverse-time direction, followed by a zero-lag cross-correlation among all these wavefields, to provide passive-source imaging. This method is known as GmRTM, which provides passive-seismic source estimation with better focusing over conventional time-reversal imaging (Nakata & Beroza, 2016). Further, we perform a passive-source FWI with these estimated source locations, to optimize the velocity model. In the next iteration, we repeat these two sequential steps using the optimized source locations and velocity model from previous iteration until convergence.

In this paper, we focus on this iterative approach of passive-source estimation and velocity inversion. Additionally, we can provide subsurface structural imaging using the optimized source locations and velocity model (see Appendix A). It is implemented by passive-source RTM using both the source- and receiver-side wavefields with a squared excitation-amplitude imaging condition. GmRTM and passive-source FWI are the key techniques used in the proposed iterative passive-source estimation and velocity inversion method.

Passive-source imaging using GmRTM

We start with the wave equation in isotropic acoustic media from a point source with location $\mathbf{x}_s$:

$$\left[\frac{1}{v^2(\mathbf{x})}\frac{\partial^2}{\partial t^2}-\nabla^2\right]u(t,\mathbf{x})=f(t)\delta(\mathbf{x}-\mathbf{x}_s), \tag{1}$$

where $v(\mathbf{x})$ represents the medium velocity, $u(t,\mathbf{x})$ is the wavefield at time t and location $\mathbf{x}=(x,y,z)$, ∇^2 represents the Laplacian operator, and $f(t)$ is the wavelet function.

In equation 1, $u(t,\mathbf{x})$ could represent both the forward-propagated wavefield $u_s(t,\mathbf{x})$ and the backward-propagated wavefield $u_r(t,\mathbf{x})$. For the time-reverse wave propagation method (e.g., Steiner et al., 2008), if the onset time is known, a passive source could be represented by the focusing of all backward-propagated events at the origin time. However, the time information is usually not available. We generally perform a scanning on the 4D receiver wavefields $u_r(t,\mathbf{x})$, to find the time when the wavefields show the maximum amplitude and provide a focused image.

If we consider each receiver or receiver group independently, we can perform a cross-correlation between two or more receiver wavefields, for example the ones with different time lags, to provide another imaging condition. Because the recordings at these receivers are generated by the same seismic source, their corresponding wavefields pass the source location at the same time. We only need to consider the situation when the time lag equals

zero (Claerbout, 1971), which provides a new imaging condition known as GmRTM (Nakata & Beroza, 2016),

$$\Im(\mathbf{x}) = \sum_{t} \prod_{i} u_{r_i}(t, \mathbf{x}). \tag{2}$$

In GmRTM, we first extrapolate the wavefields at the desired receivers, to generate a 4D data volume $u_{r_i}(t, \mathbf{x})$. Next, we multiply all these independent receiver wavefields at the whole space and time, and then sum them over the time axis, which is equivalent to the zero-lag cross-correlation. We can notice that the time axis is collapsed in equation 2 after the summation, which means that GmRTM reduces the dimensions of wavefields scanning method from 4D to 3D. The multiplication in GmRTM will produce images with non-zeros only at the focuses, while in the wavefields scanning method the summation over all the receiver wavefields will lead to images with non-zeros along the wave propagation path. This explains why the GmRTM provides source imaging results with higher spatial resolution.

To compute $u_{r_i}(t, \mathbf{x})$ in equation 2, we need to perform wavefield extrapolation independently for each receiver or receiver group, which could be computationally expensive. A practical solution is to use the same Green's function for different time steps at each receiver (Nakata et al., 2016), to reduce the computational cost, which is due to the linear relationship between the Green's function and the recorded data. This idea is based on the fact that the length of our continuous seismic data is often days to years. This is much longer than the wave propagation time from the source to the receiver, which is typically in seconds. If we directly apply numerical wavefield extrapolation to the continuous data, we need to compute extrapolation for the entire data. Instead, Nakata et

al. (2016) proposed that we first calculate the Green's function for each receiver, and then convolute between this Green's function and the recorded data in the image domain. Although we need to store each Green's function, the computational cost is much smaller than extrapolation of the entire records.

Since we do summation over the time axis as a part of cross-correlation, the source onset time is not a problem in GmRTM. If we are interested in that time, we can find it by selecting the summing time carefully. The source function is another important parameter and varies for different events. In this study, we used a known Ricker wavelet as the source function. We focus on estimating the source location in this paper. Similar to active-source cases (Pratt, 1999), we can invert the source wavelet as well by updating the proposed method.

Velocity optimization using passive-source FWI

FWI uses a non-linear data-fitting procedure to provide detailed estimation of subsurface properties. Here, we primarily focus on the subsurface velocity variations. The general steps of FWI started from an initial velocity model, which could be obtained using a ray-based tomography method. We compute predicted data from this initial model by solving the wave equation. We then update the velocity model, in order to decrease the misfit between the predicted data and the observed data. This optimization procedure is repeated in an iterative way, until the misfit is small enough to meet this criterion.

For passive-source FWI, the source-location is required to perform forward modeling, which is more challenging than active-seismic data. We optimize the passive-source locations and velocity model in an iterative way. In one iteration, an initial estimation of

the source location $\mathbf{x}_{s0}$ is provided by the GmRTM using equation 2, which is used to implement forward modeling using equation 1, to generate the predicted data. The objective function is defined as the data misfit between the predicted data $\mathbf{d}_{pre}$ and the observed data $\mathbf{d}_{obs}$ at each receiver location $\mathbf{x}_g$ measured by the L_2 norm:

$$J = \sum_{\mathbf{x}_s} \sum_{\mathbf{x}_g} \frac{1}{2} \int \left(\mathbf{d}_{obs}\left(\mathbf{x}_{s0}, \mathbf{x}_g, t\right) - \mathbf{d}_{pre}\left(\mathbf{x}_{s0}, \mathbf{x}_g, t\right) \right)^2 dt \,. \tag{3}$$

To solve the above nonlinear problem, local optimization methods are usually preferred due to their computational efficiency. The computation of the gradient with respect to the velocity model is important for FWI. Using the adjoint-state method (Plessix, 2006), we calculate the gradient through the zero-lag cross-correlation between the forward-propagated source wavefields and the backward-propagated wavefields of the data residuals,

$$g\left(\mathbf{x}\right) = \frac{2}{v_0^{\,3}\left(\mathbf{x}\right)} \sum_s \int \frac{\partial u_f\left(\mathbf{x}, t \middle| \mathbf{x}_{s0}\right)}{\partial t} \frac{\partial \delta u_f\left(\mathbf{x}, t \middle| \mathbf{x}_{s0}\right)}{\partial t} dt \,, \tag{4}$$

where $v_0\left(\mathbf{x}\right)$ is the velocity model to be updated, $u_f\left(\mathbf{x}, t \middle| \mathbf{x}_{s0}\right)$ denotes the forward-propagated wavefield, and $\delta u_f\left(\mathbf{x}, t \middle| \mathbf{x}_{s0}\right)$ represents the backward-propagated wavefields of the data residuals.

After calculating the gradient with equation 4, we use the conjugate gradient (CG) method (Mora, 1987; Tarantola, 1987) to update the velocity model. The step length is estimated by a line-search optimization scheme in each iteration. In the next iteration, we repeat GmRTM and passive-source FWI using the optimized source locations and velocity model from the previous iteration until convergence.

Numerical experiments

Experiment setup

We perform a numerical test on the Marmousi model to indicate the effectiveness of the full wave-equation workflow for the passive-seismic imaging and velocity inversion. The true velocity model is shown in Figure 2.2a, with 576 lateral and 188 vertical samples both at 16 m cell size. However, the receivers are usually sparse in microseismic monitoring. In our experiment, the receivers are placed sparsely on the surface with 100 m interval.

The initial velocity model is shown in Figure 2.2b, which is seriously smoothed and relatively far from the true velocity model (Figure 2.2a). This initial velocity model could be generated using a ray-based tomography method. We start with one source located at lateral position of 2.00 km and depth of 2.27 km (black dot in Figure 2.2b). A 2D acoustic finite-difference (FD) modeling method (e.g., McMechan, 1983) is used to generate the synthetic recording.

Source location estimation and velocity inversion with single source

Using the initial velocity model (Figure 2.2b), we first implement GmRTM using 5 receivers to estimate the source location. The enlarged display of GmRTM result is shown in Figure 2.3, which has no time axis. We only need to scan the space axis to find the source location. The source location estimation is provided by finding the focusing in the imaging result (Figure 2.3). However, there is an obvious deviation between the focusing and the true source location (red dot in Figure 2.3) due to the velocity errors. The best focusing is found at the lateral location 1.93 km and depth 2.21 km. It is also noted that the focusing is poor, which also challenges the source location estimation.

Next, we perform passive-source FWI on the recording of the single source in an iterative way, to optimize the initial velocity model (Figure 2.2b). The forward modeling in FWI is implemented using equation 1, starting from the estimated source location (Figure 2.3) using the initial velocity model (Figure 2.2b). The predicted recording using the initial velocity model is shown in Figure 4b, which is far away from the observed recording (Figure 2.4a). In Figure 2.4c, we show the predicted data using the FWI-inverted velocity model after 50 iterations, which reveals most of the details in the observed recording (Figure 2.4a).

Figure 2.5 shows the normalized misfit function versus iteration numbers. Fast convergence rate is observed in the first 17 iterations, and then the convergence becomes slower in the remaining iterations. The inverted velocity model after 50 iterations is shown in Figure 2.6. The source location is indicated by the black dot. The source imprints are observed especially around the source. At present, we are using a smoothing method to reduce this source imprint artifact. More advanced technique is worthy for future research to better eliminate the source imprint and further improve the quality of FWI inverted velocity. Compared with the initial velocity (Figure 2.2b), the FWI-inverted velocity (Figure 2.6) recovers more detailed features and improves the resolution. We can also notice that the improvement of the right part is minor due to the poor illumination caused by the sparse sources, which will be discussed later.

The GmRTM image using the FWI-inverted velocity model is shown in Figure 2.7. It provides a better focusing and a reduced deviation between the focusing and the true source location (red dot in Figure 2.7). The best focusing in Figure 2.7 is found at the lateral location 1.99 km and depth 2.26 km, which effectively improves the prediction precision

of the source location compared to the GmRTM result using the initial velocity model (Figure 2.3).

In simultaneous inversion of passive source location and velocity model, the inversion result depends seriously on the initial velocity model. If the initial velocity is too far away from the true velocity, it is easy to fall into local minima in the simultaneous inversion. In the proposed method of this paper, we use a sequential method for passive source imaging and velocity inversion. Since the source location estimation is performed by finding the best focusing provided by high-resolution GmRTM, which is separate from the passive FWI. This could relax the dependency on the initial velocity model.

Influence of seismic noise on velocity inversion

The field microseismic data are generally noisy, which causes additional challenges for the source location estimation and velocity inversion. To evaluate the influence of seismic noise on passive FWI, we use Madagascar software to generate seismic random noise with broadband spectral, and add it to the noisy-free seismic recording (Figure 2.4a). We use a pseudo-random algorithm for random noise generation, which is realized by setting an initial "seed" for the random number generator. In our research, we use a nearly uniformly distributed sequence for random noise generation. In Figure 2.8a, we show the generated noisy recording with *S/N (signal-to-noise ratio)* = 20 *dB* (decibel). The inverted velocity model (Figure 2.8b) after 50 iterations using this noisy recording contains some artifacts but recovers similar velocity features compared to the FWI-inverted velocity using the noise-free data (Figure 2.6). In Figure 2.8c, we show the normalized misfit function versus iteration numbers using the noisy recording. Similar convergence rate is observed

compared to the misfit function curve using noise-free recording (Figure 2.5), but it is noted that there is relatively larger data residual due to the existence of random noise.

If we further increase the level of noise and generate much noisier recording with *S/N*=5 *dB* (Figure 2.9a) for inversion, the inverted model (Figure 2.9b) can still recover most of the velocity features compared to the model using the noise-free data (Figure 2.6), but much more artifacts are introduced, especially in the shallower part.

Influence of source distribution and density

The velocity structures and resolution of the FWI-inverted model (Figure 2.6) in the right part are improved over the initial velocity model (Figure 2.2b), but are not good enough due to insufficient illumination, as only one source located in the left part is used for inversion. A practical way to improve the illumination is to increase the number of passive-sources used. This is easy to achieve in field surveys; for example, we record numerous microseismic events during hydraulic fracturing.

We first increase the source number to three and still place them in the left part with lateral positions 1.20 km, 2.00 km, and 2.80 km. The receivers are still distributed sparsely, which are the same with our previous experiments. The FWI-inverted velocity model using these three sources are shown in Figure 2.10, which provides higher resolution in the left part and clearer fault features in the middle part over the inverted velocity model using only one source (Figure 2.6). However, the improvement in the right part of the model is still not significant. Next, we still use three sources and sparse receivers for inversion, but place the sources more uniformly in the subsurface with lateral positions 2.00 km, 4.40 km, and 6.80 km. The FWI-inverted velocity model (Figure 2.11) using these more uniformly distributed sources indicates higher resolution and reveals clearer features of the faults and

the anticline in the middle and right part of the Marmousi model over the inverted result shown in Figure 2.10. However, it is also noted that the inverted velocity model using more uniformly distributed sources (Figure 2.11) behaves more artifacts and lower resolution in the left part over the one generated using three sources all located in the left part (Figure 2.10).

We further use 15 uniformly distributed sources for inversion, which are located in the subsurface with starting lateral location 1.200km and 0.480 km interval. We use the same receiver distribution with the previous experiments. The FWI-inverted velocity model using 15 sources is shown in Figure 12a (source locations indicated by black dots), which indicates an obvious improvement of the velocity precision over the results using fewer sources (Figure 2.6, 2.10, and 2.11). Especially, the FWI-inverted velocity model using 15 sources (Figure 2.12a) reveals more and clearer features of the entire Marmousi model, such as the faults, the anticline, and some other small-scale features, compared to the initial velocity model (Figure 2.2b). Figure 2.12b shows the normalized misfit function versus iteration numbers using 15 sources, indicating faster convergence rate compared to the result using single source (Figure 2.5).

Influence of receiver density

We use sparse receivers with the same distribution for all the previous experiments. We also investigate the influence of the receiver density on the inversion, even though the dense receivers are not common in microseismic monitoring. The inversion is performed using 15 uniformly distributed sources at the same locations with the sources used in Figure 2.12a. However, the receiver space is reduced to 16 m. The FWI-inverted velocity model using 15 sources with dense receivers are shown in Figure 2.13. It behaves higher

resolution and reveals more small-scale features over the inverted velocity model using 15 sources with sparse receivers (Figure 2.12a). It is also noted that the influence of source distribution and density play a more important role for inversion over the receiver density.

Discussions

Since we estimate the source location and optimize the velocity model sequentially in the proposed method, the cross-talk limitation in the simultaneous FWI inversion could be partly relaxed. Especially, we use the high-resolution GmRTM to provide a better focusing, which helps to estimate the passive-source location more accurately. However, there is a demanding requirement of the data storage and computation cost of this iterative passive-source estimation and velocity inversion approach.

Both the GmRTM used in passive-source estimation and passive-source FWI used in velocity inversion are time-consuming. For GmRTM, if we perform wavefield extrapolation independently for each receiver or receiver group, it could be computationally expensive. In our research, we first compute and storage the Green's function for each receiver, and then convolute between this Green's function and the recorded data in the image domain, similar to Nakata et al. (2016). This will increase the storage to some extent but will effectively reduce the computation cost. Other effective approaches to reduce the storage and computation cost in the proposed iterative passive-source estimation and velocity inversion method remains an interesting future research topic.

Cycle-skipping challenges both active-source and passive-source FWI. Several theory-based approaches are developed to relax the limitation of cycle-skipping problem in FWI,

but most of the researches focus on the active-source, such as starting FWI with super-low-frequency data (e.g., Wu et al., 2014; Li & Demanet, 2016), separating the tomographic and migration components (e.g., Mora, 1989; Alkhalifah, 2015), or introducing additional dimensions to increase the convexity in waveform inversion (e.g., Sava & Fomel, 2003; Biondi & Almomin, 2014; Warner & Guasch, 2014). For passive-source FWI, since we need to consider the influence of source-locations besides the velocity model, the cycle-skipping problem is more severe than active-source case. In the proposed method, we perform the source location estimation and velocity inversion in a sequential way. GmRTM provides an improved estimation of the source location with high-quality focusing, which helps relax the limitation of cycle-skipping in the simultaneous passive seismic inversion. However, further research is necessary to avoid the cycle-skipping problem in passive imaging and inversion more effectively. A potential solution is to bring the methods used in active-source FWI into passive-source FWI.

Conclusions

We have developed an iterative approach for passive-source estimation and velocity inversion based on full wave-equation methods. In each iteration, we first use the high-resolution GmRTM to estimate the source location. Then passive-source FWI is followed to update the velocity model using the estimated source locations by GmRTM. Passive source location estimation and velocity inversion are implemented sequentially. This iteration is indeed the key for the passive-seismic imaging with velocity estimation, because this iteration allows us to have better focusing of source locations compared to conventional wavefields scanning method, better sensitivity to structural velocities, and the fact that we do not need to rely on the initial source location for the inversion.

The numerical experiments on the Marmousi model indicate that the proposed iterative passive-source estimation and velocity inversion method could be adapted to complicated structures and noisy passive recordings. Increasing source density plays an important role to improve the imaging illumination and inversion quality. This passive-source estimation and velocity inversion is naturally extendable to 3D datasets.

Acknowledgements

The authors would like to thank the colleagues in University of Oklahoma for valuable suggestions. We also thank the Madagascar project for the free software package (Fomel et al., 2013).

Appendix A: Structural imaging using passive-source RTM

Besides passive-source estimation and velocity inversion, we provide the structural imaging using passive-source data in Figure 2.1. The passive-source RTM using multi-component recorded data is performed by a zero-lag cross-correlation between the decoupled P- and S-wavefields (Shang et al., 2012). Only the receiver-side wavefields are used, which is different from the active-source case, which uses both the source- and receiver-side wavefields. Multi-component seismic recordings are needed to perform the cross-correlation, but sometimes we only have vertical-component data. In our research, we adopt a similar idea borrowed from the active-source RTM (McMechan, 1983; Baysal et al., 1983; Whitmore, 1983), to implement the passive-source RTM, which only uses the vertical-component data.

With the estimated source location $\mathbf{x}_s$ and the inverted velocity model $v(\mathbf{x})$ from the iterative approach using GmRTM and passive-source FWI, we first generate the source-

side P-wavefield u_{SP}, followed by the application of imaging conditions with the receiver-side back-propagated P-wavefield u_{RP}, to provide the structural imaging results. There are several different imaging conditions for RTM, such as amplitude-ratio (Claerbout,1971), zero-lag cross-correlation (Claerbout,1971), source-normalized cross-correlation (Claerbout, 1971; Kaelin & Guitton, 2006), excitation time (Chang & McMechan, 1986; Loewenthal & Hu, 1991), excitation amplitude (Nguyen & McMechan, 2013), and squared excitation amplitude (Lyu et al., 2017, 2018).

In this paper, we implement the squared excitation-amplitude imaging condition on the passive-seismic data to provide structural images with high-resolution and fewer migration artifacts. The squared excitation-amplitude imaging condition is expressed as

$$I(\mathbf{x}) = \int_0^T \frac{\left|u_{\mathrm{RP}}(\mathbf{x},t)\right| u_{\mathrm{RP}}(\mathbf{x},t)\,\delta(\mathbf{x},t_e)}{u_{\mathrm{SP\_max}}(\mathbf{x},t_e)\,u_{\mathrm{SP\_max}}(\mathbf{x},t_e)}\,dt \tag{A1}$$

where t_e is the excitation time defined as the maximum source amplitude arrival time, and this amplitude is known as the excitation amplitude $u_{\mathrm{SP\_max}}$. δ represents the delta function of t_e. Equation A1 means that the imaging is only performed at the locations that satisfy the excitation-time. The squared excitation-amplitude imaging condition is actually performed non-linearly, but available to be used for structural imaging. We only need to save the excitation-time and excitation-amplitude during wave propagation, which sidesteps the large storage requirement in the cross-correlation RTM. The imaging is only implemented at the locations that satisfy the excitation-time, which improves the resolution and reduces the migration artifacts.

Following Figure 2.1, we provide the subsurface structural imaging using the passive-source RTM: we first perform the forward modeling of the source wavefields using the

optimized source locations and velocity model, followed by an application of imaging condition with the back-propagated receiver wavefields. We use the high-resolution squared excitation-amplitude imaging condition for passive-source RTM. It faces the multipathing challenge in areas with complicated subsurface structures, as only the most energetic parts of the wavefields are used for imaging. For the left structures of the Marmousi model with relatively small dipping angles, we only need to save one amplitude arrival for imaging. However, it doesn't work in other areas with complicated structures, such as faults and steep reflectors. To deal with this multipathing issue, we save three amplitude arrivals for RTM imaging. It does not require additional wavefield extrapolation, but requires additional three times storage cost of excitation-time and excitation-amplitude. However, the storage cost of three amplitude arrivals is even much smaller than the one in cross-correlation method which saves all the extrapolated wavefields.

We then compute the structural imaging using 15 sources with sparse receivers and show the RTM images in Figure 2.A-1. Compared with the RTM image using the initial velocity model (Figure 2.A-1a), the RTM image using the FWI-inverted (Figure 2.A-1b) provides higher resolution and better focusing. It is also noted that the faults, anticline and some other structures are better imaged in the RTM result using the FWI-inverted velocity model.

References

Aki, K., A. Christofferson, and E. S. Husebye, 1977, Determination of the three-dimensional seismic structure of the lithosphere, Journal of Geophysical Research, **82**, 277–296.

Alkhalifah, T., 2015, Scattering-angle based filtering of the waveform inversion gradients:

Geophysical Journal International, **200**, 363–373.

Artman, B., I. Podladtchikov, and B. Witten, 2010, Source location using time-reverse imaging: Geophysical Prospecting, **58**, 861–873.

Baysal, E., D. D. Kosloff, and J. W. C. Sherwood, 1983, Reverse-time migration: Geophysics, **48**, 1514–1524.

Biondi, B., and A. Almomin, 2014, Simultaneous inversion of full data bandwidth by tomographic full-waveform inversion: Geophysics, **79**, WA129–WA140.

Brossier, R., S. Operto, and J. Virieux, 2010, Which data residual norm for robust elastic frequency-domain full waveform inversion?: Geophysics, **75**, R37–R46.

Chang, W. F., and G. A. McMechan, 1986, Reverse-time migration of offset vertical seismic profiling data using the excitation-time imaging condition: Geophysics, **51**, 67–84.

Claerbout, J., 1971, Toward a unified theory of reflector mapping: Geophysics, **36**, 467–481.

Dohmen, T., J.-P. Blangy, and J. Zhang, 2014, Microseismic depletion delineation: Interpretation, **2**, SG1–SG13.

Dueker, K. G., and A. F. Sheehan, 1997, Mantle discontinuity structure from midpoint stacks of converted P to S waves across the Yellowstone hotspot track, Journal of Geophysical Research, **102**, 8313–8327.

Duncan, P. M., and L. Eisner, 2010, Reservoir characterization using surface microseismic monitoring: Geophysics, **75**, 75A139–75A146.

Fomel, S., P. Sava, I. Vlad, Y. Liu, and V. Bashkardin, 2013, Madagascar: Open-source software project for multidimensional data analysis and reproducible computational

experiments: Journal of Open Research Software, **1**, e8.

Gajewski, D., and E. Tessmer, 2005, Reverse modelling for seismic event characterization: Geophysical Journal International, **163**, 276–284.

Igonin, N., and K. A. Innanen, 2018, Analysis of simultaneous velocity and source parameter updates in microseismic FWI: 88th Annual International Meeting, SEG, Expanded Abstracts, 1033–1037.

Innanen, K. A., 2014, Seismic AVO and the inverse hessian in precritical reflection full waveform inversion: Geophysical Journal International, **199**, 717–734.

Kaelin, B., and A. Guitton, 2006, Imaging condition for reverse time migration: 76th Annual International Meeting, SEG, Expanded Abstracts, 2594–2598.

Kamei, R., and D. Lumley, 2014, Passive-seismic imaging and velocity inversion using full wavefield methods: 84th Annual International Meeting, SEG, Expanded Abstracts, 2273–2277.

Kamei, R., and D. Lumley, 2017, Full waveform inversion of repeating seismic events to estimate time-lapse velocity changes: Geophysical Journal International, **209**, 1239–1264.

Kao, H., and S.-J. Shan, 2004, The source-scanning algorithm: Mapping the distribution of seismic sources in time and space: Geophysical Journal International, **157**, 589–594.

Li, F., Y. Qin, and W. Song, 2019, Waveform inversion-assisted distributed reverse time migration for microseismic location: IEEE Journal of Selected Topics in Applied Earth Observations and Remote Sensing, **12**(4), 1327-1332.

Li, F., T. Bai, N. Nakata, B. Lyu, and W. Song, 2020, Efficient Seismic Source Localization Using Simplified Gaussian Beam Time Reversal Imaging: IEEE Transactions on

Geoscience and Remote Sensing, **58**(6), 4472-4478.

Li, Y. E., and L. Demanet, 2016, Full-waveform inversion with extrapolated low-frequency data: Geophysics, **81**, R339–R348.

Lyu, B., F. Li, and K. J. Marfurt, 2017, High-resolution reverse time migration with squared excitation-amplitude imaging condition: 87th Annual International Meeting, SEG, Expanded Abstracts, 4438–4442.

Lyu, B., N. Nakata, and K. J. Marfurt, 2018, A reverse-time migration workflow of passive source with joint imaging conditions: 88th Annual International Meeting, SEG, Expanded Abstracts, 2947–2951.

Loewenthal, D., and L.Z. Hu, 1991, Two methods for computing the imaging condition for common-shot prestack migration: Geophysics, **56**, 378–381.

Maxwell, S., 2014, Microseismic imaging of hydraulic fracturing: Improved engineering of unconventional reservoirs: SEG.

McMechan, G. A., 1982, Determination of source parameters by wavefield extrapolation, Geophysical Journal of the Royal Astronomical Society, **71**, 613–628.

McMechan, G. A., 1983, Migration by extrapolation of time-dependent boundary values: Geophysical Prospecting, **31**, 413–420.

Mora, P. R., 1987, Nonlinear two-dimensional elastic inversion of multi-offset seismic data: Geophysics, **52**, 1211–1228.

Mora, P., 1989, Inversion = migration + tomography: Springer.

Nakata, N., and G. C. Beroza, 2015, Reverse-Time Migration for Microseismic Sources Using the Geometric Mean as an Imaging Condition: 85th Annual International Meeting, SEG, Expanded Abstracts, 2451–2455.

Nakata, N., G. C. Beroza, J. Sun, and S. Fomel, 2016, Migration-based passive-source imaging for continuous data: 86th Annual International Meeting, SEG, Expanded Abstracts, 2607–2611.

Nakata, N., and G. C. Beroza, 2016, Reverse time migration for microseismic sources using the geometric mean as an imaging condition: Geophysics, **81**, no. 2, KS51–KS60.

Nguyen, B. D., and G. A. McMechan, 2013, Excitation-amplitude imaging condition for prestack reverse-time migration: Geophysics, **78**, S37–S46.

Operto, S., Y. Gholami, V. Prieux, A. Ribodetti, R. Brossier, L. Metivier, and J. Virieux, 2013, A guided tour of multiparameter full-waveform inversion with multicomponent data: From theory to practice: The Leading Edge, **32**, 1040–1054.

Pan, W., K. A. Innanen, G. F. Margrave, M. C. Fehler, X. Fang, and J. Li, 2016, Estimation of elastic constants for HTI media using gauss-newton and full-newton multiparameter full-waveform inversion: Geophysics, **81**, R275–R291.

Plessix, R.-E., 2006, A review of the adjoint-state method for computing the gradient of a functional with geophysical applications: Geophysical Journal International, **167**, 495–503.

Pratt, R. G., and C. H. Chapman, 1992, Traveltime tomography in anisotropic media – II. Application, Geophysical Journal International, **109**, 20–37.

Pratt, R. G., 1999, Seismic waveform inversion in the frequency domain, Part I: Theory and verification in a physical scale model: Geophysics, **64**, 888–901.

Rietbrock, A., and F. Scherbaum, 1994, Acoustic imaging of earthquake sources from the Chalfant Valley, 1986, aftershock series, Geophysical Journal International, **119**, 260–268.

Sava, P. C., and S. Fomel, 2003, Angle-domain common-image gathers by wavefield continuation methods: Geophysics, **68**, 1065–1074.

Shang, X., M. V. Hoop, and R. D. Hilst, 2012, Beyond receiver functions: Passive source reverse time migration and inverse scattering of converted waves: Geophysical Research Letters, **39**, L15308.

Steiner, B., E.H. Saenger, and S. M. Schmalholz, 2008, Time reverse modeling of low-frequency microtremors: A potential method for hydrocarbon reservoir localization: Geophysical Research Letters, **35**, L03307.

Sun, J., T. Zhu, S. Fomel, and W. Song, 2015, Investigating the possibility of locating microseismic sources using distributed sensor networks: 85th Annual International Meeting, SEG, Expanded Abstracts, 2485–2490.

Sun, J., Z. Xue, T. Zhu, S. Fomel, and N. Nakata, 2016, Full-waveform inversion of passive-seismic data for sources and velocities: 86th Annual International Meeting, SEG, Expanded Abstracts, 1405–1410.

Tarantola, A., 1984, Inversion of seismic reflection data in the acoustic approximation: Geophysics, **49**, 1259–1266.

Tarantola, A., 1987, Inverse problem theory: Methods for data fitting and model parameter estimation: Elsevier Science Publ. Co., Inc.

Virieux, J., and S. Operto, 2009, An overview of full-waveform inversion in exploration geophysics: Geophysics, **74**, WCC1–WCC26.

Waldhauser, F., and W. L. Ellsworth, 2000, A double-difference earthquake location algorithm: Method and application to the Northern Hayward Fault, California: Bulletin of the Seismological Society of America, **90**, 1353–1368.

Wang, Y., L. Dong, Y. Liu, and J. Yang, 2016, 2D frequency-domain elastic full-waveform inversion using the block-diagonal pseudo-Hessian approximation: Geophysics, **81**, R247–R259.

Wang, H., and T. Alkhalifah, 2018, Microseismic imaging using a source function independent full waveform inversion method: Geophysical Journal International, **214**, 46–57.

Warner, M., A. Ratcliffe, T. Nangoo, J. Morgan, A. Umpleby, N. Shah, V. Vinje, I. Štekl, L. Guasch, C. Win, G. Conroy, and A. Bertrand, 2013, Anisotropic 3D full-waveform inversion: Geophysics, **78**, R59–R80.

Warner, M., and L. Guasch, 2014, Adaptive waveform inversion: Theory: 84th Annual International Meeting, SEG, Expanded Abstracts, 1089–1093.

Wessels, S. A., A. De La Pena, M. Kratz, S. Williams-Stroud, and T. Jbeili, 2011, Identifying faults and fractures in unconventional reservoirs through microseismic monitoring: First Break, **29**, 99–104.

Witten, B., and J. Shragge, 2017, Microseismic image-domain velocity inversion: Marcellus Shale case study: Geophysics, **82**, KS99–KS112.

Whitmore, D. N., 1983, Iterative depth imaging by back time propagation: 53rd Annual International Meeting, SEG, Expanded Abstracts, 382–386.

Williamson, P. R., and M. H. Worthington, 1993, Resolution limits in ray tomography due to wave behavior: numerical experiments, Geophysics, **58**, 727–735.

Wu, R.-S., J. Luo, and B. Wu, 2014, Seismic envelope inversion and modulation signal model: Geophysics, **79**, WA13-WA24.

Xu, S., D. Wang, F. Chen, Y. Zhang, and G. Lambare, 2012, Full waveform inversion for

reflected seismic data: 74th Annual International Conference and Exhibition, EAGE, Extended Abstracts, W024.

Yang, J., and H. Zhu, 2019, Locating and monitoring microseismicity, hydraulic fracture and earthquake rupture using elastic time-reversal imaging: Geophysical Journal International, **216**, 1919–1937.

Zhu, H., E. Bozdağ, and J. Tromp, 2015, Seismic structure of the European upper mantle based on adjoint tomography: Geophysical Journal International, **201**, 18–52.

Zhu, T., 2014, Time-reverse modelling of acoustic wave propagation in attenuating media: Geophysical Journal International, **197**, 483–494.

Chapter 2 figures

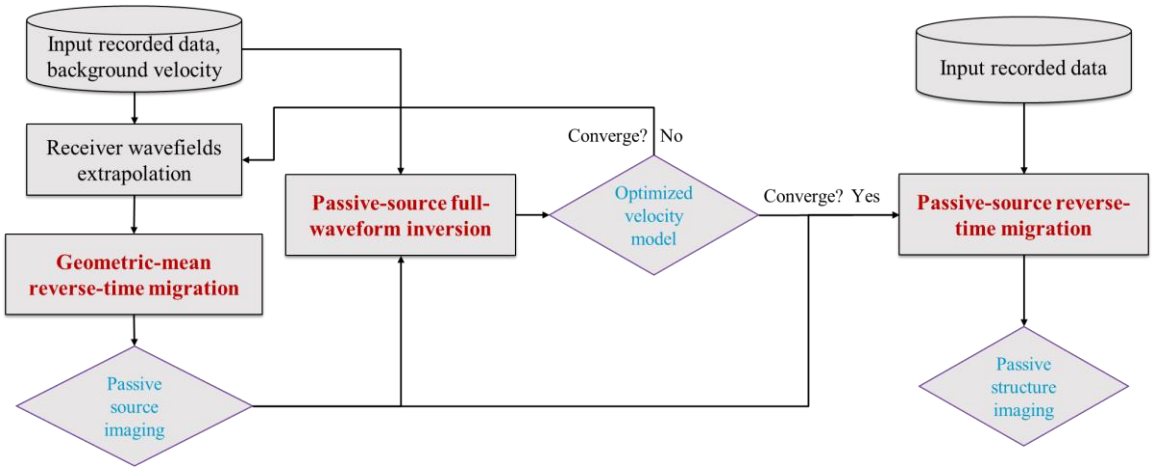

Figure 2.1. Iterative passive-source estimation and velocity inversion method using GmRTM and passive-source FWI.

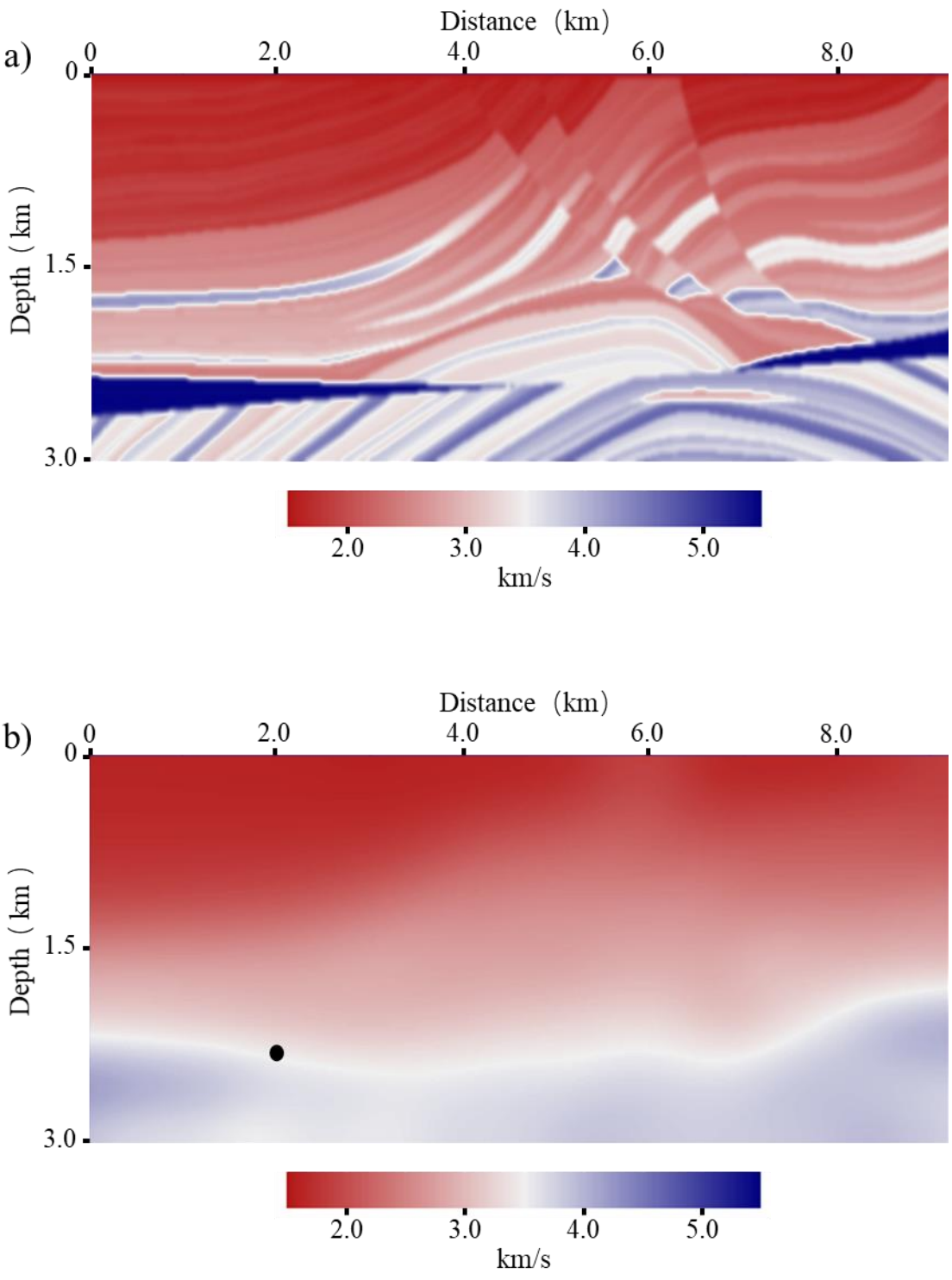

Figure 2.2. (a) True Marmousi velocity model. (b) Initial velocity model.

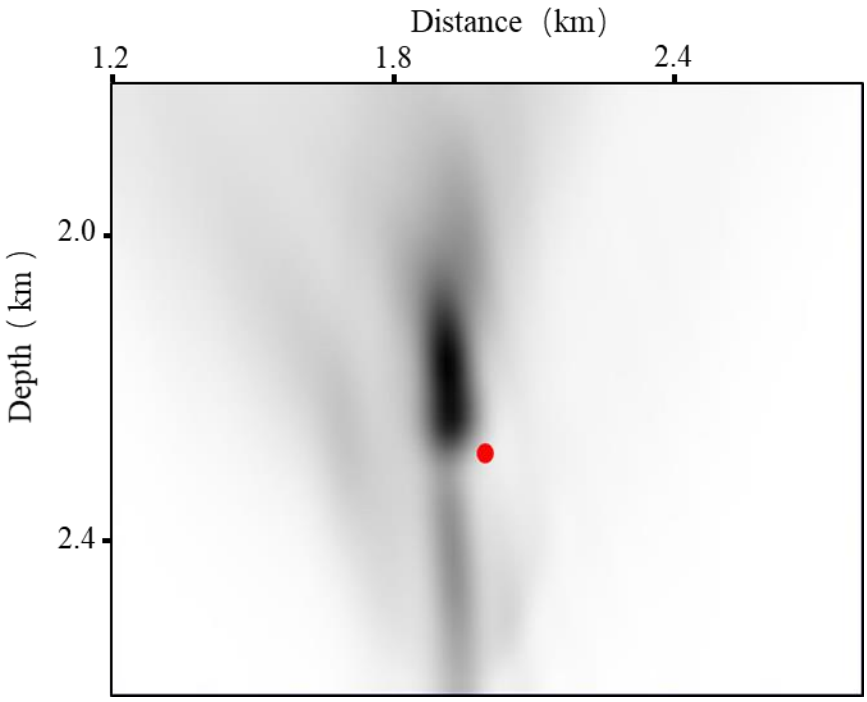

Figure 2.3. GmRTM result using the initial velocity model, behaving poor focusing and an obvious deviation between the focusing and the true source location (red dot).

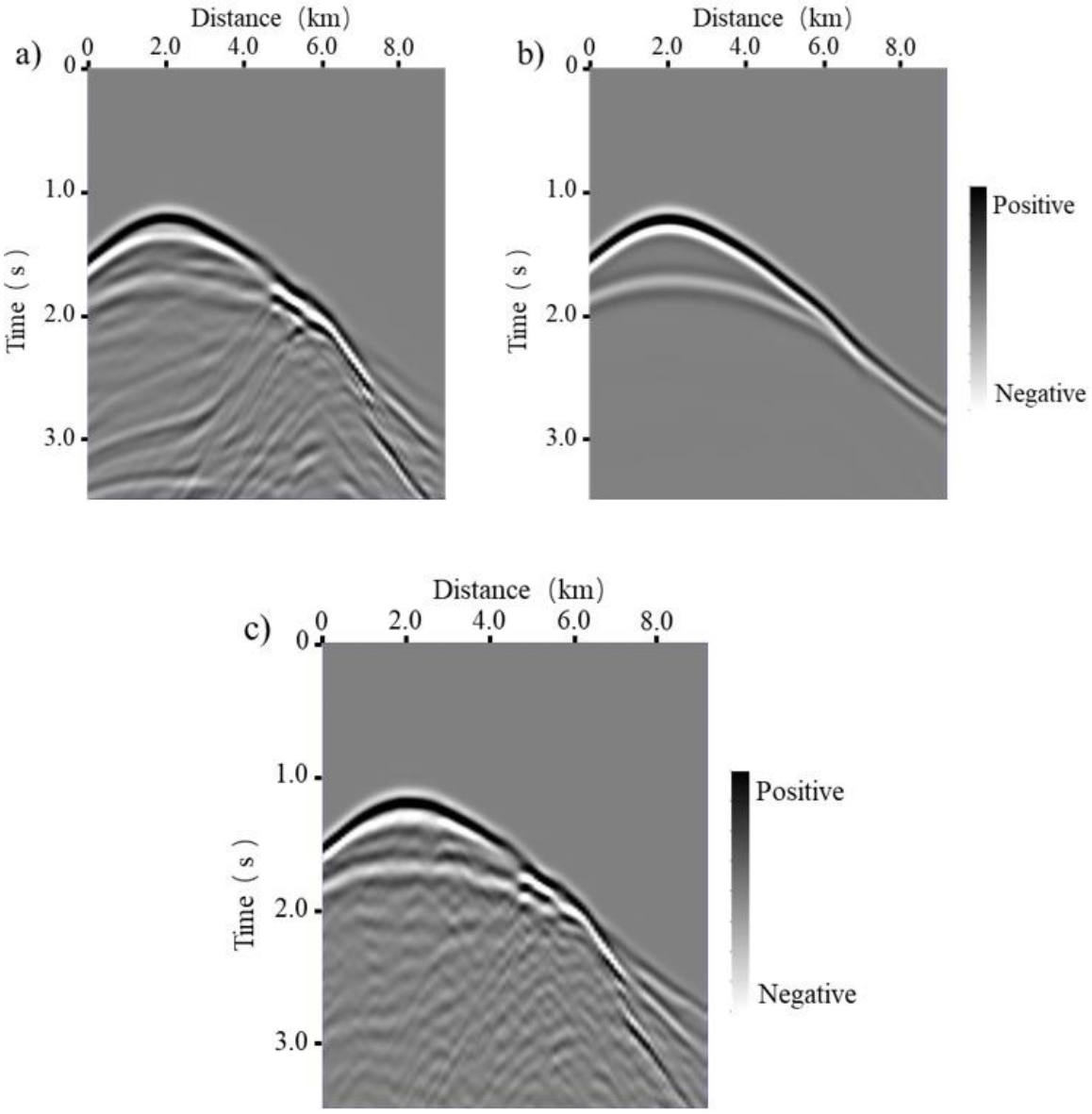

Figure 2.4. (a) Observed recording, (b) predicted recording using the initial velocity model, and (c) predicted recording using the FWI-inverted velocity model.

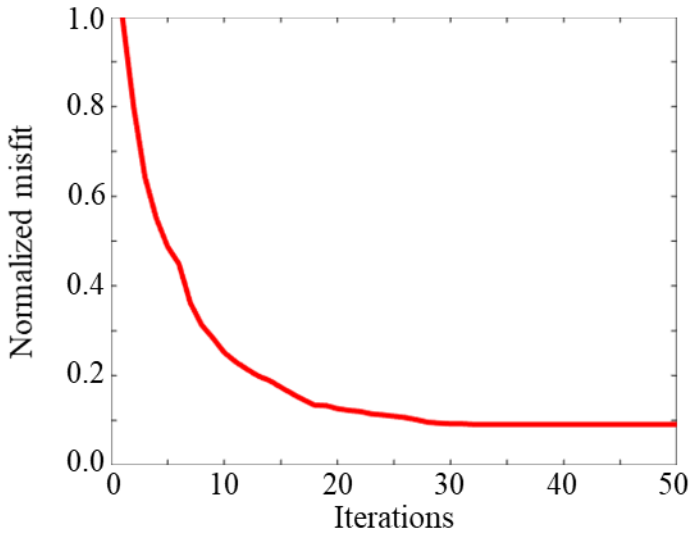

Figure 2.5. Normalized misfit function versus iteration numbers using single source.

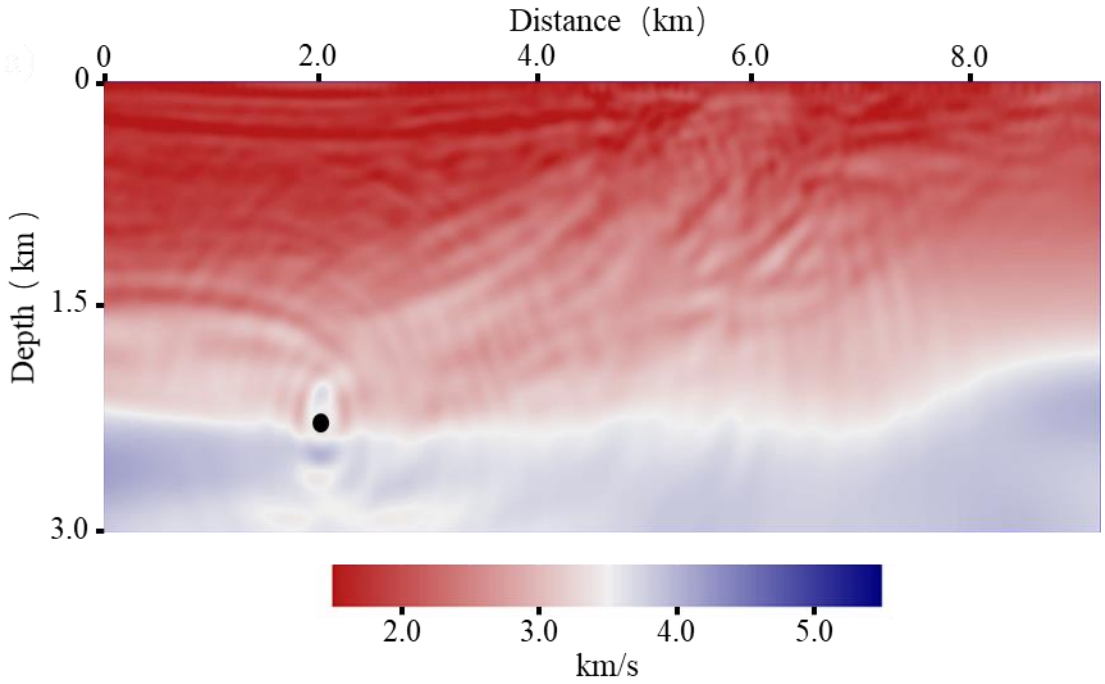

Figure 2.6. FWI-inverted velocity model using only one source located at lateral position 2.00 km and depth 2.27 km. Note that the FWI-inverted velocity recovers more detailed features and improves the resolution over the initial velocity model. It is also noted that the improvement of the right part is minor due to the poor illumination caused by the sparse sources.

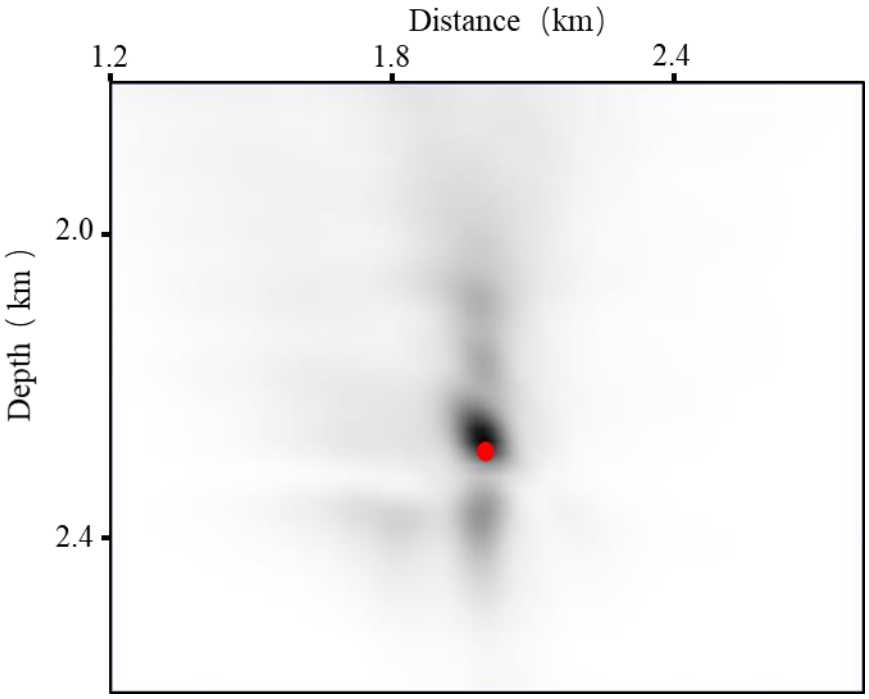

Figure 2.7. GmRTM recalculated using the FWI-inverted velocity model, providing a better focusing and a reduced deviation between the focusing and the true source location (red dot) compared to the GmRTM result using the initial velocity model (Figure 2.3).

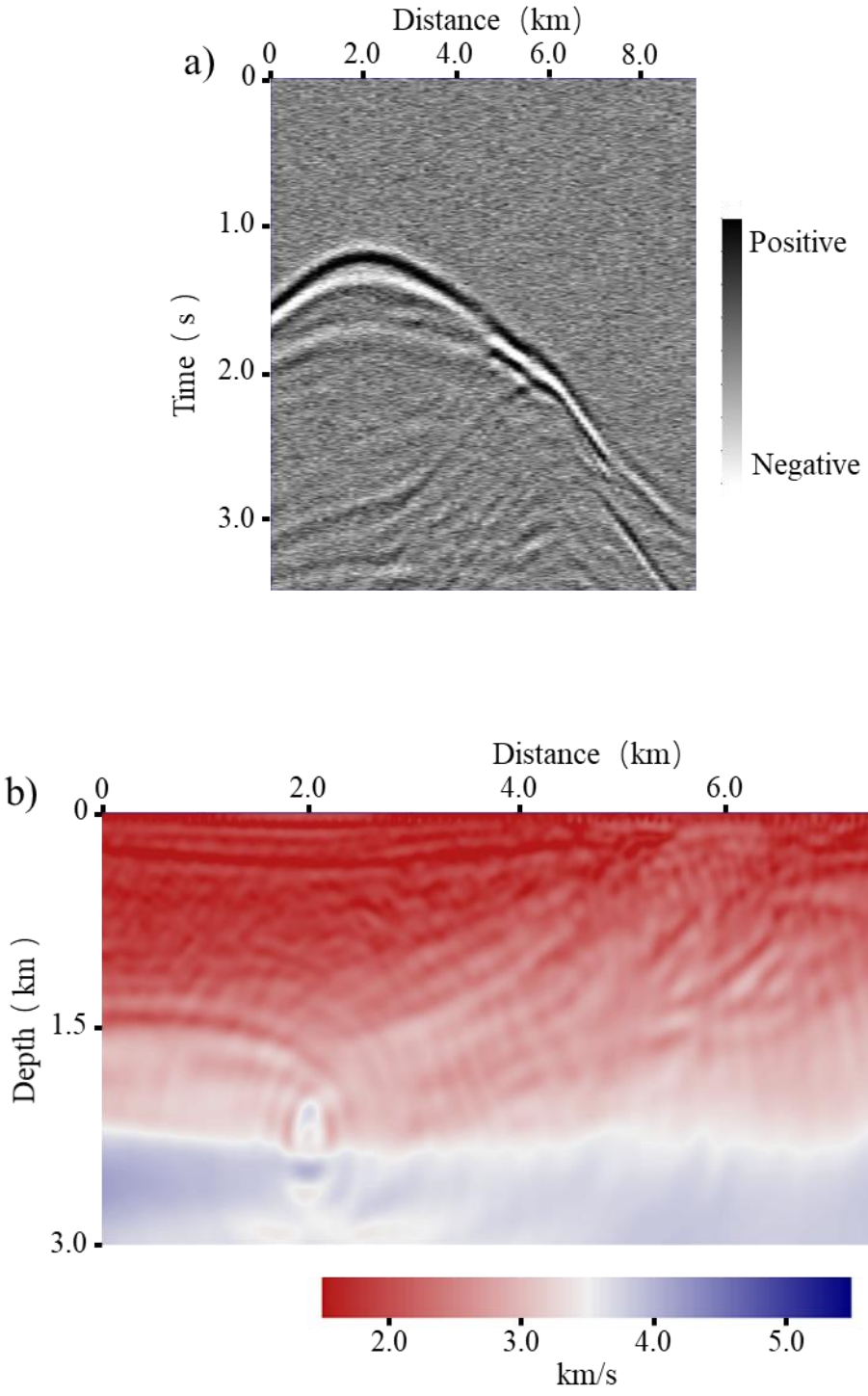
a)
Distance (km)
0
2.0
4.0
6.0
8.0
Time (s)
1.0
2.0
3.0
Positive
Negative
b)
Distance (km)
0
2.0
4.0
6.0
8.0
Depth (km)
1.5
3.0
2.0
3.0
4.0
5.0
km/s

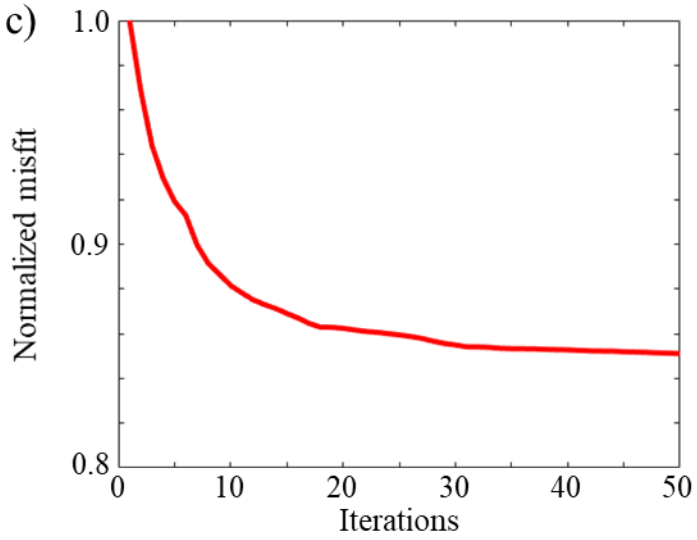

Figure 2.8. (a) Noisy passive-source recording with *S/N*=20 *db*, and (b) the corresponding FWI-inverted velocity model, behaving more artifacts but recovering similar velocity features compared to the FWI-inverted velocity using the noise-free data (Figure 2.6). (c) Normalized misfit function versus iteration numbers using the noisy recording, showing similar convergence rate but relatively larger data residual compared to the result using noise-free recording (Figure 2.5).

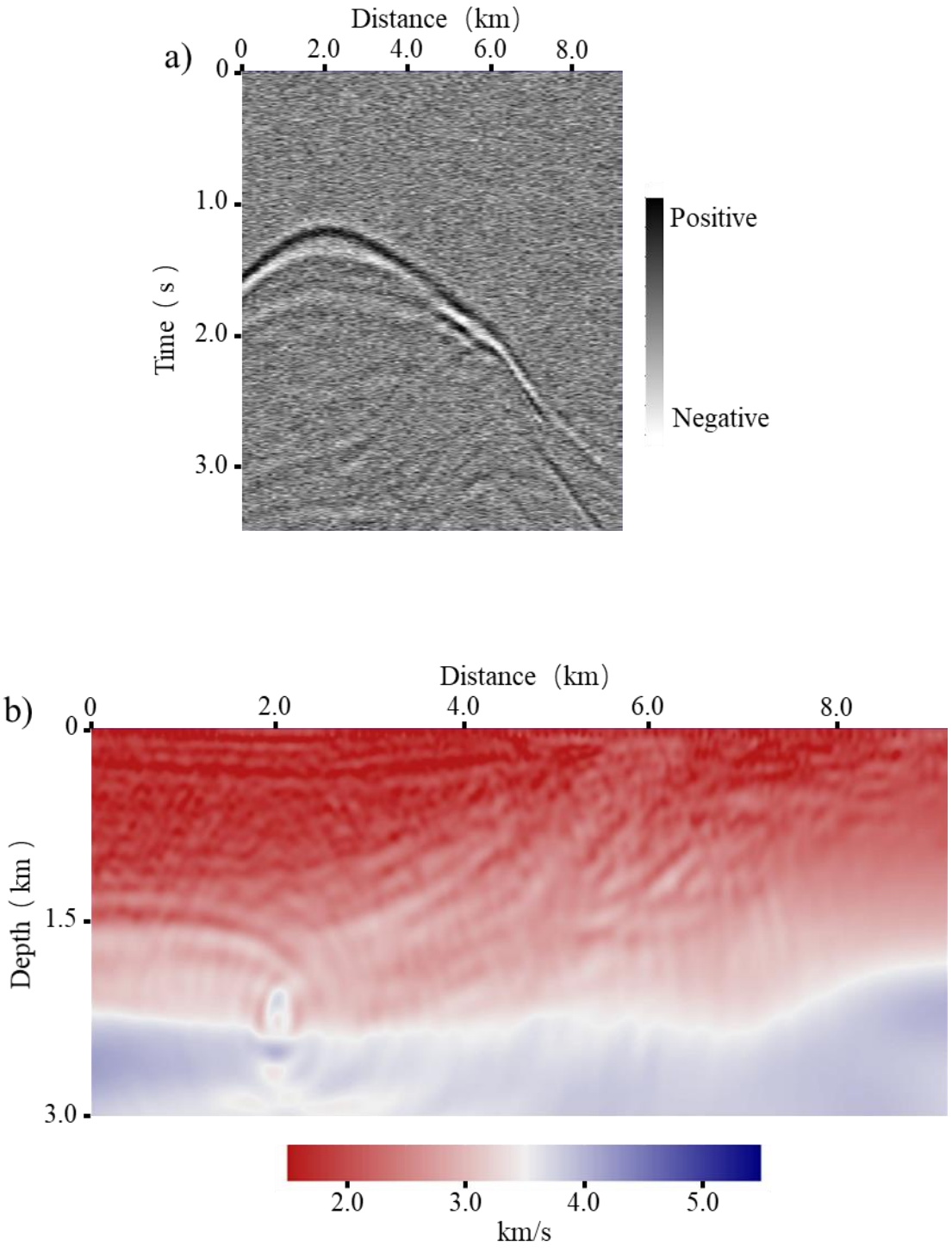

Figure 2.9. (a) Noisy passive-source recording with *S/N*=5 *db*, and (b) the corresponding FWI-inverted velocity model.

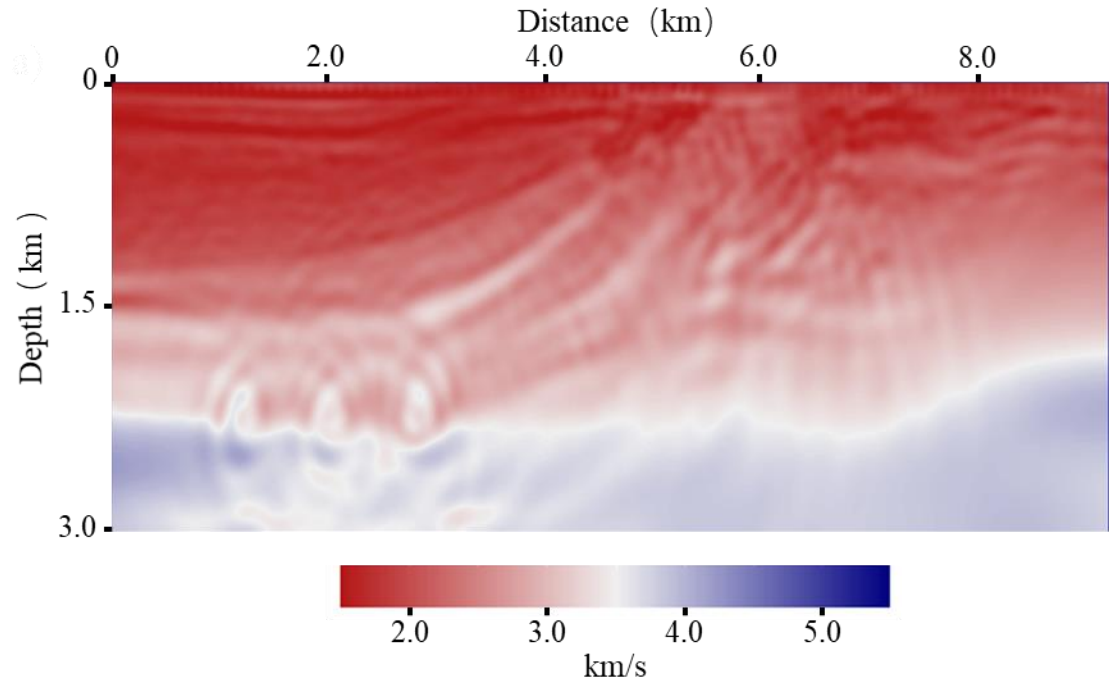

Figure 2.10. FWI-inverted velocity model using three sources located in the left part with lateral positions 1.200 km, 2.000 km, and 2.800 km. Note the higher resolution in the left part and clearer fault features in the middle part compared to the inverted velocity model using only one source (Figure 2.6). However, the improvement in the right part of the model is still not significant.

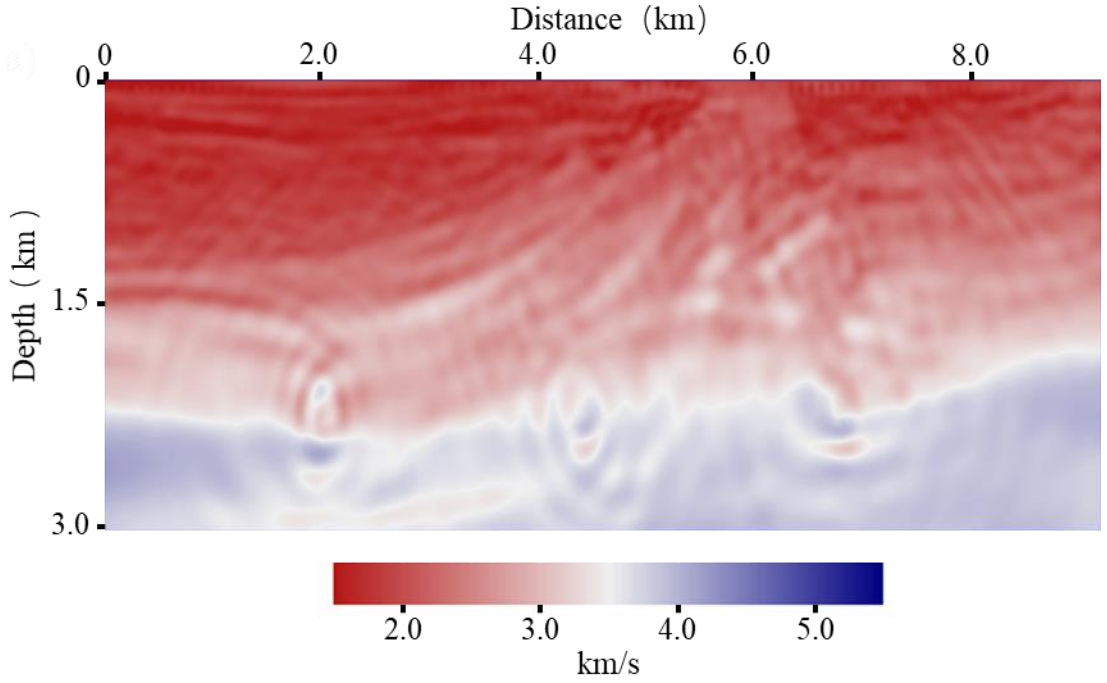

Figure 2.11. FWI-inverted velocity model using three more uniformly distributed sources with lateral positions 2.00 km, 4.40 km, and 6.80 km. Note the higher resolution and clearer features of the faults and the anticline in the middle and right part over the inverted velocity model shown in Figure 2.10. However, it behaves more artifacts and lower resolution in the left part over the one generated using three sources all located in the left part (Figure 2.10).

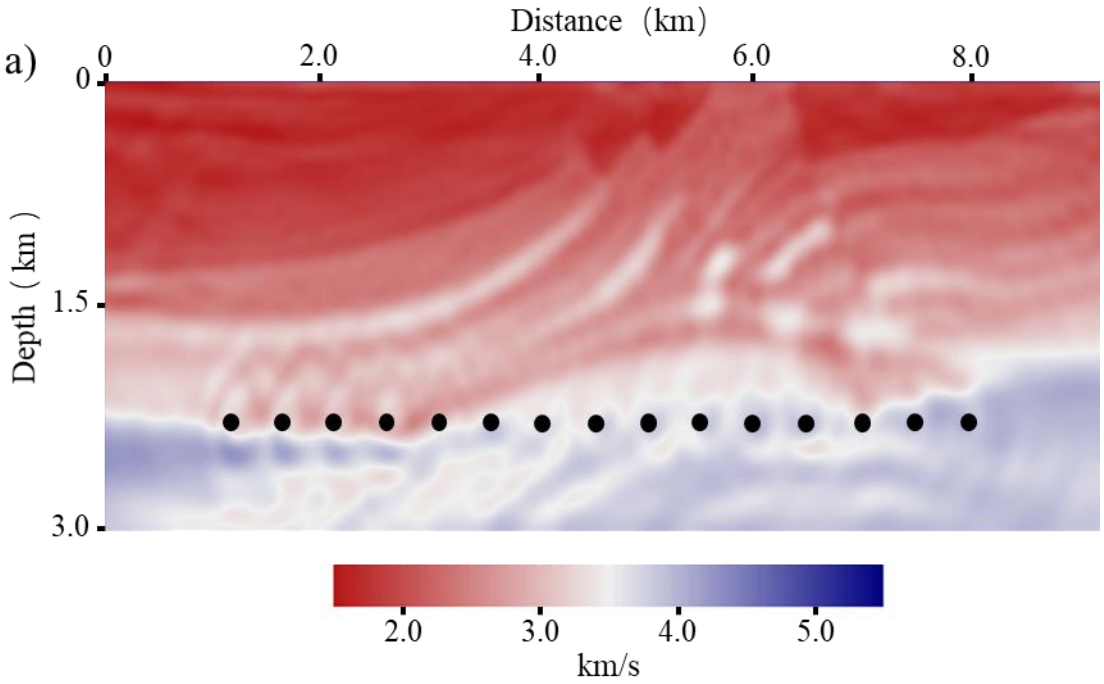

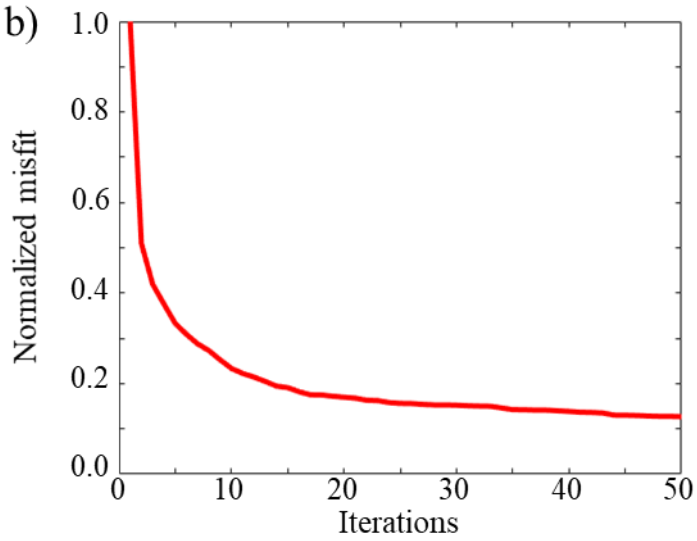

Figure 2.12. (a) FWI-inverted velocity model using 15 sources with sparse receivers, indicating an obvious improvement over the results using fewer sources and revealing much clearer features. (b) Normalized misfit function versus iteration numbers using 15 sources, indicating faster convergence rate compared to the result using single source (Figure 2.5).

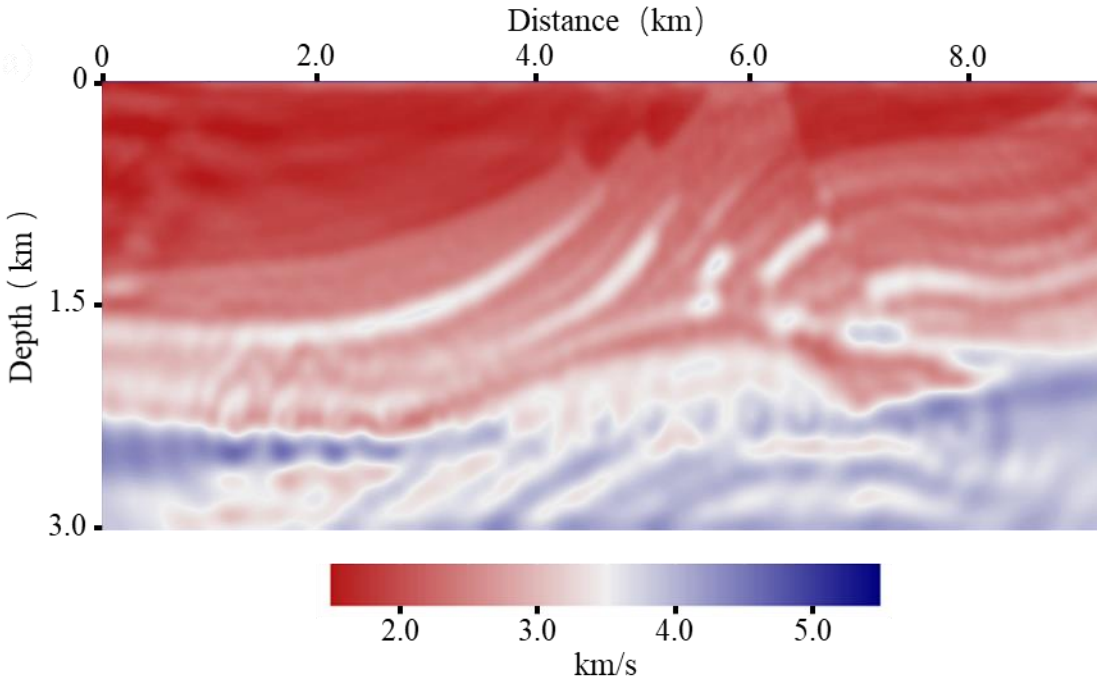

Figure 2.13. FWI-inverted velocity model using 15 sources with dense receivers, behaving higher resolution and revealing more small-scale features over the FWI-inverted model using 15 sources with sparse receivers (Figure 2.12a).

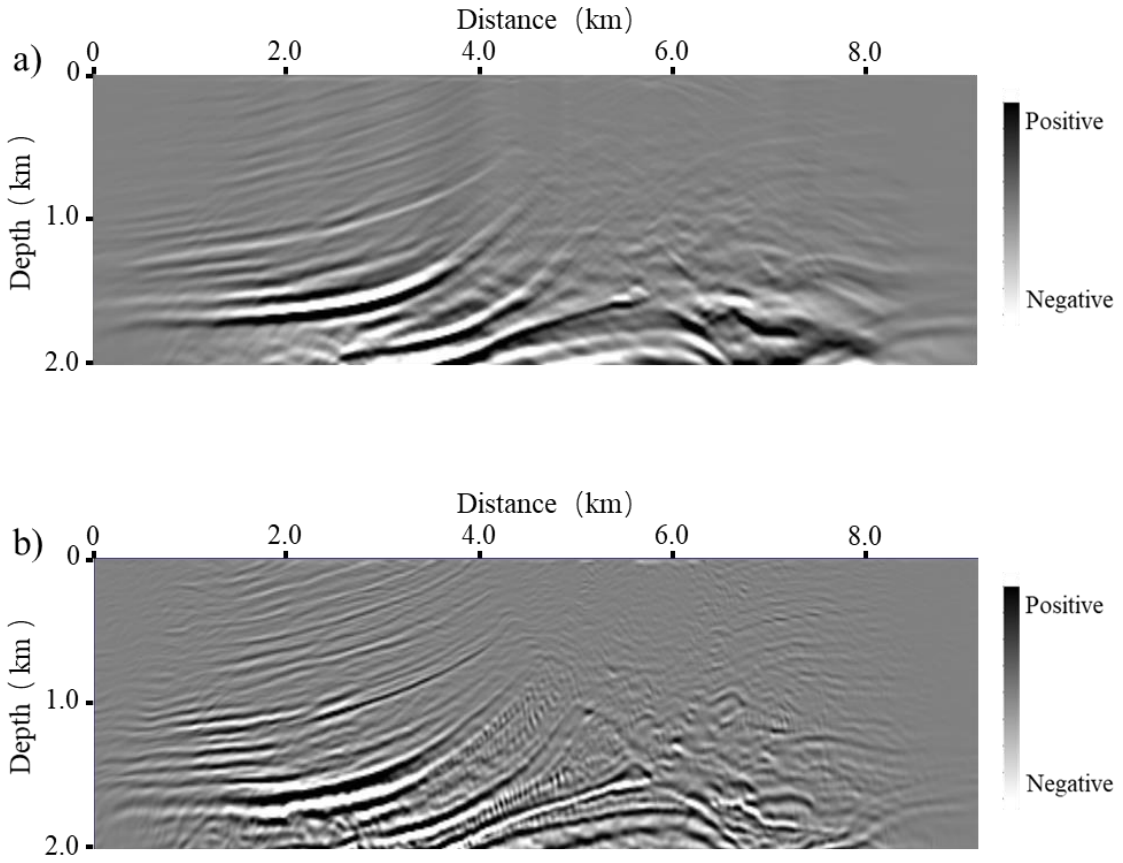

Figure 2.A-1. Structural image by passive-source RTM with 15 sources using (a) the initial velocity model, and (b) the FWI-inverted velocity model, providing higher resolution, better focusing, and clearer structures.

CHAPTER 3: MULTISPECTRAL COHERENCE: WHICH DECOMPOSITION SHOULD WE USE?

Abstract

Seismic coherence is commonly used to delineate structural and stratigraphic discontinuities. We generally use full-bandwidth seismic data to calculate coherence. However, some seismic stratigraphic features may be buried in this full-bandwidth data, but can be highlighted by certain spectral components. Due to thin-bed tuning phenomena, discontinuities in a thicker stratigraphic feature may be tuned and thus better delineated at a lower-frequency, while discontinuities in the thinner units may be tuned and thus better delineated at a higher-frequency. Additionally, whether due to the seismic data quality or underlying geology, certain spectral components exhibit higher quality over other components, resulting in correspondingly higher quality coherence images. Multispectral coherence provides an effective tool to exploit these observations. We evaluate the performance of multispectral coherence using different spectral decomposition methods: continuous wavelet transform (CWT), maximum entropy, amplitude volume technique (AVT), and spectral probe. Applications to a 3D seismic data volume show that multispectral coherence images are superior to full-bandwidth coherence, providing better delineation of incised channels with less noise. From the CWT experiments, we find that providing exponentially-spaced CWT components provides better coherence images than equally-spaced components for the same computation cost. The multispectral coherence image computed using maximum entropy spectral voices further improves the resolution of the thinner channels and small-scale features. The coherence from AVT dataset provides continuous images of thicker channel boundaries, but poor images of the small-scale

features inside the thicker channels. Additionally, multispectral coherence computed using the nonlinear spectral probes exhibits more balanced and reveals clear small-scale geologic features inside the thicker channel. However, because amplitudes are not preserved in the nonlinear spectral probe decomposition, noise in the noisier shorter-period components have an equal weight when building the covariance matrix, resulting in increased noise in the generated multispectral coherence images.

Introduction

Seismic coherence is a measure of the similarity between the waveforms or traces in seismic data volumes. It is a powerful tool to delineate seismic discontinuities such as faults and stratigraphic edges, incoherent zones such as the karst collapse and mass transport complexes, as well as areas contaminated by seismic noise. Bahorich and Farmer (1995) evaluated 3D seismic discontinuity coherence by calculating the maximum cross-correlation value with neighboring traces. Marfurt et al. (1998) developed a more robust coherence estimation method, which is based on a multi-trace semblance algorithm, to improve the noise reduction ability. Gersztenkorn and Marfurt (1999) introduced another coherence calculation method, which is realized by calculating the energy-ratio between the dominant eigenvalues and the sum of all eigenvalues of the covariance matrix, to improve the lateral resolution. Marfurt et al. (1999) further improved the algorithm, which considers the structural dip effect on the coherence estimation, to provide better results.

Coherence is generally calculated from the full-bandwidth seismic data. The quality of the coherence images is dependent on the quality of the input seismic data, which could be improved using the structural-oriented filtering (SOF), spectral balancing, and other post-migration data conditioning methods (Chopra and Marfurt, 2007). Furthermore,

different spectral components often illuminate different geologic features (Partyka et al., 1999), where Peyton et al. (1998) found that the 36 Hz spectral component image among the results between 20 Hz and 50 Hz could best delineate the edges of incised valleys in a Red Fork, Oklahoma formation. Marfurt and Kirlin (2001), and Laughlin et al. (2002) showed that the thickness of the channels is strongly related with their spectral amplitude due to the thickness tuning: a lower peak frequency indicating thicker formations while a higher peak frequency indicating thinner formation. Zeng (2014) interpreted the spatial geometry and stacking pattern of seismically thin-beds using seismic sedimentology-based approach. An observation was obtained from a synthetic model that one can characterize a thin-bed depositional system by a seismic-geomorphologic pattern of the same spatial shape on sequential relative geologic time slices, but the amplitude, phase, and polarity would vary depending upon the estimated seismic wavelet. Hardage (2009), and Lyu et al. (2018) reported that certain spectral components of the seismic data provide higher quality results over the other components.

Alaei (2012), and Li and Lu (2014) computed coherence from different spectral components and co-rendered them using RGB blending to illuminate channels, caves, and karsts. Wang et al. (2018) developed a 3D geosteering coherence attribute and used it to detect deep-formation discontinuities. Wang et al. (2019) further used the multispectral phase information to combine the geosteering coherence and displayed the result using RGB blending. Noticing that such analysis was limited to only three spectral coherence volumes, Marfurt (2017), and Li et al. (2018) generalized these concepts by introducing what they called multispectral coherence, where the covariance matrices from each bandpass filtering bank are added prior to computing the coherence attribute. The case

studies of channel boundary highlighting (Li et al., 2018) and fault enhancement (Lyu et al., 2019) indicate the effectiveness of this multispectral coherence method. Qi et al. (2019), and Chopra and Marfurt (2019) generalized this concept further to compute coherence not only from multiple spectral components, but also from multiple azimuth and offset components.

There are several popular seismic spectral decomposition algorithms including the continuous wavelet transform (CWT) (Sinha et al., 2005), matching pursuit (Castagna et al., 2003; Liu and Marfurt, 2007), and a technique based on maximum entropy called constrained least-squares spectral analysis (Puryear et al., 2012). This later approach has superior time and frequency resolution. Other techniques are similar to spectral decomposition in that they enhance certain window spectral components to facilitate the identification of lateral discontinuities and vertical unconformities, but do not attempt to reconstruct the original data. Gao (2013) introduced a spectral probe technique, which simply cross-correlates sines and cosines with the seismic data, and outputs the cross-correlation coefficient as an attribute. A related (also nonlinear) technique is called the amplitude volume technique (AVT) (Bulhões, 1999; Bulhões and Amorin, 2005), which enhances the low-frequency information in the seismic data.

Although more expensive than computing coherence from a single full-bandwidth seismic volume, multispectral coherence provides significantly enhanced images. In this paper, we first examine which multispectral coherence provides better images: computed using equally or exponentially sampled frequencies. We further examine whether multispectral coherence computed from the high-resolution maximum entropy spectral decomposition provides higher resolution images. Besides the CWT and maximum entropy

decomposition methods, we augment this relatively long list of decomposition algorithms with the nonlinear spectral probe and AVT methods.

We begin our paper by illustrating the generalized workflow used to compute the multispectral coherence from the original full-bandwidth seismic data. We then discuss the theory of seismic spectral decomposition methods. Next, we evaluate these methods using a 3D seismic data volume with a complex suite of incised channels, acquired over the southwest coast of the North Island, New Zealand. Finally, we conclude with summary comments and recommendations.

Method

Multispectral coherence workflow

In Figure 3.1, we show the workflow to compute the multispectral coherence attribute on the decomposed spectral components from the original full-bandwidth seismic data. The quality of the coherence images is dependent on the quality of the input seismic data. Chopra and Marfurt (2007) gave suggestions to improve the seismic data quality using some post-migration data conditioning methods.

There are different types of noise in the coherence images. Marfurt and Alves (2014) discussed the pitfalls in seismic interpretation caused by seismic noise and processing errors. The coherence images may suffer from two categories of noise: seismic noise and "geology" noise.

Seismic noise, for example acquisition footprint, random noise, and migration aliasing, plays a negative role in delineating geologic features. The quality of the coherence images

is definitely decreased in presence of such noise, which is expected to be suppressed before coherence computation.

Another type of noise in coherence images is from chaotic geology features such as fault damage zones, or condensed sections, etc. These features also exhibit discontinuities in the coherence images, which should always be preserved. They are considered as geology "noise" if we try to delineate the incised channel boundaries, but they may be geologic indicators for other geology purposes (Marfurt and Alves, 2014).

In our workflow, we first perform the structure-oriented filtering (SOF) on the input full-bandwidth seismic amplitude volume, to suppress the seismic noise and improve the data quality. SOF is a robust filtering method, avoiding the smearing of faults, fractures, and other seismic discontinuities.

Next, we decompose the full-bandwidth seismic data after SOF into different spectral components. We evaluate several different spectral decomposition methods, including not only the CWT and maximum entropy decomposition, but also the AVT and spectral probe methods.

We then build the covariance matrix, to combine multiple coherence attributes together into a single volume. Dewett and Henza (2015) used a self-organizing map method for combination. Sui et al. (2015) computed coherence using only the spectral magnitudes without the phase information, which couldn't handle the complicated structures. To improve the adaptability, we follow the idea of Marfurt (2017) to build the covariance matrix using the spectral voices, considering both the spectral magnitude and phase information.

The spectral voices are defined as

$$u(f_l, t_k, x_m, y_m) = a(f_l, t_k, x_m, y_m)\mathbf{exp}\left[i\varphi(f_l, t_k, x_m, y_m)\right] \quad (1)$$

where u represents the spectral voice of frequency f, a is the magnitude component, φ denotes the phase component, and l is the component number. t_k denotes the structurally interpolated time sample at a distance (x_m, y_m) from the coordinate origin point.

The spectral voice u in equation 1 and the corresponding analytic trace u^H are used to compute each element C_{mn} of the covariance matrix **C** along the structures, which considers both the magnitude and phase components:

$$C_{mn} = \sum_{l=1}^{L}\sum_{k=-K}^{K}\left[u(t_k, f_l, x_m, y_m)u(t_k, f_l, x_n, y_n) + u^H(t_k, f_l, x_m, y_m)u^H(t_k, f_l, x_n, y_n)\right] \quad (2)$$

We use equation 2 to build the covariance matrix from different spectral components, which adapts to complicated geologic structures. For a specific spectral component, we can improve the quality of particular structures in the coherence image because the signal appears stronger than noise, further resulting in an improvement in the combined coherence attribute.

The final step is to compute the coherence attributes on the generated covariance matrix. The fact that coherence should be computed along structural dip has been known for some time (Marfurt et al., 1999). In our research, we used a Gradient Structure Tensor (GST) method to compute the inline and crossline dip attributes for the following coherence computation. We can output both the coherence volumes from each spectral component and the combined multispectral coherence dataset. In our research, we use the

energy-ratio method of Gersztenkorn and Marfurt (1999) for coherence computation, which is also used to provide the input for the fault skeletonization (Qi et al., 2016, 2019). This coherence computation method is realized by calculating the energy-ratio between the dominant eigenvalues and the sum of all eigenvalues of the covariance matrix. The details of the energy-ratio method are shown in Appendix A.

Seismic spectral decomposition algorithms

Seismic spectral decomposition (Partyka et al., 1999) is an important step in the multispectral coherence computation workflow (Figure 3.1). We can decompose the full-bandwidth seismic data into different spectral components using linear or nonlinear decomposition methods. In our research, we first evaluate the application of CWT and maximum entropy decomposition methods for multispectral coherence computation, which could reconstruct the original full-bandwidth seismic data.

CWT (continuous wavelet transform) is defined based on the scaled and shifted versions of a "mother wavelet", which is a complex exponential of a frequency within a Gaussian temporal window (Grossmann and Morlet, 1984). We perform CWT by first cross-correlating the library of these wavelets with seismic trace then followed by summation over time (Appendix B). CWT is widely used in seismic interpretation, for example, Matos et al. (2011) indicated that we can use the Morlet complex wavelet transform to detect the phase discontinuities, and Davogustto et al. (2013) used the spectral ridges and phase residues to correlate with subtle stratigraphic features.

CWT provides time-scale maps instead of the time-frequency spectrum produced by the short-time Fourier transform over a chosen time window. The "mother wavelet" selection is critical for CWT decomposition. Some factors should be considered during the

selection procedure, such as the vertical resolution reduction due to the side lobes of the wavelet (Castagna and Sun, 2006), even though there is not an optimum wavelet among the commonly used ones. The short-time Fourier transform uses a window with predefined length to produce time-frequency spectrum, which has a fixed time-frequency resolution. On the contrary, there is no requirement of predefining window length in the CWT method, resulting in a better time resolution at higher-frequencies and a better frequency resolution at lower-frequencies.

However, the application of a sliding temporal window in CWT limits the temporal and frequency resolutions. Puryear et al. (2012) analyzed this fundamental issue in spectral decomposition using a thin-layer model surrounded by strong reflections. They observed that a short window is required to avoid the interference, but a long enough window is preferable to avoid the incorrect estimation of the notch location due to the window-smearing effect on the spectrum. If we try to improve the frequency resolution, a longer window length is desirable, but resulting a poor time resolution.

To further improve the time and frequency resolution of the CWT spectral analysis, we use a maximum entropy implementation of the short-time Fourier transform to decompose the full-bandwidth seismic data and compute the multispectral coherence. To reduce this window effect in seismic spectral analysis, the maximum entropy algorithm solves an inverse problem using an objective function to fit the data with the minimum of sines and cosines. Different empirical criteria can be used in the inversion based spectral analysis, for example, Portniaguine and Castagna (2004) used an iteratively reweighted least-squares regularization algorithm to invert the normal equations for approaching the seismic wavelet decomposition problem. We follow the constrained least-squares spectral

analysis method of Puryear et al. (2012), to compute the Fourier series coefficients as a function of time, which is inverted based on a basis of truncated sinusoidal kernels for a moving time window. It reduces the window smearing and provides a better resolution over the short-time Fourier transform and CWT. An important parameter in this iterative spectral analysis method is the number of iterations. A larger number of iterations provides more accurate least-squares approximations, but consumes more computation time.

Besides the CWT and maximum entropy decomposition methods, we further evaluate two nonlinear spectral decomposition methods: AVT (amplitude volume technique) and spectral probe. Ten Kroode et al. (2013) indicated the benefits of the super-low-frequency information of seismic data. First, it could reduce the side lobes of the wavelet to improve the resolution. Second, it suffers less from the attenuation and scattering, which helps the waves to penetrate deeper in the earth. Further, it could assist the background model building for seismic inversion and migration velocity analysis. Additionally, the low-frequency seismic data could help identify some geologic features, such as faults (Hardage, 2009). Bulhões (1999), and Bulhões and de Amorin (2005) developed an AVT method to extract the super-low-frequency information from the original seismic data. Vernengo and Trinchero (2015), and Vernengo et al. (2017) showed several case studies, to indicate that the AVT data volume could help highlight geological features. AVT is realized by a nonlinear conversion of the full-bandwidth seismic data. The steps of the conventional AVT workflow (Bulhões, 1999) include calculation of the rms (root-mean-square) of the seismic amplitude, and then followed by the inverse Hilbert transform. In our research, we develop an optimized workflow using the envelope instead of the seismic amplitude. The details are illustrated in Appendix C.

We further evaluate another nonlinear spectral probe algorithm to decompose the full-bandwidth seismic data and produce the multispectral coherence images. Gao (2013) originally computed a new attribute using a spectral probe process to improve the precision and resolution of the conventional seismic amplitude profiles for geometric interpretation. It is implemented by considering a full wavelength of a cosine wave as a wavelet probe and then cross-correlating with the seismic data (Appendix D). The spectral probe result can be considered as an approximation of a spectral voice subjected to a short-window automatic gain control in a mathematically loose sense. The outputs of the cross-correlation are normalized coefficients, ranging from -1.0 to +1.0. The generated components using spectral probe method are insensitive to the amplitude variation and are acceptable for geometric attributes computation. The wavelet spectral probe analysis has a higher computational efficiency compared to other Fourier transform based decomposition methods.

Data description

We perform a case study on a 3D field seismic data to evaluate the multispectral coherence computation workflow (Figure 3.1) using different spectral decomposition methods. The Tui3D seismic survey is located in the southwest coast of the North Island, New Zealand (Figure 3.2, after King et al. (1993), Infante-Paez and Marfurt (2017), and Lubo-Robles and Marfurt (2019)). The data is acquired by Veritas DGC Australia Pty in 2003, which covers approximately 352 km^2 offshore of the Taranaki Basin. The streamer separation is 150 m, and the source separation is 75 m, and the bin size is 12.5 m by 12.5 m. The time sample rate of the original seismic data is 4 ms.

The Taranaki Basin is located above the subduction zone where the Pacific Plate is subducting beneath the Australian Plate (Yagci, 2016). The basin contains two primary structural elements: The Eastern Taranaki Graben Complex and the Western Platform. Tui3D survey is located on the Western Platform, which is affected by the normal block faulting during the Late Cretaceous-Eocene, but remains relatively stable during most of the Tertiary (Pilaar and Wakefield, 1984; Lubo-Robles and Marfurt, 2019).

The Moki A sands unit is the target in our research, which is deposited as a base of the slope turbidite and characterized by major submarine meandering channel complex (Bussell, 1994). A geophysical challenge is how to clearly delineate the boundaries of the incised sinusoidal channels, such as the ones shown in a representative vertical slice AA' (Figure 3.3a) and time slice at 2.16 s (Figure 3.3b) indicated by the green arrows in Figure 3.3b.

Data conditioning

Libak et al. (2017) observed that coherence attribute has the potential to identify the small-scale displacement in the case of noise free in synthetic data, but the detectability will be decreased in the field seismic data due to the presence of noise. This motivates us to perform a noise attenuation process prior to coherence computation to improve the quality of coherence images.

There are several different types of noise attenuation methods. We need to preserve the subtle geologic features such as the minor channels, which are indicated by the small-scale edges in seismic data. We apply a structure-oriented filtering (SOF) on the post-stack full-bandwidth seismic data, following the suggestion of Chopra and Marfurt (2007). SOF

is robust to suppress the incoherent noise and coherent footprint artifacts, but preserves the subtle geologic features.

The original full-bandwidth seismic data (Figure 3.3a and 3.3b) are good quality with relatively high S/N ratio but still have some random noise, which result in artifacts in the coherence attribute (Figure 3.4), decreasing its detectability of the incised channels. We performed SOF on the original data to suppress the noise. The coherence image computed using the SOF processed data (Figure 3.5) exhibits better quality with less noise over the result from the original seismic data (Figure 3.4).

Which spectral voices to choose in multispectral coherence?: CWT experiments

We first use the CWT method to decompose the full-bandwidth seismic data after SOF into different spectral voices, followed by the computation of the energy-ratio coherence for each component. An important issue in multispectral coherence is how to choose the appropriate components for computation among tens of decomposed spectral voices. In Figure 3.6a, we show the normalized spectrum of the SOF processed data in our target area from 1.8 s to 2.4 s. It is noted that the effective frequency bandwidth ranges from about 8 Hz to 95 Hz. We choose six CWT spectral voices within the effective bandwidth, starting from central frequency 10 Hz and ending with 85 Hz. We can use different spacing method for choosing the spectral voices between the starting and ending frequencies. A natural option is to choose equally-spaced CWT spectral voices with constant linear bandwidth. In Figure 3.6b, we show the series of wavelets used in equally-spacing method with a constant 15 Hz increment, including central frequencies 10 Hz, 25 Hz, 40 Hz, 55 Hz, 70 Hz, and 85 Hz. Another alternative to choose the CWT spectral voices is to use the exponentially-spaced components with constant octave bandwidth. We show

the wavelets used in the exponentially-spacing method in Figure 3.6c, using the same starting and ending frequencies with the equally-spacing case. The lateral axis in Figure 3.6c indicates the constant exponent increment in exponentially-spacing method, resulting in the spectral voices with central frequencies 10 Hz, 15 Hz, 24 Hz, 36 Hz, 55 Hz, and 85 Hz.

In Figure 3.7, we show the coherence images computed using equally-spaced CWT spectral voices. It is noted that the channels with different scales are highlighted in the coherence images from different components. The boundaries of the thicker channels are much clearer in the coherence images using the lower-frequency voices, such as the 10 Hz (Figure 3.7a) and 25 Hz (Figure 3.7b) components, while the thinner channels and the geologic details inside the thicker channels are much clearer using the higher-frequency voices, such as the coherence images from 40 Hz (Figure 3.7c) and 55 Hz (Figure 3.7d) components. Artifacts associated with acquisition footprint (red arrows in Figure 3.7a, 3.7e and 3.7f) are stronger in the coherence images computed from several spectral voices. The quality seen in Figure 3.7f for the 85 Hz component is significantly lower, resulting in a coherence image containing less useful information.

We then combine these different coherence volumes into one single coherence dataset using the workflow in Figure 3.1, which is shown in Figure 3.8. It is noted that this multispectral coherence computed using the equally-spaced spectral voices (Figure 3.8) has less noise (red circles) and clearer channel boundaries (green arrows) over the coherence image computed using the full-bandwidth seismic data (Figure 3.5). Additionally, the multispectral coherence image reveals more abundant structural details, such as the geologic features inside the thicker channels.

We further use six exponentially-spaced CWT spectral voices to compute coherence volumes, which are centered at 10 Hz (Figure 3.9a), 15 Hz (Figure 3.9b), 24 Hz (Figure 3.9c), 36 Hz (Figure 3.9d), 55 Hz (Figure 3.9e), and 85 Hz (Figure 3.9f). The observations from Figure 3.9 are similar with the coherence images computed using the equally-spaced spectral voices (Figure 3.7). The thicker channels are more highlighted in the coherence images using the lower-frequency CWT spectral voices, while the higher-frequency components provide much clearer images of the thinner channels and small-scale geologic features.

In Figure 3.10, we show the multispectral coherence image combined using the coherence volumes computed from the exponentially-spaced CWT spectral voices using the workflow in Figure 3.1. We can observe that it appears higher quality over the full-bandwidth result (Figure 3.5). Especially, it is noted that the multispectral coherence image using the exponentially-spaced CWT components (Figure 3.10) exhibits fewer artifacts and clearer channel boundaries (green arrows in Figure 3.10) over the multispectral coherence using the equally-spaced CWT components (Figure 3.8). We recommend to compute multispectral coherence using the exponentially-spaced spectral voices.

Octave is defined in electronics as a logarithm unit for the ratio between frequencies, and in music an octave can express a musical interval. In terms of physics, we can consider an octave as the distance between one musical note and another note. Similarly, if we use the exponentially-spaced components with constant octave bandwidth, it will potentially provide clearer physical meaning of seismic signals in multispectral coherence compared to equally-spaced components. Deeper understanding of spacing methods in spectral voice selection still remains an interesting research topic.

Coherence on maximum entropy decomposed components

We further use the maximum entropy method to improve the resolution of the CWT spectral voices by reducing the window smearing effect in the spectral analysis (Puryear et al., 2012). We choose the exponentially-spaced maximum entropy spectral voices to compute multispectral coherence.

The coherence images computed from each maximum entropy spectral voice are shown in Figure 3.11, using the same starting and ending frequencies with the ones in the CWT experiments. We take the 15 Hz spectral voice component for example to compare the coherence images computed using the maximum entropy (Figure 3.11b) and CWT (Figure 3.9b) spectral voices. It is noted that the coherence from the maximum entropy spectral voice (Figure 3.11b) provides much more details and exhibits higher resolution (red circle) of the channel boundaries over the coherence using the corresponding CWT component (Figure 3.9b). We can get similar observations from the comparison of other lower-frequency spectral voice components. We then generate the multispectral coherence (Figure 3.12) using the maximum entropy spectral voices, which exhibits higher resolution of small-scale features (green arrows in Figure 3.12) over the multispectral coherence image computed from the corresponding CWT components (Figure 3.10).

In Figure 3.13, we use an example of the enlarged vertical amplitude slice to illustrate the reason why the multispectral coherence works. Figure 3.13b and 3.13c show the 24 Hz and 36 Hz spectral voice components using the maximum entropy decomposition from the full-bandwidth seismic amplitude (Figure 3.13a). Compared with the full-bandwidth data (red circles in Figure 3.13a), the boundaries of the thicker channels are much sharper in the 24 Hz component (red circles in Figure 3.13b), while the thinner channel boundaries are

sharper and clearer in the 36 Hz spectral voice (red circles in Figure 3.13c). The channels with different scales are more highlighted in specific spectral voices, resulting in improved images of channel boundaries in the multispectral coherence.

Coherence on AVT data volume

We use an optimized nonlinear AVT algorithm (Appendix C) to extract the super-low-frequency information (window length 16 ms), which helps delineate the large-scale geologic features. AVT produces only one data volume, not several different spectral components, which requires a relatively low computation cost and small storage of the following energy-ratio coherence calculation over other spectral decomposition methods.

The AVT time slice is shown in Figure 3.14a, which contains less noise and weaker reflections compared with the original seismic amplitude time slice (Figure 3.3b). We then use this AVT dataset to compute the energy-ratio coherence attribute, which is shown in Figure 3.14b. It is clearer with less noise over the coherence computed using the SOF full-bandwidth seismic data (Figure 3.5). Especially, it provides more continuous boundaries of the thicker channels (green arrows in Figure 3.14b) compared to the coherence images computed from other spectral decomposition methods. However, the imaging of small-scale features inside the thicker channels are decreased due to the lack of the higher-frequency components in the AVT data.

Coherence on spectral probes

The wavelet spectral probe analysis produces spectral voice components from the full-bandwidth seismic data with high computational efficiency. In Figure 3.15, we show an example of the decomposed spectral voice using period 36 Hz. It is noted that the spectral

probe is insensitive to the amplitude variation. In a mathematically loose sense, the result approximates a spectral "voice" that has been subjected to a short-window automatic gain control. The energy is much more balanced than other spectral decomposition methods. The spectral probe components are available for the seismic geometric attribute calculation, such as coherence.

We decompose the full-bandwidth seismic data into six spectral probes using period 10 Hz, 15 Hz, 24 Hz, 36 Hz, 55 Hz, and 85 Hz. We then use these spectral probes to compute the multispectral coherence (Figure 3.16). Besides the improvement over the full-bandwidth coherence image (Figure 3.5), the multispectral coherence computed using spectral probes (Figure 3.16) exhibits more balanced over the multispectral coherence images from other spectral decomposition methods. However, because amplitudes are not preserved in the spectral probes, we use an equal weight for the noise in the noisier shorter-period components when we build the covariance matrix. This increases the noises in the shorter-period component coherence images, and further decreases the quality of the multispectral coherence image using spectral probes (red circles in Figure 3.16).

Conclusions

We use a 3D seismic data volume to evaluate four different spectral decomposition methods in multispectral coherence computation. We recommend computing multispectral coherence using the exponentially-spaced spectral voices, as it provides better coherence images over the results using equally-spaced components for the same computation cost. The resolution of thinner channels and small-scale features is further improved in the multispectral coherence image computed using the maximum entropy spectral voices over the CWT results. The images of the thicker channel boundaries are the most continuous in

the coherence computed using the AVT dataset, but the quality of small-scale features inside the thicker channels is decreased. Further, multispectral coherence computed using the nonlinear spectral probes appears more balanced to help reveal the small-scale geologic features inside the thicker channel. However, because amplitudes are not preserved in the nonlinear spectral probe decomposition, we use an equal weight for the noise in noisier shorter-period components to build the covariance matrix, resulting in increased noise in the multispectral coherence images. Based on the observations in these experiments, we recommend computing multispectral coherence on the spectral voices decomposed using the maximum entropy method. The window length in spectral decomposition plays an important role in the generated coherence images. If we use a longer window, the geology features such as the incised channels are more averaged with greater geologic "overprinting". The influence of window length in different spectral decomposition methods on the channel morphology remains an interesting research topic.

Acknowledgements

The authors would thank the sponsors of the Attribute-Assisted Seismic Processing and Interpretation (AASPI) consortium in the University of Oklahoma. We also thank New Zealand Petroleum and Minerals for providing the Tui3D seismic survey to the public for use in research and education.

Appendix A: Coherence computation based on the energy-ratio method

Each element of the covariance matrix is calculated using the analytic trace, to avoid the artifacts due to the small windows over the zero-crossings:

$$C_{mn} = \sum_{k=-K}^{K} \left[d\left(t_k, x_m, y_m\right) d\left(t_k, x_n, y_n\right) + d^H\left(t_k, x_m, y_m\right) d^H\left(t_k, x_n, y_n\right) \right] \tag{A-1}$$

where d denotes the original seismic data, d^H is the corresponding Hilbert transform, C_{mn} represents the element of the covariance matrix, and t_k denotes the structurally interpolated time sample at a distance $\left(x_m, y_m\right)$ from the coordinate origin point.

We then generate the energy-ratio coherence by computing the ratio of the coherent energy E_c and the total energy E_t within an analysis window:

$$s = \frac{E_c}{E_t + \varepsilon^2} \tag{A-2}$$

where ε is a small positive value to avoid division by zero. We define the Karhunen-Lo ève (KL)-filtered coherent energy and the total energy as

$$E_c = \sum_{m=1}^{M} \sum_{k=-K}^{K} \left\{ \left[d_{KL}\left(t_k, x_m, y_m\right) \right]^2 + \left[d_{KL}^H\left(t_k, x_m, y_m\right) \right]^2 \right\} \tag{A-3}$$

$$E_t = \sum_{m=1}^{M} \sum_{k=-K}^{K} \left\{ \left[d\ \left(t_k, x_m, y_m\right) \right]^2 + \left[d^H\left(t_k, x_m, y_m\right) \right]^2 \right\} \tag{A-4}$$

Appendix B: Continuous wavelet transform (CWT) theory

Grossmann and Morlet (1984) formally introduce that a function with zero mean is called a "wavelet", which has finite energy concentrated in time and satisfies certain well-established conditions. We can generate a family of the wavelet functions from a "mother wavelet" $\psi(t)$, which is centered about $t = 0$, scaled using a dilation factor s, and shifted by time τ:

$$\psi_{s,\tau}(t) = \frac{1}{\sqrt{s}}\psi\left(\frac{t-\tau}{s}\right) \tag{B-1}$$

CWT is performed by cross-correlating the library of wavelets of equation B-1 with a seismic time series:

$$W(\tau,s) = \int_{-\infty}^{+\infty} d(t)\frac{1}{\sqrt{s}}\psi^*\left(\frac{t-\tau}{s}\right)dt \tag{B-2}$$

where $W(\tau,s)$ is the time scale map, $d(t)$ represents the seismic time series, and $\psi^*\left(\frac{t-\tau}{s}\right)$ is the complex conjugate of $\psi\left(\frac{t-\tau}{s}\right)$. The local spectrum is defined by the cross-correlation coefficients at each time sample.

Appendix C: Optimized AVT workflow

The optimized AVT workflow is implemented using the following three steps:

1) Envelope calculation from the analytic transform of the seismic data,

$$D(t_i) = d(t_i) + id^{\mathrm{H}}(t_i) \tag{C-1}$$

where D is the analytic signal, which is composed by the seismic amplitude d and its Hilbert transform d^{H}. The envelope is then calculated by taking the magnitude of this analytic signal,

$$E(t_i) = \left|D(t_i)\right| = \sqrt{\left[d(t_i)\right]^2 + \left[d^{\mathrm{H}}(t_i)\right]^2} \tag{C-2}$$

2) Calculation of the rms envelope within a defined window,

$$\bar{E}_{rms}(t_i)=\sqrt{\frac{\sum_{t_j=t_i-N/2}^{t_j=t_i+N/2}E^2(t_j)}{N}} \tag{C-3}$$

3) Inverse Hilbert transform of the rms envelope,

$$\bar{E}_{AVT}(t_i)=\mathrm{H}^{-1}\left\{\bar{E}_{rms}(t_i)\right\} \tag{C-4}$$

Appendix D: Spectral probe theory

In spectral probe technique, we generate the normalized cross-correlation coefficients between a wavelet $w(t)$ and the seismic amplitude $d(t)$:

$$\rho(t)=\frac{\sum_{j=-J}^{+J}w(t-j\Delta t)d(t-j\Delta t)}{\sqrt{\sum_{j=-J}^{+J}\left[w(t-j\Delta t)\right]^2\sum_{j=-J}^{+J}\left[d(t-j\Delta t)\right]^2}} \tag{D-1}$$

We set the wavelet probe using a cosine wave,

$$w(j\Delta t)=\cos(2\pi fj\Delta t) \tag{D-2}$$

where f is the frequency, Δt is the sample increment, and j is the sample index. If we choose the correlation range $2J\Delta t = 1/f$, which means exactly one period, equation D-1 could be simplified to be

$$\rho(t)=\frac{\sum_{j=-J}^{+J}\cos\left[2\pi(t-j\Delta t)\right]d(t-j\Delta t)}{\sqrt{\sum_{j=-J}^{+J}\left[d(t-j\Delta t)\right]^2}} \tag{D-3}$$

We produce different data volumes of cross-correlation coefficients with different periods (or corresponding frequencies) using equation D-3.

References

Alaei, B., 2012, Improved fault imaging by integration of frequency decomposition and fault attributes, example from mid Norwegian sea: Proceedings of the 3rd EAGE Fault and Top Seal Conference, C13.

Bahorich, M. S., and S. L. Farmer, 1995, 3-D seismic coherency for faults and stratigraphic features: The coherence cube: The Leading Edge, **14**, 1053–1058.

Bulhões, E. M., 1999, Técnica "VOLUME DE AMPLITUDES" para mapeamento de feições estruturais: 6th International Congress of the Brazilian Society of Geophysics, Rio de Janeiro, RJ, Brazil (in Portuguese).

Bulhões, E. M., and W. de Amorin, 2005, Princípio da Sismocamada Elementar e sua Aplicação à Técnica de Volume de Amplitudes (tec. VA): 9th International Congress of the Brazilian Geophysical Society, Salvador, Brasil (in Portuguese).

Bussell, M. R., 1994, Seismic interpretation of the Moki Formation on the Maui 3D survey, Taranaki Basin: New Zealand Petroleum Conference Proceedings, Ministry of Economic Development, 240–255.

Castagna, J., S. Sun, and R. Siegfried, 2003, Instantaneous spectral analysis: Detection of low-frequency shadows associated with hydrocarbons: The Leading Edge, **22**, 120–127.

Castagna, J. P., and S. Sun, 2006, Comparison of spectral decomposition methods: First Break, **24**, 75–79.

Chopra, S., and K. J. Marfurt, 2007, Seismic attributes for prospect identification and reservoir characterization: SEG.

Chopra, S., and K. J. Marfurt, 2019, Multispectral, multiazimuth, and multioffset coherence attribute applications: Interpretation, **7**, SC21–SC32.

Davogustto, O., M. C. Matos, C. Cabarcas, T. Dao, and K. J. Marfurt, 2013, Resolving subtle stratigraphic features using spectral ridges and phase residues: Interpretation, **1**, SA93–SA108.

Dewett, D. T, and A. A. Henza, 2015, Spectral similarity fault enhancement: Interpretation, **4**, SB149–SB159.

Gao, D., 2013, Wavelet spectral probe for seismic structure interpretation and fracture characterization: A workflow with case studies: Geophysics, **78**, O57–O67.

Gersztenkorn, A., and K. J. Marfurt, 1999, Eigenstructure-based coherence computations as an aid to 3-D structural and stratigraphic mapping: Geophysics, **64**, 1468–1479.

Grossmann, A., and J. Morlet, 1984, Decomposition of Hardy functions into square integrable wavelets of constant shape: SIAM Journal on Mathematical Analysis, **15**, 723–736.

Hardage, B., 2009, Frequencies are fault finding factors: looking low aids data interpretation: AAPG Explorer, **30**, 34.

Infante-Paez, L., and K. Marfurt, 2017, Seismic expression and geomorphology of igneous bodies: A Taranaki Basin, New Zealand, case study: Interpretation, **5**, 121–140.

King, P. R., G. H. Scott, and P. H. Robinson, 1993, Description, correlation and depositional history of Miocene sediments outcropping along North Taranaki coast: Institute of Geological & Nuclear Sciences Ltd., p. 199.

Laughlin, K., P. Garossino, and G. Partyka, 2002, Spectral decomposition applied to 3D: AAPG Explorer, **23**, 28–31.

Li, F., and W. Lu, 2014, Coherence attribute at different spectral scales: Interpretation, **2**, SA99–SA106.

Li, F., J. Qi, B. Lyu, and K. J. Marfurt, 2018, Multispectral coherence: Interpretation, **6**, T61–T69.

Libak, A., B. Alaei, A. Torabi, 2017, Fault visualization and identification in fault seismic attribute volumes: Implications for fault geometric characterization: Interpretation, **5**, B1–B16.

Liu, J., and K. J. Marfurt, 2007, Instantaneous spectral attributes to detect channels: Geophysics, **72**, P23–P31.

Lubo-Robles, D., and K. J. Marfurt, 2019, Independent component analysis for reservoir geomorphology and unsupervised seismic facies classification in the Taranaki Basin, New Zealand: Interpretation, **7**, SE19–SE42.

Lyu, B., F. Li, J. Qi, T. Zhao, and K. J. Marfurt, 2018, Highlighting discontinuities with variational mode decomposition based coherence: 88th Annual International Meeting, SEG, Expanded Abstracts, 1798–1802.

Lyu, B., J. Qi, G. Machado, F. Li, and K. J. Marfurt, 2019, Seismic fault enhancement using spectral decomposition assisted attributes: 89th Annual International Meeting, SEG, Expanded Abstracts, 1938–1942.

Marfurt, K. J., S. L. Farmer, M. S. Bahorich, and R. L. Kirlin, 1998, 3-D seismic attributes using a semblance-based coherency algorithm: Geophysics, **63**, 1150–1165.

Marfurt, K. J., V. Sudhaker, A. Gersztenkorn, and K. D. Crawford, 1999, Coherency calculations in the presence of structural dip: Geophysics, **64**, 104–111.

Marfurt, K. J., and R. Kirlin, 2001, Narrow-band spectral analysis and thin-bed tuning: Geophysics, **66**, 1274–1283.

Marfurt, K. J., and T. M. Alves, 2014, Pitfalls and limitations in seismic attribute interpretation of tectonic features: Interpretation, **3**, SB5–SB15.

Marfurt, K. J., 2017, Interpretational aspects of multispectral coherence: 79th Annual International Conference and Exhibition, EAGE, Extended Abstracts.

Matos, M. C., and K. J. Marfurt, 2011, Inverse continuous wavelet transform "deconvolution": 81st Annual International Meeting, SEG, Expanded Abstracts, 1861–1865.

Partyka, G. A., J. Gridley, and J. Lopez, 1999, Interpretational applications of spectral decomposition in reservoir characterization: The Leading Edge, **18**, 353–360.

Peyton, L., R. Bottjer, and G. Partyka, 1998, Interpretation of incised valleys using new-3D seismic techniques: A case history using spectral decomposition and coherency: The Leading Edge, **17**, 1294–1298.

Pilaar, W. F. H., and L. L. Wakefield, 1984, Hydrocarbon generation in the Taranaki Basin, New Zealand: AAPG Special Volumes M35, Petroleum Geochemistry and Basin Evaluation, 405–423.

Portniaguine, O., and J. P. Castagna, 2004, Inverse spectral decomposition: 74th Annual International Meeting, SEG, Expanded Abstracts, 1786–1789.

Puryear, C. I., O. N. Portniaguine, C. M. Cobos, and J. P. Castagna, 2012, Constrained lest-squares spectral analysis: Application to seismic data: Geophysics, **77**, V143–V167.

Qi, J., F. Li, B. Lyu, B. Zhang, O. Olorunsola, and K. J. Marfurt, 2016, Seismic fault enhancement and skeletonization: 86th Annual International Meeting, SEG, Expanded Abstracts, 1966–1970.

Qi, J., B. Lyu, A. Alali, G. Machado, Y. Hu, and K. J. Marfurt, 2019, Image processing of seismic attributes for automatic fault extraction: Geophysics, **84**, O25–O37.

Sinha, S., R. Routh, P. Anno, and J. Castagna, 2005, Spectral decomposition of seismic data with continuous-wavelet transform: Geophysics, **70**, P19–P25.

Sui, J., X. Zheng, and Y. Li, 2015, A seismic coherency method using spectral attributes: Applied Geophysics, **12**, 353–361.

Ten Kroode, A. P. E., S. Bergler, C. Corsten, J. W. de Maag, F. Strijbos, and H. Tijhof, 2013, Broadband seismic data - The importance of low frequencies: Geophysics, **78**, WA3–WA14.

Vernengo, L., and E. Trinchero, 2015, Application of amplitude volume technique attributes, their variations, and impact: The Leading Edge, **34**, 1246–1253.

Vernengo, L., E. Trinchero, M. G. Torrejón, and I. Rovira, 2017, Amplitude volume technique attributes and multidimensional seismic interpretation: The Leading Edge, **36**, 776–781.

Wang, T., S. Yuan, J. Gao, S. Li, and S. Wang, 2019, Multispectral phase-based geosteering coherence attributes for deep stratigraphic feature characterization: IEEE Geoscience and Remote Sensing Letters, **16**, 1309–1313.

Wang, S., S. Yuan, T. Wang, J. Gao, and S. Li, 2018, Three-dimensional geosteering coherence attributes for deep-formation discontinuity detection: Geophysics, **83**, O105–O113.

Yagci, G., 2016, 3D seismic structural and stratigraphic interpretation of the Tui-3D field, Taranaki Basin, New Zealand: Master's Thesis, Missouri University of Science and Technology.

Zeng, H., 2015, Predicting geometry and stacking pattern of thin beds by interpreting geomorphology and waveforms using sequential stratal-slices in the Wheeler domain: Interpretation, **3**, SS49–SS64.

Chapter 3 figures

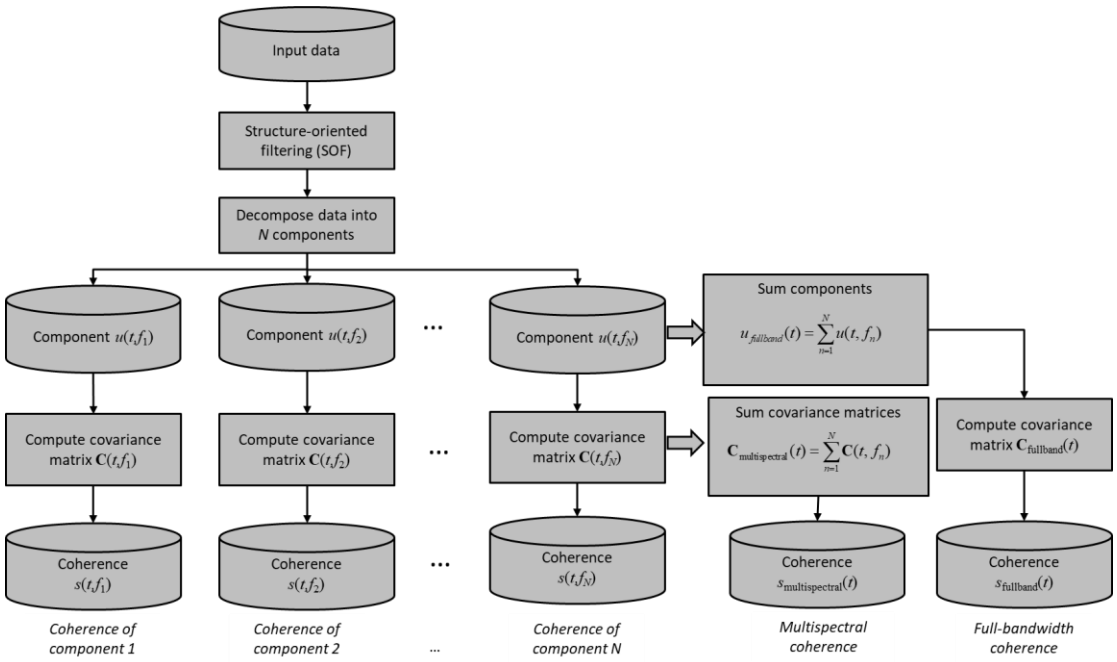

Figure 3.1. A workflow showing the computation of multispectral coherence from the original full-bandwidth seismic data. In this paper, we evaluate the impact of alternative decomposition algorithms, including CWT (continuous wavelet transform) of equal-space and exponential-space, and maximum entropy spectral decomposition, which can reconstruct the original seismic data. We also evaluate the impact of several nonlinear decomposition algorithms, including the AVT (amplitude volume technique) and spectral probe, which cannot reconstruct the original data. (Figure modified from Marfurt, 2017).

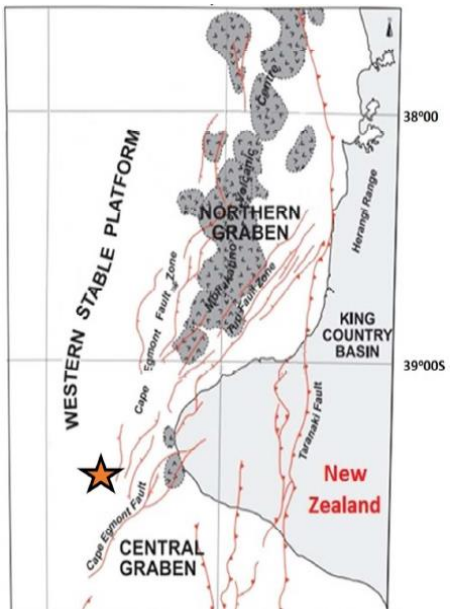

Figure 3.2. The location of Tui3D seismic survey (orange star) and the structural style of the offshore Taranaki Basin, New Zealand. After King et al. (1993), Infante-Paez and Marfurt (2017), and Lubo-Robles and Marfurt (2019). The data is acquired by Veritas DGC Australia Pty in 2003, covering approximately 352 km^2. The acquisition parameters are: streamer separation 150 m, source separation 75 m, bin size 12.5 m by 12.5 m, and time sample rate 4 ms.

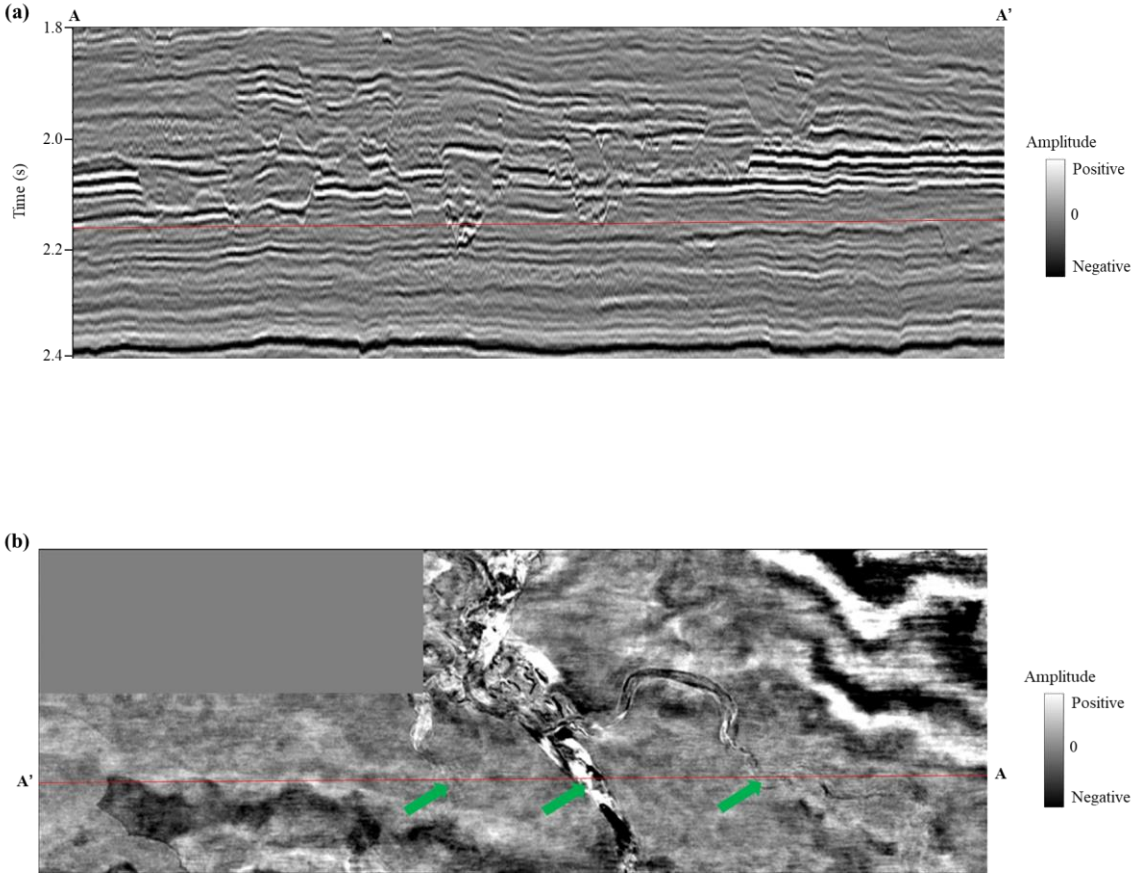

Figure 3.3. (a) A representative vertical slice AA ′, and (b) time slice at t=2.16 s through the seismic amplitude volume at the level of several incised channels (green arrows in Figure 3.3b).

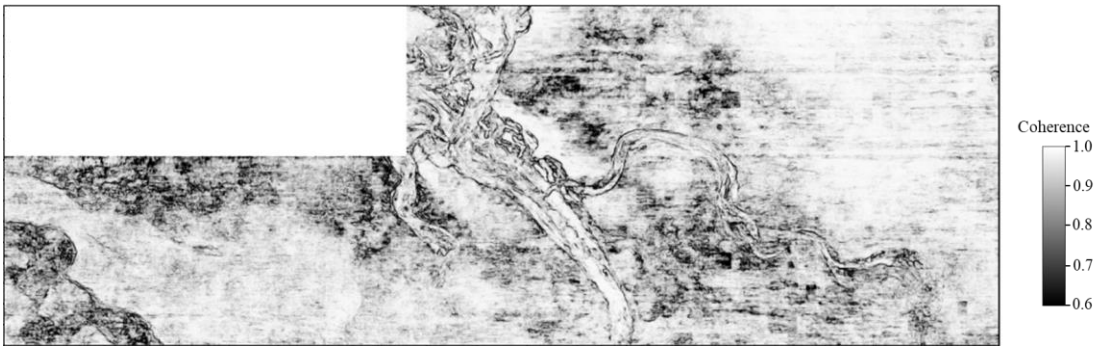

Figure 3.4. Coherence attribute time slice at 2.16 s computed using the original full-bandwidth seismic data, showing strong noises, which decrease its detectability of the incised channels.

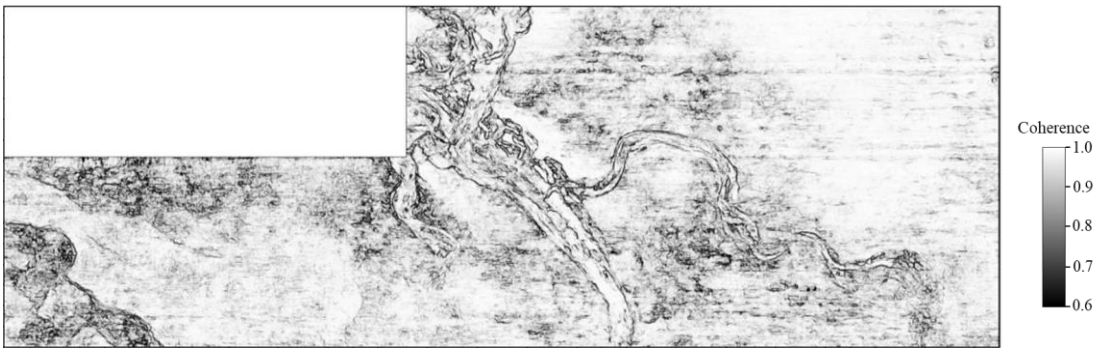

Figure 3.5. Coherence image computed using the SOF processed full-bandwidth seismic data, showing better quality with less noise compared to the coherence computed using the original data (Figure 3.4).

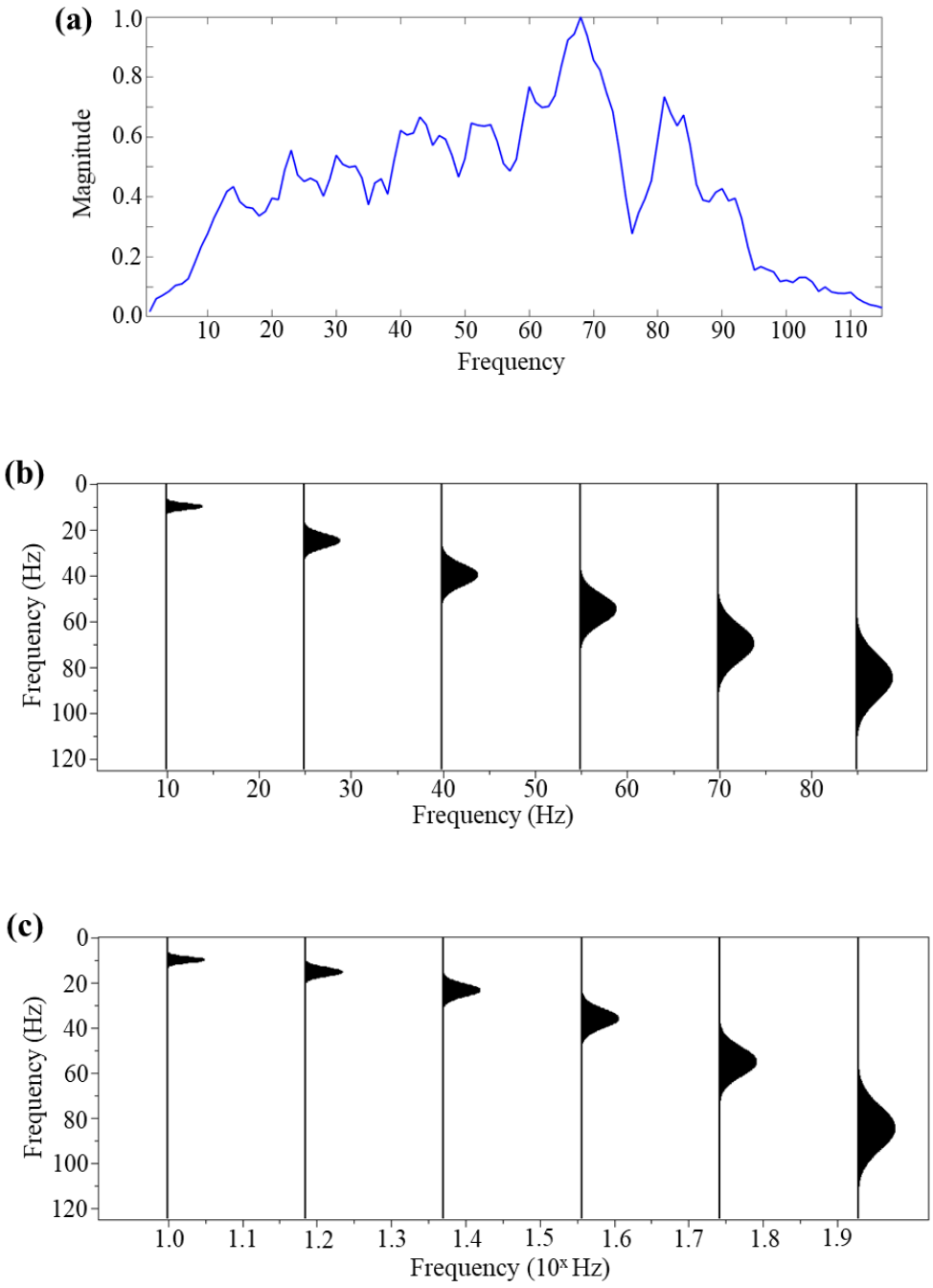

Figure 3.6. (a) The normalized spectrum of SOF processed data in target area form 1.8 s to 2.4 s, and (b) the wavelets used in equally-spaced CWT with a constant linear increment, including central frequencies 10 Hz, 25 Hz, 40 Hz, 55 Hz, 70 Hz, and 85 Hz, and (c) the wavelets used in exponentially-spaced CWT with a constant octave bandwidth. Note that the lateral axis in Figure 3.6c indicates the constant exponent increment, resulting in CWT spectral voices with central frequencies 10 Hz, 15 Hz, 24 Hz, 36 Hz, 55 Hz, and 85 Hz.

(a)

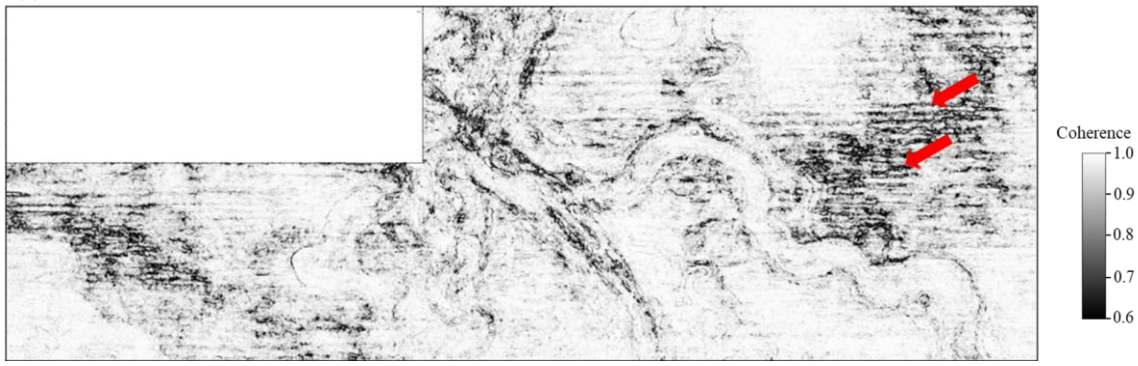
Coherence
1.0
0.9
0.8
0.7
0.6

(b)

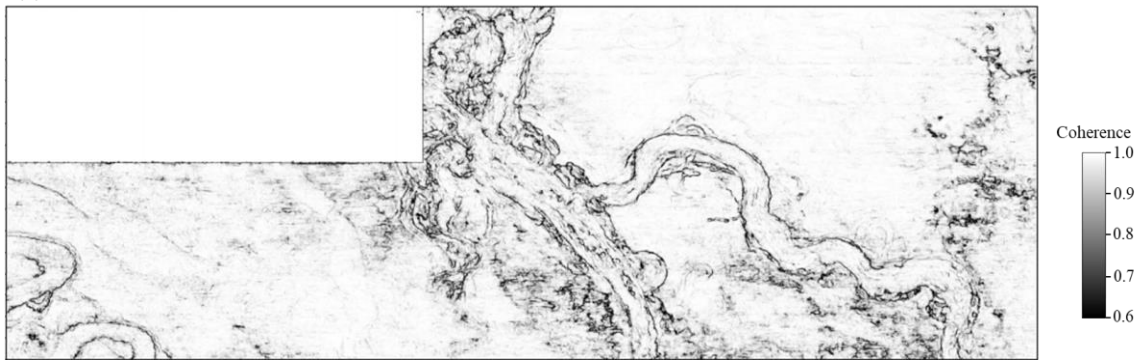
Coherence
1.0
0.9
0.8
0.7
0.6

(c)

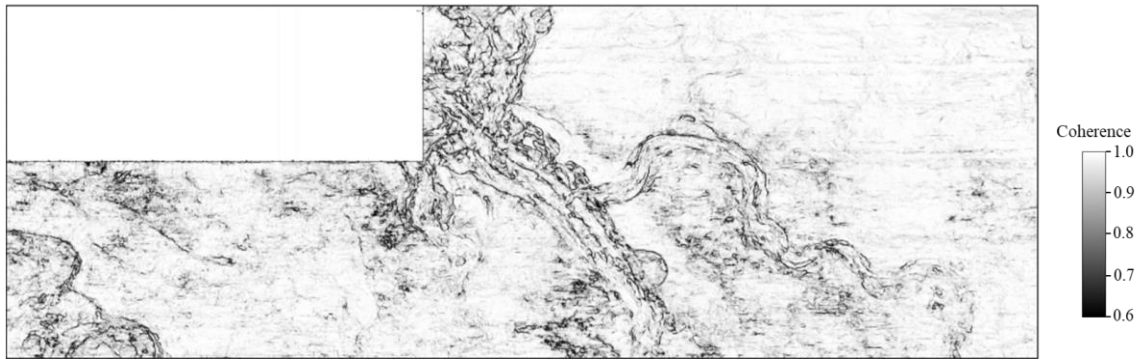
Coherence
1.0
0.9
0.8
0.7
0.6

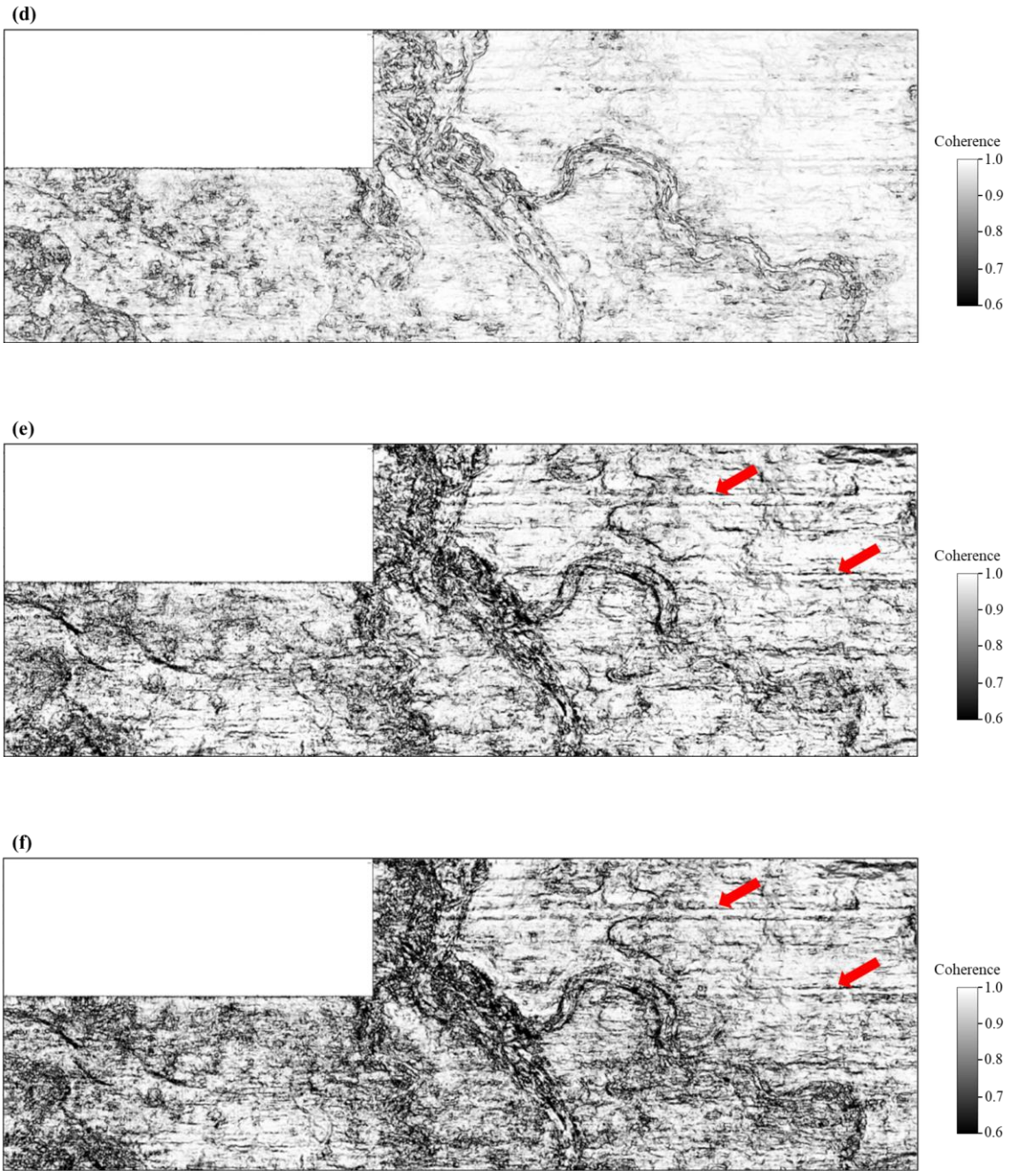

Figure 3.7. Coherence images computed using six equally-spaced CWT spectral voices centered at: (a) 10 Hz, (b) 25 Hz, (c) 40 Hz, (d) 55 Hz, (e) 70 Hz, and (f) 85 Hz. Note that the boundaries of the thicker channels are much clearer in the coherence images using the lower-frequency spectral voices, while the thinner channels and the geologic details inside the thicker channels are more highlighted using the higher-frequency components. Artifacts associated with acquisition footprint (red arrows in Figure 3.7a, 3.7e and 3.7f) are stronger in the coherence images computed from several components. The quality seen in Figure 3.7f for the 85 Hz component is significantly lower resulting in a coherence image containing less useful information over other components.

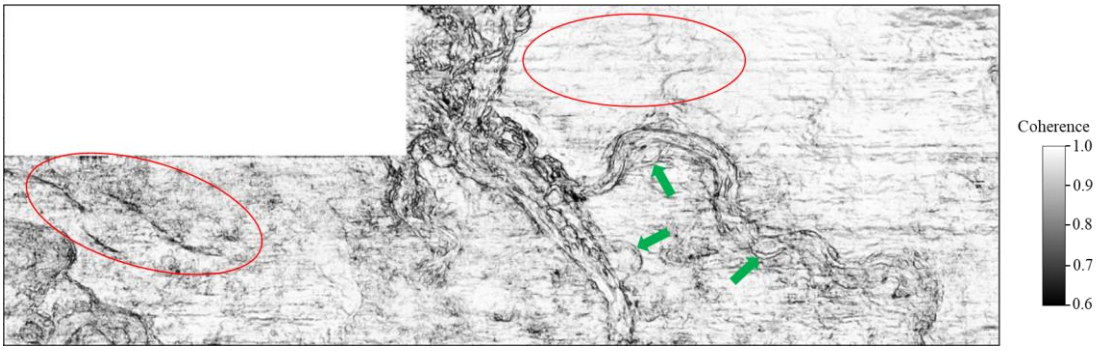

Figure 3.8. Multispectral coherence computed using six equally-spaced CWT spectral voices (Figure 3.7), providing an image with less noise (especially red circles) and clearer channel boundaries (especially green arrows) over the full-bandwidth coherence (Figure 3.5).

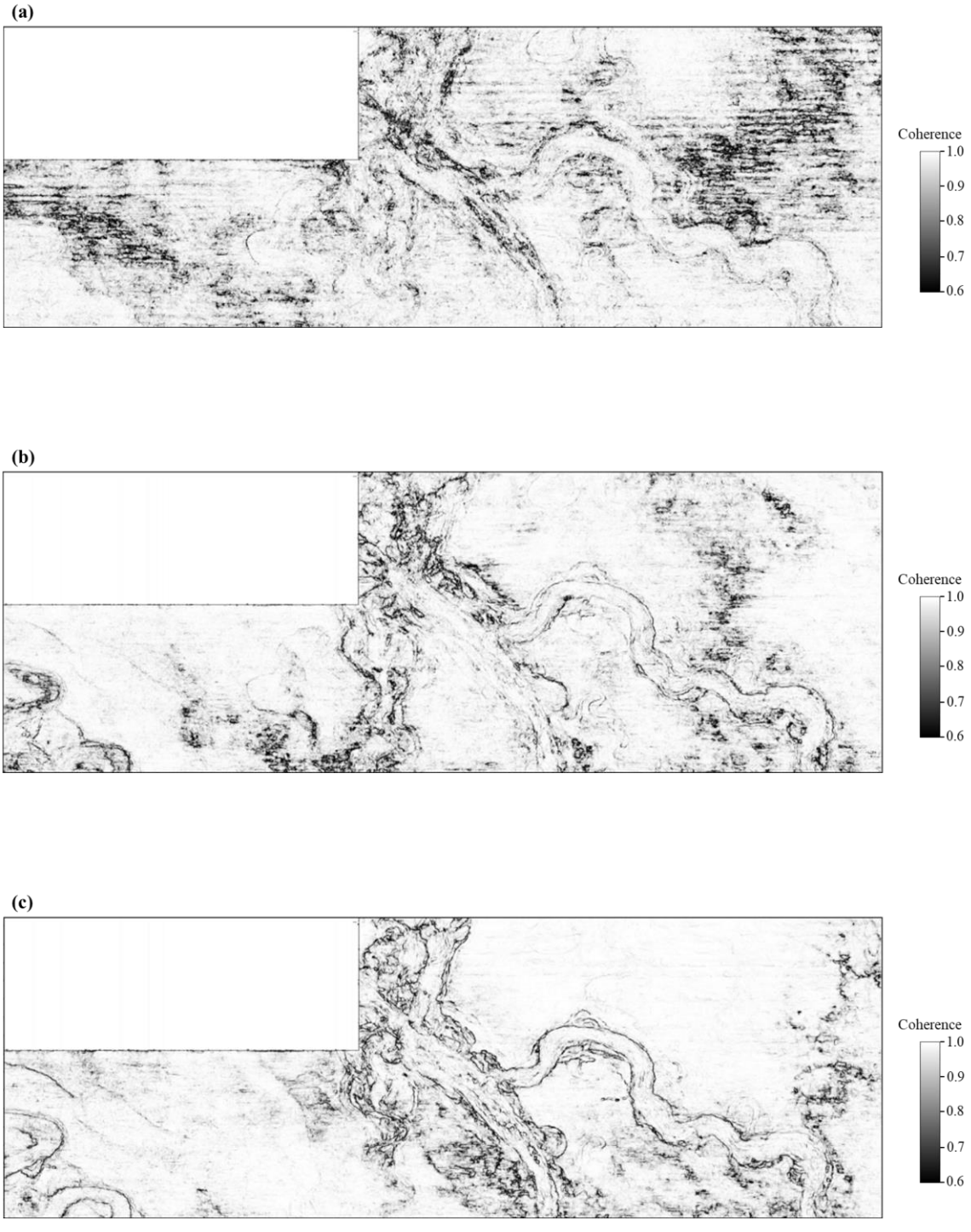
(a)
Coherence
1.0
0.9
0.8
0.7
0.6
(b)
Coherence
1.0
0.9
0.8
0.7
0.6
(c)
Coherence
1.0
0.9
0.8
0.7
0.6

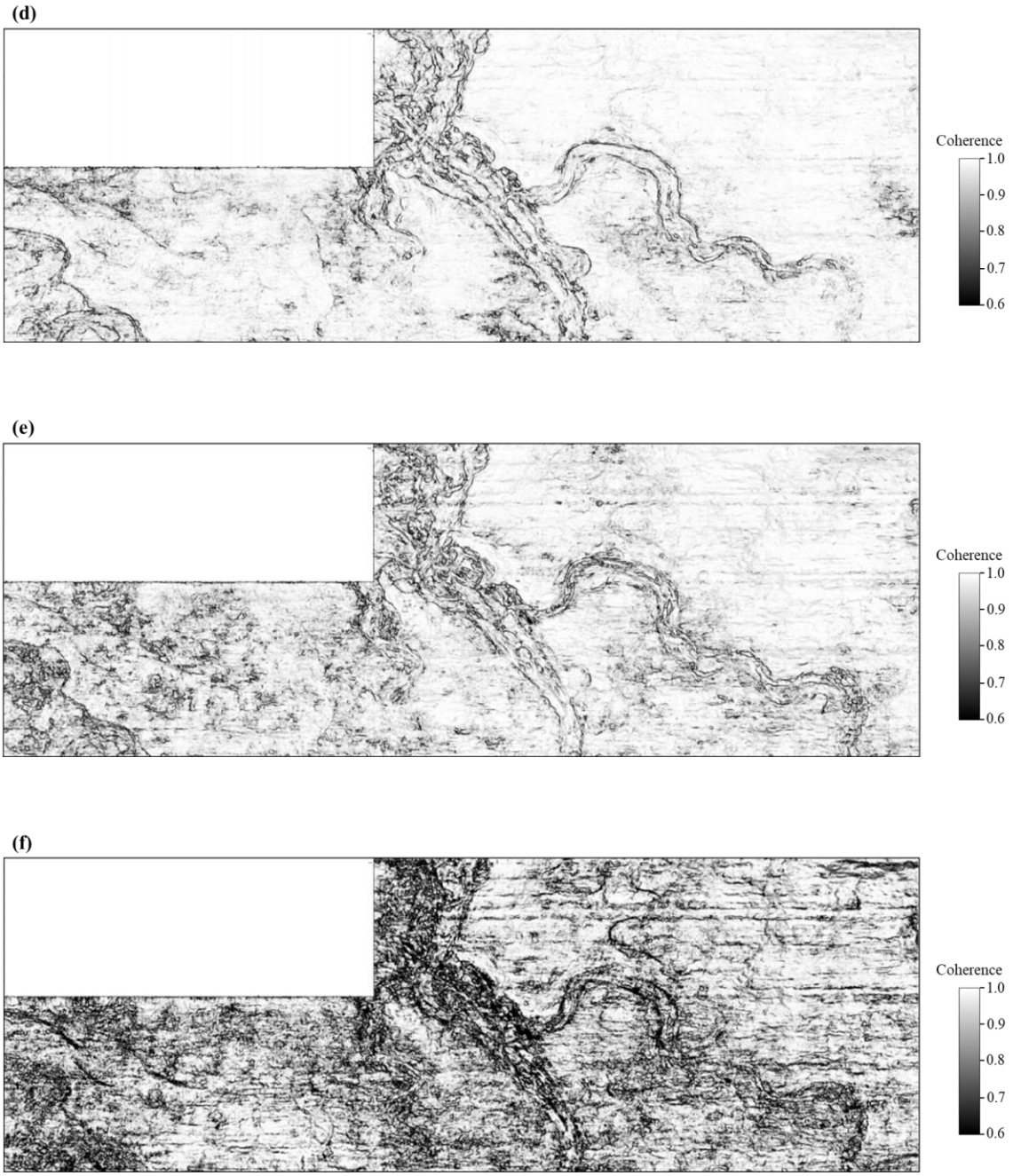

Figure 3.9. Coherence images computed using exponentially-spaced CWT components with central frequencies at: (a) 10 Hz, (b) 15 Hz, (c) 24 Hz, (d) 36 Hz, (e) 55 Hz, and (f) 85 Hz. The observations are similar with Figure 3.7, indicating that thicker channels are more highlighted in lower-frequency CWT spectral voices, while the higher-frequency components provide much clearer images of the thinner channels and small-scale geologic features. Noise in the 85 Hz component coherence (Figure 3.9f) is much stronger than other components.

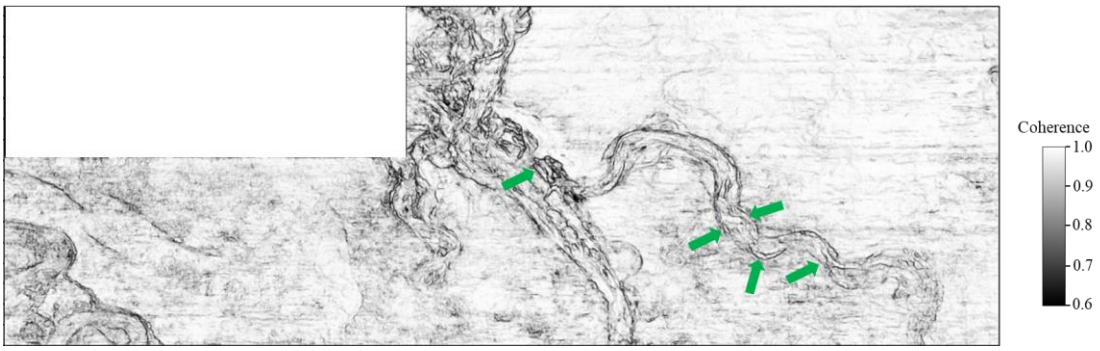

Figure 3.10. Multispectral coherence computed using six exponentially-spaced CWT components (Figure 3.9). Note that it exhibits fewer artifacts and clearer channel boundaries (green arrows) over the multispectral coherence using the equally-spaced CWT components (Figure 3.8).

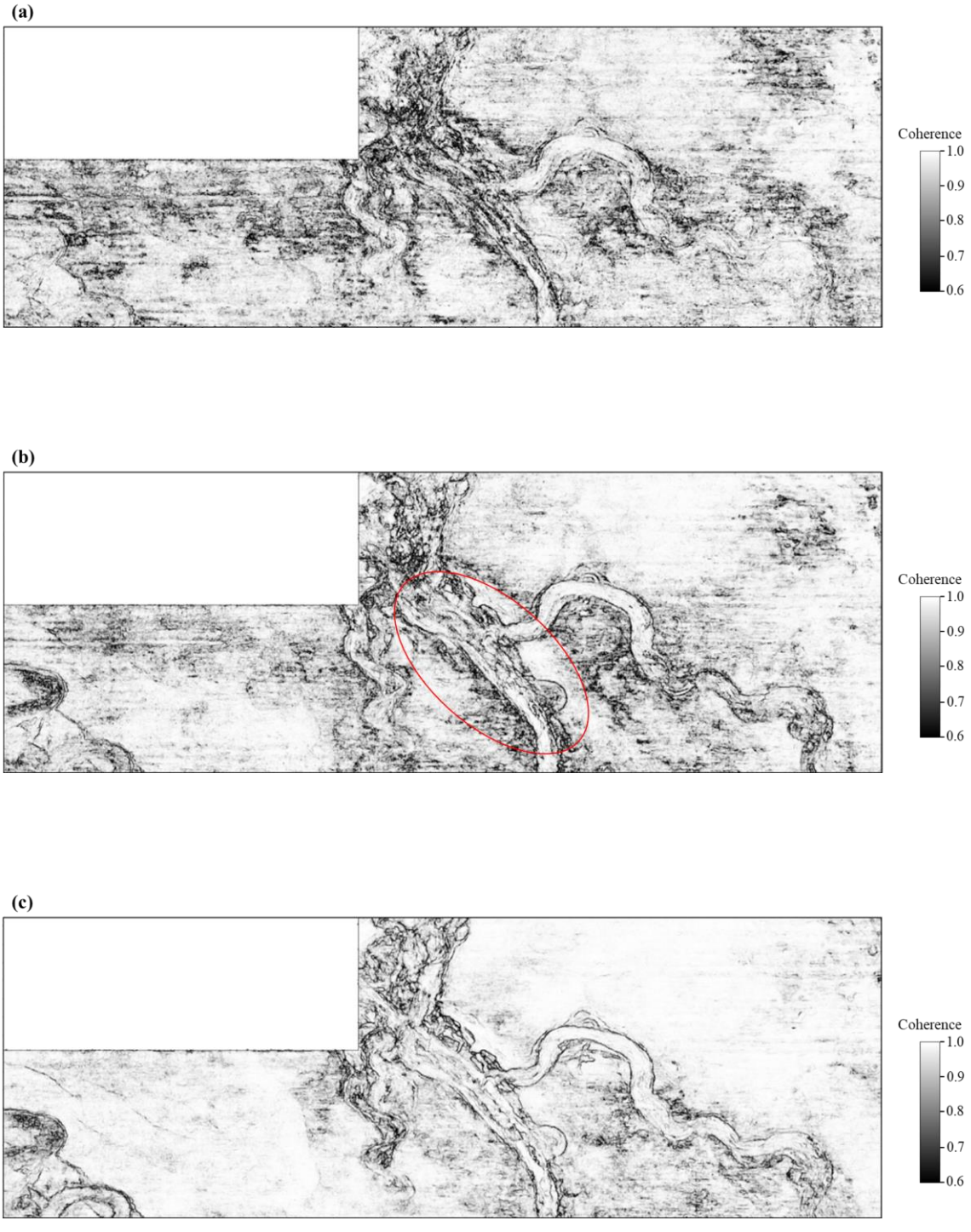
(a)
Coherence
1.0
0.9
0.8
0.7
0.6
(b)
Coherence
1.0
0.9
0.8
0.7
0.6
(c)
Coherence
1.0
0.9
0.8
0.7
0.6

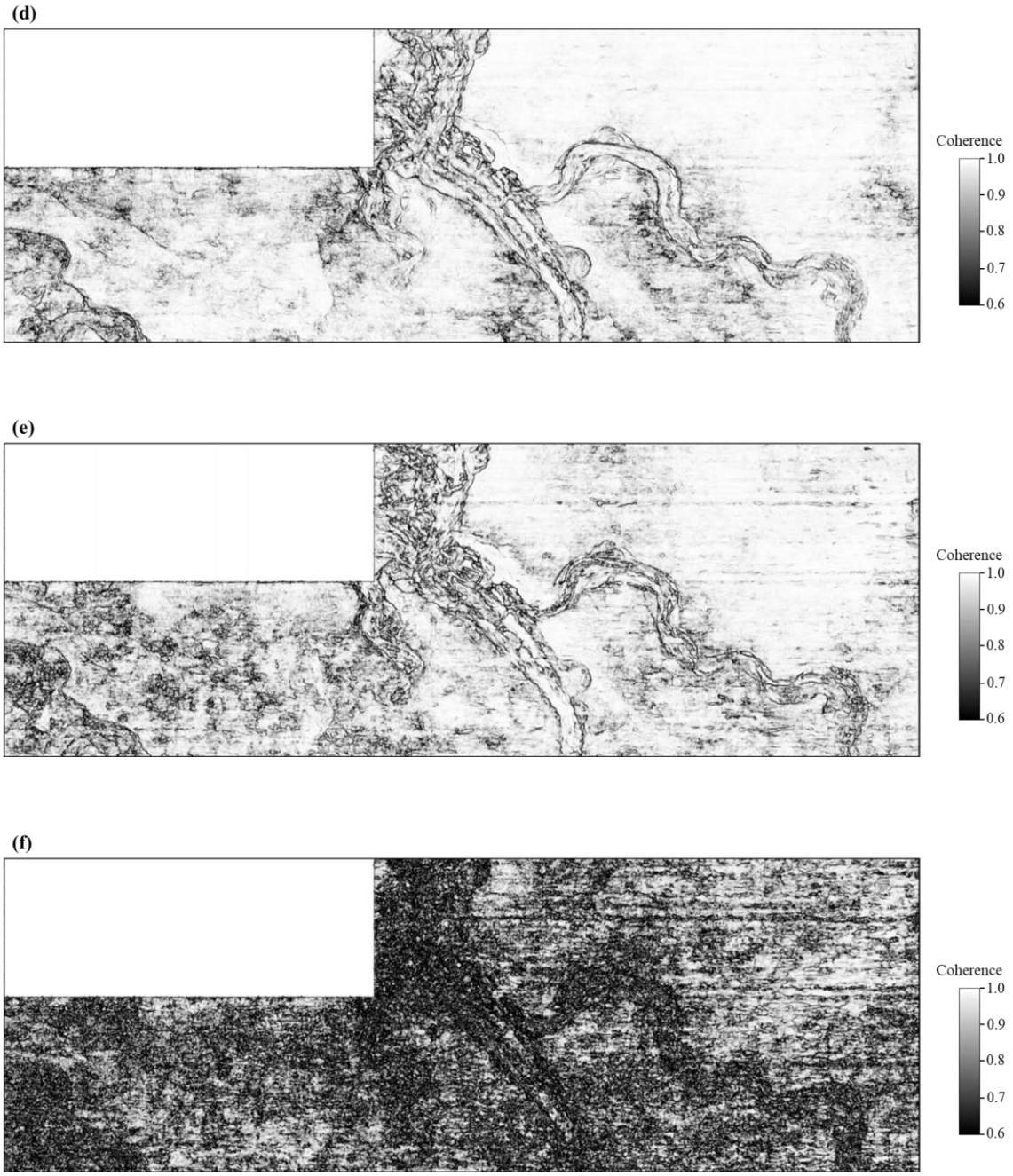

Figure 3.11. Coherence images computed using maximum entropy spectral voice components at: (a) 10 Hz, (b) 15 Hz, (c) 24 Hz, (d) 36 Hz, (e) 55 Hz, and (f) 85 Hz. Note that the coherence images from the lower-frequency maximum entropy spectral voices provide more details and exhibit higher resolution of the channel boundaries over the coherence images using the corresponding CWT components, such as the red circle area in Figure 3.11b compared with Figure 3.9b.

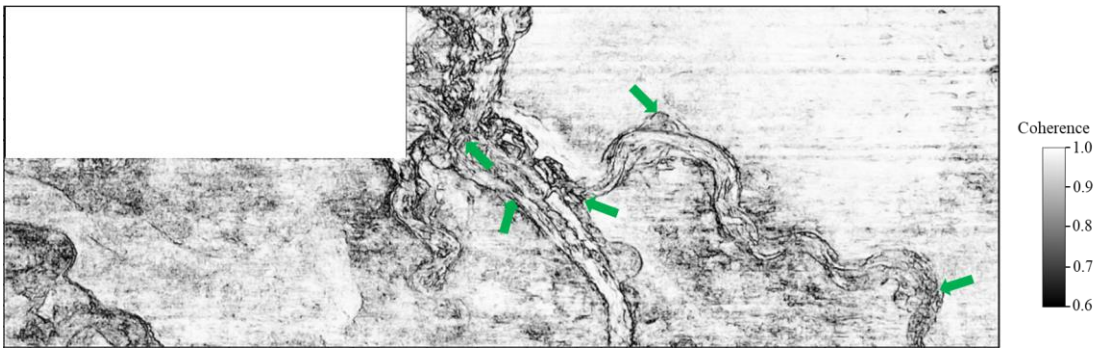

Figure 3.12. Multispectral coherence image computed using maximum entropy spectral voice components, exhibiting higher resolution of small-scale features (green arrows) compared with the multispectral coherence image computed from the corresponding CWT components (Figure 3.10).

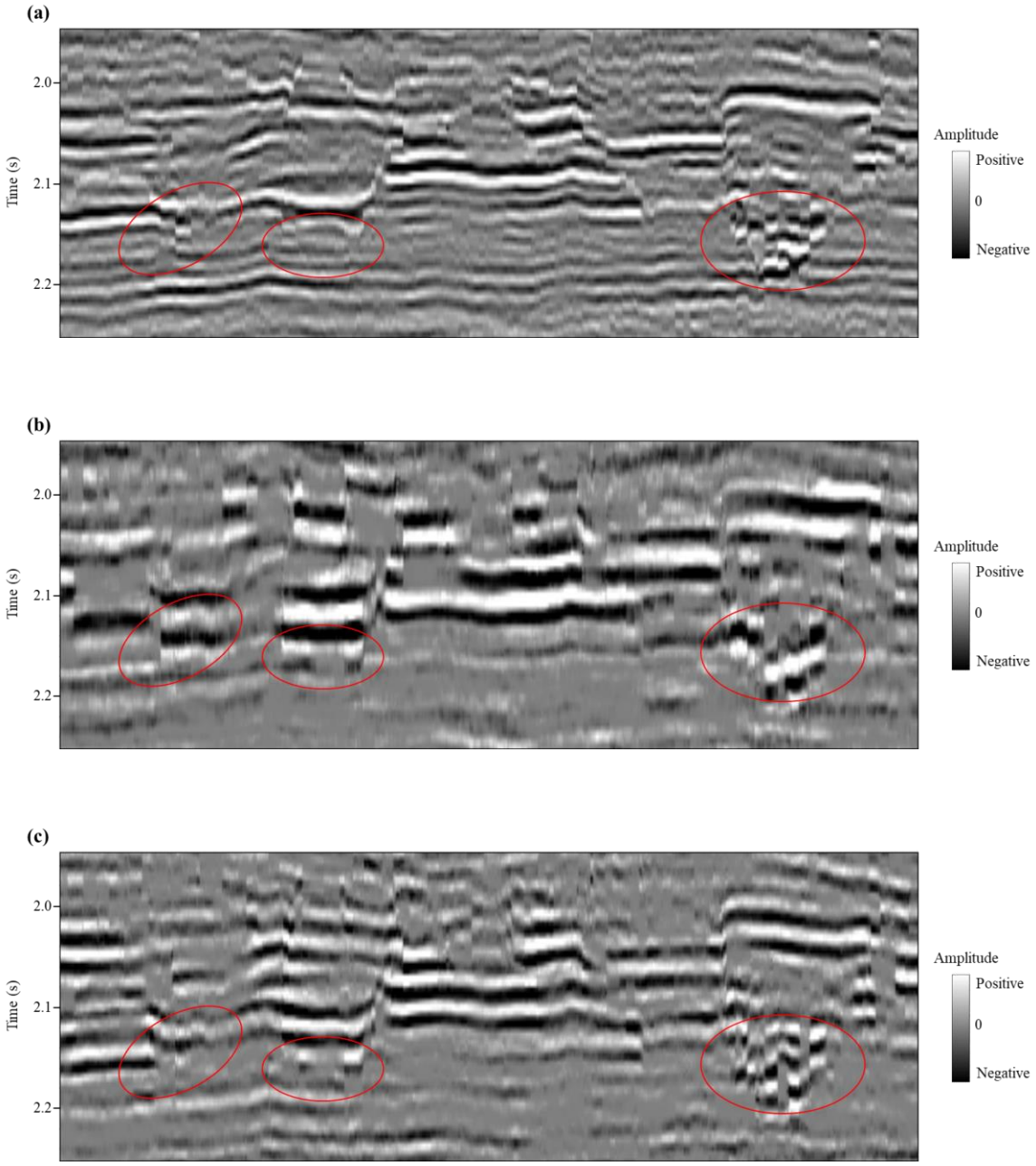

Figure 3.13. (a) Enlarged full-bandwidth vertical seismic amplitude slice. (b) 24 Hz spectral voice and (c) 36 Hz spectral voice after maximum entropy decomposition. Compared with the full-bandwidth data (red circles in Figure 3.13a), the boundaries of the thicker channels are much sharper in the 24 Hz component (red circles in Figure 3.13b), while the thinner channel boundaries are sharper and clearer in the 36 Hz spectral voice (red circles in Figure 3.13c). The channels with different scales are more highlighted in specific spectral voices, resulting in improved images of channel boundaries in the multispectral coherence.

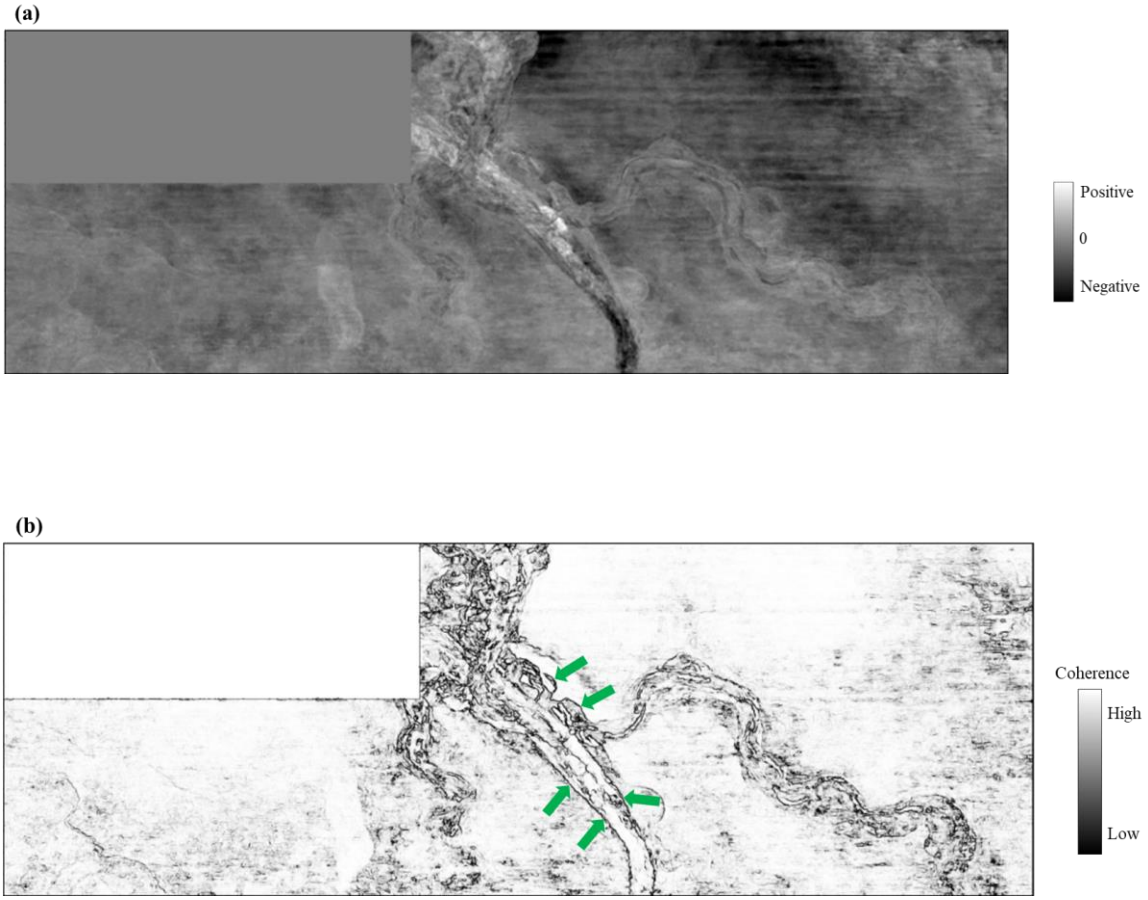

Figure 3.14. (a) AVT time slice, showing less noise and weaker reflections compared with the original seismic amplitude time slice (Figure 3.3b). (b) Coherence attribute computed using the AVT volume, appearing much clearer with less noise over the coherence computed using the SOF full-bandwidth seismic data (Figure 3.5). Note the more continuous boundaries of the thicker channels (green arrows in Figure 3.14b) compared with the coherence images computed from other spectral decomposition methods. However, the imaging of some small-scale features inside the thicker channels are decreased due to the lack of the higher-frequency components in the AVT data.

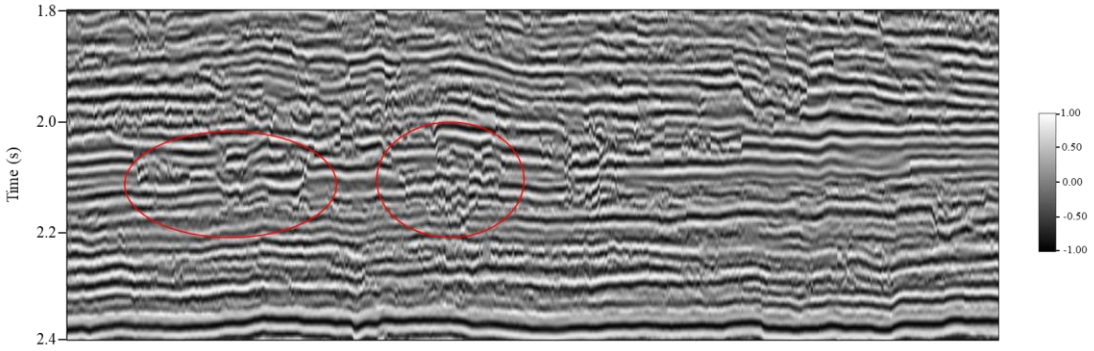

Figure 3.15. Vertical slice of spectral probe component using period 36 Hz, which is insensitive to the amplitude variation and the energy is much more balanced than other spectral decomposition methods, especially the channels indicated by red circles.

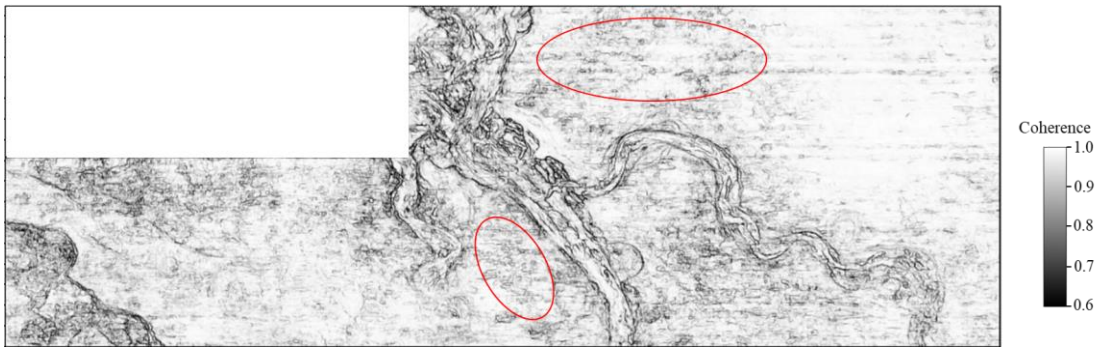

Figure 3.16. Multispectral coherence image computed using six spectral probes. It appears more balanced than the multispectral coherence images from other spectral decomposition methods, but noisier due to the equal weight for the noise in the shorter-period components when we build the covariance matrix (red circles).

CHAPTER 4: IMPROVING FAULT DELINEATION USING MAXIMUM ENTROPY MULTISPECTRAL COHERENCE

Abstract

The knowledge of fault geometry plays an important role in reservoir modeling and characterization. Seismic attributes, such as volumetric dip, coherence, and curvature, provide an efficient and objective tool to extract the fault geometric attributes. Traditionally, we use the noise-attenuated full-bandwidth seismic data to compute coherence followed by smoothing, sharpening, and skeletonization. However, different stratigraphic reflectors with relatively similar waveforms and amplitudes juxtaposing across a fault will algorithmically appear to be continuous, with the resulting fault image being broken. This leads to pseudo fault breakpoints and challenges the accurate extraction of other fault geometric attributes. Because the phase of the similar reflections across the faults varies with different spectral components, such non-stratigraphic alignments occur for only a few spectral components such that a multispectral coherence algorithm produces more continuous fault images. We evaluate the influence of spectral voice selection and spectral decomposition algorithm on the quality of fault imaging in multispectral coherence images using a 3D seismic survey acquired in the Taranaki Basin, New Zealand. Of the algorithms evaluated, we find the high-resolution maximum entropy based multispectral coherence method provides better result than those based on other spectral decomposition algorithms, which especially improves the fault continuity. However, the lateral resolution of fault imaging in multispectral coherence is decreased compared to the full-bandwidth coherence, because the fault image is smeared when we combine the coherence volumes computed using different spectral voices. We perform a fault enhancement workflow on the

maximum entropy based multispectral coherence volume to improve the lateral resolution of fault imaging, which helps delineate the minor faults.

Introduction

A geologic fault is defined as an approximately planar fracture or discontinuity in a rock volume across which there is visible displacement caused by rock mass movement. There are three basic types of faults: normal faults, reverse faults, and strike-slip faults. Identification and visualization of faults have indicated important applications in petroleum geology (e.g., Rotevatn and Fossen, 2011).

How to accurately delineate the fault geometric attributes still remains a big challenge, especially in the areas with complicated structures and poor data quality. Fault height is defined as the fault dimension measured along the dip direction, while the fault length is the fault dimension estimated along the strike. In seismic scale, a large fault often appears as a suite of smaller fault segments (Libak et al., 2017). The locations of the breakpoints for each fault segment determine the height and length of these fault segments.

The traditional fault interpretation approach is to hand-pick a suit of coarsely spaced lines perpendicular to the fault strike, which is a time-consuming task and can be highly dependent on the interpreters' experience. Additionally, this traditional approach faces the potential risk of ignoring subtle details along the faults that falls between the picked lines.

Seismic attributes provide a more modern workflow for fault identification and visualization (Chopra and Marfurt, 2007). Here, the interpreter examines time slices through fault-sensitive seismic attribute volumes, such as coherence, volumetric dip, and curvature, to confirm whether the faults seen on vertical amplitude images are laterally

continuous or disjoint. Curvature is excellent for visualizing faults but not necessarily for picking them. The most common situation is a most-positive and most-negative curvature anomaly pair that brackets the exact location of fault (Bhattacharya and Verma, 2019). For this reason, picking a curvature anomaly is biased to one side of the fault (Qi and Marfurt, 2018). However, when multiple faults cross-cut each other, Jahan et al. (2017) found that curvature anomalies become overly complex. Variations of seismic coherence attribute family are routinely used to detect faults, which could be computed using algorithms based on maximum cross-correlation (Bahorich and Farmer, 1995), Sobel filter (Luo et al., 1996), semblance (Marfurt et al., 1998), eigen-decomposition (Gersztenkorn and Marfurt, 1999), gradient structure tensor (Randen et al., 2000), or energy-ratio (Chopra and Marfurt, 2007). Unlike a human interpreter, all of these coherence algorithms operate in a small window consisting of perhaps 5 or 9 traces and 3 to 15 time samples, and therefore measure the local continuity of the seismic data. For this reason, all of these algorithms suffer from the alignment effect of different stratigraphic horizons with similar seismic waveforms across a fault, leading to holes in the subsequent coherence images.

Especially, these coherence gaps due to similar seismic reflections play a negative role in the interpretation of segmented faults. A segmented fault is composed of two or more fault segments arranged in echelon patterns (Davison, 1994; Schultz et al., 2010), compared to an isolated fault with no major mechanical interaction with nearby faults. A fault can be segmented vertically, horizontally, or in 3D. Fault segments can be hard-linked by fault splaying, or soft-linked by ductile strain of the rock volume between them (Walsh et al., 2003). In seismic profiles, if different stratigraphic reflectors with relatively similar waveforms juxtapose across the faults, the generated coherence image appears

discontinuous, which results in pseudo fault breakpoints. We face the risk of misinterpreting other faults to be segmented faults using this coherence attribute with poor fault continuity.

The seismic data come to the interpreter from the processing shop as a broadband, often spectrally whitened single volume. Depending on the data quality, the interpreter may use footprint suppression and structure-oriented filtering (SOF) to precondition the data to improve the quality of the subsequent coherence result (e.g., Chopra and Marfurt, 2007). Libak et al. (2017) observe that a larger temporal window in coherence computation can increase the fault continuity and reduce the noise content, but will overestimate the height of smaller faults. If the faults are not vertical, a large vertical analysis window can lead to lateral smearing of the discontinuities and even to small lateral shifts in the fault trace as seen on time slices. This latter artifact, along with the annoying stair-step artifacts (Lin and Marfurt, 2017) leads to misties when picking faults on coherence time slices and faults picked on vertical slices through the seismic amplitude data.

Fault breakpoints on seismic profile can be misinterpreted due to different reasons. For example, migration velocity analysis is sometimes performed to increase the continuity of reflectors while the actual geology is not continuous. Additionally, transition from competent to incompetent beds and improper selection of seismic migration algorithm for complicated structures can also lead to misinterpretation of fault breakpoints. Especially, the pitfalls associated with different horizons with similar waveforms aligned across a fault are well known by interpreters using auto-pickers (Figure 4.1, after Herron, 2011). The same problem leads to holes in coherence images that a human interpreter would manually pick through using a geologic model of sedimentary processes and tectonic deformation

(Libak et al., 2017; Lyu et al., 2019). In addition to increasing the size of temporal analysis window in the coherence computation (Libak et al., 2017), we can filter the coherence image using swarm intelligence (Pedersen et al., 2002), moment tensors and eigen-decomposition followed by image dilation and image erosion (Barnes, 2006), dynamically warping the seismic images using windows larger than a single event (Hale, 2013), or constructing a linked data structure (Wu and Hale, 2016).

Alaei (2012), Dewett and Henza (2016), Marfurt (2017), Li et al. (2018), Lyu et al. (2018), and Chopra and Marfurt (2019) show that multispectral coherence can improve the quality of coherence images compared to conventional full-bandwidth coherence. In some cases, this improvement is linked to certain spectral component exhibiting a higher S/N (signal-to-noise ratio) than other components, sometimes due to seismic data quality (Hardage, 2009) and sometimes due to the geologic features such as tuning (Zeng, 2015) and reflector alignment. In other cases, multispectral coherence measures the lateral change in phase across faults for different spectral components. Whatever the reason, multispectral coherence has been proven to be an effective tool to delineate the channel boundaries (Li et al., 2015; Li et al., 2018; Lyu et al., 2018) and detect the faults (Alaei, 2012; Dewett and Henza, 2016; Marfurt, 2017; Lyu et al., 2019; Qi et al., 2019).

Multispectral coherence is implemented by combining the coherence volumes computed using different spectral voices. There are two important issues for the computation of multispectral coherence: How to choose appropriate spectral voices, and which spectral decomposition algorithm to use. Dewett and Henza (2016) chose their components interactively. Lyu et al. (2020) evaluated both alternative spectral voice spacing methods and spectral decomposition algorithms as input to multispectral coherence.

When applied to a 3D volume with incised channels, their analysis showed that multispectral coherence images computed from exponentially spaced rather than equally spaced spectral voices better delineate the incised channel boundaries, and that high-resolution maximum entropy spectral decomposition algorithm further improves the resolution and quality of thinner channels and small-scale features than spectral decomposition methods.

Additionally, because the coherence images computed using different spectral voices depict different lateral resolution, the generated multispectral coherence image is smeared with lower lateral resolution after combination, which challenges the identification of minor faults. To address this issue, a directional skeletonization (Qi et al., 2016) after a Laplacian of a Gaussian filtering (Machado et al., 2016) is performed on the coherence volume to improve the lateral resolution.

In this paper, we extend the analysis of multispectral coherence by Lyu et al. (2020) for incised channels to determine the best workflow to fill the coherence gaps caused by relatively similar reflectors juxtaposed across the faults, improving the fault continuity. Because the phase of seismic reflections appears different in various spectral components, the alignment effects occur for only a few spectral voices but not for all spectral voices. This is the reason why we can improve the fault continuity and minimize the pseudo fault breakpoints using multispectral not full-bandwidth coherence images. We further evaluate that if the high-resolution maximum entropy spectral decomposition algorithm improves the resolution and quality of fault imaging in multispectral coherence volume. Additionally, we compute a fault enhancement workflow on the multispectral coherence volume to further improve the lateral resolution, which helps identify the minor faults.

We begin with a description of the 3D seismic data volume. Next we precondition the data for fault detection by applying footprint suppression and SOF, and illustrate the gaps in the faults due to alignment of similar reflectors on the full-bandwidth data volume. Then we attempt to ameliorate these shortcomings through the use of different spectral voice computation algorithms and multispectral coherence. A 3D case study in offshore Taranaki Basin is shown to indicate that maximum entropy based multispectral attributes effectively improve fault continuity and minimize pseudo fault breakpoints. Finally, we conclude with a summary of our findings and recommendations.

Data description

We illustrate the problem and our proposed solution using the highly fault Opunake 3D seismic dataset, located in the south-eastern part of the offshore Taranaki Basin, New Zealand (Figure 4.2). The Taranaki Basin is characterized as an extension from the Taranaki Fault Zone along the eastern margin (Smith et al., 1989) and exhibits complex subsurface geology with thick sedimentary sequences (Reilly et al., 2015). All of the structural elements within the Taranaki Basin are developed by the continuous tectonic activities and clockwise movement of the plate boundaries (King and Thrasher, 1992; Kumar and Mandal, 2017).

The study area (Figure 4.2) is characterized by a complex fault system between the Western Platform and the Taranaki Graben (Nodder, 1993), which is cut by the Cape Egmont Fault Zone and its splay. Seismic imaging and interpretation of this highly deformed fault system remain big challenges.

The 215 km^2 60-fold 3D seismic data were prestack time migrated, into bin sizes 6.25 m × 25.0 m with a time sample increment of 4 ms. Figure 4.3 shows a representative vertical slice AA' and time slice at t=0.40 s of the original seismic data exhibiting complex faulting. Note that the seismic data are contaminated by random noise, which decreases the detectability of the faults. We can also observe serious acquisition footprint in the amplitude time slice (Figure 4.3b), which will generate unexpected artifacts in the following coherence attribute computation.

Data conditioning

Coherence should always be computed along structural dip (Marfurt et al., 1999). Gradient structure tensors (GST) (Bakker, 2002; Luo et al., 2006) provide one of the most computationally efficient means of computing structural dip. In our implementation, we generalize the more commonly used algorithms by using an analytic versus the measured seismic trace, a short-window filter to minimize amplitude changes and maximize phase changes within the window, followed by a Kuwahara filter (Kuwahara et al., 1976; Marfurt, 2006) that assigns the dip to be that of the overlapping window with the greatest alignment. We then use the generated structural dip to guide the coherence computation using an energy-ratio method described in Appendix A of chapter 3.

The quality of the input seismic data is critical for the quality of the coherence images. The coherence vertical slice (Figure 4.4a) and time slice (Figure 4.4b) computed using the original full-bandwidth seismic are quite noisy, hindering identification of faults.

In addition to seismic noise, chaotic reflectors or "geologic" can also mask the coherence fault signature (Marfurt and Alves, 2014). Although the stronger reflectors are

relatively noise free, zones of lower reflectivity caused by subtle variations in the acoustic impedance of two layers exhibit a much lower S/N, giving rise to coherence anomalies parallel to local dip. Careful inspection will show some of these anomalies are geologic in nature and correspond to areas a geologist would define as possible condensed section. Mass transport deposits that sometimes appear as small rotated blocks and sometimes as chaotic reflectors also give rise to low coherence anomalies in this data volume. Gouges with apparent outrunner blocks and scours provide still more stratigraphic anomalies. In general, we want to preserve geologic features and suppress anomalies due to seismic noise.

There are several different types of methods to suppress the seismic noise before coherence computation (Chopra and Marfurt, 2007). In this data volume, we observe acquisition footprint on the original seismic amplitude (Figure 4.3b) and coherence (Figure 4.4b) time slices. To suppress these footprint artifacts, we use k_x-k_y filters followed by adaptive subtraction (Falconer and Marfurt, 2008), resulting in the vertical and time slices shown in Figure 4.5. Note that some "geologic" noise is suppressed by this footprint attenuation workflow, such as the noise in coherence vertical slices (Figure 4.4a and 4.5a) caused by the strong reflections, because some of these noises appear periodic.

In addition to acquisition footprint, random noise in the seismic amplitude volume also decreases the detectability of faults in the coherence images. We therefore apply SOF (structure-oriented filtering) to the seismic amplitude volume after footprint attenuation and obtain the coherence images shown in Figure 4.6 that further improve the quality of fault images.

Data-adaptive windows in coherence computation

The analysis window plays an important role in delineating the fault geometric attributes in the coherence images. On coherence images, the fault height and length can depend on size of the analysis window, with larger windows potentially smearing a fault anomaly beyond its true extent. We generally use an analysis window with constant size in the coherence computation. A constant sized large analysis window "vertically stacks" the discontinuities which may improve the S/N of near vertical faults, but smears the lateral resolution more gently dipping faults, and artificially extends the limits of small faults. In contrast, a constant-sized small analysis window preserves high resolution events but may provide inferior images in areas with low S/N.

Marfurt et al. (1998) recognized that for moderate quality data the optimum window size is a function of the spectral content. For example, if the dominant frequency is 50 Hz, and dominant period 20 ms, significantly increasing the window size beyond 20 ms adds little to the coherence anomaly at the target level but risks mixing discontinuities at different stratigraphic levels into the result. Like coherence, spectral decomposition is routinely used in seismic interpretation. Lin et al. (2014) therefore defined a data-adaptive coherence analysis window based on the laterally and vertically smoothed spectrum of the data. In their implementation, the window size is defined to be the inverse of the frequency at a user defined percentile (e.g. 50 or 80 percent).

In Figure 4.7, we show the coherence vertical slices computed with a constant ±8 ms analysis window (Figure 4.7a), a constant ±24 ms analysis window (Figure 4.7b), and a data-adaptive analysis window (Figure 4.7c) using the same noise attenuated full-bandwidth seismic data. Note that the larger ±24 ms constant window provides a coherence

image with better continuity than that using the smaller ±8 ms, but smears the minor faults. The smaller constant window improves the resolution of the coherence image, but appears noisier. The data-adaptive analysis window provides coherence result with both good continuity and high resolution.

Pseudo fault breakpoints due to alignment of similar reflections

The coherence images computed using the noise attenuated seismic data (Figure 4.6) provide a significant improvement over the coherence results computed using the original seismic amplitude volume (Figure 4.4). However, if we zoom in the right part of the coherence vertical slices and co-render them with seismic amplitude (Figure 4.8), we observe multiple gaps and stair-step artifacts in the faults seen on the vertical slices computed using both the original and noise attenuated seismic data, especially the ones indicated by red arrows in Figure 4.8b. Unlike a human interpreter who looks at the entire seismic section and draws a fault through such "continuous" zones using discontinuities above and below as a guide, algorithms like coherence are purely local, using only the information available in the analysis window.

The coherence algorithms are all based on measuring the waveform similarity. Relatively similar reflections across the faults are common in our survey, which challenges the detection of waveform dissimilarity around the faults. Although different coherence algorithms exhibit different sensitivity to areas where similar reflections juxtapose across a fault, they all show high coherence values (Libak et al., 2017), such as the obvious gaps in coherence image (red arrows in Figure 4.8b). The fault breakpoints will be misinterpreted on this coherence image, further resulting in inaccurate measurement of fault height and length.

Reflector alignment at different spectral voices

As with the failure of auto-pickers shown in Figure 4.1, algorithmic gaps that suggest segmented rather than continuous faults can lead to inaccurate estimates of the fault height, length, and style. We can observe obvious alignment effects in the zoomed full-bandwidth seismic vertical slice (Figure 4.9a) indicated by the red arrows. To avoid such fault gaps, we will want to compute the coherence attribute for a version of the seismic data exhibiting a weaker alignment effect.

Spectral decomposition has been widely used in seismic exploration (e.g., Peyton et al., 1998; Partyka et al., 1999; Castagna et al., 2003; Hu et al., 2020; Liu et al., 2020), which transforms a single full-bandwidth seismic amplitude volume into multiple frequency component volumes. Because of thin-bed tuning and other phenomena, a specific spectral component may show the edges of stratigraphic features such as channels and carbonate buildups better than others. For example, a thicker channel is better delineated at a lower frequency, while a narrower channel is highlighted at a higher frequency (Marfurt and Kirlin, 2001; Laughlin et al., 2002; Li et al., 2018; Lyu et al., 2020).

Gao (2013) found that spectral probe based on a specific frequency better delineated faults than the original full-bandwidth data. There are several kinds of spectral decomposition algorithms, such as simple band-pass filtering, continuous wavelet transform (CWT) (Grossmann and Morlet, 1984), maximum entropy spectral analysis (Puryear et al., 2012), and spectral probes (Gao, 2013), etc.

Although a full-bandwidth seismic signal may provide false alignment across a fault, the phase of each spectral component will exhibit different alignments from each other, that together provide a means to map the fault. Figure 4.9 shows the aligned reflectors

around the faults indicated by red arrows in Figure 4.9a are less aligned in the 36 Hz (yellow ellipses in Figure 4.9b) and 55 Hz (yellow ellipses in Figure 4.9c) spectral voices.

Figure 4.10 shows the corresponding coherence images computed using the full-bandwidth seismic data (Figure 4.10a), 36 Hz (Figure 4.10b), and 55 Hz spectral voice (Figure 4.10c). Obvious gaps in what a human interpreter would determine to be a continuous fault appear in the full-bandwidth coherence (red arrows in Figure 4.10a). The coherence images computed using spectral voices provide a significant improvement of different faults indicated by the green ellipses in Figure 4.10b and 4.10c.

Review of multispectral coherence theory

Based on the physical explanation why certain spectral voice provides better imaging for specific faults in the previous subsection, we try to minimize pseudo fault breakpoints and improve fault continuity by combining coherence images computed using various spectral voices.

A traditional way is to co-render the coherence volumes from different spectral voices using RGB (red-green-blue) blending. It has been applied to help delineate channels, caves, and karsts (Alaei, 2012; Li and Lu, 2014; Wang et al., 2019). However, this combination approach is limited to only three coherence volumes, which is not available if we want to combine more spectral voices' results. To relax the limitation of RGB blending, Dewett and Henza (2016) combined the coherence volumes using a self-organizing map method. Sui et al. (2015) used only the spectral magnitude without phase information to generate the combined coherence volume.

To adapt to more complicated subsurface structures, Marfurt (2017) introduced multispectral coherence considering both the spectral magnitude and phase information through the use of spectral voices. Unlike RGB blending, there is no limit of the number of input spectral voices that can be used. For simplicity, Marfurt (2017) used a suite of filter banks (equivalent to CWT voice components) as input to multispectral coherence; here we will examine alternative decomposition algorithms as input. The details of multispectral coherence theory are provided in chapter 3.

The role of spectral voice selection in multispectral coherence on fault imaging

There are two important factors in multispectral coherence that affect the quality of the fault imaging: spectral component selection and spectral decomposition algorithm. We first estimate the effective frequency bandwidth by analyzing the noise-attenuated full-bandwidth seismic dataset, defining the starting and ending spectral voices in multispectral coherence. We then sample the bandwidth using two methods - equal spacing and exponential spacing (constant number of components per octave) to determine if one is better than the other for fault delineation.

Equal-spacing method means that we choose spectral voices with a constant linear increment, while exponential-spacing method provides the spectral voices with a constant octave bandwidth. In our survey, we divide the bandwidth from 10 to 85 Hz into six CWT spectral voices using the equally spaced (10, 25, 40, 55, 70, 85 Hz) and exponentially spaced (10, 15, 24, 36, 55, 85 Hz) components and show the corresponding multispectral coherence time slices in Figure 4.11.

Although these two coherence images exhibit comparable imaging quality of the primary faults. However, more detailed analysis indicates that the coherence image using the exponentially-spaced spectral voices (red arrows in Figure 4.11b) exhibits better continuity over the result using the equally-spaced spectral voices (red arrows in Figure 4.11a). We therefore recommend computing multispectral coherence for fault imaging using the exponentially-spaced spectral voices.

The role of spectral decomposition algorithm on fault imaging

Spectral decomposition algorithm is another important factor on the quality of multispectral coherence images. Band-pass filters (equivalent to CWT filter banks) are easy to incorporate internally to a multispectral coherence algorithm and were used by Marfurt (2017), Li et al. (2018), Lyu et al. (2019), and Qi et al. (2019).

A library of CWT filter banks (Grossmann and Morlet, 1984) are cross-correlated with each seismic trace, thereby constructing a CWT spectral voice. The temporal resolution of the CWT results depends on the size of the center frequency of the filter (Castagna and Sun, 2006; Puryear et al., 2012). High frequency components can be computed in a short window, while the low frequency components require a longer window, where the window size is approximately two times the period of the center frequency.

Maximum entropy algorithms provide a least-squares estimate of the contribution of a given spectral component (Puryear et al., 2012), which does not require the analysis window to contain a full period. We solve an inverse problem using the objective function, which tries to fit the data with the minimum of sines and cosines. The Fourier series coefficients are considered as a function of time and inverted using the truncated sinusoidal

kernels for a moving time window. For this reason, maximum entropy based spectral decomposition can reduce smearing and provide superior time and frequency resolution over CWT methods.

We can decompose the full-bandwidth seismic data into different spectral voices using either linear methods (e.g. band-pass filtering, CWT, and maximum entropy based algorithm) or nonlinear method (e.g. spectral probe algorithm (Gao, 2013)). The linear spectral decomposition algorithms can preserve amplitude information and try to reconstruct the original full-bandwidth seismic data. However, the nonlinear spectral decomposition does not preserve the amplitude information and could not be used to reconstruct the original seismic data.

In Figure 4.12 and 4.13, we show the multispectral coherence vertical and time slices computed using the spectral voices decomposed by band-pass filtering (Figure 4.12a and 4.13a), CWT (Figure 4.12b and 4.13b), spectral probes (Figure 4.12c and 4.13c), and maximum entropy based method (Figure 4.12d and 4.13d). All multispectral coherence images provide significantly improved fault imaging compared to the coherence results computed using the full-bandwidth seismic data (Figure 4.6).

If we further compare the multispectral coherence images computed using different spectral decomposition algorithms, the band-pass filtering results (Figure 4.12a and 4.13a) exhibit relatively poor continuity. The CWT (Figure 4.12b and 4.13b) results improves the continuity, but the resolution is not good enough to identify the minor faults. The multispectral coherence images computed using spectral probes (Figure 4.12c and 4.13c) appear more comparable energy comparison between the fault imaging and noise. Due to amplitude insensitivity of spectral probes, an equal weight is assigned to noisy and less

noisy components during the construction of the covariance matrix, which decreases the quality of fault imaging in the generated multispectral coherence attribute. Similarly, the multispectral coherence images computed using cosine of instantaneous phase or small-window AGC (automatic gain control) dataset appear noisy due to the application of very similar weights for various spectral voices with different S/N. We recommend to avoid computing multispectral coherence using the decomposed spectral voices without amplitude information. The multispectral coherence results computed using the maximum entropy spectral voices (Figure 4.12d and 4.13d) show good continuity of the primary faults, and provide higher resolution image to help identify the minor faults.

Fault segmentation is a phenomena taking place in faults, such as strike slip faults. Accurate estimation of the real fault breakpoints vertically and laterally is important to characterize the faults. However, the pseudo fault breakpoints caused by relatively similar reflections juxtaposing faults in coherence image will lead to misinterpretation of faults. Focusing on the fault gaps due to non-stratigraphic alignments, we show the zoomed multispectral coherence vertical slices co-rendered with seismic amplitude in Figure 4.14. Note that all multispectral coherence images (Figure 4.14) improve the fault continuity over the full-bandwidth coherence (Figure 4.8b), allowing us to better estimate fault breakpoints and further fault height and length.

Of the alternative spectral decomposition algorithms, it is observed that the maximum entropy based multispectral coherence (Figure 4.14d) provides the best fault continuity with minimum gaps compared to other spectral decomposition algorithms (Figure 4.14a, 4.14b and 4.14c). Based on the preceding observations, we recommend to compute

multispectral coherence attribute for fault detection using this high-resolution maximum entropy spectral decomposition algorithm to further improve the fault imaging quality.

Improving lateral resolution of faults in multispectral coherence

Multispectral coherence, especially the maximum entropy based multispectral coherence images (Figure 4.12d, 4.13d, and 4.14d), optimizes the imaging quality of faults over the corresponding full-bandwidth coherence slices (Figure 4.6a, 4.6b, and 4.8b). Especially, the pseudo fault breakpoints caused by non-stratigraphic alignments of similar seismic reflections are effectively minimized in the maximum entropy based multispectral coherence images.

However, it is further noted that the multispectral coherence images appear lower lateral resolution compared to the full-bandwidth coherence results. To illustrate the reason why multispectral coherence decreases the lateral resolution, we show the vertical coherence slices of a single fault computed using 10 Hz (Figure 4.15a), 24 Hz (Figure 4.15b), and 55 Hz (Figure 4.15c) maximum entropy spectral voices. The 10 Hz coherence image (Figure 4.15a) appears good continuity but low lateral resolution of the fault imaging. The 24 Hz coherence slice (Figure 4.15b) appears both good continuity and acceptable lateral resolution of the fault. The 55 Hz coherence image (Figure 4.15c) shows high lateral resolution but appears poor imaging quality. In Figure 4.15d, we co-render the coherence vertical slices computed using these maximum entropy spectral voices (Figure 4.15a, 4.15b, and 4.15c) and use RGB blending method for display. It is noted that when we combine these coherence volumes computed using different spectral voices, the fault imaging in the co-rendered display (Figure 4.15d) is smeared with decreased lateral resolution. In

multispectral coherence, more spectral voices are included in the computation, which further decreases the lateral resolution of the fault imaging in the coherence volume.

In order to further suppress other structural discontinuity artifacts and improve the lateral resolution of the fault imaging, we apply a fault enhancement workflow (Qi et al., 2019) on the maximum entropy based multispectral coherence volume. We first implement a structure-oriented median filter on the multispectral coherence dataset, which aims to reject the steeply dipping faults but reserve the stratigraphic anomalies. Next, we subtract these stratigraphic anomalies parallel to the reflector dip, generating a residual volume with the remaining discontinuities correlated to the faults and stratigraphic edges. Finally, the generated residual volume is input to compute an energy-weighted directional LoG (Laplacian of a Gaussian) filter, sharpening and smoothing the faults through an iterative approach. The fault enhancement vertical (Figure 4.16a) and time (Figure 4.16b) slices further reduce other stratigraphic discontinuity artifacts and improve the lateral resolution of fault imaging compared to the maximum entropy based multispectral coherence images (Figure 4.12d and 4.13d).

Conclusions

Accurate fault detection and delineation faces the challenge of pseudo fault breakpoints due to the non-stratigraphic alignments of similar reflections juxtaposing across the faults, even though we use the full-bandwidth coherence attribute computed from carefully noise-attenuated seismic dataset. The 3D case study in offshore Taranaki Basin indicates that multispectral coherence effectively minimizes the pseudo fault breakpoints and improves the fault continuity, because different spectral voices appear different phase information of the similar reflections, resulting in alignment effect in only a few but not all spectral voices.

Based on the observations in the experiments, we suggest to avoid computing multispectral coherence using a transformed dataset without amplitude information, which will introduce more noise in coherence image. We further recommend to improve the quality of fault imaging in multispectral coherence using a high-resolution maximum entropy spectral decomposition algorithm with exponentially-spaced spectral voices. We further perform a fault enhancement workflow on the maximum entropy based multispectral coherence volume, improving the lateral resolution of the fault imaging. In this paper, we focus on improving coherence algorithm to minimize the pseudo fault breakpoints due to relatively similar reflections juxtaposing across the faults. This is not the only reason for misinterpreting fault breakpoints. Other potential reasons (e.g. migration velocity analysis, transition from competent to incompetent beds) should also be considered in your given research survey. Additionally, how to determine which spectral voice represents the best for a specific fault remains an interesting future research topic.

Acknowledgements

The authors thank all sponsors of Attribute Assisted Seismic Processing and Interpretation (AASPI) consortium group for their generous sponsorship, and colleagues for their valuable suggestions. We also thank New Zealand Petroleum and Minerals for providing their survey for use in this study.

References

Alaei, B., 2012, Improved fault imaging by integration of frequency decomposition and fault attributes, example from mid Norwegian sea: Proceedings of the 3rd EAGE Fault and Top Seal Conference, C13.

Bahorich, M. S., and S. L. Farmer, 1995, 3-D seismic coherency for faults and stratigraphic features: The coherence cube: The Leading Edge, **14**, 1053–1058.

Bakker, P., 2002, Image structure analysis for seismic interpretation: Ph.D. thesis, Delft University of Technology.

Barnes, A. E., 2006, A filter to improve seismic discontinuity data for fault interpretation: Geophysics, **71**, P1–P4.

Bhattacharya, S., and S. Verma, 2019, Application of Volumetric Seismic Attributes for Complex Fault Network Characterization on the North Slope, Alaska: Journal of Natural Gas Science and Engineering, **65**, 56–67.

Castagna, J. P., S. Sun, and R. Siegfried, 2003, Instantaneous spectral analysis: Detection of low-frequency shadows associated with hydrocarbons: The Leading Edge, **22**, 120–127.

Castagna, J. P., and S. Sun, 2006, Comparison of spectral decomposition methods: First Break, **24**, 75–79.

Chopra, S., and K. J. Marfurt, 2007, Seismic attributes for prospect identification and reservoir characterization: SEG.

Chopra, S., and K. J. Marfurt, 2019, Multispectral, multiazimuth, and multioffset coherence attribute applications: Interpretation, **7**, SC21–SC32.

Davison, I., 1994, Linked fault systems; extensional, strike-slip and contractional. In: Hancock, P.L. (Ed.), Continental Deformation, pp. 121–142.

Dewett, D. T, and A. A. Henza, 2016, Spectral similarity fault enhancement: Interpretation, **4**, SB149–SB159.

Falconer, S., and K. J. Marfurt, 2008, Attribute-driven footprint suppression: 78th Annual International Meeting, SEG, Expanded Abstracts, 2667–2671.

Gao, D., 2013, Wavelet spectral probe for seismic structure interpretation and fracture characterization: A workflow with case studies: Geophysics, **78**, O57–O67.

Gersztenkorn, A., and K. J. Marfurt, 1999, Eigenstructure-based coherence computations as an aid to 3-D structural and stratigraphic mapping: Geophysics, **64**, 1468–1479.

Grossmann, A., and J. Morlet, 1984, Decomposition of Hardy functions into square integrable wavelets of constant shape: SIAM Journal on Mathematical Analysis, **15**, 723–736.

Hale, D., 2013, Dynamic warping of seismic images: Geophysics, **78**, S105–S115.

Hardage, B., 2009, Frequencies are fault finding factors: looking low aids data interpretation: AAPG Explorer, **30**, 34.

Herron, D., 2011, First Steps in Seismic Interpretation: Society of Exploration Geophysics.

Hu, Y., H. Chen, H. Qian, X. Zhou, Y. Wang, and B. Lyu, 2020, A high-precision time–frequency analysis for thin hydrocarbon reservoir identification based on synchroextracting generalized S-transform: Geophysical Prospecting, **68**(3), 941–954.

Jahan, I., J. Castagna, M. Murphy, and M. A. Kayali, 2017, Fault detection using principal component analysis of seismic attributes in the Bakken Formation, Williston Basin, North Dakota, USA: Interpretation, **5**, T333–T344.

King, P. R., and G. P. Thrasher, 1992, Post-Eocene development of the Taranaki Basin, New Zealand: convergent overprint of a passive margin, in J. S. Watkins, Z. Feng, and K. J. McMillen, eds., Geology and geophysics of continental margins: American Association of Petroleum Geologists Memoir **53**, 93–118.

Kumar, P. C., and A. Mandal, 2017, Enhancement of fault interpretation using multi-attribute analysis and artificial neural network (ANN) approach: A case study from Taranaki Basin, New Zealand: Exploration Geophysics, **49**.

Kuwahara, M., K. Hachimura, S. Eiho, and M. Kinoshita, 1976, Digital processing of biomedical images: Plenum Press, 187–203.

Laughlin, K., P. Garossino, and G. Partyka, 2002, Spectral decomposition applied to 3D: AAPG Explorer, **23**, 28–31.

Libak, A., B. Alaei, A. Torabi, 2017, Fault visualization and identification in fault seismic attribute volumes: Implications for fault geometric characterization: Interpretation, **5**, B1–B16.

Li, F., and W. Lu, 2014, Coherence attribute at different spectral scales: Interpretation, **2**, SA99–SA106.

Li, F., J. Qi, and K. J. Marfurt, 2015, Attribute mapping of variable-thickness incised valley-fill systems: The Leading Edge, **34**(1), 48–52.

Li, F., J. Qi, B. Lyu, and K. J. Marfurt, 2018, Multispectral coherence: Interpretation, **6**, T61–T69.

Lin, T., D. Chang, B. Zhang, J. Guo, and K. Marfurt, 2014, Seismic attributes estimation using a self-adaptive window: 84th Annual International Meeting, SEG, Expanded Abstracts, 1654–1658.

Lin, T., and K. J. Marfurt, 2017, What causes those annoying stair step artifacts on coherence volumes?: AAPG Explorer Geophysical Corner, March, Article 37830.

Liu, N., Z. Li, F. Sun, F. Li, and J. Gao, 2020, Seismic geologic structure characterization using a high-order spectrum-coherence attribute: Interpretation, **8**, T391–T401.

Luo, Y., W. G. Higgs, and W. S. Kowalik, 1996, Edge detection and stratigraphic analysis using 3-D seismic data: 66th Annual International Meeting, SEG, Expanded Abstracts, 324–327.

Luo, Y., Y. C. E. Wang, N. M. AlBinHassan, and M. N. Alfaraj, 2006, Computation of dips and azimuths with weighted structural tensor approach: Geophysics, **71**, V119–V121.

Lyu, B., F. Li, J. Qi, T. Zhao, and K. J. Marfurt, 2018, Highlighting discontinuities with variational mode decomposition based coherence: 88th Annual International Meeting, SEG, Expanded Abstracts, 1798–1802.

Lyu, B., J. Qi, G. Machado, F. Li, and K. J. Marfurt, 2019, Seismic fault enhancement using spectral decomposition assisted attributes: 89th Annual International Meeting, SEG, Expanded Abstracts, 1938–1942.

Lyu, B., J. Qi, F. Li, Y. Hu, T. Zhao, S. Verma, and K. J. Marfurt, 2020, Multispectral coherence: Which decomposition should we use?: Interpretation, **8**, T115–T129.

Machado, G., A. Alali, B. Hutchinson, O. Olorunsola, and K. J. Marfurt, 2016, Display and enhancement of volumetric fault images: Interpretation, **4**, SB51–SB61.

Marfurt, K. J., S. L. Farmer, M. S. Bahorich, and R. L. Kirlin, 1998, 3-D seismic attributes using a semblance-based coherency algorithm: Geophysics, **63**, 1150–1165.

Marfurt, K. J., 2006, Robust estimates of 3D reflector dip and azimuth: Geophysics, **71**, P29–P40.

Marfurt, K. J., V. Sudhaker, A. Gersztenkorn, and K. D. Crawford, 1999, Coherency calculations in the presence of structural dip: Geophysics, **64**, 104–111.

Marfurt, K. J., and R. Kirlin, 2001, Narrow-band spectral analysis and thin-bed tuning: Geophysics, **66**, 1274–1283.

Marfurt, K. J., and T. M. Alves, 2014, Pitfalls and limitations in seismic attribute interpretation of tectonic features: Interpretation, **3**, SB5–SB15.

Marfurt, K. J., 2017, Interpretational aspects of multispectral coherence: 79th Annual International Conference and Exhibition, EAGE, Extended Abstracts.

Nodder, D. S., 1993, Neotectonics of the offshore Cape Egmont Fault Zone, Taranaki Basin, New Zealand: New Zealand Journal of Geology and Geophysics, **36**, 167–184.

Partyka, G. A., J. Gridley, and J. Lopez, 1999, Interpretational applications of spectral decomposition in reservoir characterization: The Leading Edge, **18**, 353–360.

Pedersen, S. I., T. Randen, L. Sønneland, and Ø. Steen, 2002, Automatic fault extraction using artificial ants: 72nd Annual International Meeting, SEG, Expanded Abstracts, 512–515.

Peyton, L., R. Bottjer, and G. Partyka, 1998, Interpretation of incised valleys using new-3D seismic techniques: A case history using spectral decomposition and coherency: The Leading Edge, **17**, 1294–1298.

Puryear, C. I., O. N. Portniaguine, C. M. Cobos, and J. P. Castagna, 2012, Constrained least-squares spectral analysis: Application to seismic data: Geophysics, **77**, V143–V167.

Qi, J., F. Li, B. Lyu, B. Zhang, O. Olorunsola, and K. J. Marfurt, 2016, Seismic fault enhancement and skeletonization: 86th Annual International Meeting, SEG, Expanded Abstracts, 1966–1970.

Qi, J., B. Lyu, A. Alali, G. Machado, Y. Hu, and K. J. Marfurt, 2019, Image processing of seismic attributes for automatic fault extraction: Geophysics, **84**, O25–O37.

Qi, X., and K. J. Marfurt, 2018, Volumetric aberrancy to map subtle faults and flexures: Interpretation, 6, T349–T365.

Randen, T., E. Monsen, C. Signer, A. Abrahamsen, J. O. Hansen, T. Saeter, J. Schlaf, and L. Sønneland, 2000, Three-dimensional texture attributes for seismic data analysis: 70th Annual International Meeting, SEG, Expanded Abstracts, 668–671.

Reilly, C., A. Nicol, J. J. Walsh, and H. Seebeck, 2015, Evolution of faulting and plate boundary deformation in the Southern Taranaki Basin, New Zealand: Tectonophysics, **651–652**, 1–18.

Rotevatn, A., and H. Fossen, 2011, Simulating the effect of subseismic fault tail and process zones in siliciclastic reservoir analogue: Implications for aquifer support and trap definition: Marine and Petroleum Geology, **28**, 1648–1662.

Schultz, R. A., R. Soliva, C. H. Okubo, and D. Mège, 2010, Fault populations: T.R. Watters, R.A. Schultz (Eds.), Planetary Tectonics, Cambridge University Press, pp. 457–510

Smith, E. G. C., T. Stern, and M. Reyners, 1989, Subduction and back-arc activity at the Hikurangi convergent margin, New Zealand: Pure and Applied Geophysics, **129**, 203–231.

Sui, J., X. Zheng, and Y. Li, 2015, A seismic coherency method using spectral attributes: Applied Geophysics, **12**, 353–361.

Wang, T., S. Yuan, J. Gao, S. Li, and S. Wang, 2019, Multispectral phase-based geosteering coherence attributes for deep stratigraphic feature characterization: IEEE Geoscience and Remote Sensing Letters, **16**, 1309–1313.

Walsh, J. J., W. R. Bailey, C. Childs, A. Nicol, and C. G. Bonson, 2003. Formation of segmented normal faults: a 3-D perspective: Journal of Structural Geology, **25**, 1251–1262.

Wu, X., and D. Hale, 2016, 3D seismic image processing for faults: Geophysics, **81**, IM1–IM11.

Zeng, H., 2015, Predicting geometry and stacking pattern of thin beds by interpreting geomorphology and waveforms using sequential stratal-slices in the Wheeler domain: Interpretation, **3**, SS49–SS64.

Chapter 4 figures

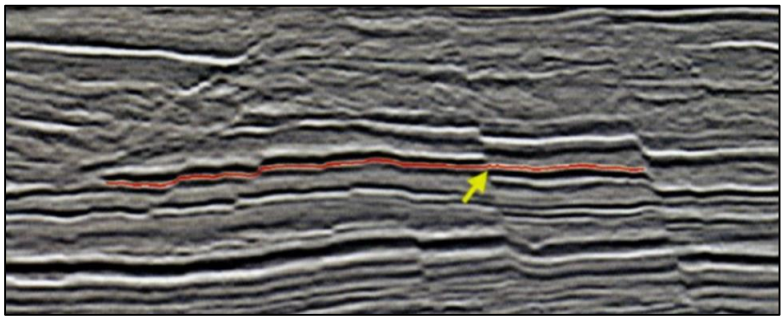

Figure 4.1. A well-known pitfall in auto-tracking of a seismic horizon. If the auto-picker correlation window is too short, or if the faults are not somehow flagged by the interpreter, the auto-picker (or inexperienced human interpreter!) can miss pick the seismic event across the fault (after Figure 17a in Chapter 7 of Herron (2011)).

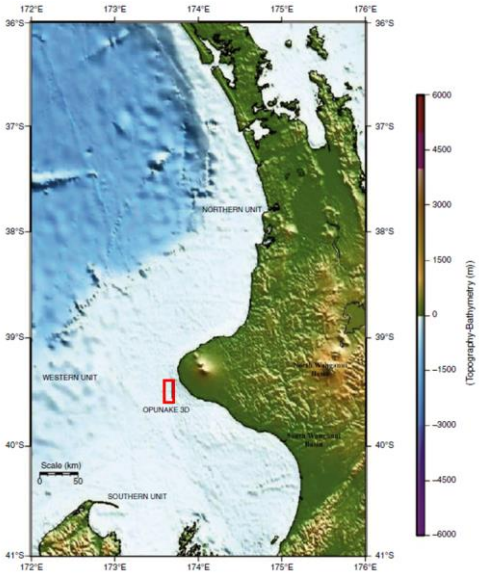

Figure 4.2. The location of Opunake 3D seismic survey (red rectangle) in the south-eastern part of offshore Taranaki Basin, New Zealand (after Kumar and Mandal, 2017). The Opunake 3D covers approximate 215 km^2 with bin sizes 6.25 m × 25.0 m, 60-fold coverage, and a 4 ms time sample.

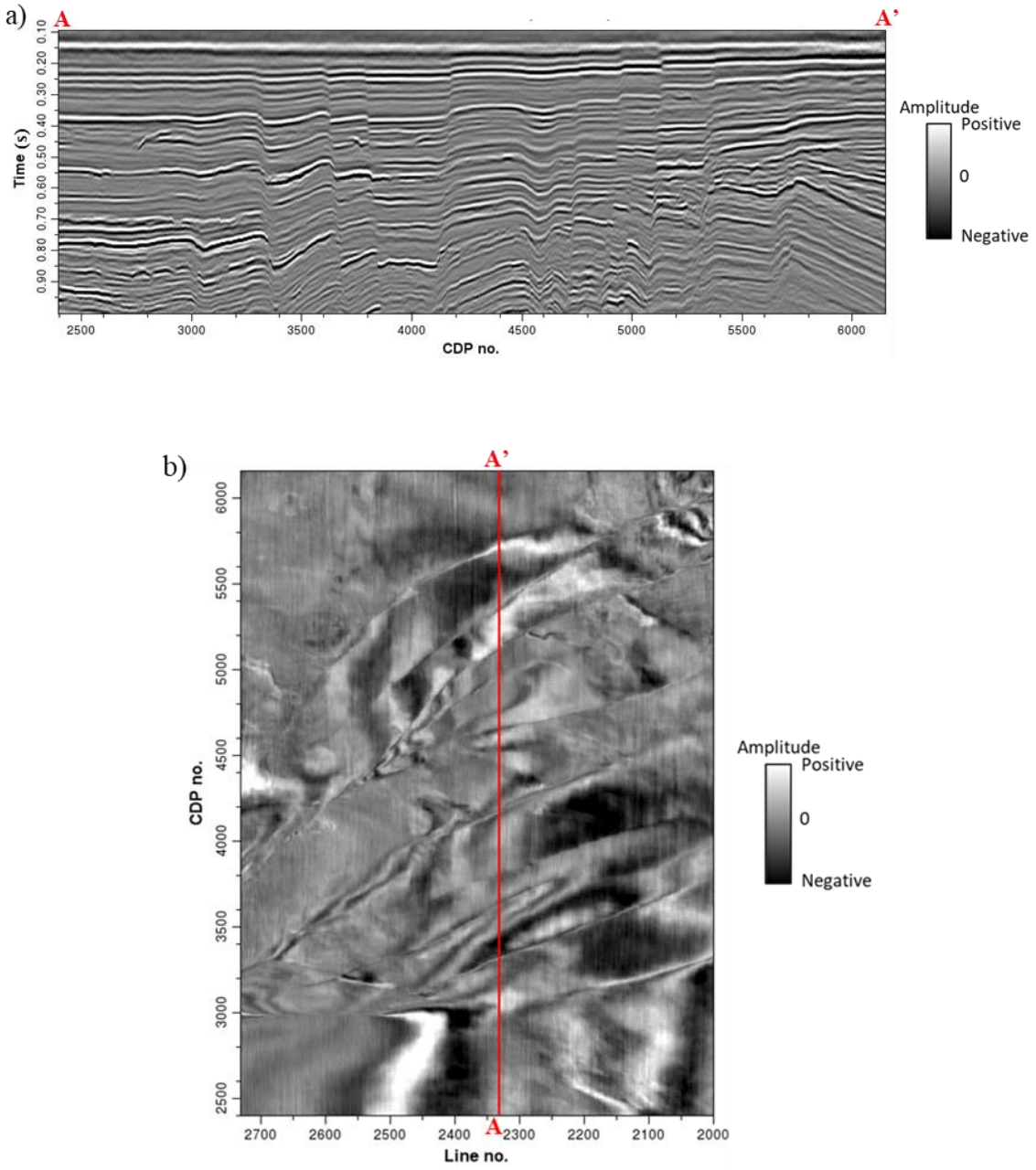

Figure 4.3. (a) A representative vertical slice AA', and (b) time slice at t=0.40 s through the original seismic amplitude dataset. Note that the original seismic data suffer from a small amount of random and migration aliasing noise, which decreases the detectability of faults. Note the N-S trending acquisition footprint in the sail (inline) direction on the amplitude time slice (Figure 4.3b), which will generate undesired artifacts in subsequent coherence computation.

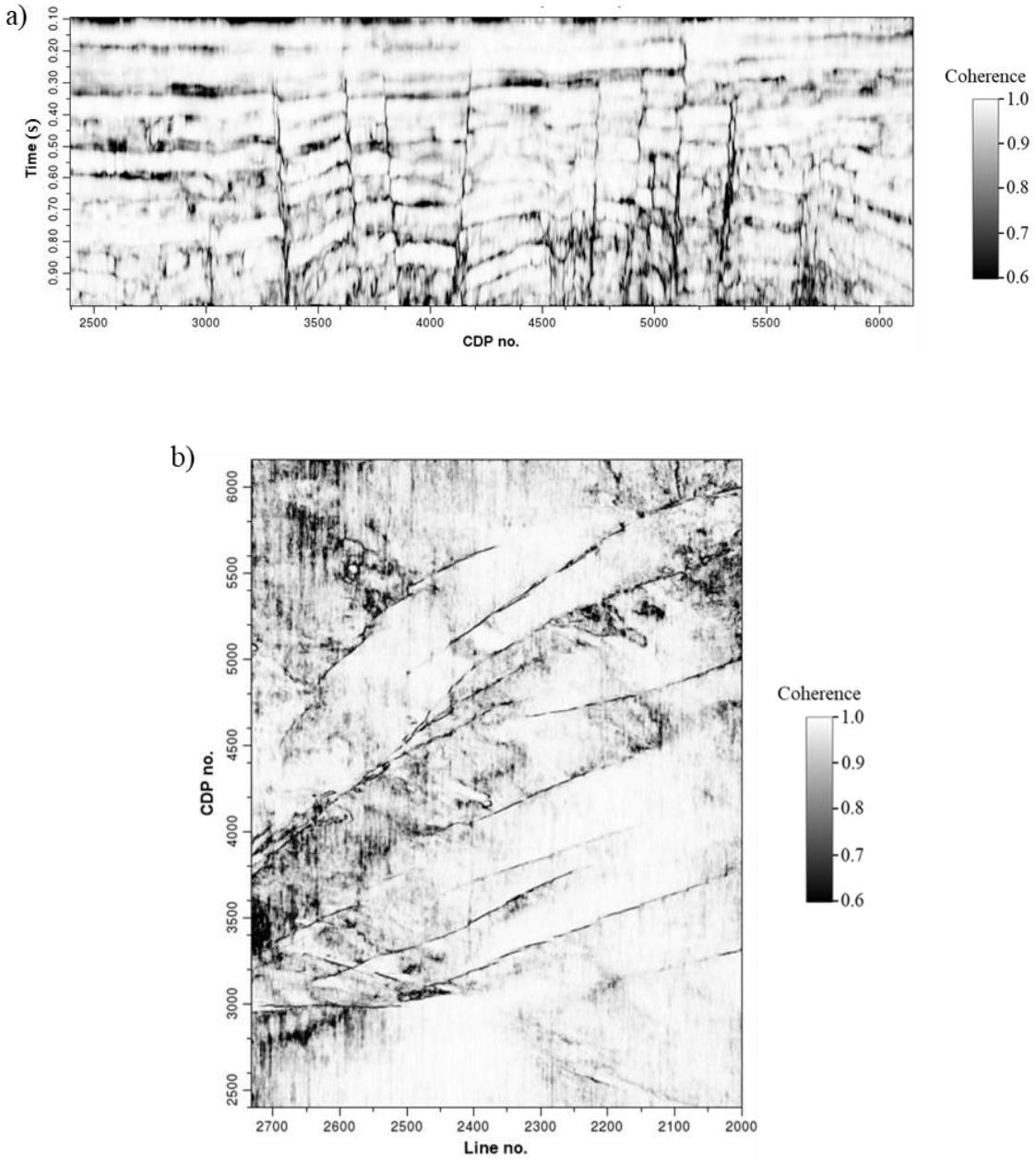

Figure 4.4. (a) Coherence vertical slice and (b) time slice at t=0.4 s computed using the original full-bandwidth seismic amplitude dataset, appearing seriously noisy, which challenges the identification of faults.

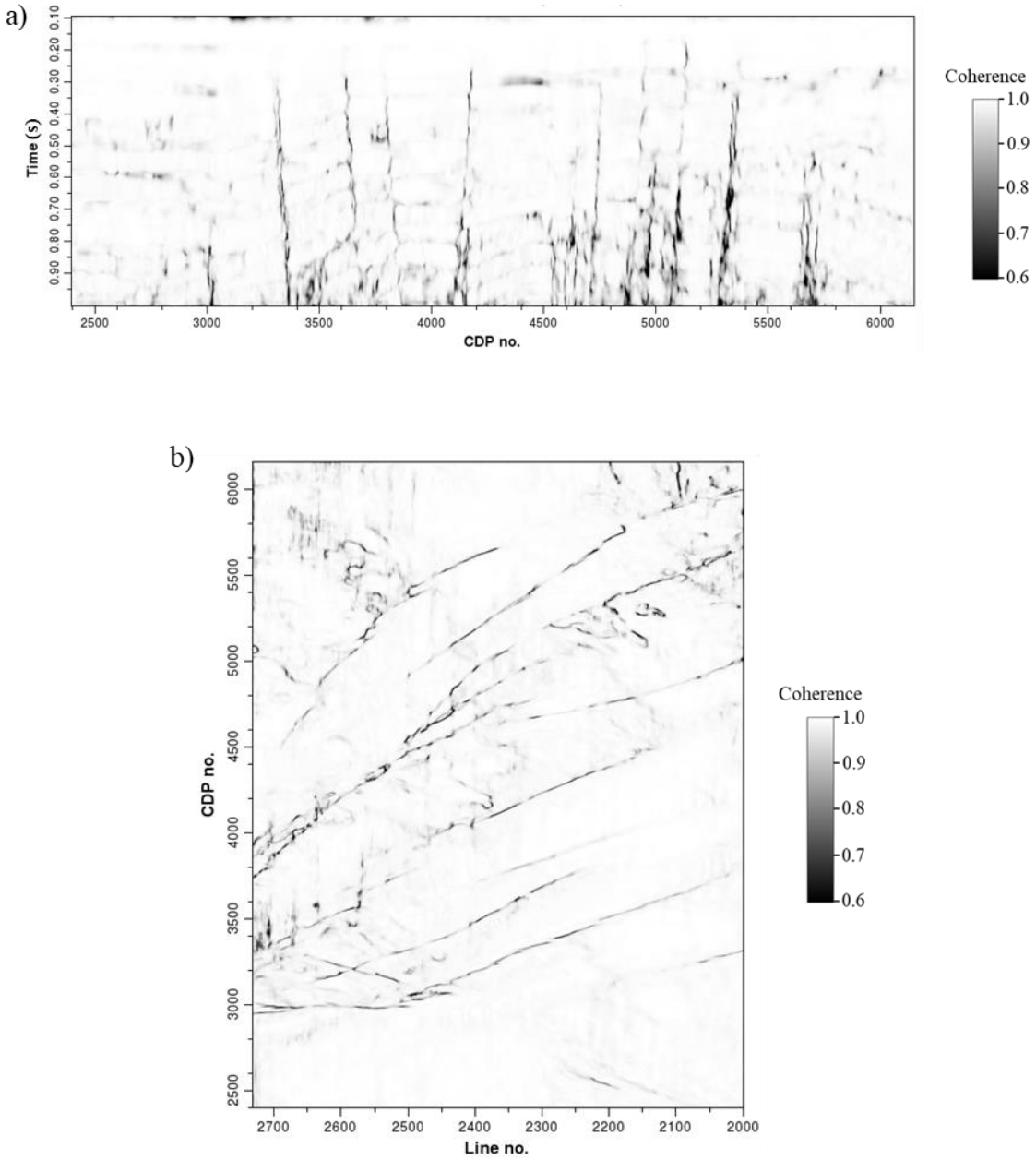

Figure 4.5. (a) Vertical slice AA' and (b) time slice at t=0.4 s through the coherence volume after acquisition footprint suppression, which effectively suppress the footprint artifacts compared to the coherence images computed using the original seismic data (Figure 4.4a and 4.4b).

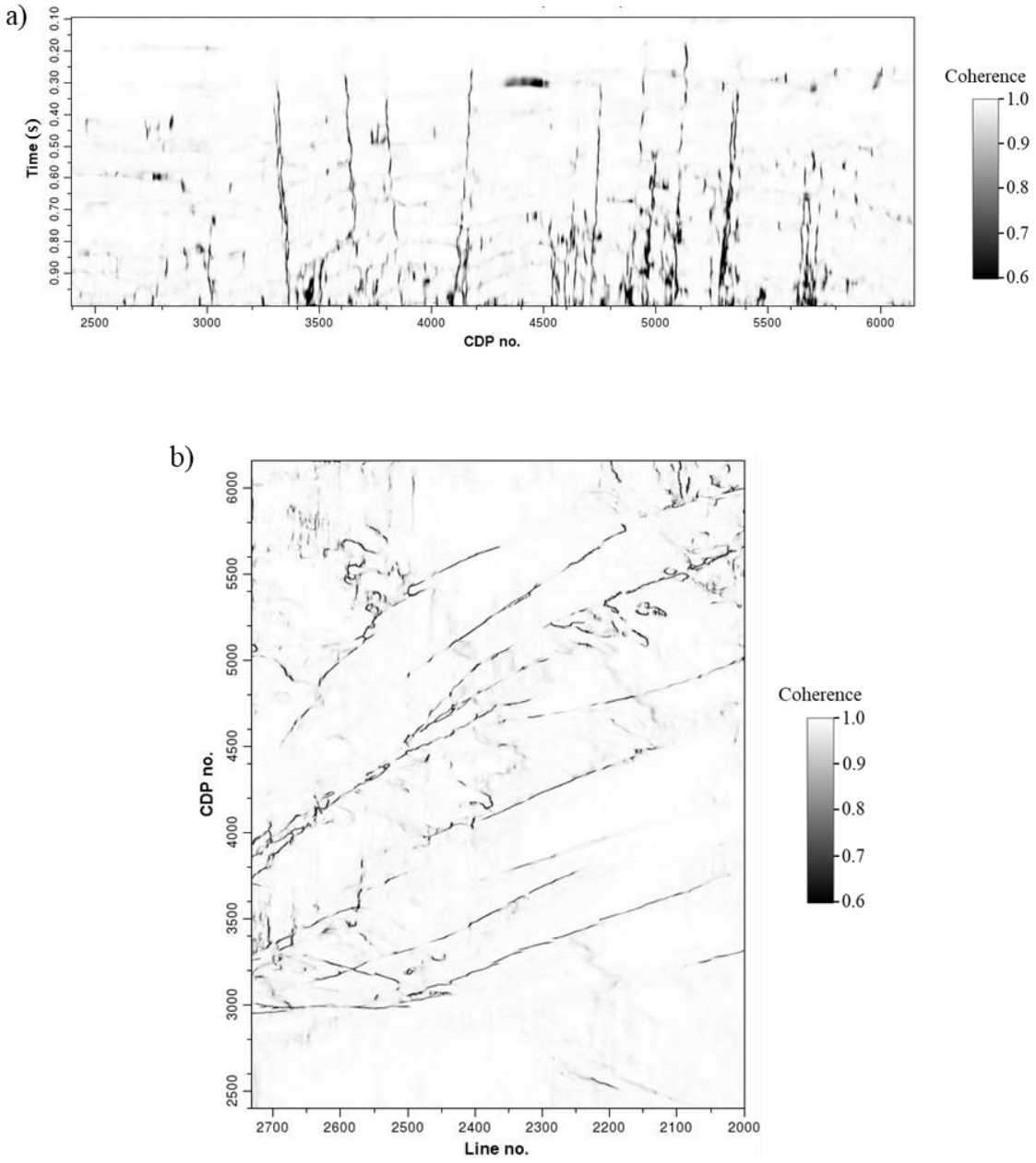

Figure 4.6. (a) Vertical slice AA', and (b) time slice at t=0.4 s through the coherence volume computed after both footprint attenuation and SOF (structure-oriented filtering), further suppressing the random noise and improving the quality of fault imaging, helping the identification of minor faults.

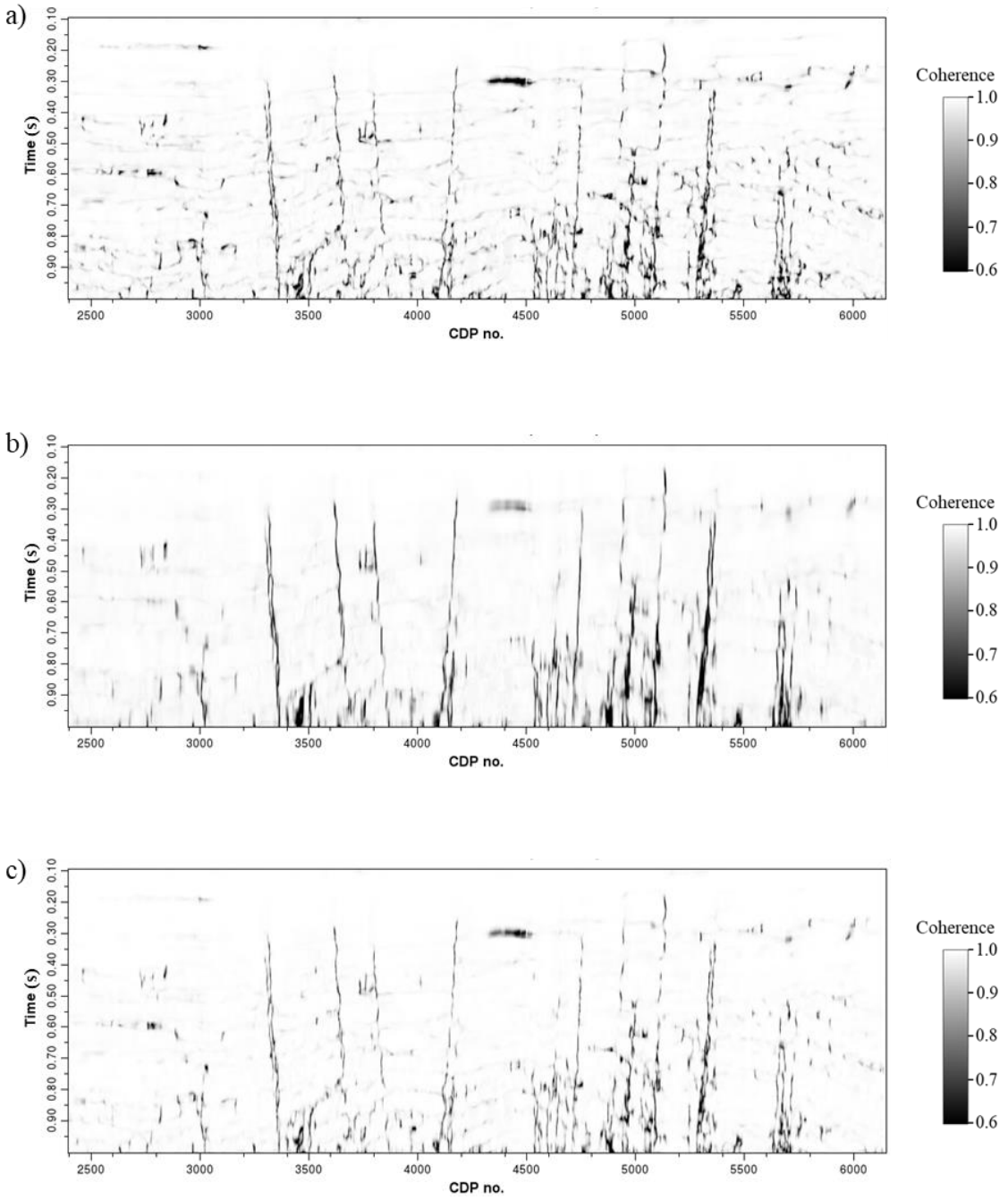

Figure 4.7. Coherence vertical slices computed with (a) a constant 8 ms analysis window, (b) a constant 24 ms analysis window, and (c) a data-adaptive analysis window using the same noise attenuated full-bandwidth seismic data. Note that larger constant window provides a coherence image with better continuity, but smears the minor faults. Smaller constant window improves the resolution of the coherence image, but appears noisier. The data-adaptive analysis window provides coherence result with both good continuity and high resolution.

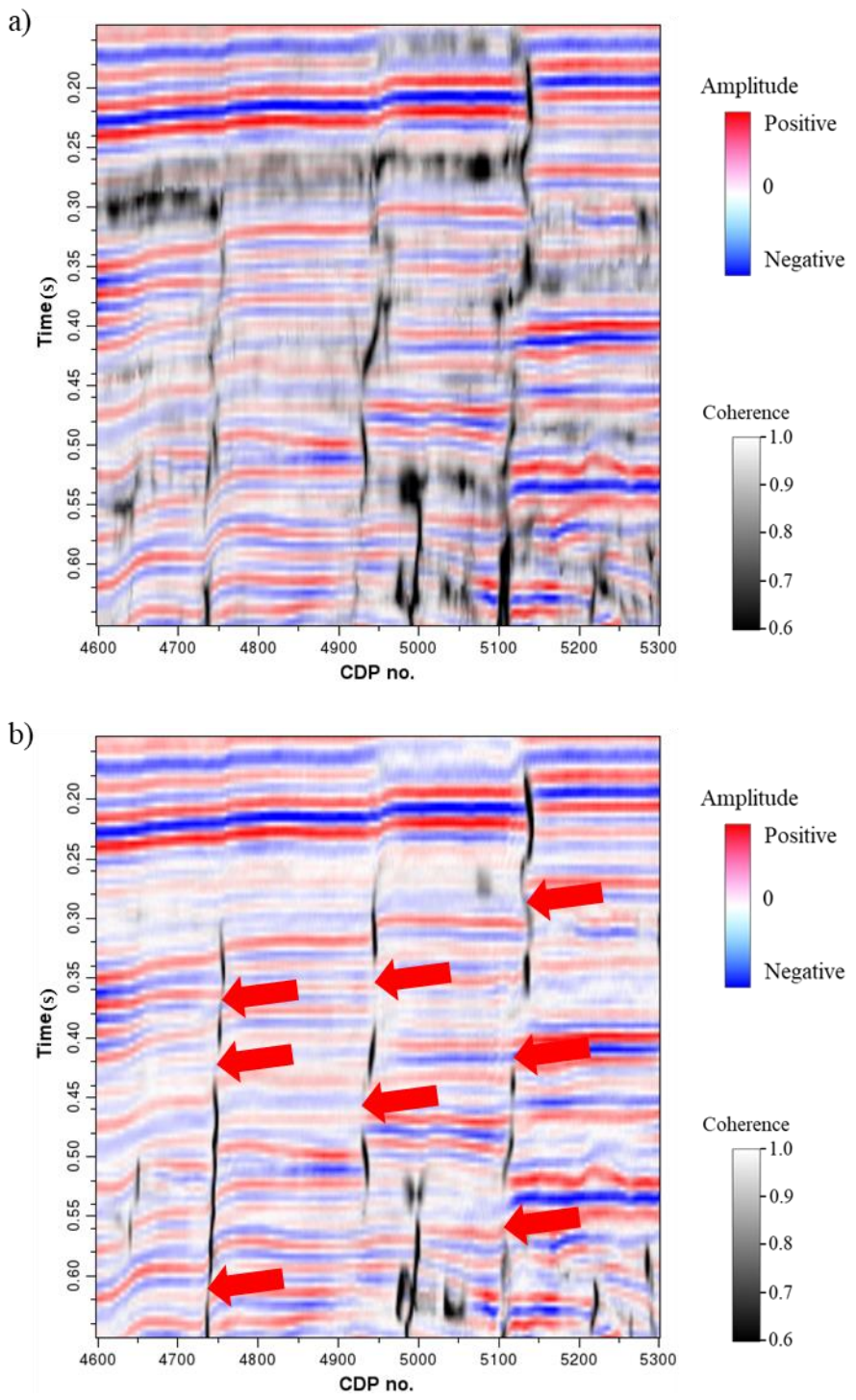

Figure 4.8. Enlarged coherence vertical slices computed using (a) the full-bandwidth original and (b) noise attenuated seismic data co-rendered with seismic amplitude. The noise attenuation workflow effectively improves the quality of fault imaging, but the noise attenuated full-bandwidth coherence image still appears pseudo fault segmentations due to the existence of relatively similar seismic reflections juxtaposing the faults (especially the red arrows in Figure 4.8b), challenging the accurate extraction of fault geometric attributes.

a)

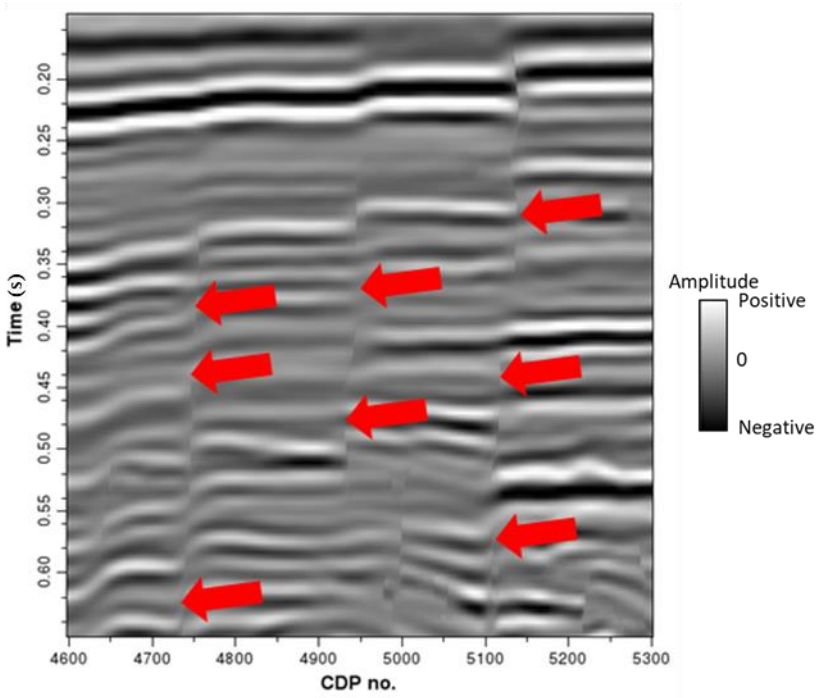
Time (s)
0.20
0.25
0.30
0.35
0.40
0.45
0.50
0.55
0.60
4600
4700
4800
4900
5000
5100
5200
5300
CDP no.
Amplitude
Positive
0
Negative

b)

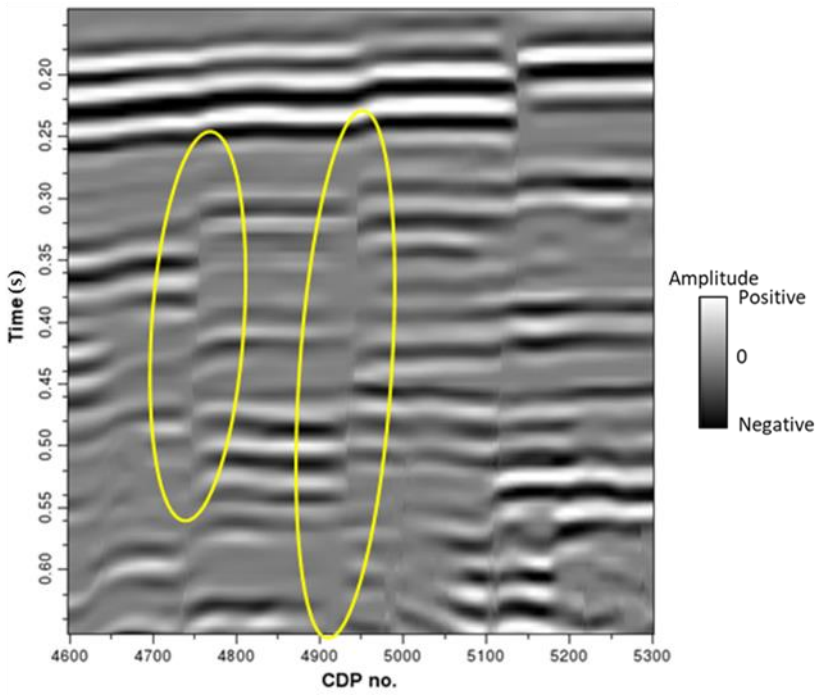
Time (s)
0.20
0.25
0.30
0.35
0.40
0.45
0.50
0.55
0.60
4600
4700
4800
4900
5000
5100
5200
5300
CDP no.
Amplitude
Positive
0
Negative

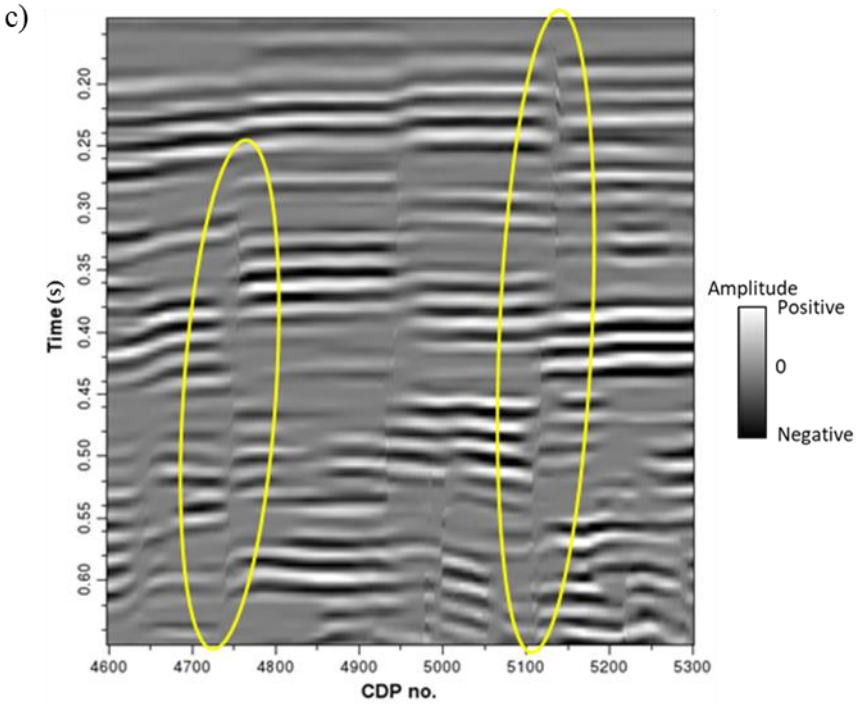

Figure 4.9. (a) Enlarged full-bandwidth seismic vertical slice indicates obvious alignment effect (red arrows). However, (b) the 36 Hz and (c) 55 Hz spectral voices appear significantly decreased alignment effects around the faults indicated by the yellow ellipses.

a)

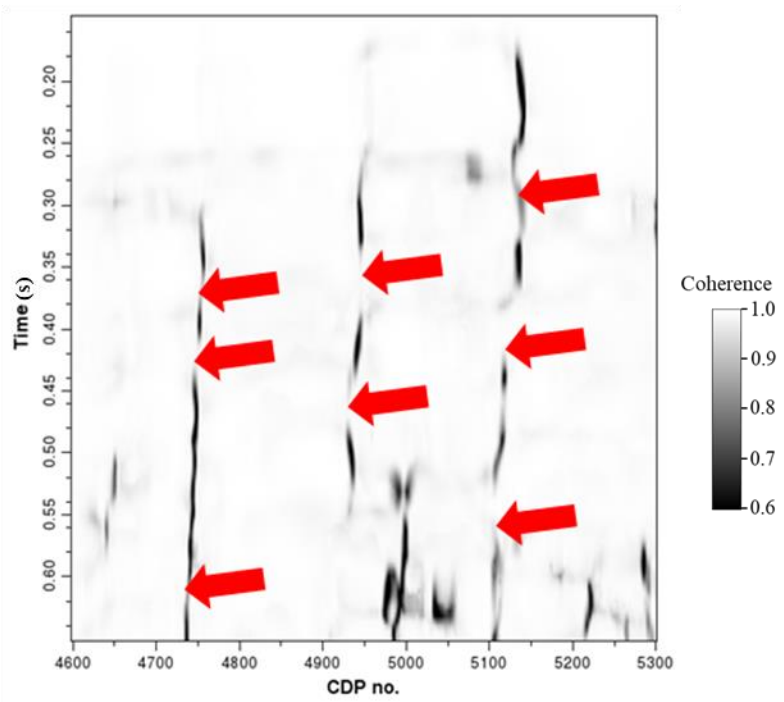
Time (s)
0.20
0.25
0.30
0.35
0.40
0.45
0.50
0.55
0.60
4600
4700
4800
4900
5000
5100
5200
5300
CDP no.
Coherence
1.0
0.9
0.8
0.7
0.6

b)

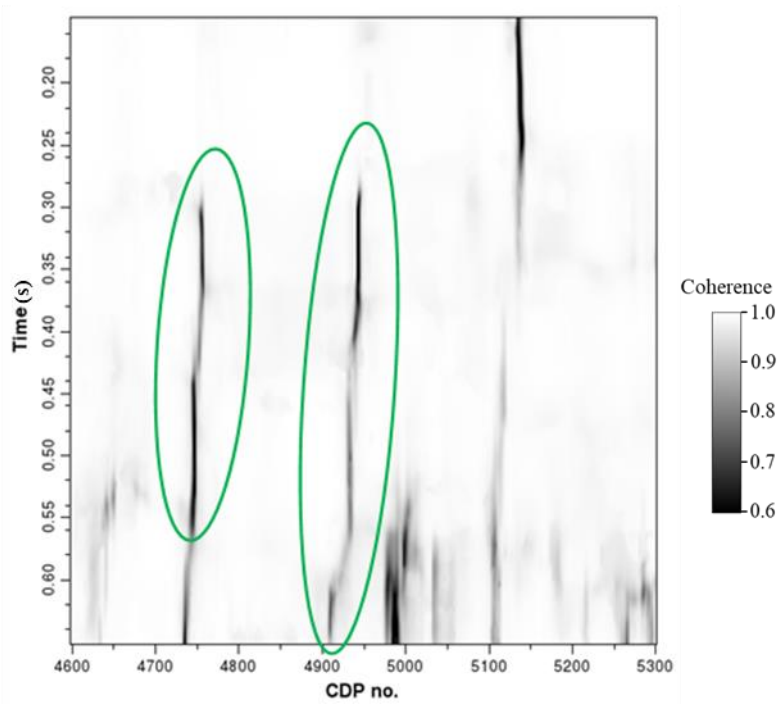
Time (s)
0.20
0.25
0.30
0.35
0.40
0.45
0.50
0.55
0.60
4600
4700
4800
4900
5000
5100
5200
5300
CDP no.
Coherence
1.0
0.9
0.8
0.7
0.6

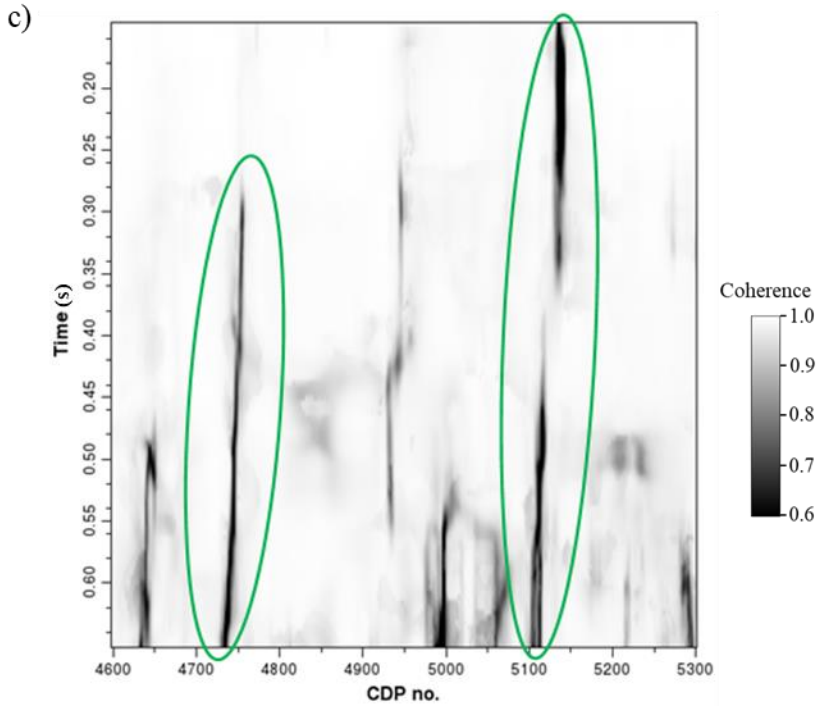

Figure 4.10. Coherence images computed using the corresponding (a) full-bandwidth seismic data, (b) 36 Hz spectral voice, and (c) 55 Hz spectral voice in Figure 4.9. Note the obvious pseudo fault segmentations in the full-bandwidth coherence (red arrows in Figure 4.10a), and the significant continuity improvement of different faults in the coherence images computed using different spectral voices indicated by the green ellipses in Figure 4.10b and 4.10c.

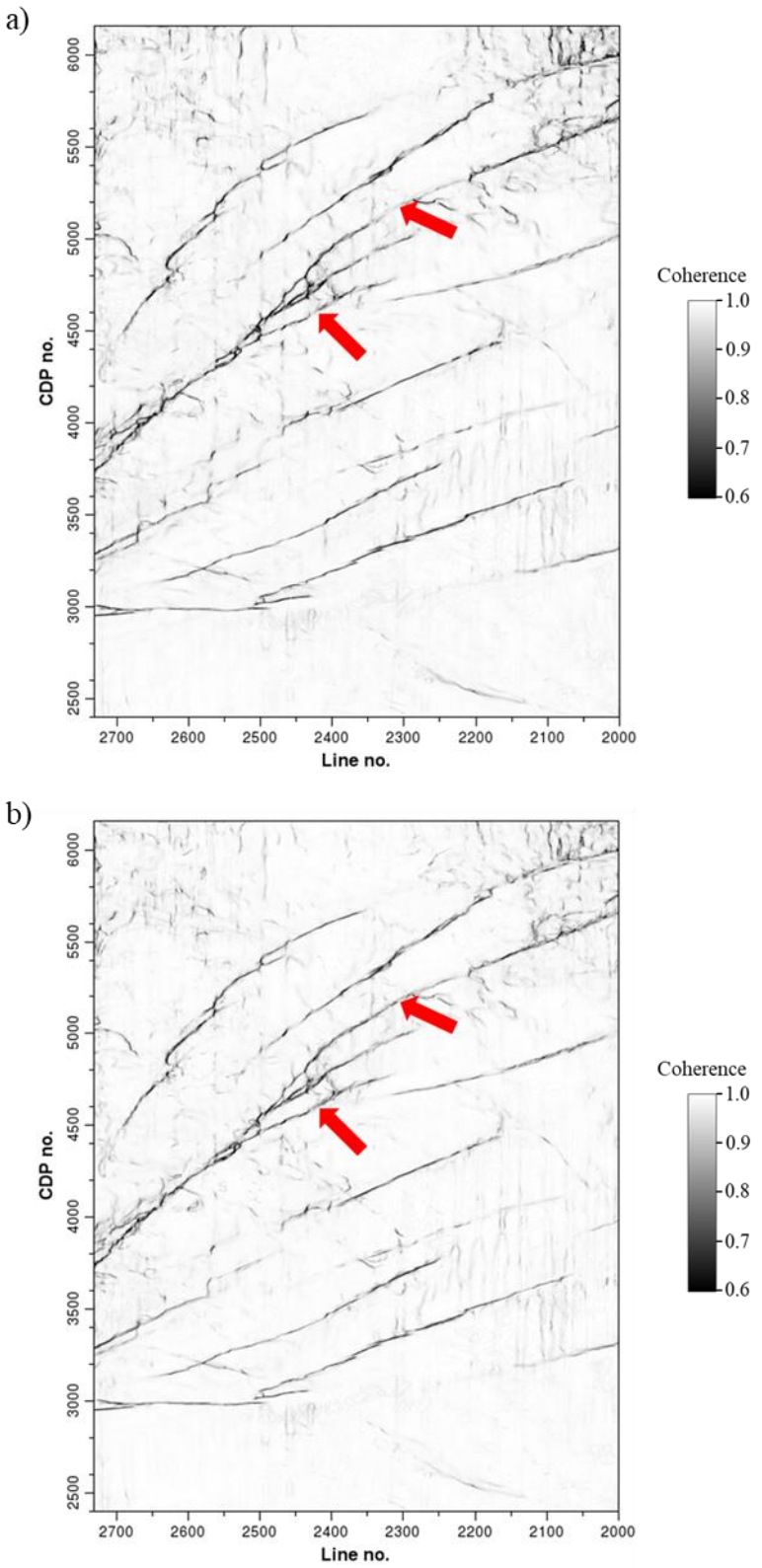

Figure 4.11. Multispectral coherence time slice computed using the exponentially-spaced spectral voices (b) appears better continuity of fault imaging compared to the coherence attribute computed using the equally-spaced spectral voices (a) indicated by the red arrows.

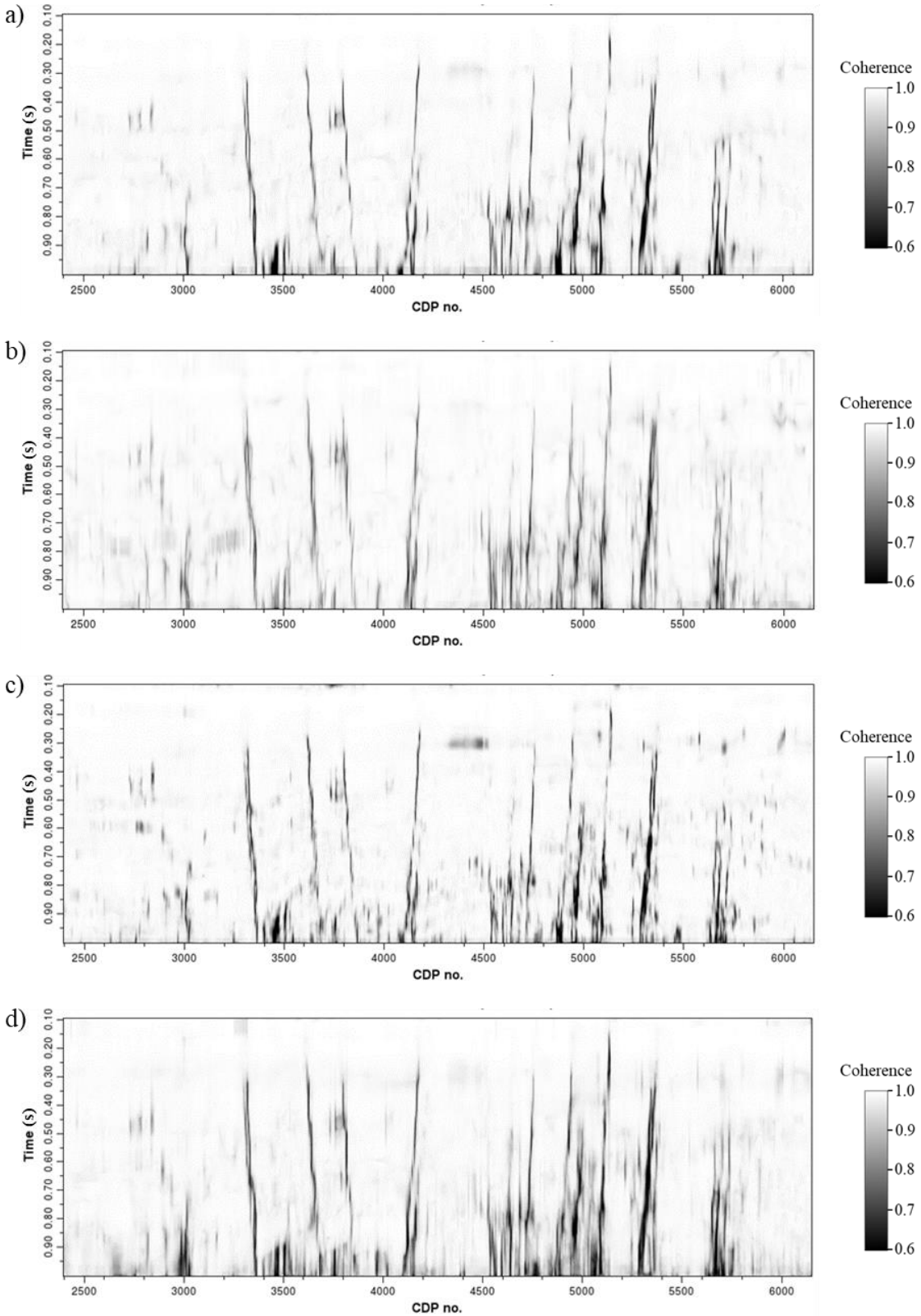

Figure 4.12. Multispectral coherence vertical slices computed using the spectral voices decomposed by (a) band-pass filtering, (b) CWT, (c) spectral probes, and (d) maximum entropy algorithm.

a)

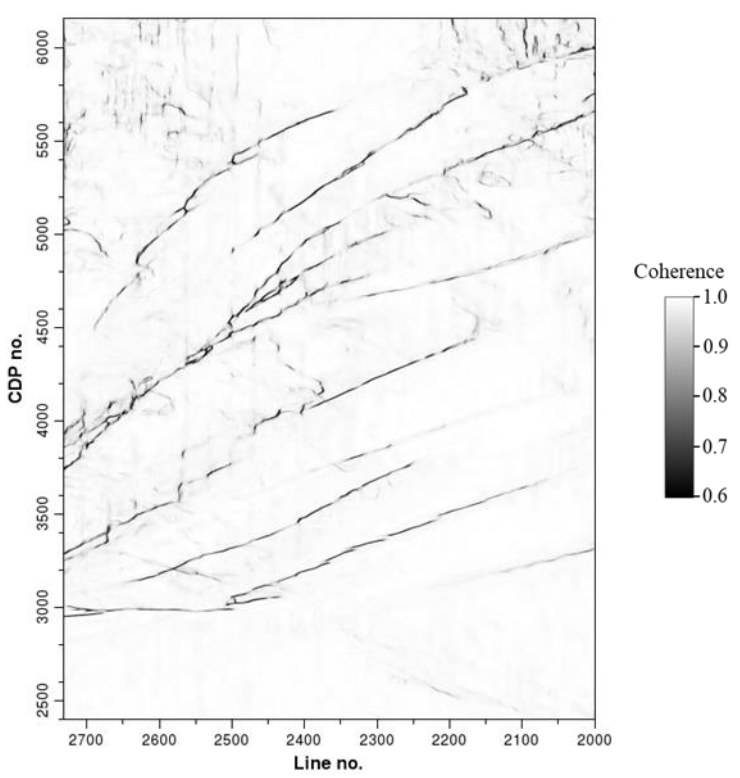
CDP no.
6000
5500
5000
4500
4000
3500
3000
2500
2700
2600
2500
2400
2300
2200
2100
2000
Line no.
Coherence
1.0
0.9
0.8
0.7
0.6

b)

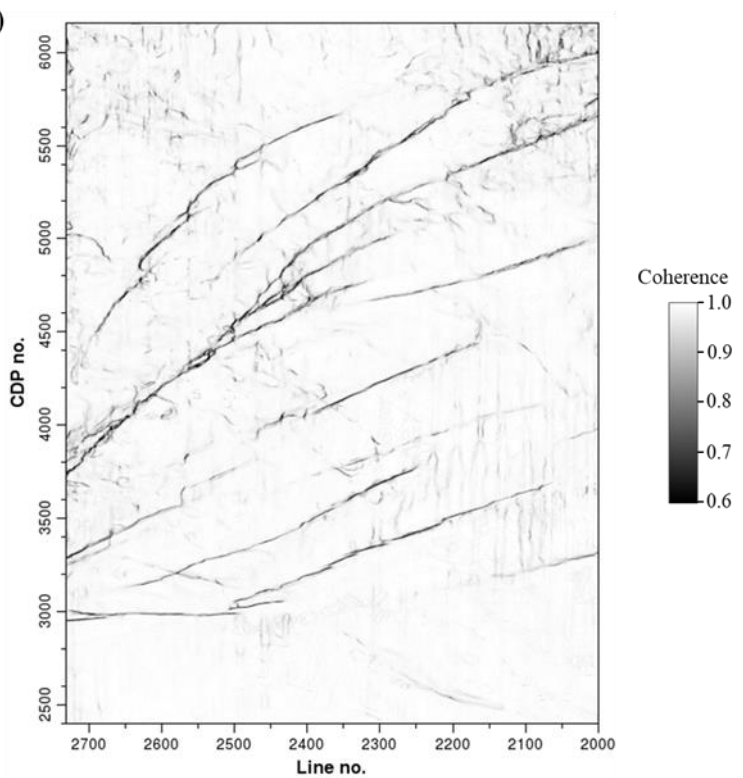
CDP no.
6000
5500
5000
4500
4000
3500
3000
2500
2700
2600
2500
2400
2300
2200
2100
2000
Line no.
Coherence
1.0
0.9
0.8
0.7
0.6

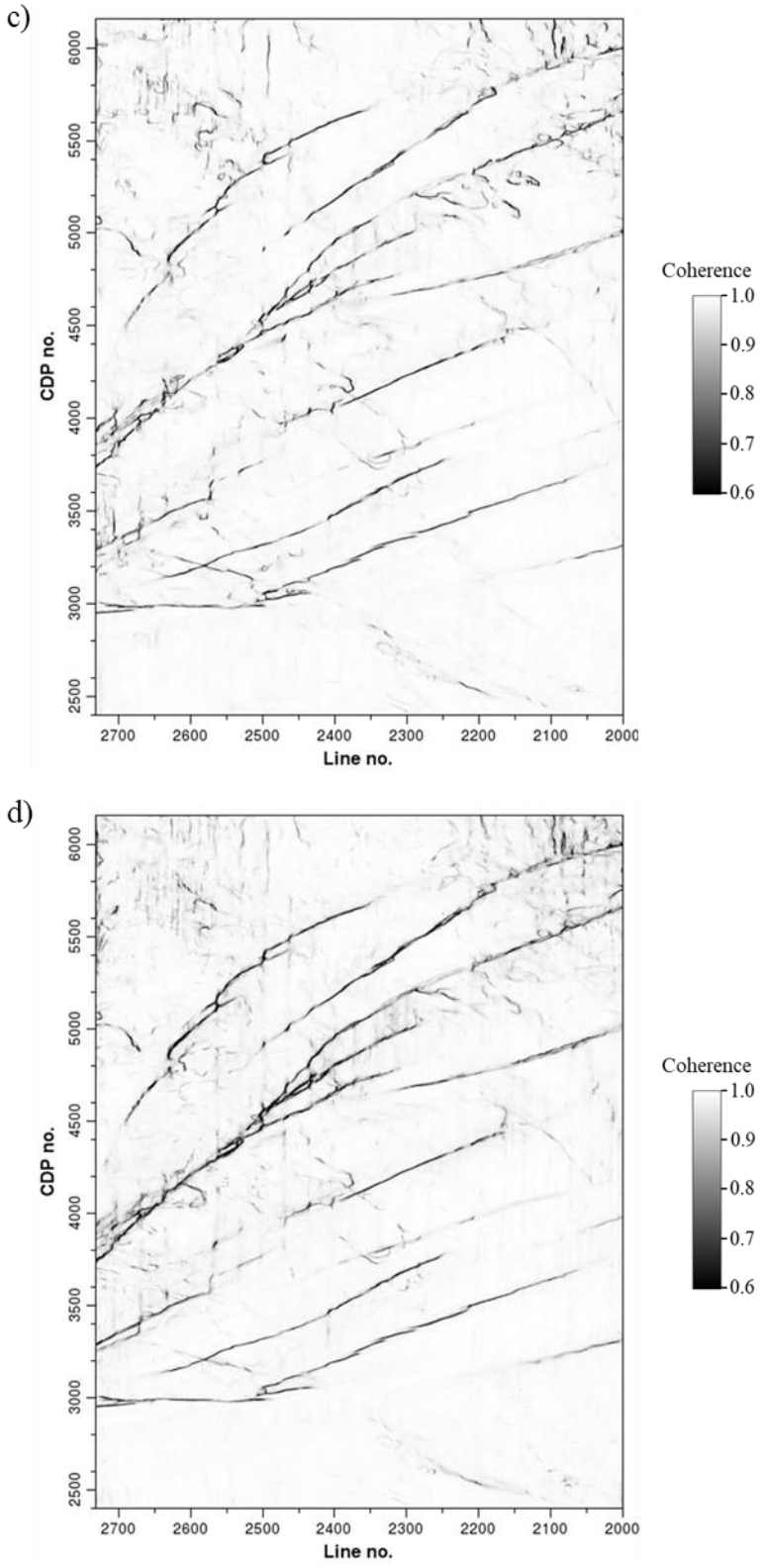

Figure 4.13. Multispectral coherence time slices computed using the spectral voices decomposed by (a) band-pass filtering, (b) CWT, (c) spectral probes, and (d) maximum entropy algorithms.

a)

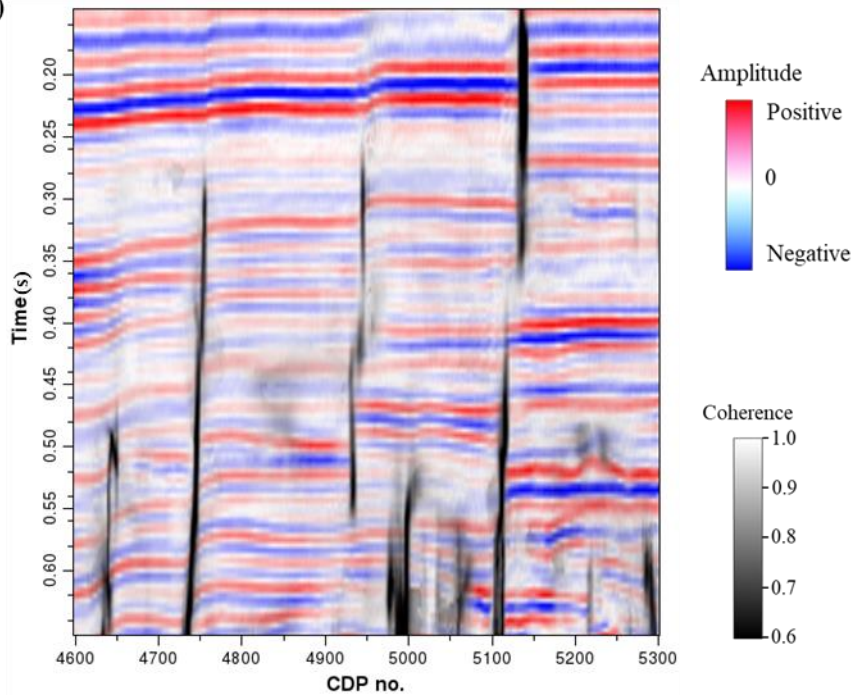
Amplitude
Positive
0
Negative
Coherence
1.0
0.9
0.8
0.7
0.6
Time(s)
0.20
0.25
0.30
0.35
0.40
0.45
0.50
0.55
0.60
4600
4700
4800
4900
5000
5100
5200
5300
CDP no.

b)

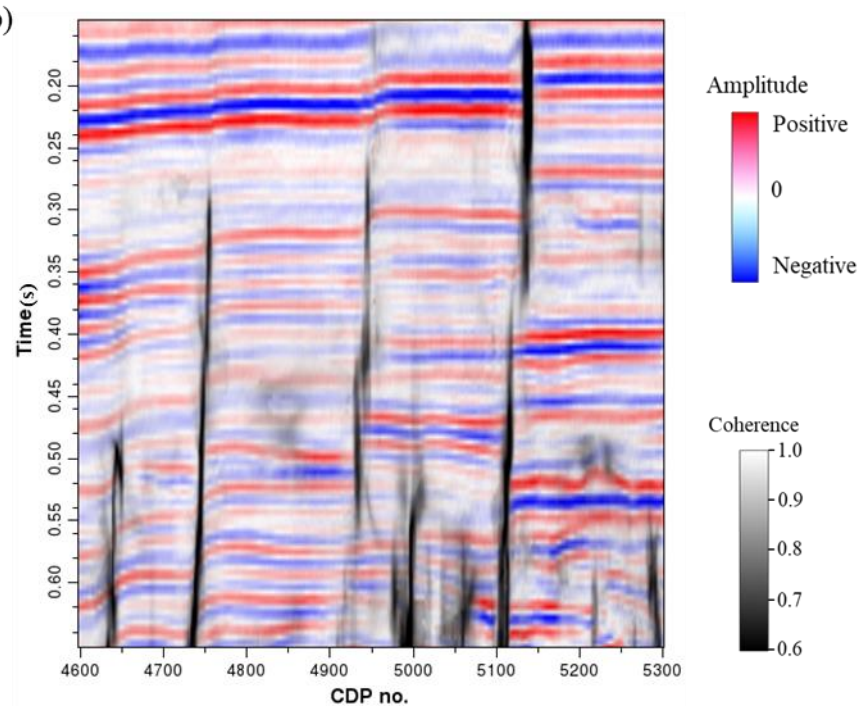
Amplitude
Positive
0
Negative
Coherence
1.0
0.9
0.8
0.7
0.6
Time(s)
0.20
0.25
0.30
0.35
0.40
0.45
0.50
0.55
0.60
4600
4700
4800
4900
5000
5100
5200
5300
CDP no.

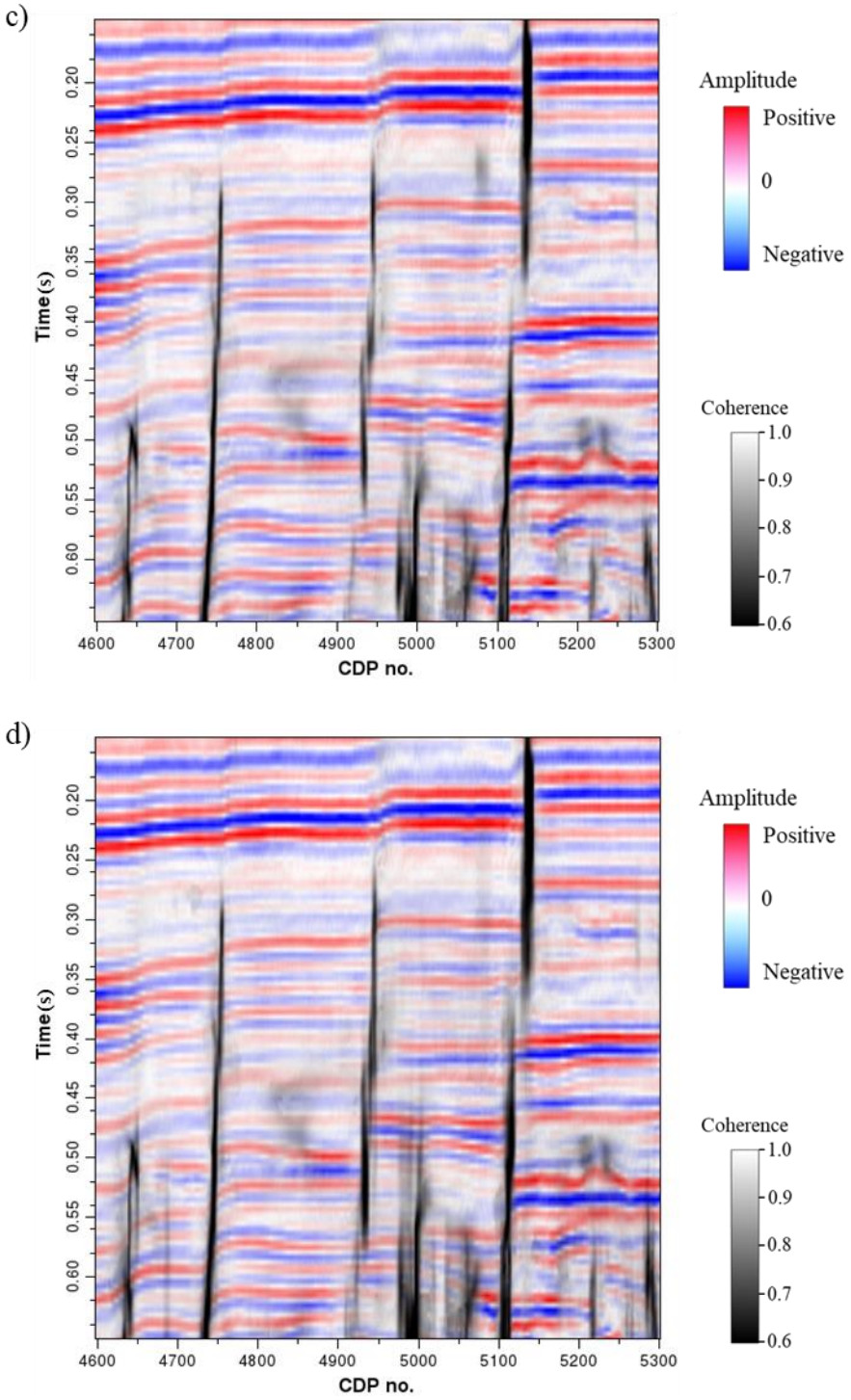

Figure 4.14. Enlarged multispectral coherence vertical slices computed using (a) band-pass filtering, (b) CWT, (c) spectral probes, and (d) maximum entropy algorithms co-rendered with seismic amplitude. Note the improvement of fault continuity by the maximum entropy based multispectral coherence.

a)

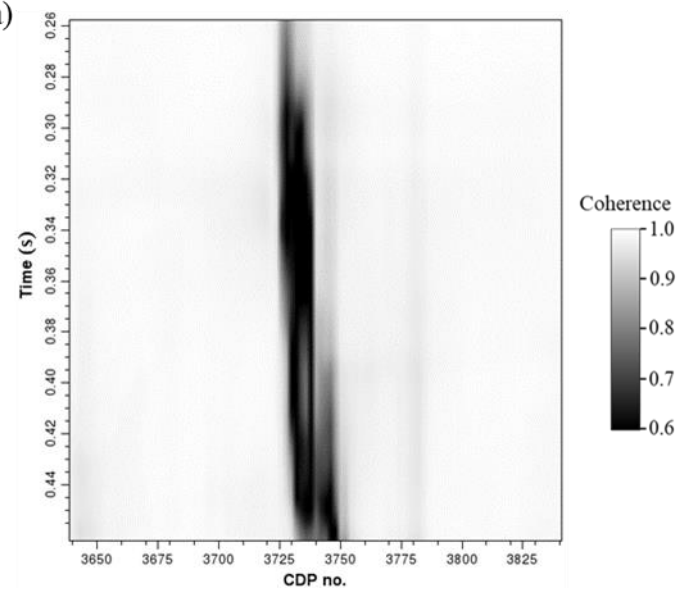
Time (s)
0.26
0.28
0.30
0.32
0.34
0.36
0.38
0.40
0.42
0.44
3650
3675
3700
3725
3750
3775
3800
3825
CDP no.
Coherence
1.0
0.9
0.8
0.7
0.6

b)

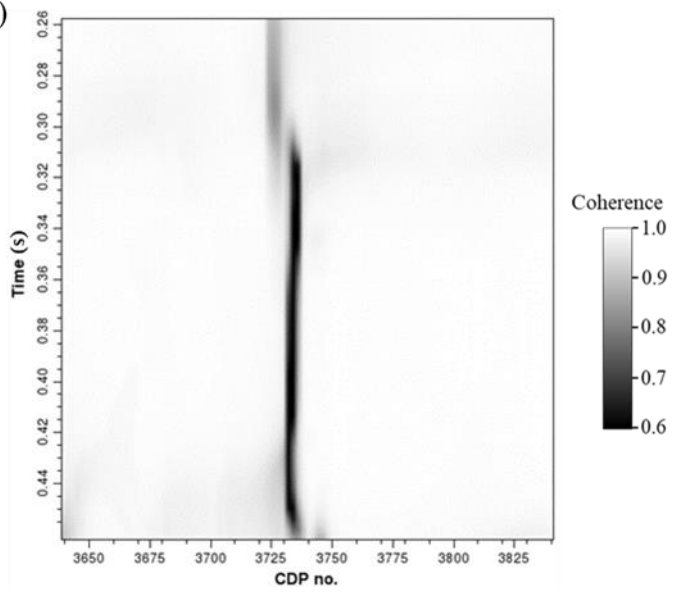
Time (s)
0.26
0.28
0.30
0.32
0.34
0.36
0.38
0.40
0.42
0.44
3650
3675
3700
3725
3750
3775
3800
3825
CDP no.
Coherence
1.0
0.9
0.8
0.7
0.6

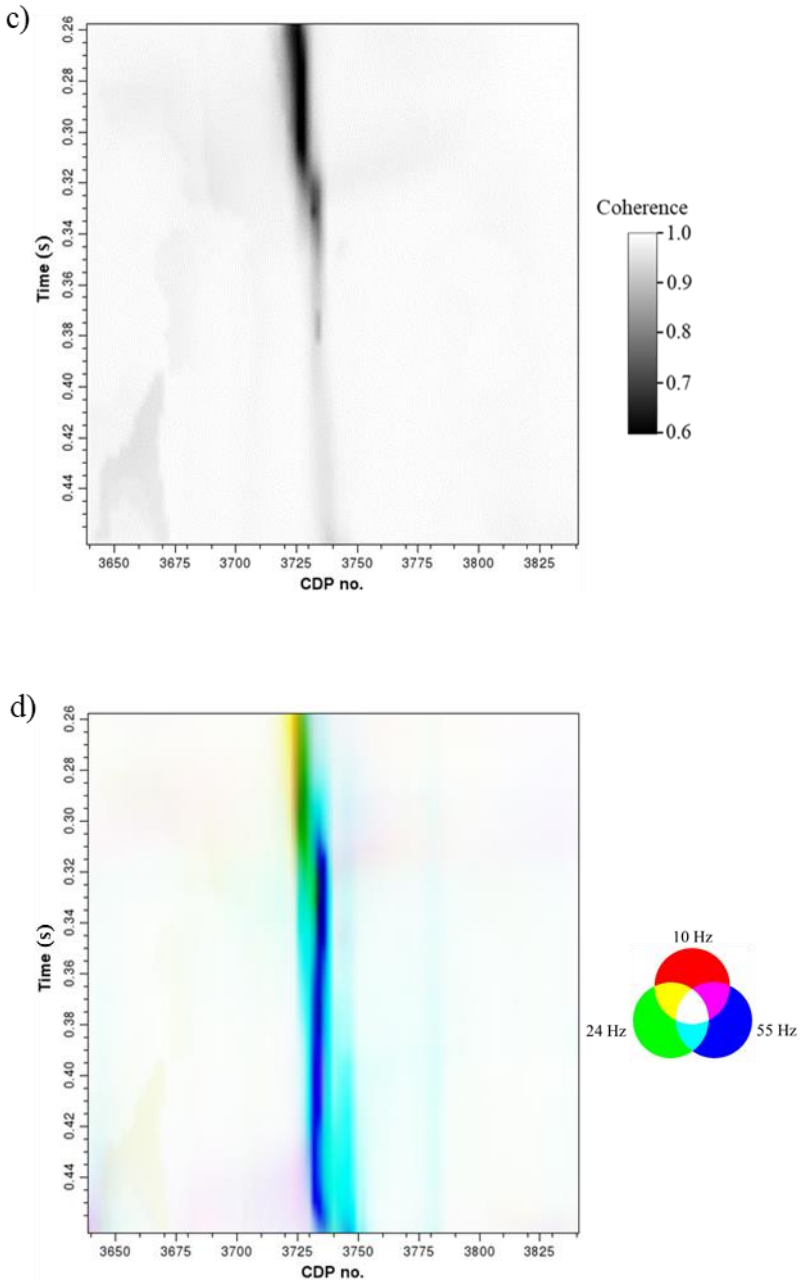

Figure 4.15. Coherence vertical slices of a single fault computed using (a) 10 Hz, (b) 24 Hz, and (c) 55 Hz maximum entropy spectral voices appear different continuity and lateral resolution. The display using RGB blending (d) shows the lateral resolution smearing if we combine coherence volumes of different spectral voices. In multispectral coherence, more spectral voices are included in the computation, which further decreases the lateral resolution of fault imaging.

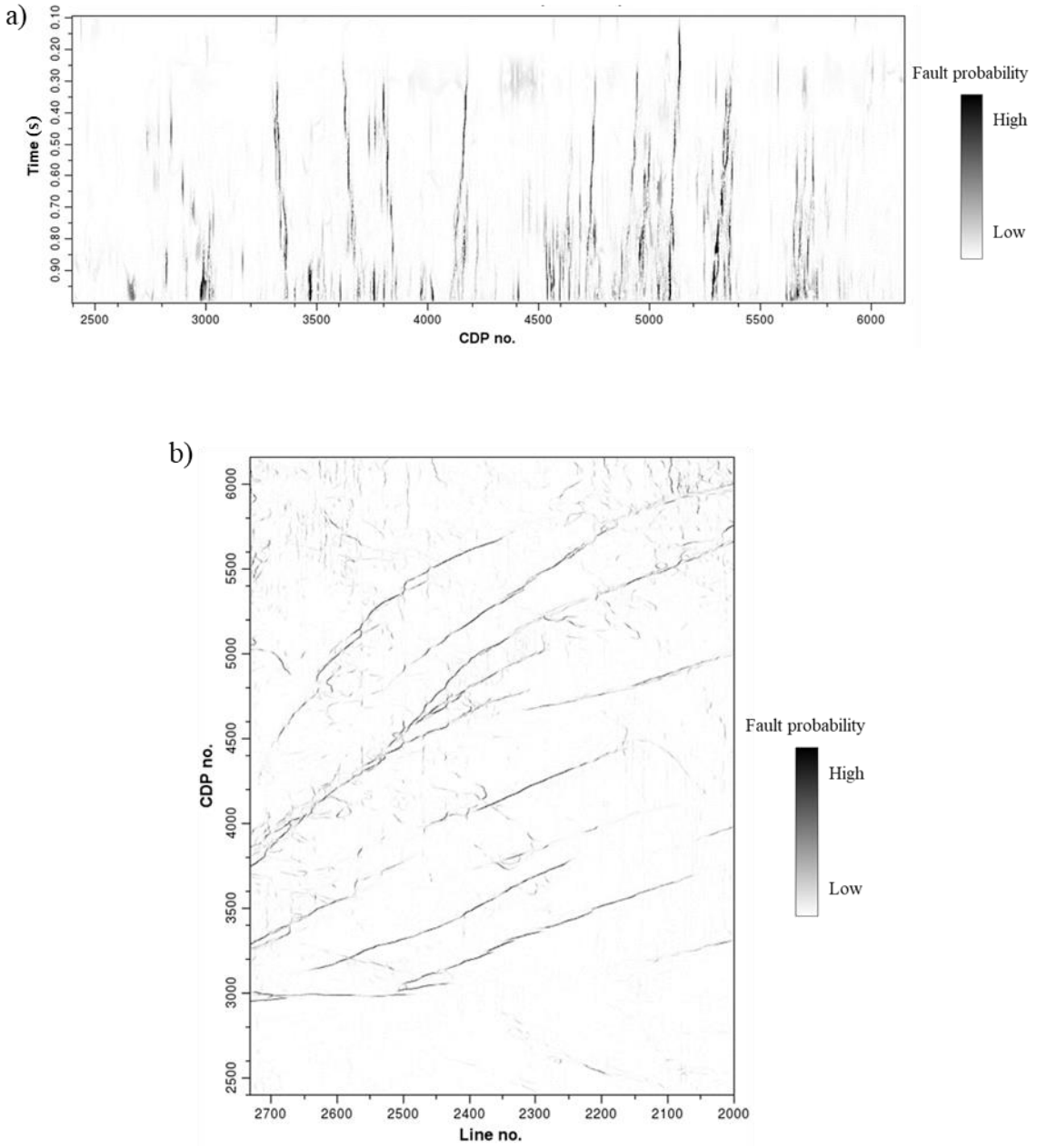

Figure 4.16. (a) Fault enhancement vertical slice and (b) time slice further reduce other stratigraphic discontinuity artifacts and improve the lateral resolution of fault imaging, which especially help identify the minor faults.

CHAPTER 5: MULTISPECTRAL GRADIENT STRUCTURE TENSOR DIP

Abstract

The surprising improvement in coherence images provided by multispectral computation motivates the reexamination of other filtering and geometric attributes to individual spectral voices in addition to the best version of the broadband seismic amplitude data volume. Due to either the seismic data signal-to-noise ratio or to the underlying geology, certain spectral components of the seismic amplitude volume often appear higher quality than others, which further result in higher quality geometric attributes. This observation provides the motivation to compute seismic geometric attributes using multiple spectral voices to determine if they provide additional insight into the underlying geology. We generalize the concept of multispectral coherence that stacks the covariance matrices computed from each spectral voice to multispectral dip that stacks the gradient structure tensor (GST) for each spectral voice. We apply the structure-oriented filtering (SOF) and spectral balancing to improve the data quality of the original full-bandwidth seismic amplitude volume, followed by the computation of the multispectral GST dip attribute. We indicate the quality improvement of the multispectral GST dip over conventional broadband dip using a land 3D seismic survey acquired over the Barnett Shale gas reservoir of the Fort Worth Basin, Texas, and a marine survey acquired in the offshore Taranaki Basin, New Zealand, and find the improved dip estimates in noisier parts of the seismic data volume.

Introduction

Spectral decomposition is widely used in seismic interpretation. Whether because of the seismic data quality or the underlying geology, specific spectral components exhibit a higher S/N (signal-to-noise) ratio compared to other spectral components. Typically, the thickness and the fill of an incised channel is different than that of the geologic layer that it cuts, giving rise to lateral changes in tuning thickness resulting in stronger signal. Similar lateral changes in waveform occur for lateral changes associated with mass transport complexes, karstification, and the deposition of fans, shoals, and bars. For this reason, coherence computed from some spectral components will delineate such stratigraphic edges better than others. Alaei (2012) showed how coherence computed from a 52 Hz bandpass-filtered (spectral voice component) version of the seismic data provided images of small faults that were not seen on coherence computed from the original broadband seismic data volume acquired in the North Sea. Li and Lu (2014) took this idea further and showed how coherence images computed from three different spectral voices can be corendered to delineate karst collapse and channels in a Tarim Basin survey using an RGB (red-green-blue) color model. Dewett and Henza (2016) showed how more than three coherence images can be used to delineate subtle faults in the Eagle Ford Shale resource play using self-organizing maps. Marfurt (2017), Li et al. (2018), Chopra and Marfurt (2019), and Lyu et al. (2019) computed covariance matrices for each spectral voice, and then summed the covariance matrices to compute a multispectral coherence volume. Multispectral coherence has been successfully used to map channel boundaries (Lyu et al., 2020a) and enhance faults (Lyu et al., 2020b; Qi et al., 2019).

Similar strategies can be adopted to estimate volumetric dip and curvature. Jones and Roden (2012) found that volumetric dip estimates computed from spectral voices provide information that is not seen in dip estimates computed from the original broadband data volume (Figure 5.1). Picking two frequencies exhibiting a high S/N ratio for an Eagle Ford Shale survey, they found that the dip computed from the 32.4 Hz spectral component showed much greater detail than those computed from the 15.3 Hz and broadband data volumes. In contrast, the dip computed from the 15.3 Hz volume showed more continuous, longer faults than the other two volumes. Furthermore, they showed that curvature volumes computed from the 32.4 Hz volume provided detailed lineation that correlated with the orientation of microseismic event clusters. Instead of stacking covariance matrices computed from different spectral voice components to compute multispectral coherence, we can stack the GST matrices computed from different spectral voice components of compute multispectral dip. Chopra and Marfurt (2020) showed the benefit of not only multispectral dip estimates, but also of multispectral curvature, but they did not provide any algorithmic details.

In this paper, we provide not only the algorithm details, but also the interpretational value of multispectral estimates of reflector dip. We first introduce the theory and workflow of the multispectral GST dip computation method. Next, we evaluate the method using two 3D seismic surveys acquired in the Fort Worth Basin and the offshore Taranaki Basin, and show how the improvement occur in areas of lower signal-to-noise ratio, providing the interpretation value of the multispectral dip algorithm.

Method of multispectral GST dip computation

There are several ways of computing volumetric dip, with the most popular algorithms involving crosscorrelation of seismic events in four directions (Aarre, 2010) and those based on instantaneous dip (Barnes, 2000), semblance search (Marfurt et al., 1998), and gradient structure tensor algorithms (Bakker, 2002). All of these methods can be applied to spectral voices, resulting in a suite of dip estimates.

To compute multispectral GST dip, we first define the spectral voices after spectral decomposition as

$$u_{rklm}(f_r) = a_{klm}(f_r)\mathbf{exp}\left[i\varphi_{klm}(f_r)\right] \tag{1}$$

where u denotes the spectral voice of the r^{th} frequency f_r, a is the spectral magnitude component, and φ is the spectral phase component. where the subscripts k, l, and m, indicate a data value at ($k\Delta t$, $l\Delta x$, $m\Delta y$) about an analysis point with local indices (k=0, l=0, m=0).

For each spectral voice, we optimize the GST computation using the gradients of both the original amplitude data and of its Hilbert transform, which a generalization of the method described by Luo et al. (2006) computed only from the amplitude. The vector gradient for the r^{th} spectral voice, $\mathbf{g}_r$, is the derivative of the seismic amplitude, u, in each of the three Cartesian directions. We approximate the gradient using central differences:

$$\mathbf{g}^{rklm} = \begin{pmatrix} g_x^{rklm} \\ g_y^{rklm} \\ g_z^{rklm} \end{pmatrix} = \begin{pmatrix} \dfrac{\partial u_{rklm}}{\partial x} \\ \dfrac{\partial u_{rklm}}{\partial y} \\ \dfrac{\partial u_{rklm}}{\partial z} \end{pmatrix} \approx \begin{pmatrix} \dfrac{u_{r,k+1,l,m} - u_{r,k-1,l,m}}{2\Delta x} \\ \dfrac{u_{r,k,l+1,m} - u_{r,k,l-1,m}}{2\Delta y} \\ \dfrac{u_{r,k,l,m+1} - u_{r,k,l,m-1}}{2\Delta z} \end{pmatrix} \tag{2}$$

In general, gradient estimates about zero crossings in the seismic wavelet exhibit a lower S/N ratio than about peaks and troughs. We can partially address this instability by augmenting the conventional estimate of the GST by including the gradient, $(\mathbf{g}^{klm})^{H}$, of the Hilbert transform of the seismic amplitude data, u^{H}. We then define the gradient structure tensor at grid location ($k\Delta t$, $l\Delta x$, $m\Delta y$) to be:

$$\mathbf{C}_{rklm} = \left(e^{rklm}\right)^2 \left\{ \begin{bmatrix} \left(g_x^{rklm}-\mu_{rx}\right)\left(g_x^{rklm}-\mu_{rx}\right) & \left(g_x^{rklm}-\mu_{rx}\right)\left(g_y^{rklm}-\mu_{ry}\right) & \left(g_x^{rklm}-\mu_{rx}\right)\left(g_z^{rklm}-\mu_{rz}\right) \\ \left(g_y^{rklm}-\mu_{ry}\right)\left(g_x^{rklm}-\mu_{rx}\right) & \left(g_y^{rklm}-\mu_{ry}\right)\left(g_y^{rklm}-\mu_{ry}\right) & \left(g_y^{rklm}-\mu_{ry}\right)\left(g_z^{rklm}-\mu_{rz}\right) \\ \left(g_z^{rklm}-\mu_{rz}\right)\left(g_x^{rklm}-\mu_{rx}\right) & \left(g_z^{rklm}-\mu_{rz}\right)\left(g_y^{rklm}-\mu_{ry}\right) & \left(g_z^{rklm}-\mu_{rz}\right)\left(g_z^{rklm}-\mu_{rz}\right) \end{bmatrix} \right. \quad (3)$$

$$\left. + \begin{bmatrix} \left(g_x^{Hrklm}-\mu_{rx}^{H}\right)\left(g_x^{Hrklm}-\mu_{rx}^{H}\right) & \left(g_x^{Hrklm}-\mu_{rx}^{H}\right)\left(g_y^{Hrklm}-\mu_{ry}^{H}\right) & \left(g_x^{Hrklm}-\mu_{rx}^{H}\right)\left(g_z^{Hrklm}-\mu_{rz}^{H}\right) \\ \left(g_y^{Hrklm}-\mu_{ry}^{H}\right)\left(g_x^{Hrklm}-\mu_{rx}^{H}\right) & \left(g_y^{Hrklm}-\mu_{ry}^{H}\right)\left(g_y^{Hrklm}-\mu_{ry}^{H}\right) & \left(g_y^{Hrklm}-\mu_{ry}^{H}\right)\left(g_z^{Hrklm}-\mu_{rz}^{H}\right) \\ \left(g_z^{Hrklm}-\mu_{rz}^{H}\right)\left(g_x^{Hrklm}-\mu_{rx}^{H}\right) & \left(g_z^{Hrklm}-\mu_{rz}^{H}\right)\left(g_y^{Hrklm}-\mu_{ry}^{H}\right) & \left(g_z^{Hrklm}-\mu_{rz}^{H}\right)\left(g_z^{Hrklm}-\mu_{rz}^{H}\right) \end{bmatrix} \right\}$$

where e^{rklm} is the envelope or reflection strength at each sample. The average gradient in the analysis window is expressed as

$$\boldsymbol{\mu}_r = \frac{1}{(2K+1)(2L+1)(2M+1)} \sum_{k=-K}^{+K} \sum_{l=-L}^{+L} \sum_{m=-M}^{+M} \mathbf{g}^{rklm} \quad (4)$$

and the corresponding Hilbert transform is written as

$$\boldsymbol{\mu}_r^{H} = \frac{1}{(2K+1)(2L+1)(2M+1)} \sum_{k=-K}^{+K} \sum_{l=-L}^{+L} \sum_{m=-M}^{+M} \left(\mathbf{g}^{rklm}\right)^{H} \quad (5)$$

We then average the gradient structure tensor $\mathbf{C}_{rklm}$ given by equation 3 for all frequencies r=1,2,…,R over their values at each of the (2K+1)(2L+1)(2M+1) voxels falling within the analysis window:

$$\bar{\mathbf{C}} = \sum_{r=1}^{R} \frac{1}{(2K+1)(2L+1)(2M+1)} \sum_{k=-K}^{+K} \sum_{l=-L}^{+L} \sum_{m=-M}^{+M} \mathbf{C}_{rklm} \quad (6)$$

The multispectral GST matrix in equation 6 measures the change of seismic amplitude in each of the three Cartesian directions. To determine the direction of the maximum change, we decompose the multispectral GST matrix into its eigenvectors and eigenvalues:

$$\bar{\mathbf{C}} = \begin{pmatrix} \mathbf{v}_1 & \mathbf{v}_2 & \mathbf{v}_3 \end{pmatrix} \begin{pmatrix} \lambda_1 & 0 & 0 \\ 0 & \lambda_2 & 0 \\ 0 & 0 & \lambda_3 \end{pmatrix} \begin{pmatrix} \mathbf{v}_1^{\mathrm{T}} \\ \mathbf{v}_2^{\mathrm{T}} \\ \mathbf{v}_3^{\mathrm{T}} \end{pmatrix} \tag{7}$$

where $(\lambda_n, \mathbf{v}_n)$ is the n^{th} eigenvalue-eigenvector pair and the superscript T denotes the vector transpose. Since we compute the multispectral GST by quantifying the 3D change in amplitude, its first eigenvector $\mathbf{v}_1$ represents the direction of most change in amplitude. For a constant amplitude, planar reflector,

$$\mathbf{v}_1 = \begin{pmatrix} v_{1x} \\ v_{1y} \\ v_{1z} \end{pmatrix} = \hat{\mathbf{n}} \tag{8}$$

where $\hat{\mathbf{n}}$ is the unit normal to a hypothesized reflector. We partially compensate for lateral changes in amplitude along reflector dip by applying a short-window $(2K+1)\Delta t$ AGC algorithm to the data prior to computing the GST. The multispectral GST apparent dips, p and q, are then

$$p = \frac{v_{1x}}{v_{1z}}, \qquad \text{and} \qquad q = \frac{v_{1y}}{v_{1z}} \tag{9}$$

Figure 5.2 summarizes the workflow described in the previous equations. Because the quality of geometric attributes depends on the quality of the input seismic amplitude volume, we apply edge-preserving structure-oriented filtering (e.g. Marfurt, 2006) to improve the S/N ratio and spectral balancing to improve the data quality.

After structure-oriented filtering and spectral balancing, we decompose the broadband seismic amplitude into different spectral voices. Next, we compute the GST for the broadband data and for each spectral component and compute volumetric estimates of dip as described by the equations. We also stack the GSTs from the spectral components and compute multispectral estimates of volumetric dip.

All volume-based estimates of dip provide an inaccurate apparent dip when crossing discontinuities. To avoid this shortcoming, we follow Marfurt (2006) and employ a multi-window search algorithm originally defined by Kuwahara et al. (1976),

Application to the Fort Worth Basin

Data description

We perform the first case study on a 3D seismic survey (Figure 5.3) acquired in the Fort Worth Basin, which is a shallow, north–south-elongated foreland basin in northcentral Texas (Montgomery et al., 2005). The structures in the Fort Worth Basin include major and minor faulting, local folding, fracturing, and karst-related collapse features (Qi et al., 2014). Thrust-fold structures are more common in the easternmost parts of the basin. The major faults in the basin play an important role on controlling the depositional patterns and thermal history of the Barnett Shale. The karstification in the basin is controlled by the faulting, some of which is basement controlled (Khatiwada et al., 2013).

The 3D wide-azimuth seismic survey was acquired by the Marathon Oil Company in 2006 using 16 live receiver lines with a nominal 16 × 16 m (55 × 55 ft) CDP bin size for seismic acquisition (Roende et al., 2008). We show a representative vertical slice AA’ (Figure 5.4a) and time slice at t=0.70 s (Figure 5.4b) through the seismic amplitude volume.

Red lines indicate the locations of corresponding slices. The target Barnett Shale falls between the Marble Falls and Ellenberger hydraulic fracture barriers (indicated by the arrows in Figure 5.4a). Block arrows indicate faults (orange arrows), larger karst (red arrows), and smaller karst (green arrows) features in Figure 5.4b.

Multispectral GST dip attributes

Using the workflow in Figure 5.2, Figures 5.5 shows vertical slices through the inline dip computed directly from the original broadband data (Figure 5.5a) and by using the multispectral dip workflow (Figure 5.5b). The multispectral GST results are more continuous, and exhibit fewer artifacts than those computed directly from the broadband data. To understand whether this improvement is geological or simply due to smearing, Figure 5.6 corenders the seismic amplitude with the two dip estimates. Note that the multispectral GST inline dip is vertically more continuous and is less contaminated by artifacts than the broadband inline dip, especially inside the yellow and orange boxes. Figure 5.7 shows the enlarged images within the boxes in Figure 5.6, indicating that multispectral GST inline dip provides better stability and consistency with the seismic amplitude profile over the broadband inline dip.

In Figure 5.8, we further compare another GST crossline vertical slices through the broadband crossline dip (Figure 5.8a) and the multispectral crossline dip (Figure 5.8b), which also indicates the imaging quality improvement by multispectral GST dips with optimized vertical continuity. In Figure 5.9, we further corender the seismic amplitude with the crossline vertical slices through the broadband (Figure 5.9a) and multispectral crossline component (Figure 5.9b) of reflector dip. Note the similar conclusion with the comparison

of inline dips. Multispectral GST algorithm provides crossline dip with fewer artifacts and better vertical continuity over the broadband crossline dip.

In Figure 5.10, we show the spectral voice vertical slices through the components centered at 10 Hz (Figure 5.10a), 30 Hz (Figure 5.10b), 50 Hz (Figure 5.10c), 70 Hz (Figure 5.10d), and 90 Hz (Figure 5.10e). It is noted that different geology features are illuminated in different spectral voices. Note that both 10 Hz and 90 Hz spectral voices appear noisier than other spectral voices, which will decrease the quality of the subsequent dip attributes.

In Figure 5.11a-5.11e, we show the time slices through five dip magnitude volumes computed from different spectral voices during the multispectral GST dip computation. These volumes show slightly different illumination of the linear faults and the elliptical karst collapse features. The dip estimates within the red ellipses exhibit a high signal-to-noise ratio for the 30 and 50 Hz components, but not for the 10, 70, and 90 Hz components. Likewise, the small karsts indicated by the yellow arrows are better delineated by the 30 and 50 Hz spectral components. The signal-to-noise ratio of the 70 Hz component is marginal, and that of the 90 Hz component is poor and provides little interpretational value. To better understand why there is more noise one some of the volumes, we need to examine the spectral voices themselves.

Following the workflow shown in Figure 5.2, we plot three of the dip magnitude anomalies against cyan, magenta and yellow to generate the composite multispectral dip magnitude volume shown in Figure 5.11f. In this image, the resulting colors indicate which spectral components contribute to the anomaly. Because there are 84 Ways to combine the nine computed spectral components, finding the optimum color blend can consume considerable interpreter time. For this reason, we next evaluate the multispectral GST dip

magnitude time slice and compare the result to the broadband dip magnitude time slice in Figure 5.12. Note the improvement in the multispectral GST dip magnitude (Figure 5.12b) that exhibits fewer artifacts, better continuity, and better stability over the broadband dip magnitude (Figure 5.12a). Especially, the red ellipses indicate an improved S/N whereas the yellow arrows indicate improved delineation of smaller karst collapse features.

Application to the Taranaki Basin

Data description

The 3D seismic survey of our second case study on multispectral GST dip is located in the offshore Taranaki Basin, New Zealand (Figure 5.13, modified after Kumar and Mandal, 2017). The continuous tectonic activities and the clockwise movement of the plate boundaries have developed all the structural elements within the Taranaki Basin (King and Thrasher, 1992; Kumar and Mandal, 2017), which is characterized as an extension from the complex Taranaki Fault Zone along the eastern margin and complex subsurface geology with thick sedimentary sequences (Reilly et al., 2015).

The Taranaki Basin can be tectonically divided into three major structural units: the Western unit, the Southern unit, and the Northern unit (Knox, 1982). The Parihaka 3D seismic survey (purple star in Figure 5.13) is located in the Northwest part of the offshore Taranaki Basin, which is primarily characterized as a series of major faults and complex channel system (Kumar, 2016; Amonpantang et al., 2019).

In Figure 5.14, we show a representative vertical slice BB’ (Figure 5.14a) and time slice at t=1.08 s (Figure 5.14b) through the prestack time migration (PSTM) seismic data of the Parihaka 3D survey. The red lines indicate the corresponding locations of the vertical

and time slices. This PSTM seismic data is provided by the New Zealand Crown Minerals, which was acquired with a bin size of 25.0 m × 12.5 m and 60 folds. From the seismic amplitude slices (Figure 5.14), we can observe the complex fault zone and channel system.

Multispectral GST dips

Using the multispectral GST dip workflow (Figure 5.2), we output both the broadband and multispectral GST dip volumes. We first compare the broadband and multispectral GST crossline dip vertical slices in Figure 5.15. High dips are observed (green ellipses in Figure 5.15) along the major fault. Multispectral GST crossline dip (Figure 5.15b) appears better vertical continuity (green ellipses) and higher S/N with fewer artifacts (blue and red rectangles) compared to the broadband GST crossline dip (Figure 5.15a). We then corender the crossline dip vertical slices with the seismic amplitude (Figure 5.16), which indicates that the multispectral GST dip provides better stability and consistency with the seismic amplitude profile over the broadband GST dip, especially the areas in the red and blue rectangles (Figure 5.16). Figure 5.17 shows the enlarged images of corendered seismic amplitude with the broadband and multispectral crossline dip of the area within the red and blue rectangles in Figure 5.16. In this Figure, we change the display approach to highlight the dips during the corendering. Note the improvement of stability and consistency with seismic amplitude in the multispectral GST dip.

The broadband and multispectral GST crossline dip time slices at 1.08s are shown in Figure 5.18. In the GST dip time slices, it is clear that the fault zone divides the survey into two major parts: the hanging wall part (upper left in Figure 5.18) towards the western part and the footwall part (low right in Figure 5.18) towards the eastern part. We can further

observe obvious fault scarps along the major faults due to heavy faulting and high deformation. The multispectral GST crossline dip (Figure 5.18b) appears fewer artifacts over the broadband GST crossline dip (Figure 5.18a), especially the areas indicated by the yellow arrows. Additionally, the faults appear more continuous in the multispectral GST dip result (green arrows in Figure 5.18). Further, the multispectral GST crossline dip provides better delineation of the channels (yellow ellipses in Figure 5.18a and 5.18b) compared to the broadband GST inline dip image. It is also noted that multispectral GST dip shows fewer artifacts inside the red ellipses, but the thin channels are a little smeared.

Broadband and multispectral GST dip magnitude time slices are shown in Figure 5.19. It is noted that there are fewer noises in the entire multispectral GST dip magnitude (Figure 5.19b) over the broadband GST dip magnitude (Figure 5.19a), especially the areas indicated by the red arrows. The multispectral GST dip magnitude appears more continuous imaging of the fault zone, and it provides a better delineation of the channel system over the broadband GST dip magnitude (green arrows in Figure 5.19). It is further noted that multispectral GST dip magnitude shows fewer artifacts in the green ellipses, but some thin channels are a little smeared, which is similar to the observation in Figure 5.18.

Conclusions

In general, the signal-to-noise ratio varies with different bandpass-filtered versions (or spectral voice components) of the seismic amplitude data. Because this variation in the signal-to-noise ratio directly influences the quality of volumetric dip estimates, improvements in dip estimation can be achieved by eliminating noisier components. Inspired by my previous success with multispectral coherence computed by stacking the covariance matrix corresponding to different spectral components, I hypothesized that a

multispectral dip estimation computed by stacking the GST matrices for different spectral voices would lead to still further improvement in volumetric dip. When applied to a Fort Worth Basin wide-azimuth land survey, I find the improvement in delineating karst collapse features and suppression of noise to be minimal and not worth the increase in computational effort by a factor of six. When applied to a Taranaki Basin narrow azimuth marine survey, I find a decrease in noise, but also an increase in smearing and a decrease in lateral resolution of the turbidites channels of interest. In summary, restricting the dip computation to those spectral components exhibiting a good signal-to-noise ratio can significantly improve the resulting dip estimation, but unlike multispectral coherence, the success of multispectral dip estimates appears to be data dependent and in many cases, not worth the increased computational effort.

Acknowledgements

The authors thank all sponsors of Attribute Assisted Seismic Processing and Interpretation (AASPI) consortium group for their generous sponsorship, and colleagues for their valuable suggestions. The authors would like to thank Marathon Oil Company and New Zealand Petroleum and Minerals for providing their seismic data volumes.

References

Aarre, V., 2010, Globally consistent dip estimation: 80th Annual International Meeting, SEG, Expanded Abstracts, 1387-1390.

Alaei, B., 2012, Improved fault imaging by integration of frequency decomposition and fault attributes, example from mid Norwegian sea: Proceedings of the 3rd EAGE Fault and Top Seal Conference, C13.

Amonpantang, P., H. Bedle, and J. Wu, 2019, Multiattribute analysis for channel element discrimination in the Taranaki Basin, offshore New Zealand: Interpretation, **7**, SC45–SC61.

Bakker, P., 2002, Image structure analysis for seismic interpretation: Ph.D. dissertation, University of Delft.

Barnes, A. E., 2000, Weighted average seismic attributes: Geophysics, **65**, 275–285.

Chopra, S., and K. J. Marfurt, 2007, Seismic attributes for prospect identification and reservoir characterization: SEG.

Chopra, S., and K. J. Marfurt, 2019, Multispectral, multiazimuth, and multioffset coherence attribute applications: Interpretation, **7**, SC21–SC32.

Chopra, S., and K. J. Marfurt, 2020, Adopting multispectral dip components for coherence and curvature attribute computations: The Leading Edge, **39**, 593–596.

Dewett, D. T., and A. A. Henza, 2016, Spectral similarity fault enhancement: Interpretation, **4**, SB149–SB159.

Jones, G., and R. Roden, 2012, Fracture detection interpretation beyond conventional seismic approaches, AAPG search and discovery article #41035.

Khatiwada, M., G. R. Keller, and K. J. Marfurt, 2013, A window into the Proterozoic: Integrating 3D seismic, gravity, and magnetic data to image subbasement structures in the southeast Fort Worth Basin: Interpretation, **1**, T125–T14.

King, P. R., and G. P. Thrasher, 1992, Post-Eocene development of the Taranaki Basin, New Zealand: Convergent overprint of a passive margin, in J. S. Watkins, Z. Feng, and K. J. McMillen, eds., Geology and geophysics of continental margins: American Association of Petroleum Geologists Memoir, **53**, 93–118.

Knox, G. J., 1982, Taranaki basin, structural style and tectonic setting: New Zealand Journal of Geology and Geophysics, **25**, 125–140.

Kumar, P. C., 2016, Application of geometric attributes for interpreting faults from seismic data: an example from Taranaki Basin, New Zealand: 86th Annual International Meeting, SEG, Expanded Abstracts, 2077–2081.

Kumar, P. C., and A. Mandal, 2017, Enhancement of fault interpretation using multi-attribute analysis and artificial neural network (ANN) approach: A case study from Taranaki Basin, New Zealand: Exploration Geophysics, **49**, 409–424.

Kuwahara, M., K. Hachimura, S. Eiho, and M. Kinoshita, 1976, Digital processing of biomedical images: Plenum Press, 187–203.

Li, F., and W. Lu, 2014, Coherence attribute at different spectral scales: Interpretation, **2**, SA99–SA106.

Li, F., J. Qi, B. Lyu, and K. J. Marfurt, 2018, Multispectral coherence: Interpretation, **6**, T61–T69.

Lin, T., D. Chang, B. Zhang, J. Guo, and K. J. Marfurt, 2014, Seismic attributes estimation using a self-adaptive window: 84th Annual International Meeting, SEG, Expanded Abstracts, 1654–1658.

Luo, Y., Y. E. Wang, N. M. Albinhassan, and M. N. Alfaraj, 2006, Computation of dips and azimuths with weighted structural tensor approach: Geophysics, **71**, V119-V121.

Lyu, B., J. Qi, G. Machado, F. Li, and K. J. Marfurt, 2019, Seismic fault enhancement using spectral decomposition assisted attributes: 89th Annual International Meeting, SEG, Expanded Abstracts, 1938–1942.

Lyu, B., J. Qi, F. Li, Y. Hu, T. Zhao, S. Verma, and K. J. Marfurt, 2020a, Multispectral coherence: Which decomposition should we use?: Interpretation, **8**, T115–T129.

Lyu, B., J. Qi, S. Sinha, J. Li, and K. J. Marfurt, 2020b, Improving fault delineation using maximum entropy multispectral coherence: Interpretation, **8**, T835-T850.

Marfurt, K. J., 2006, Robust estimates of reflector dip and azimuth: Geophysics, **71**, P29-P40.

Marfurt, K. J., R. L. Kirlin, S. H. Farmer, and M. S. Bahorich, 1998, 3-D seismic attributes using a running window semblance-based algorithm: Geophysics, **63**, 1150-1165.

Marfurt, K. J., 2017, Interpretational aspects of multispectral coherence: 79th Annual International Conference and Exhibition, EAGE, Extended Abstracts.

Montgomery, S. L., D. M. Jarvie, K. A. Bowker, and R. M. Pollastro, 2005, Mississippian Barnett Shale, Fort Worth basin, north-central Texas: Gas-shale play with multitrillion cubic foot potential: AAPG Bulletin, **89**, 155–175.

Qi, J., B. Zhang, H. Zhou, and K. Marfurt, 2014, Attribute expression of fault-controlled karst - Fort Worth Basin, Texas: A tutorial: Interpretation, **2**, SF91–SF110.

Qi, J., B. Lyu, A. Alali, G. Machado, Y. Hu, and K. J. Marfurt, 2019, Image processing of seismic attributes for automatic fault extraction: Geophysics, **84**, O25–O37.

Reilly, C., A. Nicol, J. J. Walsh, and H. Seebeck, 2015, Evolution of faulting and plate boundary deformation in the Southern Taranaki Basin, New Zealand: Tectonophysics, **651–652**, 1–18.

Roende, H., C. Meeder, J. Allen, S. Peterson, and D. Eubanks, 2008, Estimating subsurface stress direction and intensity from subsurface full azimuth land data: 78th Annual International Meeting, SEG, Expanded Abstracts, 217–220.

Chapter 5 figures

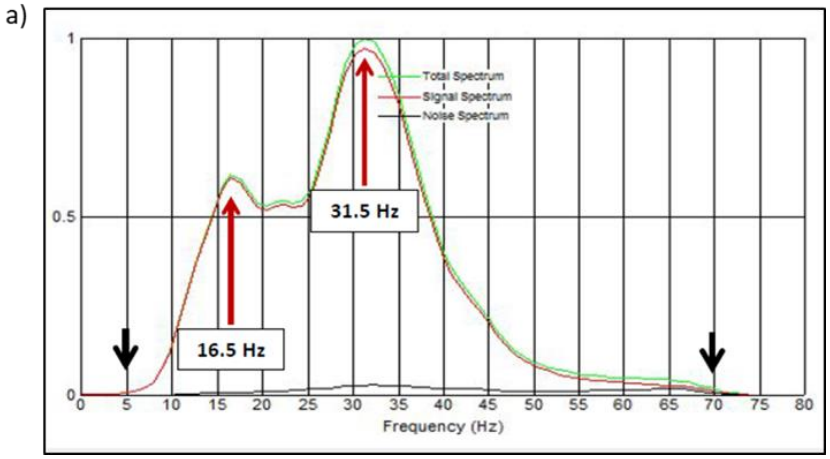

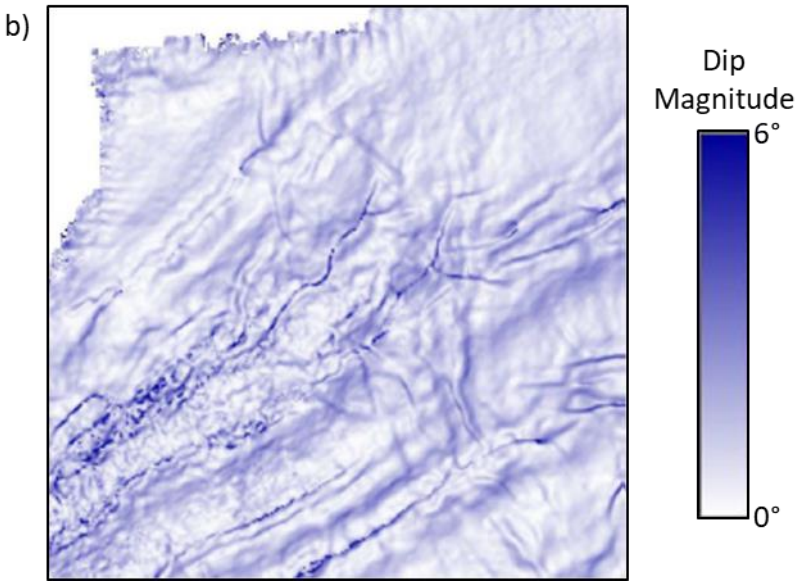

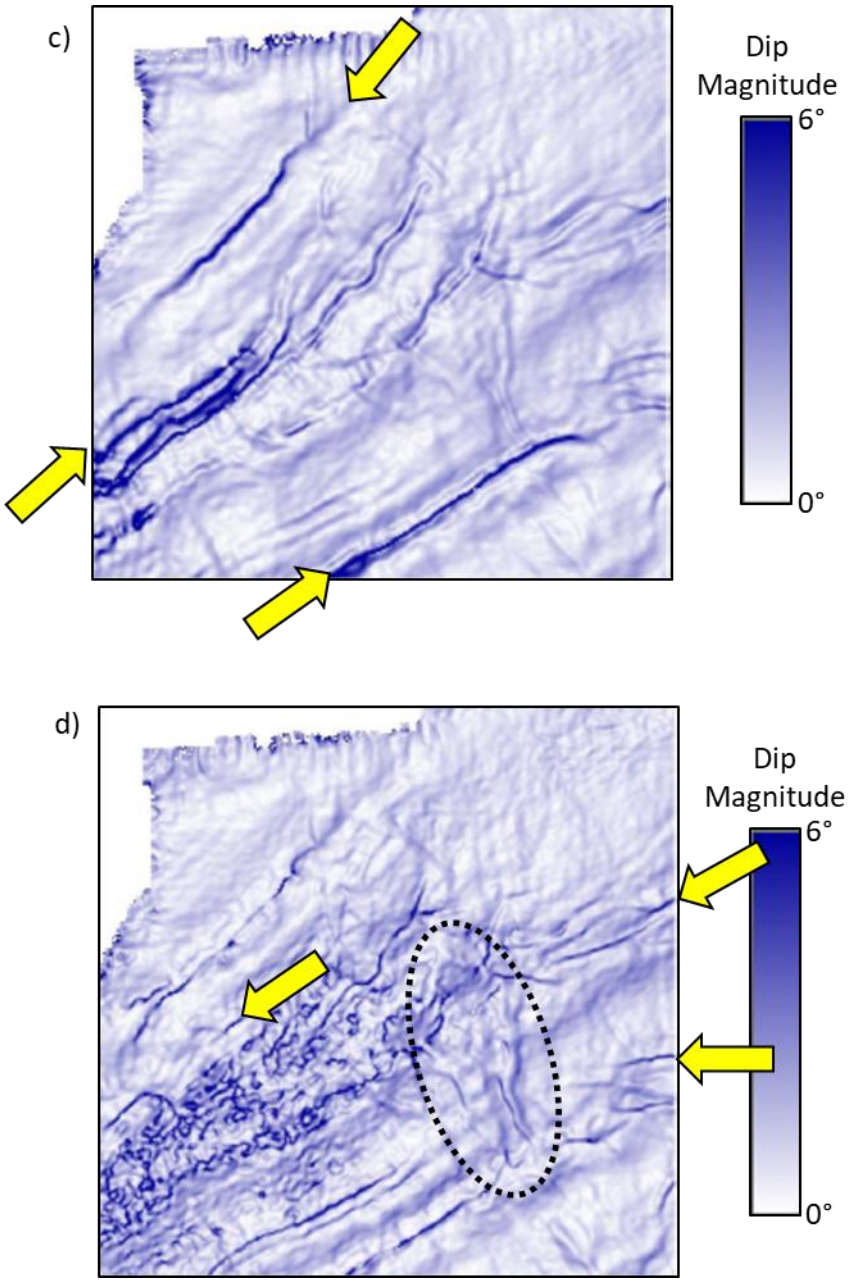

Figure 5.1: (a) The seismic amplitude spectrum of a data volume acquired over the Eagle Ford Shale play of south Texas. Note the strong response (and implied higher signal-to-noise ratio about 16.5 and 31.5 Hz). Time slices at the target level through the dip magnitude volumes computed from the (b) original broadband seismic amplitude volume and from the (c) 16.5 Hz and (d) 31.5 Hz spectral voice volumes. Yellow arrows indicate improved clarity of some of the larger faults in the 16.5 Hz volume and of smaller faults and (in black ellipse) stratigraphic edges in the 31.5 Hz image. (After Jones and Roden, 2012).

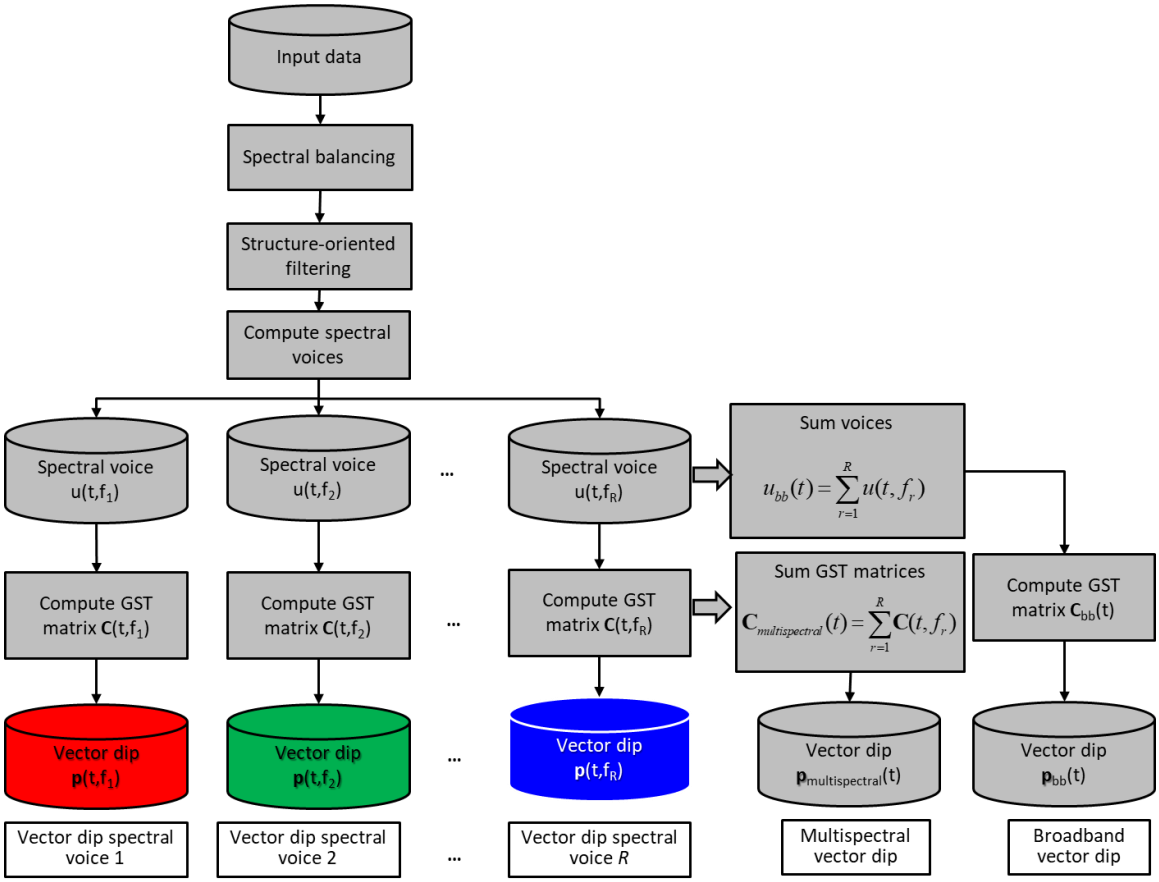

Figure 5.2: Workflow of multispectral GST dip computation. We first apply the spectral balancing and structure-oriented filtering (SOF)on the original full-bandwidth seismic amplitude volume. We then decompose the noise-attenuated full-bandwidth seismic amplitude volume into spectral voices and build the multispectral covariance matrix. Next, we compute the eigenvectors and eigenvalues from the multispectral gradient structure tensor matrix, followed by the generation of inline and crossline dip volumes. We can output the broadband, spectrally-limited, and multispectral GST dip volumes.

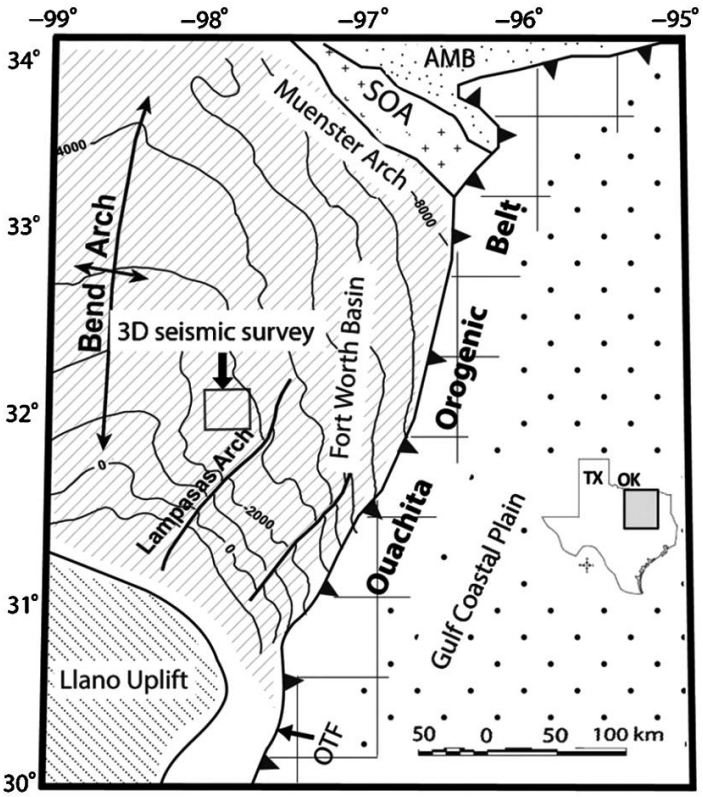

Figure 5.3: 3D seismic survey location in the index map of Fort Worth Basin and major tectonic units (modified after Khatiwada et al., 2013).

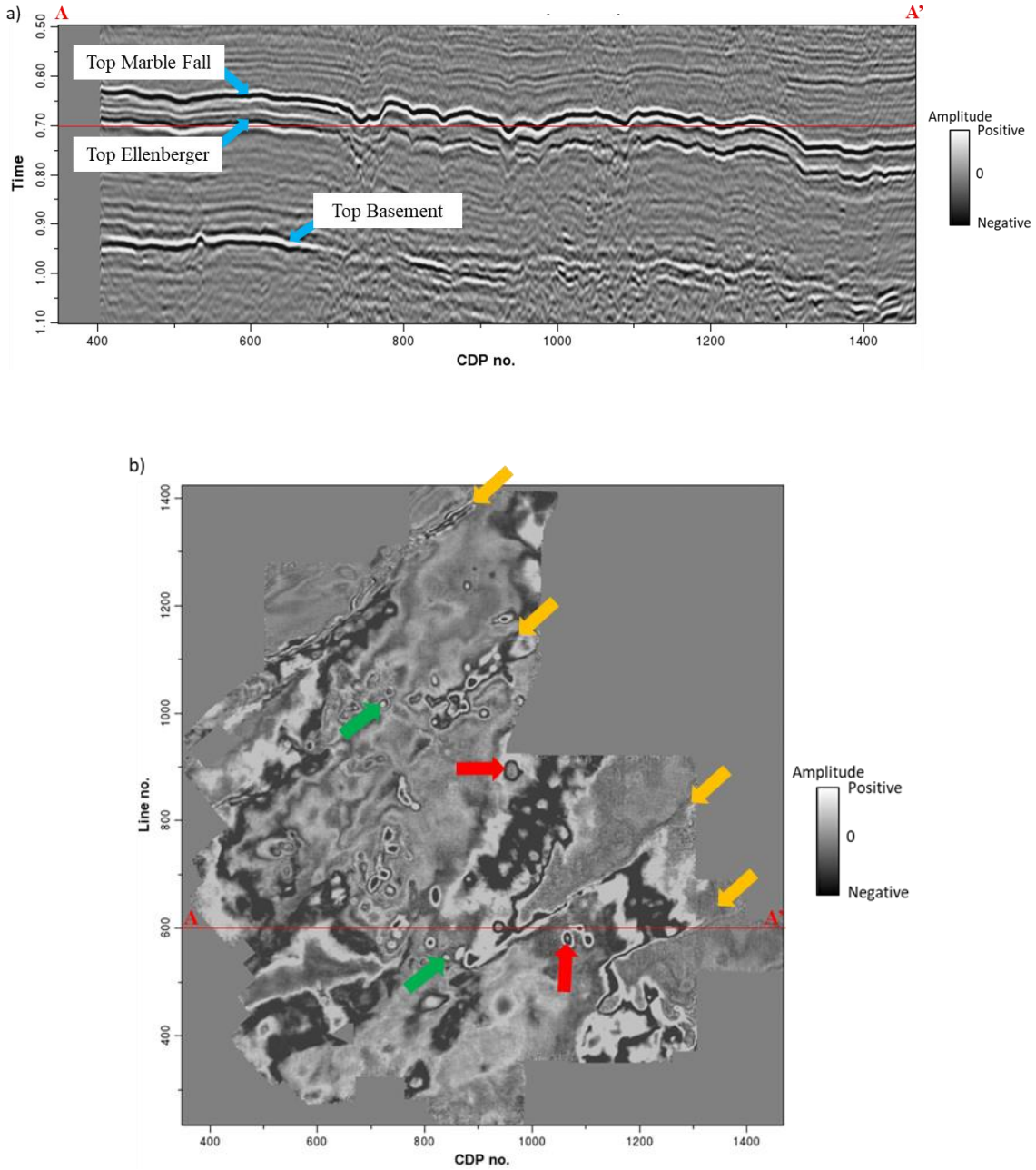

Figure 5.4: A representative (a) vertical slice and (b) time slice at t=0.70 s of the seismic amplitude in the 3D seismic survey in the Fort Worth Basin. The target Barnett Shale falls between the Marble Falls and Ellenberger hydraulic fracture barriers (indicated by the arrows in Figure 5.4a). Note the faults (orange arrows), larger karst (red arrows), and smaller karst (green arrows) features in Figure 5.4b.

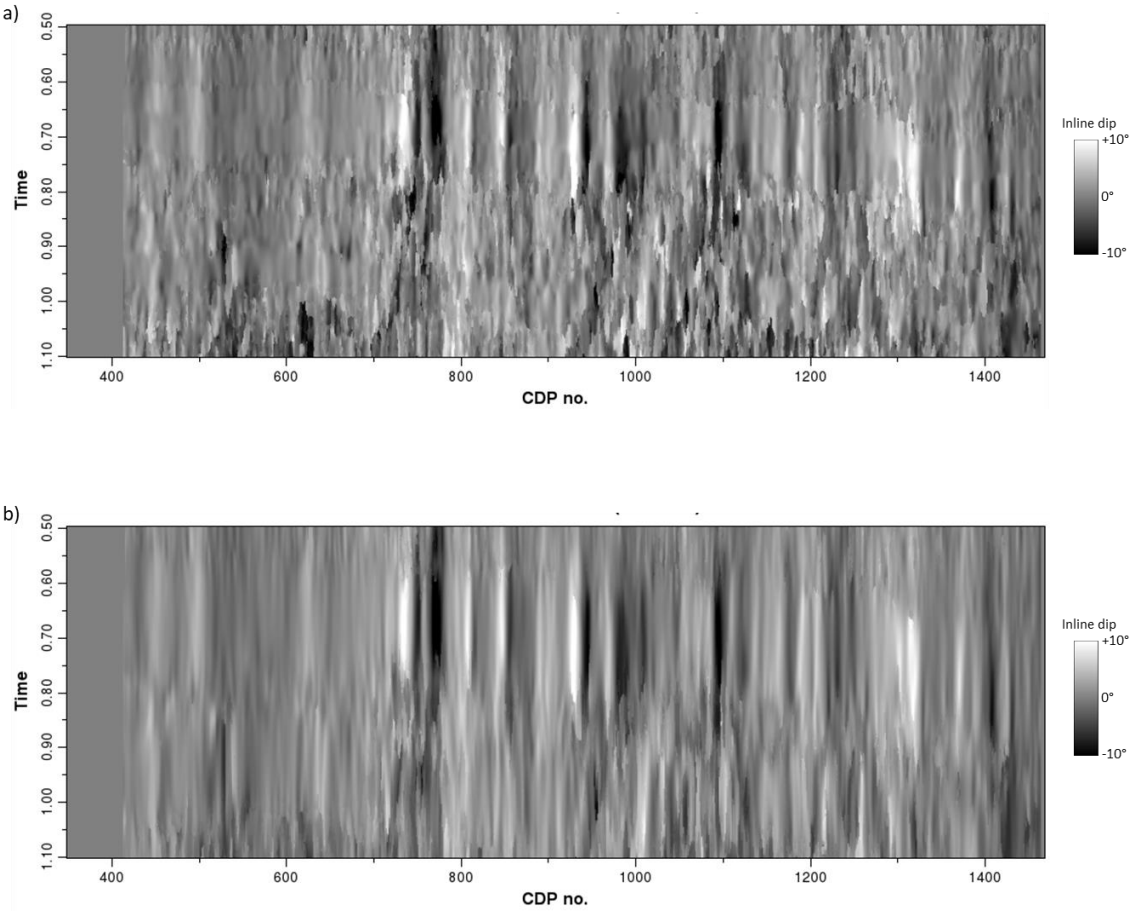

Figure 5.5: Inline dip vertical slices through the volumes of (a) broadband GST dip and (b) multispectral GST dip. Note that the multispectral GST inline dip appears higher quality with fewer artifacts, better continuity, and improved stability compare to the broadband inline dip.

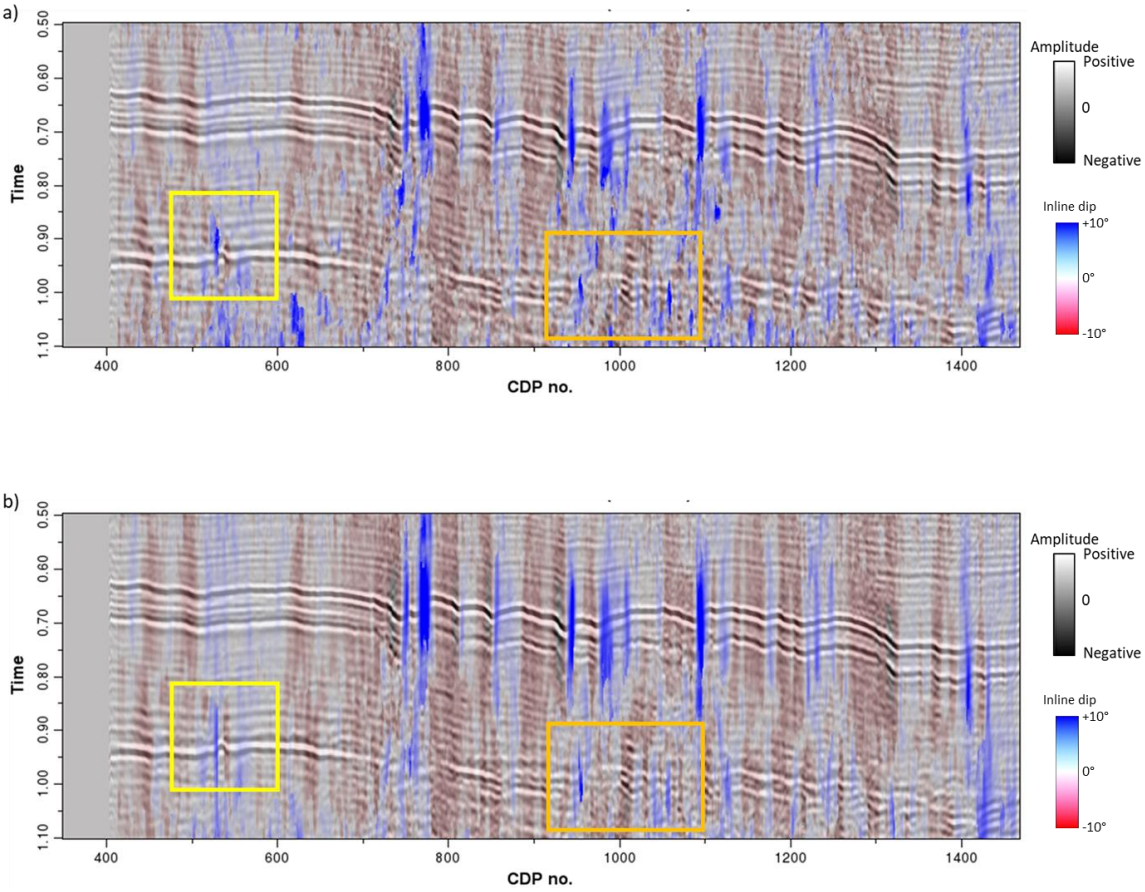

Figure 5.6: Vertical slices through the (a) broadband and (b) multispectral inline component of reflector dip corendered with the seismic amplitude volumes. Note that the multispectral GST inline dip is vertically more continuous and is less contaminated by artifacts than the broadband inline dip, especially inside the yellow and orange boxes.

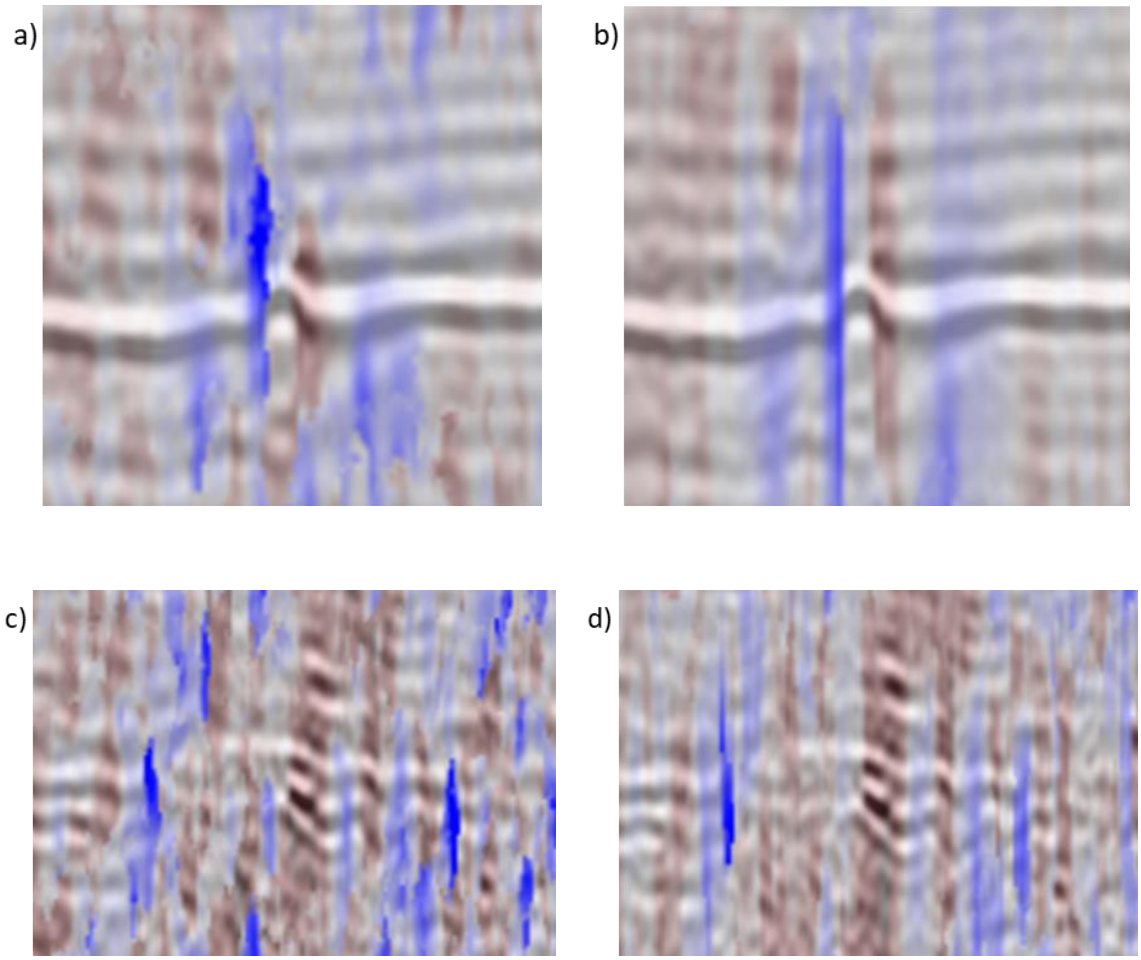

Figure 5.7: Enlarged images of corendered seismic amplitude with the (a) broadband and (b) multispectral inline dip of the area within the yellow boxes shown in the previous figure and (c) broadband and (d) multispectral inline dip of the area within the orange boxes shown in the previous figure.

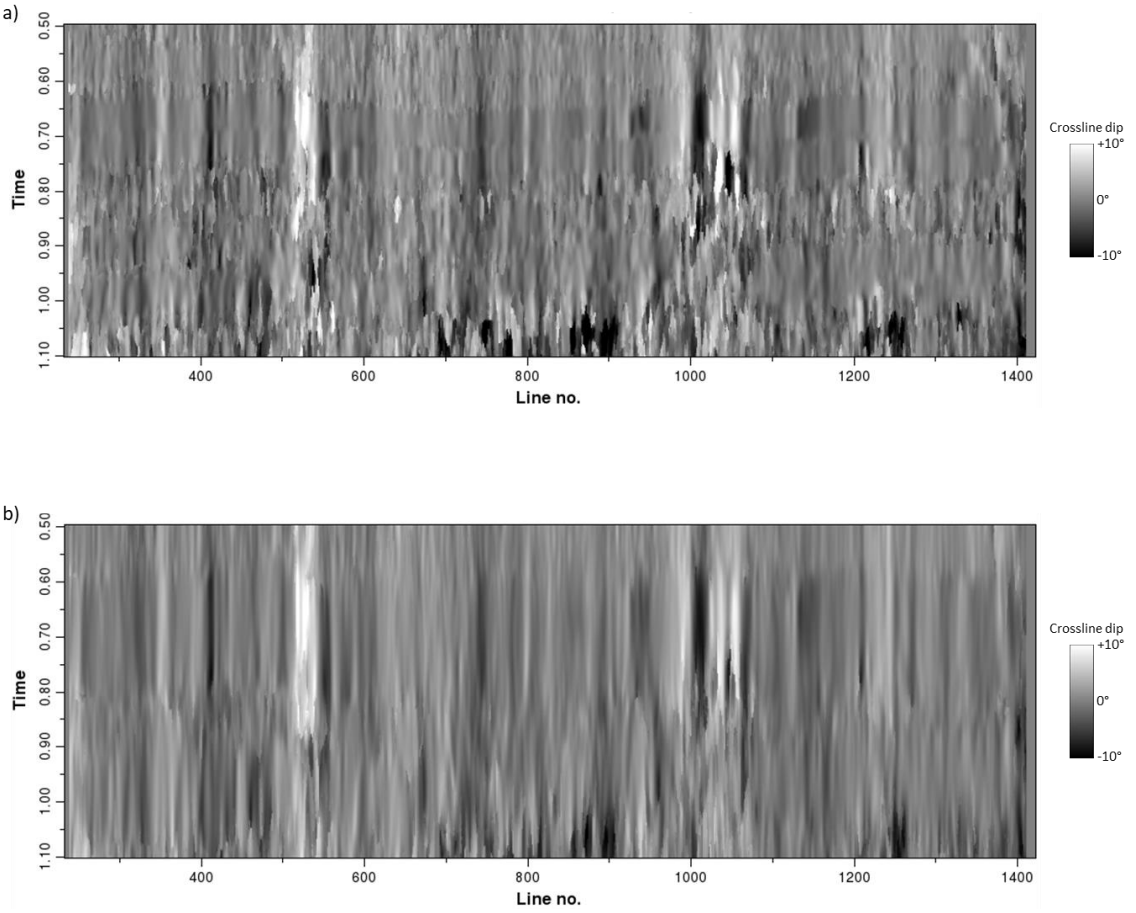

Figure 5.8: Crossline dip vertical slices through the volumes of (a) broadband GST dip and (b) multispectral GST dip. Note the imaging quality improvement in the multispectral GST dip.

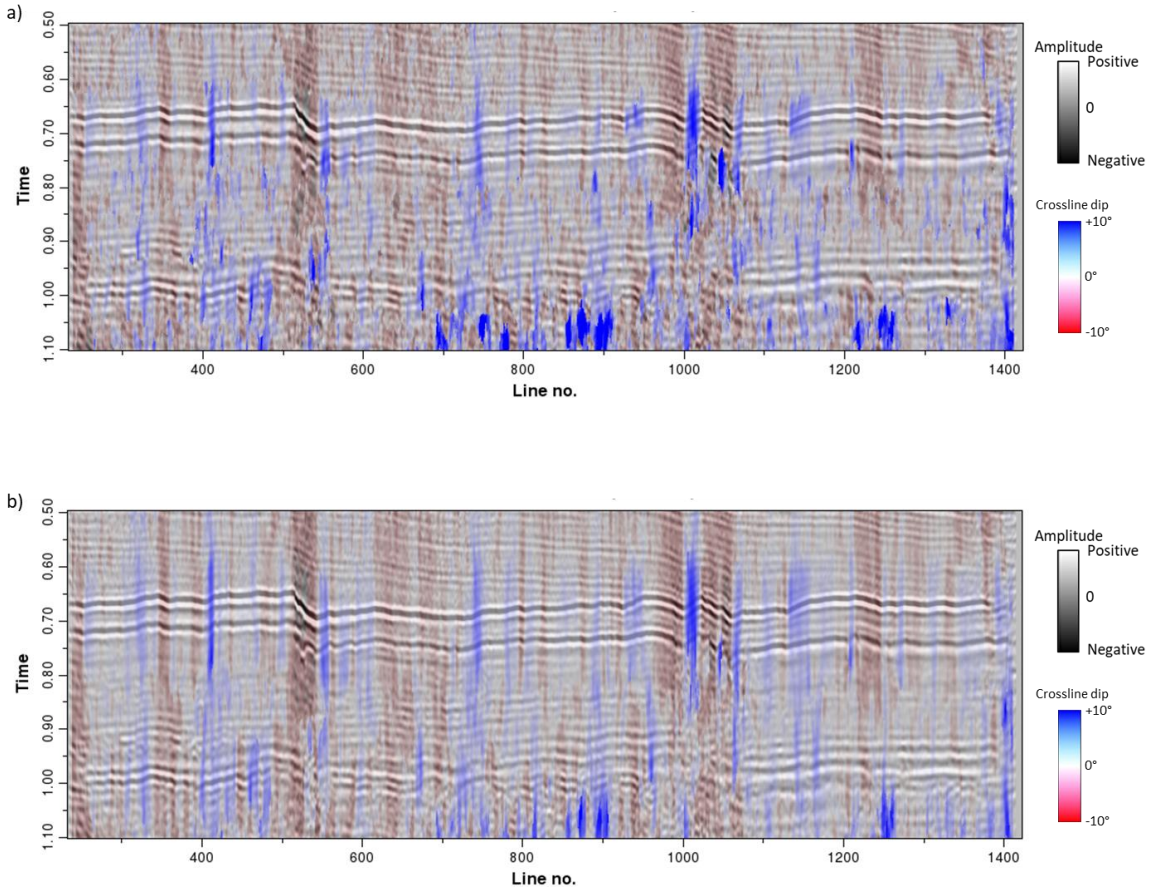

Figure 5.9: Crossline vertical slices through the (a) broadband and (b) multispectral crossline component of reflector dip corendered with the seismic amplitude volumes. Note that the multispectral GST crossline dip shows better continuity and fewer artifacts than the broadband crossline dip.

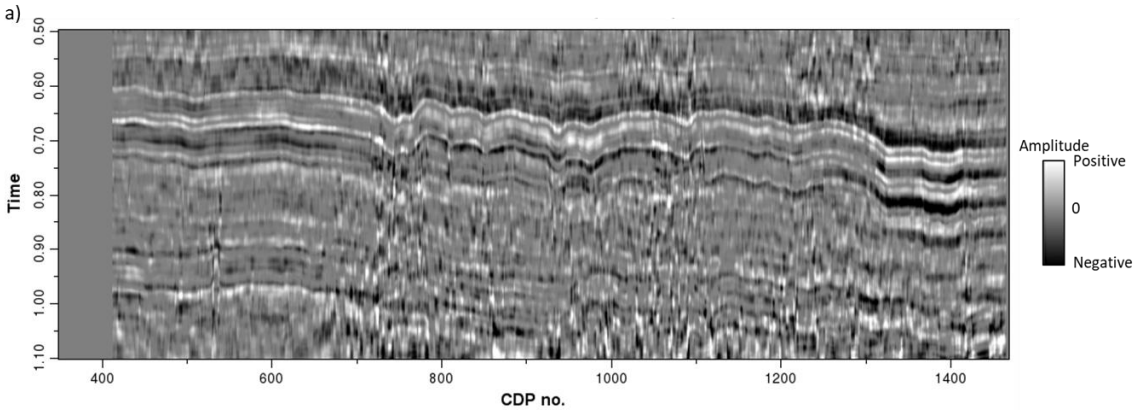
a)
Time
0.50
0.60
0.70
0.80
0.90
1.00
1.10
400
600
800
1000
1200
1400
CDP no.
Amplitude
Positive
0
Negative

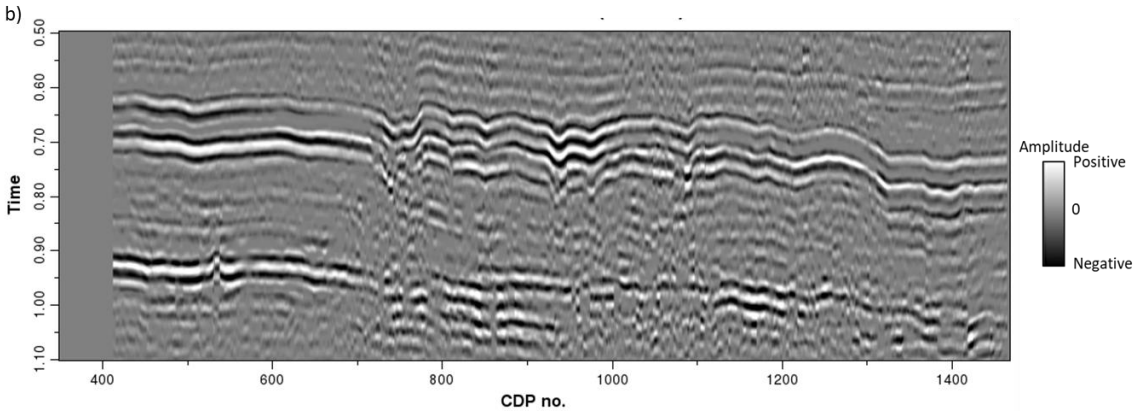
b)
Time
0.50
0.60
0.70
0.80
0.90
1.00
1.10
400
600
800
1000
1200
1400
CDP no.
Amplitude
Positive
0
Negative

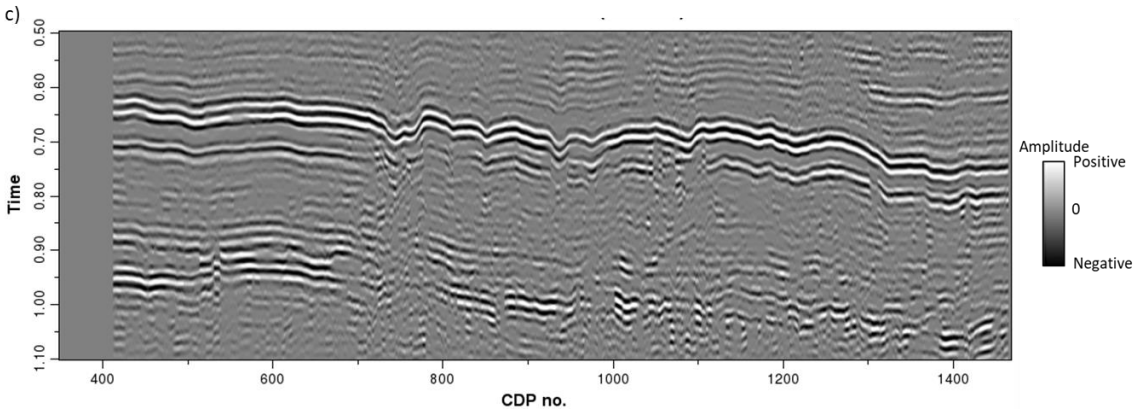
c)
Time
0.50
0.60
0.70
0.80
0.90
1.00
1.10
400
600
800
1000
1200
1400
CDP no.
Amplitude
Positive
0
Negative

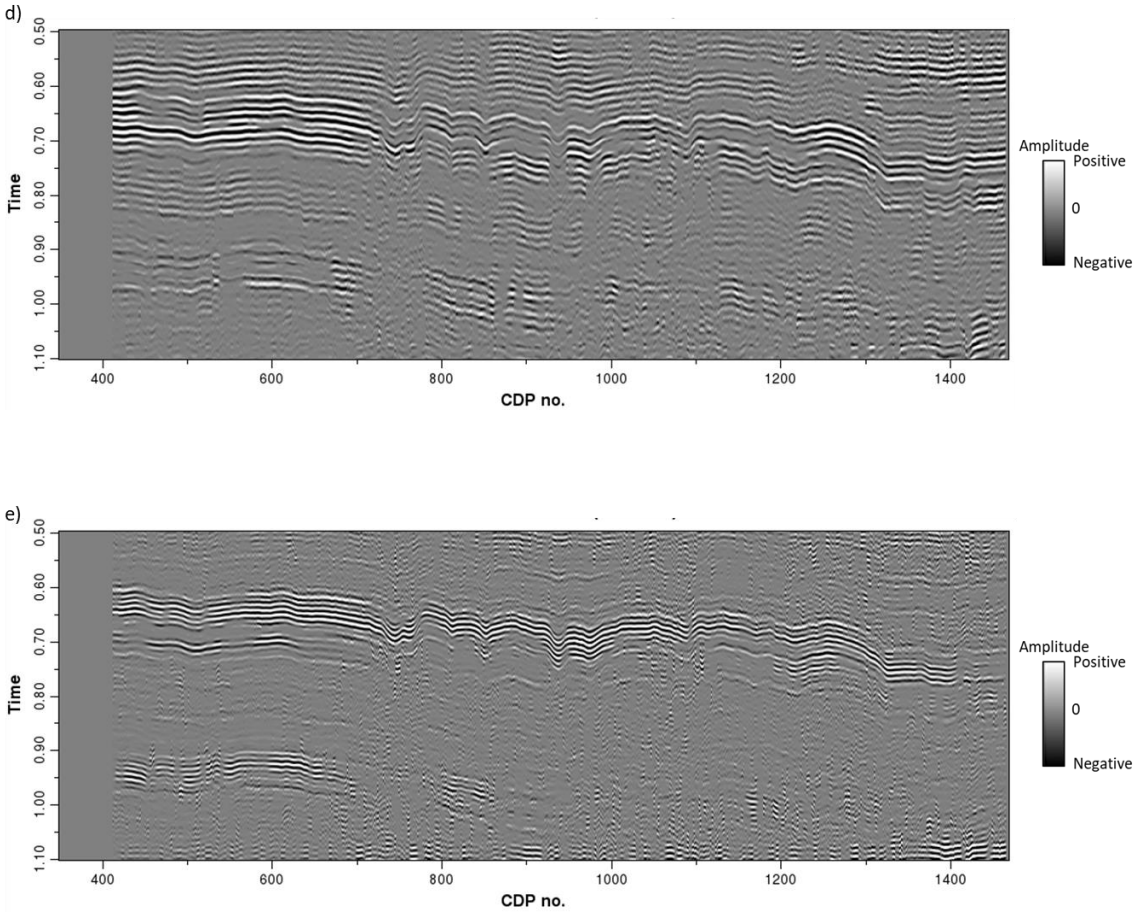

Figure 5.10: Vertical slices through the spectral voice components centered about (a) 10 Hz, (b) 30 Hz, (c) 50 Hz, (d) 70 Hz, and (e) 90 Hz. Note the 10 Hz and 90 Hz spectral voices appear noisy, while 30 Hz and 50 Hz show better signal-to-noise ratio.

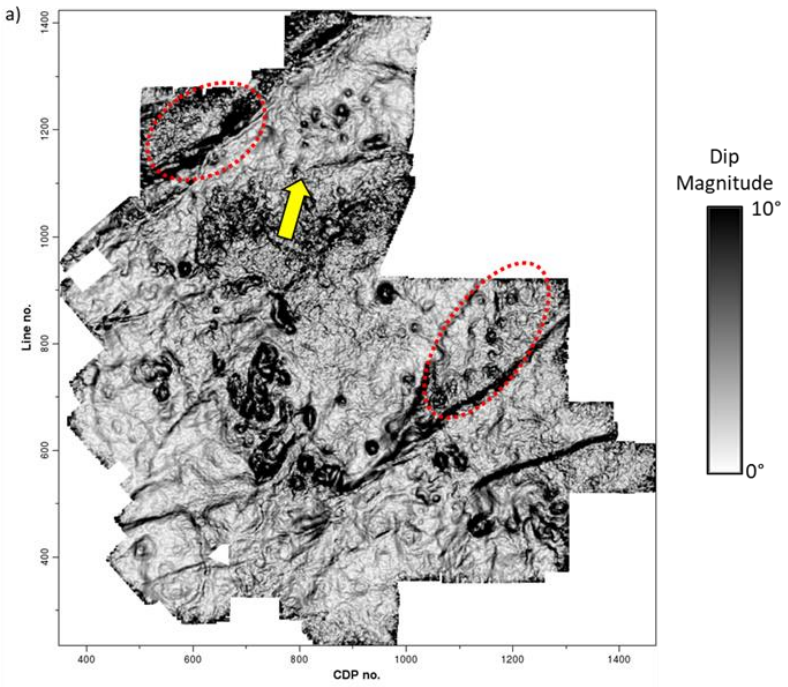
a)
Line no.
CDP no.
400
600
800
1000
1200
1400
Dip
Magnitude
10°
0°

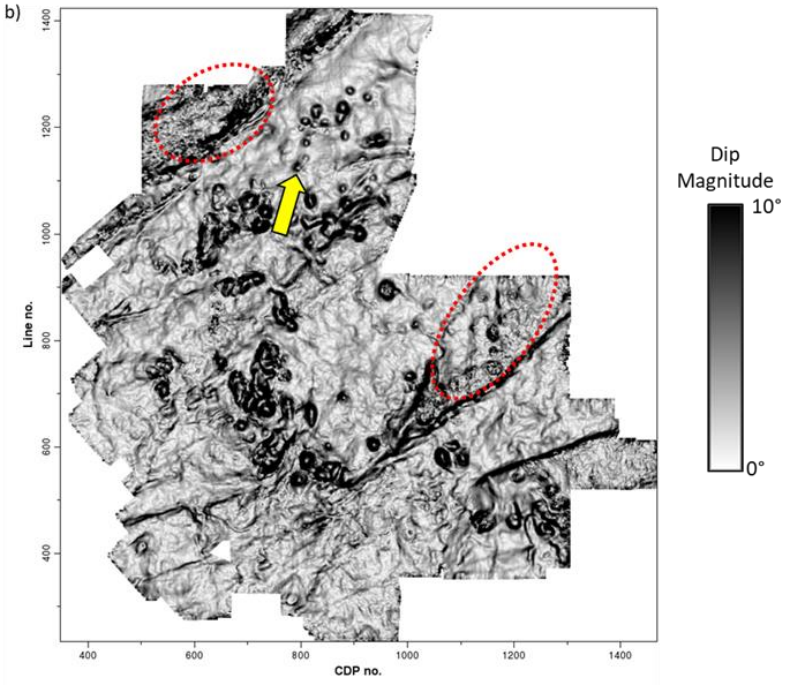
b)
Line no.
CDP no.
400
600
800
1000
1200
1400
Dip
Magnitude
10°
0°

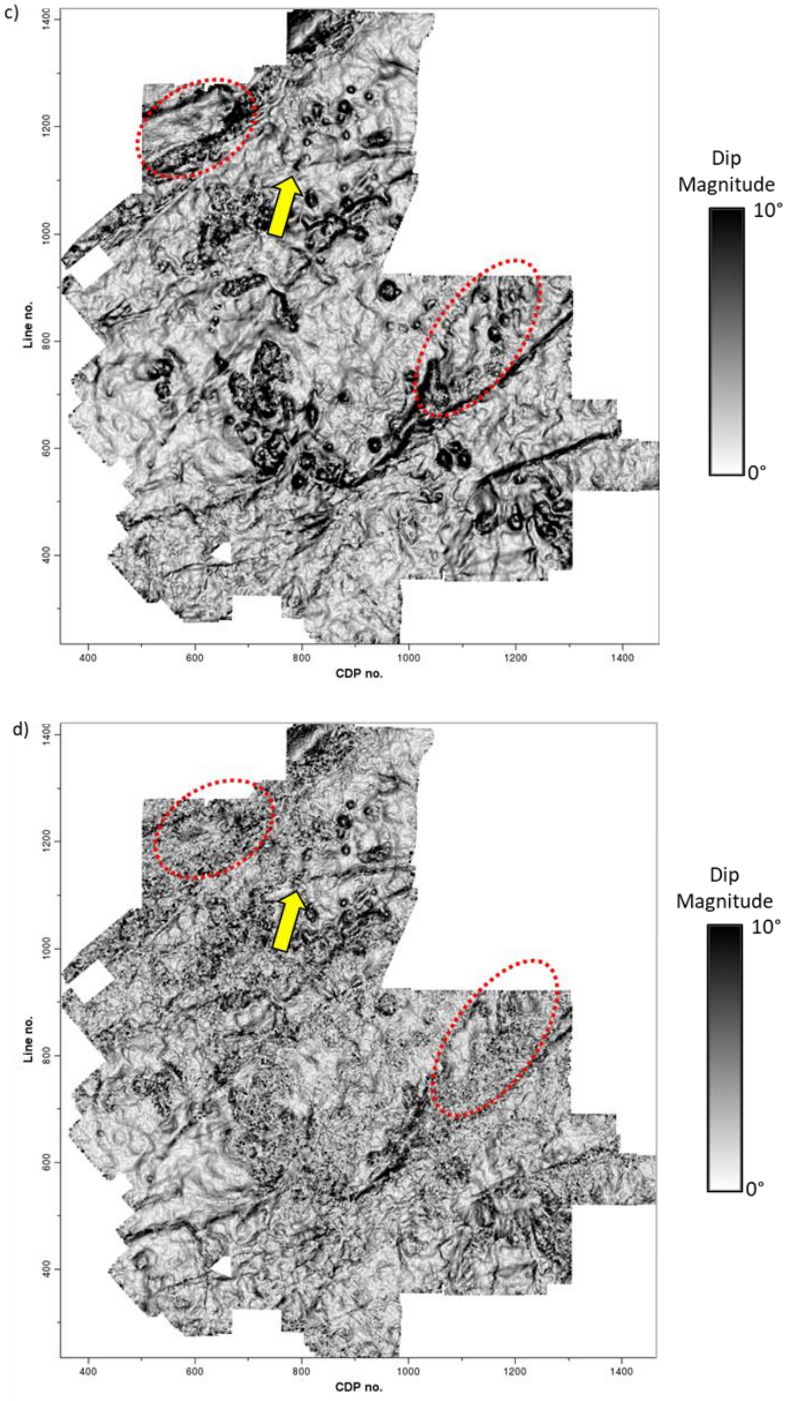
c)
Line no.
CDP no.
400
600
800
1000
1200
1400
Dip
Magnitude
10°
0°
d)
Line no.
CDP no.
400
600
800
1000
1200
1400
Dip
Magnitude
10°
0°

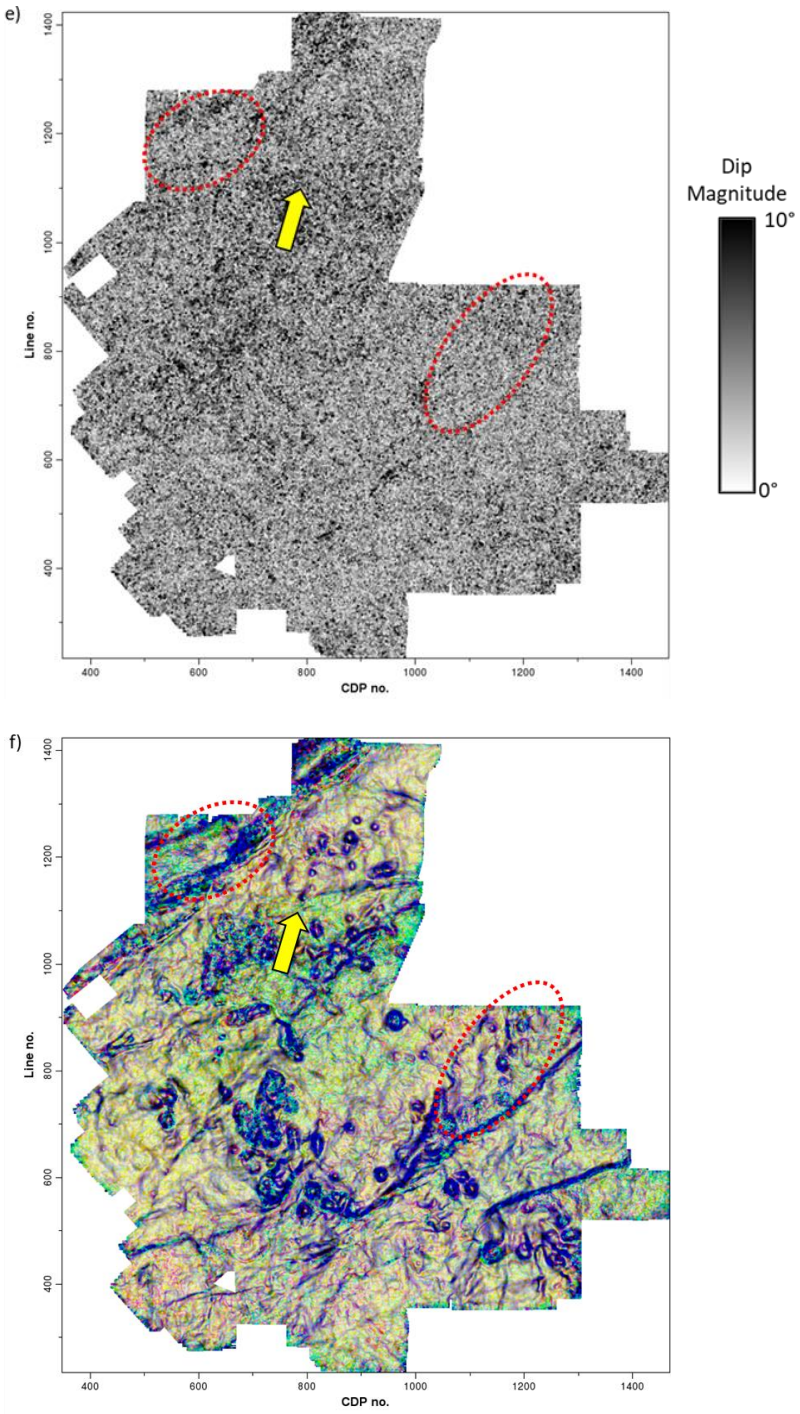

Figure 5.11: Time slices at t=0.7 s through dip magnitude volumes computed from spectral voices centered about (a) 10 Hz, (b) 30 Hz, (c) 50 Hz, (d) 70 Hz, and (e) 90 Hz. There is increasing lateral detail as well as increasing noise with increased frequency. (f) Co-rendered spectral magnitude by mapping the 10 Hz dip magnitude volume against cyan, the 50 Hz dip magnitude volume against magenta, and the 90 Hz dip magnitude volume against yellow. Anomalies that appear as black occur on all three input volumes. The circular collapse features that appear as blue exhibit anomalies at 10 Hz and 50 Hz, but not at 90 Hz. Features that appear as green exhibit anomalies at 50 Hz and 90 Hz, but not at 10 Hz. Features that appear as yellow (and are mostly noise) exhibit anomalies only on the 90 Hz dip magnitude component.

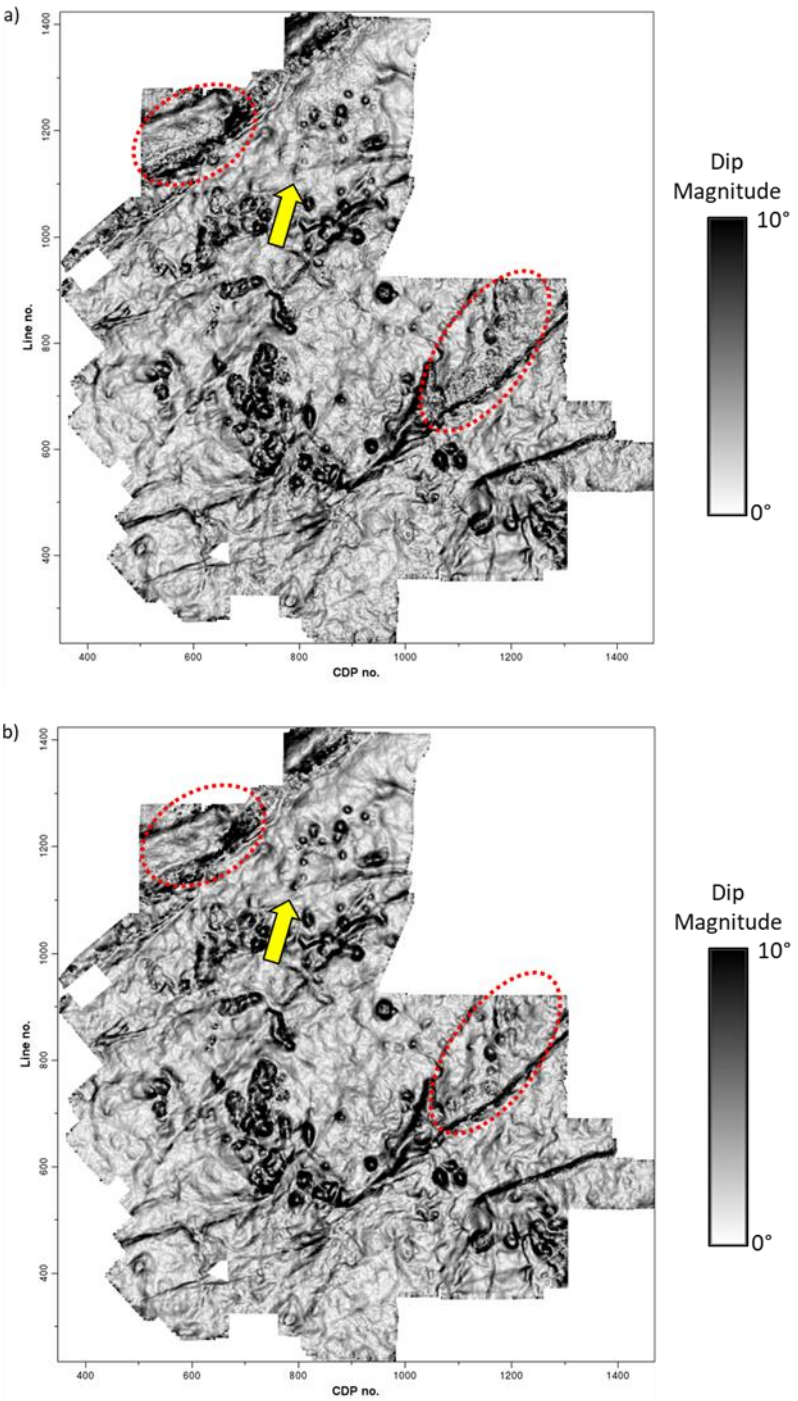

Figure 5.12: Time slices at *t*=0.7 s through dip magnitude volumes of (a) broadband GST dip and (b) multispectral GST dip. We can notice the improvement in the multispectral GST dip magnitude with fewer artifacts and better continuity over the broadband GST dip magnitude. Especially, the red ellipses indicate an improved S/N whereas the yellow arrows indicate improved delineation of smaller karst collapse features in multispectral GST dip magnitude.

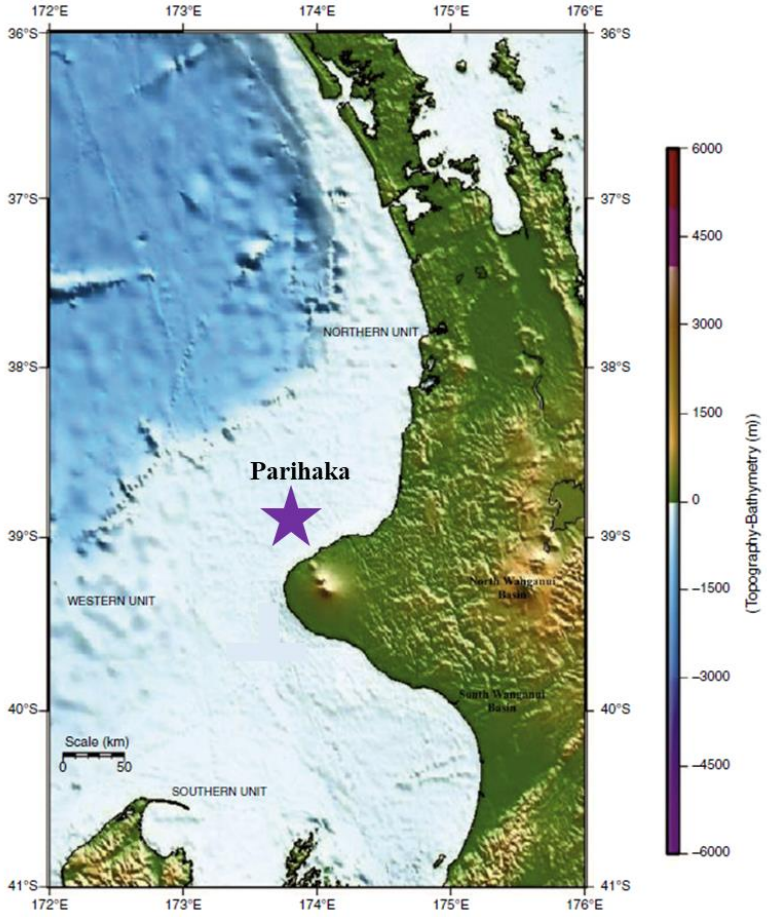

Figure 5.13: The Parihaka 3D seismic survey (purple star) is located in the Northwest part of the offshore Taranaki Basin, New Zealand (modified after Kumar and Mandal, 2017).

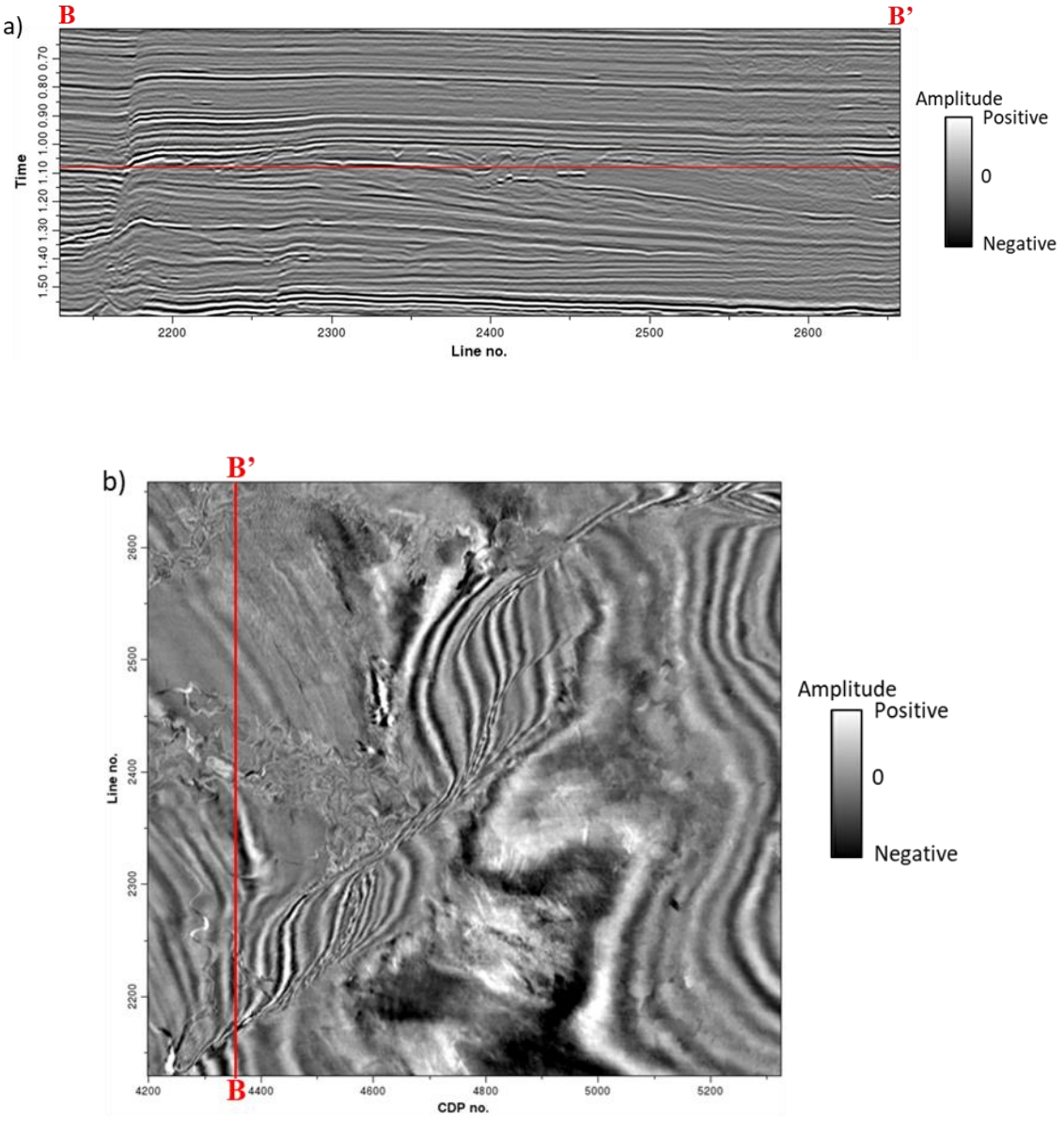

Figure 5.14: A representative (a) vertical slice BB' and (b) time slice at t=1.08 s of the PSTM seismic amplitude data in the Parihaka 3D seismic survey. The red lines indicate the corresponding locations of the vertical and time slices. The complex fault zone and channel system can be observed.

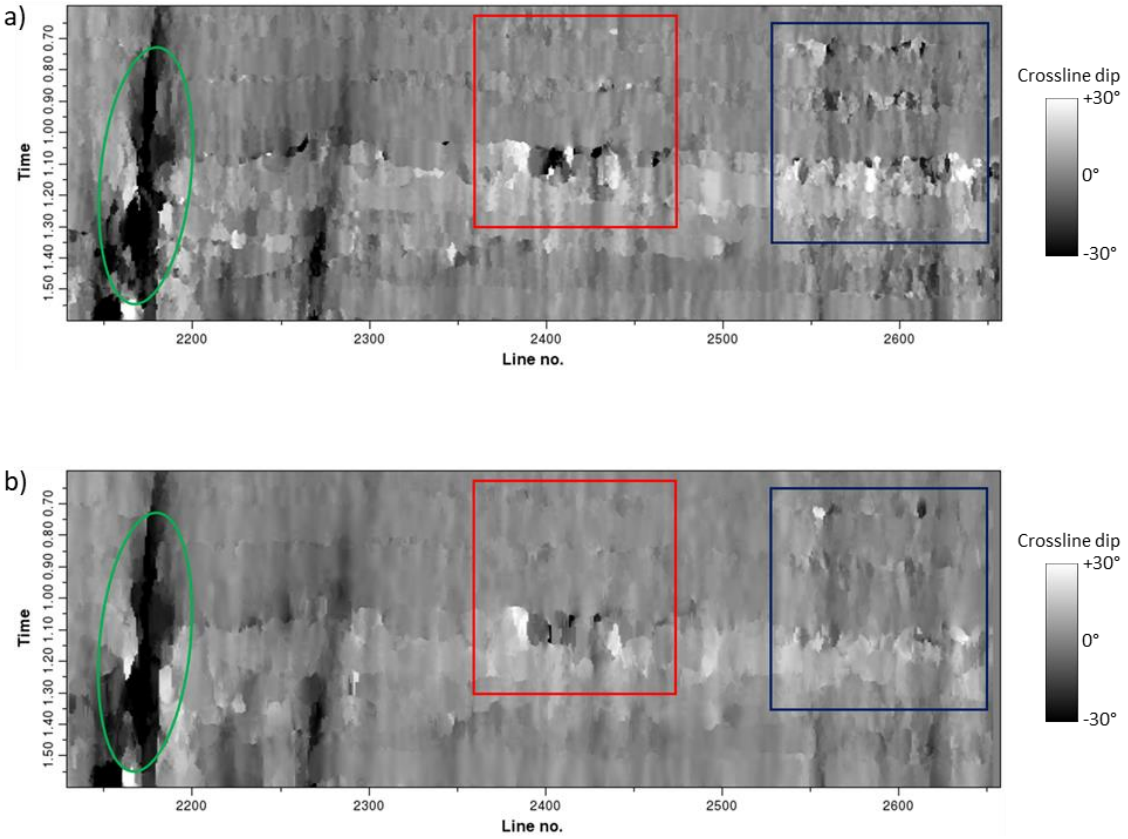

Figure 5.15: Vertical slice BB' through the (a) broadband and (b) multispectral GST estimates of the crossline dip volume. We can observe the high dips (green ellipses) along the major faults. It is noted that the multispectral GST crossline dip appears better vertical continuity (green ellipses) and higher S/N with fewer artifacts (blue and red rectangles) compared to the broadband GST crossline dip.

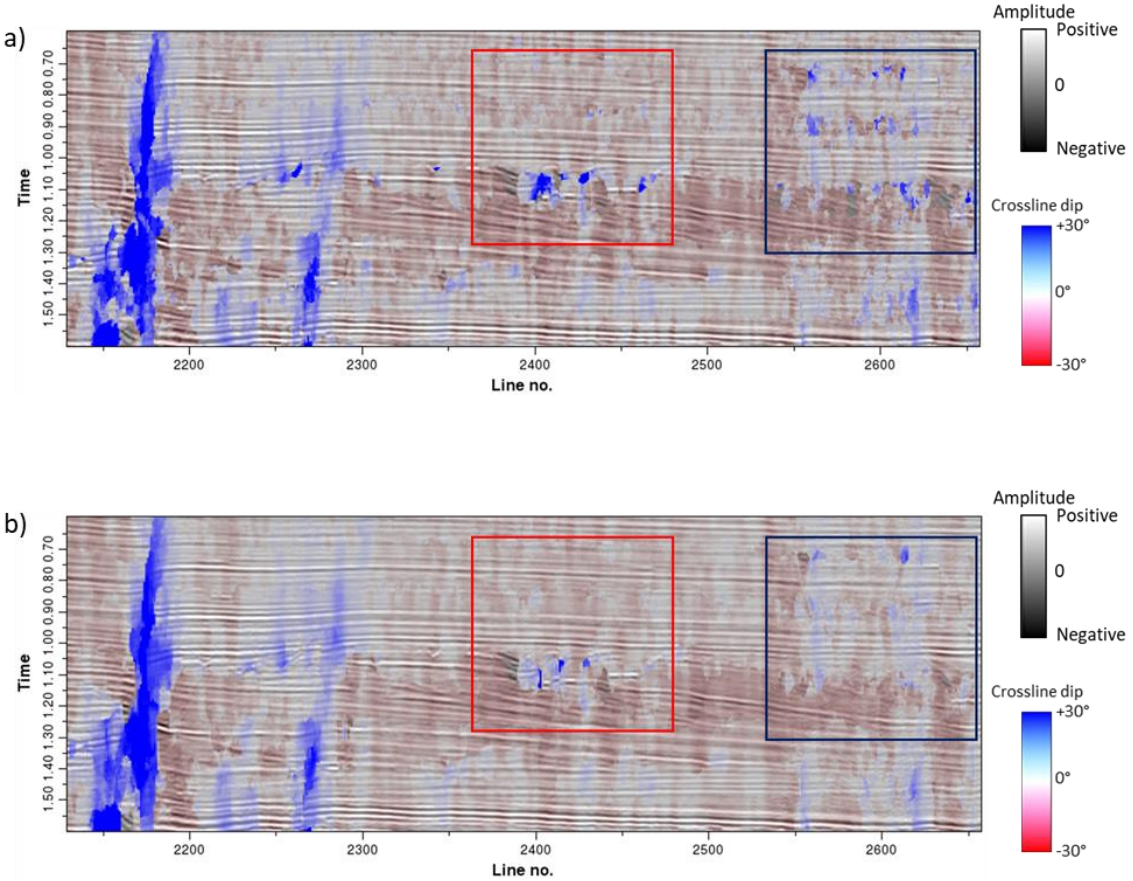

Figure 5.16: The seismic amplitude corendered with (a) broadband GST crossline dip and (b) multispectral GST crossline dip. Note the better stability and consistency with the seismic amplitude profile using multispectral GST dip (especially in the red and blue rectangles).

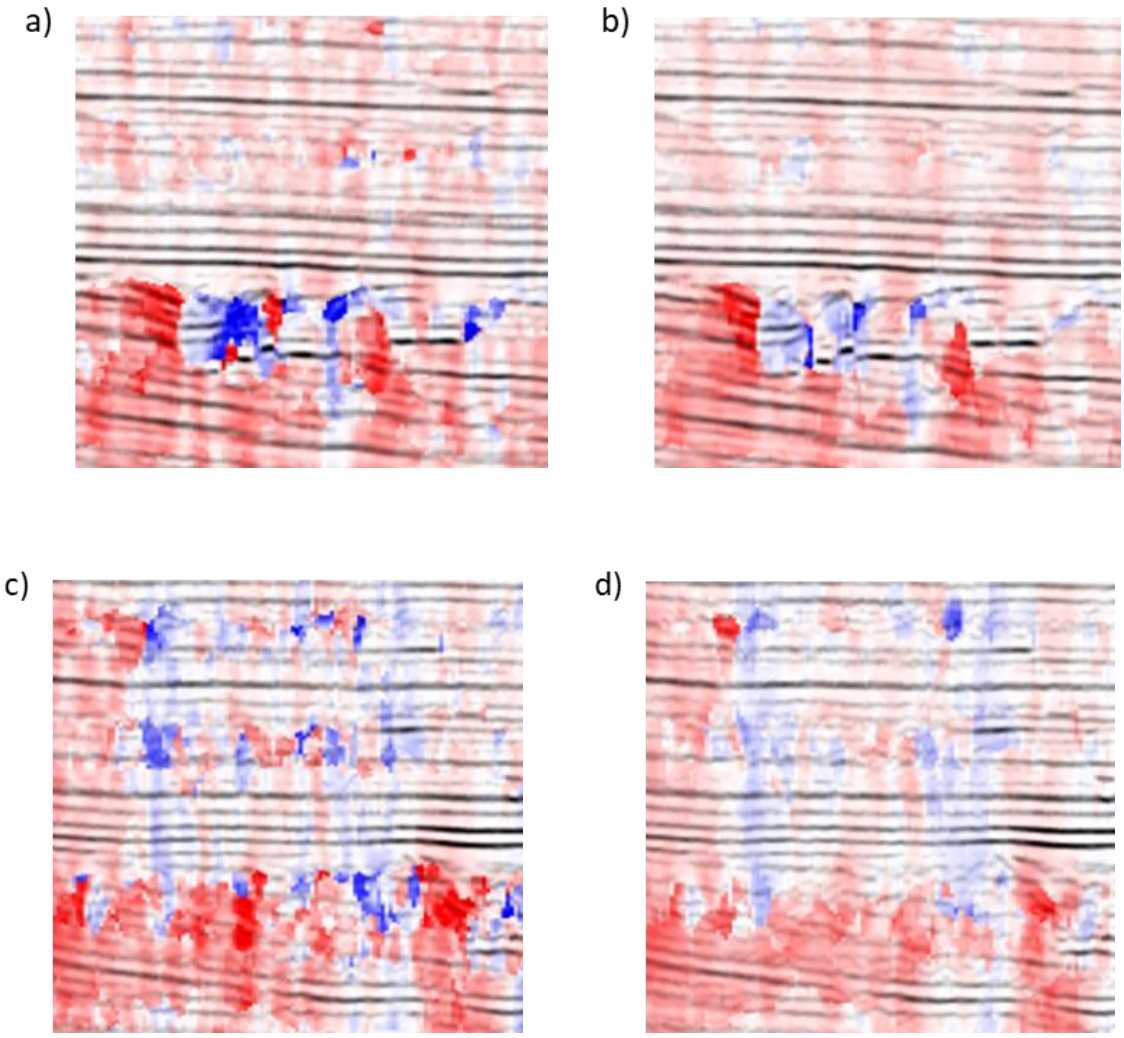

Figure 5.17: Enlarged images of corendered seismic amplitude with the (a) broadband and (b) multispectral crossline dip of the area within the red rectangles shown in the previous figure, and (c) broadband and (d) multispectral crossline dip of the area within the blue rectangles shown in the previous figure. In this Figure, we change the display approach to highlight the dips during the corendering.

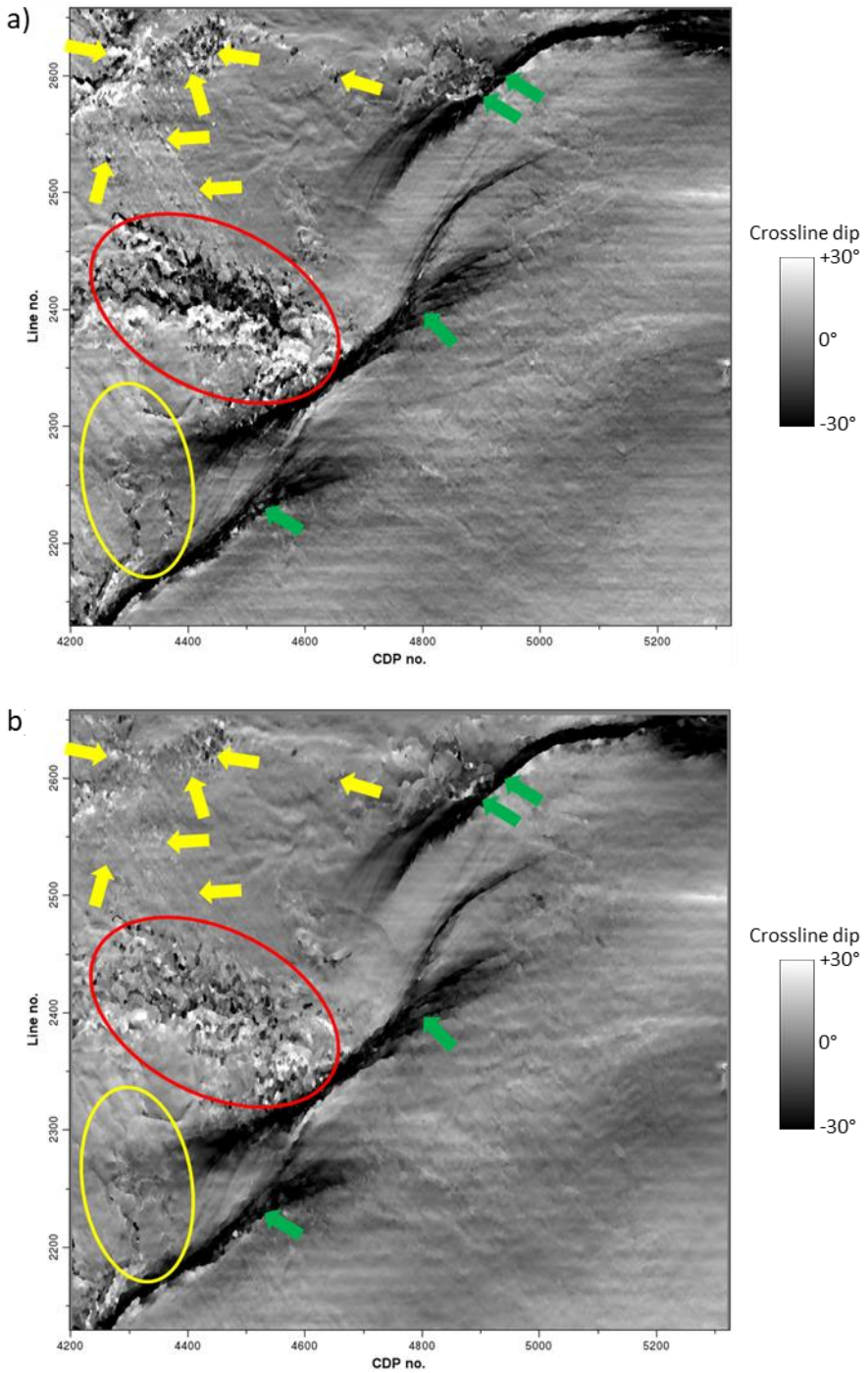

Figure 5.18: Time slices at *t*=1.08s through (a) broadband and (b) multispectral GST crossline dip volumes. Note that the multispectral GST crossline dip appears fewer artifacts (yellow arrows), improved fault continuity (green arrows), and better delineation of channels (yellow ellipses) over to the broadband GST crossline dip image. It is also noted that multispectral GST dip shows fewer artifacts inside the red ellipses, but the thin channels are a little smeared.

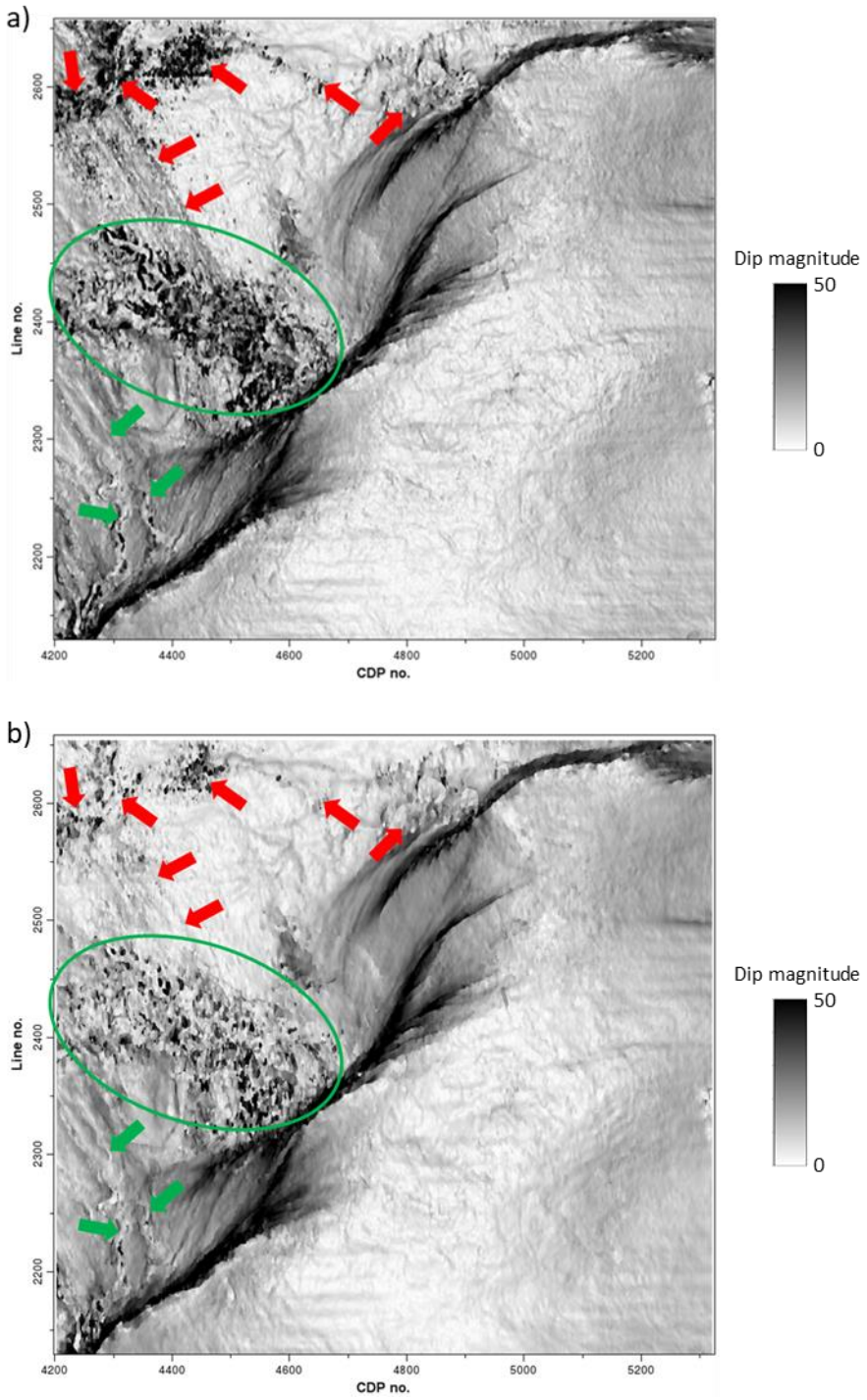

Figure 5.19. Time slices at *t*=1.08 s through the (a) broadband, and (b) multispectral GST dip magnitude volumes. Red arrows indicate zones that exhibit less noise in the multispectral GST dip magnitude volume. The multispectral GST dip magnitude appears more continuous imaging of the fault zone, and provides better delineation of the channel system (green arrows). Note that multispectral GST dip magnitude shows fewer artifacts in the green ellipses, but some thin channels are smeared.

CHAPTER 6: CONCLUSIONS

The primary contribution of this dissertation is that I have developed new passive seismic imaging method and multispectral seismic geometric attributes, which helps relax the limitation of current approaches and provides more effective tools for hydrocarbon exploration.

In passive seismic modeling, where the seismic sources consist of natural or induced microseismic events in the subsurface, in Chapter 2, I construct an iterative full wave-equation algorithm to not only locate the microseismic sources, but also a means to better estimate the subsurface velocity model. The passive source location estimation using GmRTM and the velocity inversion using passive-source FWI are implemented sequentially. The iterations used in the GmRTM algorithm to estimate the source location and the FWI algorithm to estimate the velocity model allow us to better focus the source locations compared to conventional time-reversal imaging method. This workflow not only increases their sensitivity to the subsurface velocities, but also does not need the initial source location for the inversion. Given an improved passive source location and velocity model, I can generate more accurate structural images using passive-source reverse time migration. In the future research, I wish to examine the algorithmic sensitivity to different source wavelets and ignition times, as well as develop a method to minimize cycle-skipping problem in the passive-source full waveform inversion.

3D active source seismic acquisition is the most commonly used geophysical technique to map structure and stratigraphy in the subsurface. First developed 25 years ago, seismic coherence is the most widely used attribute to map faults and stratigraphic edges. However, these edges sometimes fail to appear when similar-looking but stratigraphically different

reflectors align across a fault. In this dissertation, I determine why the recently developed multispectral coherence algorithm better delineates such faults and stratigraphic edges.

In Chapter 3, I study the response of different spectral voices (bandpassed filtered versions of the original seismic data) to a turbidites system in the Teranaki Basin, New Zealand. Because of the manner in which different spectral voice components respond to the tuning thickness of the sometimes thin, sometimes thick architectural elements of the turbidites system, these elements are easier delineated at some frequencies rather than others. I find that by combining the information content provided by exponentially-spaced rather than equally-spaced spectral voices provides superior multispectral coherence images for the same computation cost. I also find that computing multispectral coherence on the spectral voices decomposed using the maximum entropy method provides clearer images and better resolution of thinner channels and small-scale features than other spectral decomposition algorithms.

In Chapter 4, I address gaps in coherence fault images that occur when stratigraphically different reflectors with relatively similar waveforms and amplitudes juxtapose across a fault, and appear to be a locally continuous event. I first improved the signal-to-noise ratio of the seismic amplitude data volume using footprint suppression and structure-oriented filtering. Then I applied the same multispectral coherence workflow parameters obtained in the previous turbidites application and obtained improved fault continuity, filling the coherence gaps caused by the alignment of stratigraphically distinct horizons. Finally, I performed a fault enhancement workflow on the maximum entropy based multispectral coherence to improve the lateral resolution of fault imaging, helping delineate the minor faults.

In Chapter 5, I further illustrate the multispectral GST dip attribute to improve the quality of conventional broadband dip attribute, which is beneficial for the subsequent seismic geometric attributes computation, such as curvature, aberrancy, and reflector rotation. Careful examination on different spectral voices in the 3D field case study showed that the dip estimates computed for the low-frequency and high-frequency spectral voices were contaminated by noise, whereas the middle-frequencies provided good dip images. To further improve the quality of multispectral GST dip attribute, how to enhance the S/N of the low- and high-frequency components and effective analysis approach to select the most appropriate spectral voices in computation remain an interesting research topic.

APPENDIX CHAPTER: TOMOGRAPHIC VELOCITY ANALYSIS AND WAVE EQUATION DEPTH MIGRATION IN AN OVERTHRUST TERRAIN: A CASE STUDY FROM THE TUHA BASIN, CHINA

Abstract

Although the structures associated with overthrust terrains form important targets in many basins, accurately imaging remains challenging. Steep dips and strong lateral velocity variations associated with these complex structures require prestack depth migration instead of simpler time migration. The associated rough topography, coupled with older, more indurated, and thus high velocity rocks near or outcropping at the surface often lead to seismic data that suffer from severe statics problems, strong head waves, and backscattered energy from the shallow section, giving rise to a low signal-to-noise ratio that increase the difficulties in building an accurate velocity model for subsequent depth migration.

We apply a multi-domain cascaded noise attenuation workflow to suppress much of the linear noise. Strong lateral velocity variations occur not only at depth but near the surface as well, distorting the reflections and degrading all deeper images. Conventional elevation corrections followed by refraction statics methods fail in these areas due to poor data quality and the absence of a continuous refracting surface. While a seismically derived tomographic solution provides an improved image, constraining the solution to the near surface depth-domain interval velocities measured along the surface outcrop data provides further improvement. Although a one-way wave equation migration algorithm accounts for the strong lateral velocity variations and complicated structures at depth, modifying the algorithm to account for lateral variation in illumination caused by the irregular topography,

significantly improves the image, preserving the subsurface amplitude variations. We believe our step-by-step workflow of addressing the data quality, velocity model building, and seismic imaging developed for the Tuha Basin of China can be applied to other overthrust plays in other parts of the world.

Introduction

Although the structures associated with overthrust terrains form important targets in many basins, accurate seismic imaging remains challenging. There are often serious lateral velocity variations in overthrust belts, which lead to ray bending, resulting in time migrated seismic images that are poorly focused images and mispositioned reflectors and diffracting edges. Depth migration is required to image complex overthrust structures with strong lateral velocity variations. Unfortunately, the imaging problems are not confined to the deeper structures. Rough topography and outcropped older, high velocity rocks in overthrust belts (Alfonso and Guevara, 2004) often lead to seismic data contaminated by headwaves and coherent backscattered noise resulting in a low signal-to-noise (S/N) ratio and serious statics problems, which complicate the velocity model building process critical to accurate depth migration. Alfonso (2001) identifies three major challenges in overthrust imaging: topography and its correction, the lower signal to noise ratio associated with structure outcropping on the surface, and complex subsurface structures.

Other authors have addressed the rough topography and change in elevation encountered in overthrust belt imaging. Reshef (1991), Gray and Marfurt (1995), and Shragge (2005) found that depth migration directly from topography provided more accurate images compared to those computed from a flat datum after static corrections.

However, the velocity model building difficulty remains, with a key challenge being how to integrate the near surface velocity model computed from refracted waves with the deeper velocity model computed from reflected waves. Static correction plus migration from a floating datum provides a practical, but only partial solution to this difficult problem. Yilmaz (2001) summarizes several static correction solutions, including field statics, refraction statics (Schneider and Kuo, 1985; Taner et al., 1998), and tomostatics (Zhu et al., 1992; Bell et al., 1994; Osypov, 1998). Accurate refraction statics computation requires continuous refractors and good data, but often fails when the data are poor or when the refracting horizons are discontinuous. Overthrust belts exhibit different types of topography, with weathering zone occurring at lower elevations and outcrops at higher elevations, with no continuous refractor running across the entire survey. Such near surface problem cannot be solved well with only one static correction method.

Wang et al. (2012) and others have identified several types of noise common to overthrust belts. Older and more indurated rocks outcrops give rise to high amplitude headwaves, backscattered energy and other linear noise which overprints the reflections of interest. Such noise makes velocity model building much more difficult, as the linear noise masks the reflections in common-image gathers and gives rise to semblance anomalies that may introduce incorrect velocity picks.

Ritchie (2005) and others have noted the significant structural distortion due to severe thrusting or compression in overthrust belts. The structures in these areas are often very complicated and give rise to serious lateral velocity variations. Compared with lower cost Kirchhoff migration and higher cost reverse-time migration, one-way wave equation migration (Claerbout, 1971; Stoffa et al., 1990; Ristow et al., 1994) provides a practical

solution to overthrust imaging, providing the multipathing benefits of a wave equation method but at a reduced cost and somewhat reduced sensitivity to velocity errors than reverse-time migration. While Jiao et al. (2005) have applied this technique to synthetics and Shragge (2005) to field data, one-way wave equation solutions face challenges in accurately accounting for topography and high velocities near the surface overlying slower velocities at depth, thereby filtering out shorter wavelength components representing steeper dips in order to make the algorithm stable.

Constructing an accurate velocity model is key to accurate depth imaging in an overthrust belt. For the areas with relatively simple structures and high S/N ratio data, layer-based coherency inversion (Yilmaz, 2001) or simple conversion of stacking velocities (Dix, 1955) can provide an initial interval velocity model. After constructing the first pass of (approximately flattened) migrated gathers, one can use tomography to update the velocity model (Etgen,1988; Stork, 1992). However, these methods often fail where rocks outcrop at the surface and where the signal-to-noise ratio is low. In this case, geologic information needs to be incorporated as well to build a more accurate depth-domain velocity model.

We begin our paper by building a synthetic wave equation model to better evaluate the quality of the seismic images from the prestack time and depth migration methods. We then introduce the depth imaging workflow to be used in the overthrust belt. Next, we indicate the benefit of tomography in addressing statics issues associated with near surface or outcrop high velocity rocks. We address the signal-to-noise ratio through a multi-domain noise attenuation workflow. We then apply an amplitude-preserved one-way depth migration that compensates for lateral variation in wave illumination. Finally, we integrate

additional velocity information from geologic outcrops to constrain our depth-domain velocity model, thereby improving our images. We conclude with summary comments and recommendations for further analysis.

Time imaging or depth imaging?

Although laterally variable from image point to image point, the velocity model for time migration at a given image point is either constant or a simple gradient of the form $v=v_0+k_z$ such that there is no ray kinking. In contrast, the velocity model for depth migration attempts to approximate the true layer by layer interval velocities with ray bending and kinking at each abrupt change in the velocity-depth model (Gray et al., 2001). In time migration, the imaging velocity model often begins with the RMS velocity computed from unmigrated CMP gathers, which is then scaled to obtain the best focusing at every output location (Gray et al., 2001). Because there are no lateral velocity variations to focus the energy at a given image point, there is no need for explicit ray-tracing, such that time migration is much faster than depth migration. If there are significant lateral velocity variations that give rise to ray bending, time migration not only laterally mispositions a given dipping seismic event, but may separate or overlap adjoining parts of what should be a continuous reflector.

The velocity model used in depth migration is a smoothed representation of the true interval velocity, where for Kirchhoff migration the smoothness is on the order of a wavelength (Gray et al., 2001), but can be less for one-way wave equation and reverse-time migration algorithms. All three of these implementations (ray-based, one-way wav-equation, or hyperbolic two-way wave equation) algorithms accurately bend the rays at each location in the subsurface where the velocity changes, such that depth migration can

image complicated subsurface structures much more accurately than time migration.

In our study, we perform the numerical tests on a land survey with overthrust structures of the Tuha Basin. The survey exhibits both complicated subsurface structures and rugged topography. Figure A.1 shows the geology map and the near surface condition of our survey. There are plenty of faults and steeping dipping reflectors which lead to complex structures (Figure A.1a). There is significant variation in the near surface of our survey (Figure A.1b), including the relatively flat Gobi Desert covered with coarse gravels, a mountain front transition zone, and a mountain area with high velocity carboniferous rocks. The elevation of the survey varies from 500 m to 1700 m above sea level.

While some pitfalls of the time migration such as velocity pull up/push down (e.g. Fagin, 1996) are well known to interpreters working on overthrust terrains, we reveal these phenomena by constructing the model shown in Figure A.2b based on the depth-domain structural interpretation (Figure A.2a) of a typical line in the overthrust belt shown in Figure A.1. There are a shallow overthrust structure and some underlying faults in the model. We then generate a suite of common shot synthetics using a 2D finite difference scalar wave equation algorithm. The time processing steps prior to migration are similar with those applied to the field data. Figures A.2c and A.2d show the resulting prestack time- and depth-migrated images. Note the improved fidelity of the depth-migrated image compared to the true model. Faults are accurately imaged to their correct location in depth migration but are distorted and mispositioned by time migration. There are strong fault shadow effects on the deepest two reflectors (yellow arrows) in the prestack time migration image, which is caused by the rapidly varying lateral velocity contrast across the dipping faults. These reflections are non-hyperbolic around the faults, resulting in weak time-migrated images.

It is difficult to image these dipping fault zones with prestack time migration (Figure A.2c), due to its inability to handle lateral velocity variations. The fault-plane reflection is also mispositioned with prestack time migration (blue arrows). In contrast, prestack depth migration images these fault zones much better (Figure A.2d). There are fewer migration artifacts in depth imaging, with the pull-up artifacts removed. Multiples are more coherent, but easier to identify as being multiples on the prestack time-migrated volume, indicated by the red arrows in Figure A.2c. On the depth migrated data, the multiples are weaker, but are no longer periodic, and may be misidentified as primaries on the prestack depth-migrated data volume (red arrow in Figure A.2d).

The primary processing steps of the workflow are shown in Figure A.3. Other steps, such as geometry definition, first break picking, muting, and velocity picking also affect the imaging quality. There are four key steps for depth imaging in the overthrust belt: static corrections, noise attenuation, the prestack depth migration algorithm, and the depth-domain velocity model building. Each will be discussed in detail in the following sub-sections.

Computing the near surface velocity model

Properly accounting for elevation and weathering zone effects is critical for land processing (Yilmaz, 2001), and is more challenging in areas with rough topography, such as in overthrust terrains. The Tuha Basin expresses variable topography including flat plains and desert, the mountain front, and the mountains themselves. In most land surveys, the seismic data are recorded by geophones deployed on the surface of a low velocity weathering zone. Energy impinging the base of the weathering zone at shallow angles are refracted towards the normal, which for relatively flat topography and weathering zones,

towards the vertical, such that the weathering zone correction can be approximated by a vertical (static) shift of the seismic trace. In the case of rough topography, the surface and the base of the weathering zone may not be flat. In some cases, such as in the Tuha Basin overthrust belt, there is no weathering zone at all, but rather the folded rocks outcrop at the surface. In this case, there is no bending of ray paths towards the vertical as they approach the surface. Tanner et al. (1974) shows that correcting these measurements to a flat datum requires a "dynamic" rather than a "static" correction, whereby each reflection event needs to be corrected to the data by its angle of incidence back to the datum along the ray path, rather than vertically. Reshef (1991), Gray and Marfurt (1995) and Shragge (2005) showed that migration directly from topography implicitly computes such a dynamic correction, providing significantly more accurate images than the migration of data previously corrected to a flat datum using static corrections.

While migration from topography has been available for decades, estimating an accurate velocity in the low-fold shallow section is still difficult in the Tuha Basin survey, refraction statics velocity analysis based on smooth, continuous refractors fails. Furthermore, the velocity field estimated from shallow refractions and that estimated from deeper reflections have different scales, making their integration into a unified velocity-depth model difficult.

Rough topography can be considered to have low-frequency and high-frequency components. The floating datum represents the low-frequency component, which could also be considered to be a smoothed version of topography. For the Tuha Basin overthrust data, we use a two-step correction: first, we correct the high-frequency component to a floating data, followed by migration from the floating datum. By this, the inaccurate

vertical correction to a flat datum is minimized, while the data can be regularized to a grid where the one-way wave equation solutions can operate.

Yilmaz (2001) summarizes several different static correction methods to correct the high-frequency component of topography, including field statics, refraction statics (Schneider and Kuo, 1985; Taner et al., 1998), and tomostatics (Zhu et al., 1992; Bell et al., 1994; Osypov, 1998). Refraction statics works well for continuous refractors and good quality data but may fail in the presence of discontinuous refractors and poor quality data.

The Tuha Basin overthrust belt is represented by significant lateral variations in the near surface structures. In our research area, the near surface changes from Gobi Desert through a mountain front transition zone, followed by the mountain outcrop area (Figure A.1b). Figure A.4 shows the near surface model of the line in Figure A.2a, which is built using a tomographic method. The elevations vary from 500 m to 1700 m above sea level. The Gobi Desert (blue arrow) is relatively flat with small elevation variations. In the mountain front transition zone (red arrow), the elevation variation become larger, but there is still a stable refraction layer. The mountain outcrop area (orange arrow) exhibits serious lateral variations, and there are no stable refraction layers.

Given these heterogeneity, no single static correction technique works for the entire line. We illustrate our hybrid static correction workflow using a representative line drawn from the survey shown in Figure A.5. Three different static correction methods, including field statics, refraction statics and tomostatics, are used for numerical tests. Figure A.5a, A.5d and A.5g show the imaging results in the Gobi Desert area after static correction with these three different methods. In this area, the topographic variation is relatively small and there are abundant micro logging and shallow refraction data in our survey, resulting in an

accurate image using the conventional field static correction method (Figure 5a).

The comparative results for the mountain front transition belt are indicated in Figure A.5b, A.5e and A.5h. There are stable refraction layers (Figure A.4) in this area and the data quality is relatively high, which satisfy the requirement of the refraction method. The resulting image using refraction statics (Figure A.5e) is better those using the other two methods (Figure A.5b, A.5h).

Figure A.5c, A.5f and A.5i show the three results in the mountain area with outcropped structures. Refraction layers are absent and data quality is relatively poor. In this area, the refraction method fails to produce a good image (Figure A.5f). In contrast, a tomographic solution provides a significantly improved image (Figure A.5i) over the two other methods.

Because tomographic statics provides a more continuous shallow reflector (yellow arrow) and higher resolution deeper reflector (orange arrow), and refraction statics provides a more continuous reflector at depth for the mountain front example (red arrow), and field statics provides more continuous reflectors in the Gobi Desert example (blue arrow), we construct a hybrid method that use each static correction where they work best. We integrate the three solutions using co-kriging interpolation to obtain an optimum static correction spanning the different types of topography.

Multi-domain seismic noise attenuation

Wang et al. (2012) reported that land surveys acquired over overthrust structures such as those of the Tuha Basin are contaminated by multiple types of noise including backscattered ground roll and high velocity shallow refractions. The signal-to-noise ratio is exacerbated when older, more indurated rocks outcrop, giving rise to high velocity,

poorly attenuated ground roll and high amplitude headwaves that exhibit similar velocities to the vertically traveling reflections. If aliased, such noise overprints subsequent depth imaging with artifacts, masking reflections and diffractions of interest (Marfurt and Duquet, 1999). When stronger than the reflections, the noise renders velocity analysis more difficult and prone to event mispicks, resulting in an inaccurate velocity-depth model.

For the Tuha Basin survey discussed here, noise could not be adequately suppressed in either the common midpoint or common shot domain. For this reason, we follow the workflow described by Vermeer (1991) that suggests cascaded filtering, first in the common shot domain (which allows suppression of noise radiating away from the shot) followed by the common receiver domain (which allows suppression radiating towards the receivers). The latter noise trains include not just remnants of the previously suppressed shot to receiver ground roll and headwaves, but also backscattered energy from surface topography and irregular weathering zones.

Figure A.6a shows a representative common shot gather where strong linear noise masks the underlying signal. This noise leaks through the stack array indicated by the yellow arrows in Figure 6e. In our research, the linear noise is suppressed with an *f-k* filtering method (Yilmaz, 1987; Zhou and Greenhalgh, 1994). The linear event function u in the *t-x* domain can be expressed as

$$u(x,t) = s(t) * \delta(t - x\tan(\alpha) + b)$$

where $s(t)$ is a band-limited wavelet, b is the intercept of the linear event on t axis, and α is the angle between the linear event and x axis. We transform the input seismic data $u(x,t)$ from the *t-x* domain to the *f-k* domain :

$$U(k,\omega) = S(\omega)\exp(i\omega b)\delta(k - \omega\tan(\alpha)) = S(\omega)\exp(i\omega b)\delta(\omega - k\cos(\alpha))$$

where $U(k,\omega)$ and $S(\omega)$ are the Fourier transform of $u(x,t)$ and $s(t)$. The linear noise will be suppressed according to their dips in the *f-k* domain. Figure A.6b shows the same shot gather after linear noise attenuation using the *f-k* filter. Although there is little noise on the resulting gather, after stack the linear noise reappears indicated by orange arrows in Figure A.6f. Resorting the *f-k* filtered common shot gathers to common receiver gathers shows that significant linear noise remains (Figure A.6c). Application of a second pass of *f-k* filtering in the common receiver domain suppress this noise component (Figure A.6d). Two passes of *f-k* filtering, first in the common shot and then in common receiver domain results in the stacked section shown in Figure A.6g where one sees that the cascaded filter significantly reduces the noise in the stack, allowing the reflectors to show through.

Figure A.7 shows how multi-step linear noise attenuation works. There are several families of linear noise events, each with a different velocity seen on the raw common shot gather (Figure A.7a). The linear noise with low and high velocities exhibit different amplitudes. In principle, if one can identify all noise events, one can suppress them simultaneously in the *f-k* domain. In practice, this is difficult, with high amplitude noise masking the low amplitude noise. We therefore apply an *f-k* filter to suppress the stronger low velocity linear noise indicated by the yellow arrows (Figure A.7b) first. Next, we applied a second *f-k* filter to suppress the higher velocity noise indicated by the blue arrows (Figure A.7c). While the high velocity linear events are effectively suppressed, aliased components of the low velocity events, including ground roll (red arrows), have leaked through the filter. These remnant “shingled” events indicated by the green arrow exhibit a high apparent velocity and will be migrated as “signal” into the final image, damaging the overall signal-to-noise ratio and interpretability of the section.

Wave equation depth migration with illumination compensation

Etgen et al. (2009) divide depth migration into ray-based and wave equation-based methods. Kirchhoff depth migration (Schneider,1978; Bleistein,1987) is the most popular ray-based method and still plays an important role in seismic imaging and migration velocity model building. Ray theory, and therefore Kirchhoff depth migration is based on a high frequency approximation, where the seismic wavelength is much shorter than the scale of velocity changes. One can either sum events in depth along diffraction traveltime curves or distribute events along deformed ellipsoids to generate an output image. Because Kirchhoff depth migration is based on a high frequency, asymptotic solution of wave equation, it does not accurately account for low frequency phenomena such as geometric scattering and dispersion, caustics, and tunneling in the downgoing and upcoming ray paths. A larger limitation is due to implementation rather than theory. For reasons of algorithmic complexity, most software allows only a single ray path, and hence computes only one traveltime, to represent the path from a surface source or receiver to the subsurface image point. Nevertheless, Kirchhoff depth migration has several benefits. First, compared to wave equation methods, the computation cost of Kirchhoff depth migration is less, comprising precomputation of a suite of traveltime tables which can be generated either by a simple ray shooting method, wavefront extrapolation, or finite-differences solutions of the Eikonal equation, followed by summation of the data along the two-way traveltime curves. Second, Kirchhoff depth migration has great flexibility. One can migrate directly from topography and limit the output to a subset number of laterally or vertically targeted subset of the earth. This latter capability is critical for migration velocity model building, where one wishes to iterate only those parts of the model that need velocity updating. While

the ability to image sources and receivers where they are deployed is an advantage, it is also a disadvantage if the processor naively ignores operator aliasing resulting in artifacts overprinting reflectors of interest (Gray et al., 2001).

In contrast, wave equation depth migration algorithms implicitly include multipathing between any surface location and the image point of interest. Imaging through caustics and through more rugose interfaces requires no extra software; rather wave phenomena are implicitly accounted for. Wave equation solutions require the data to be resampled on a regular grid, typically with constant "receiver" spacing, requiring premigration data sampling and interpolation. This extra layer of complexity forces the processor to deal directly with the seismic aliasing problem that may be overlooked when using the more flexible Kirchhoff depth migration algorithm.

Wave equation migration includes one-way and two-way methods. The two-way RTM (reverse-time migration) method (Hemon, 1978; Baysal et al., 1983; McMechan, 1983; Whitmore, 1983) is based on the full two-way wave equation solution, rather than on an asymptotic solution, which leads to higher imaging precision compared with other migration methods. However, it is much more time-consuming, requires greater computer memory, and it exhibits greater sensitivity to velocity errors compared with other depth migration methods (Shan et al., 2008). In contrast, the computationally more efficient one-way wave equation depth migration method (Claerbout, 1971; Stoffa et al., 1990; Ristow et al., 1994) has the advantages of multipathing and imaging through caustics of a wave equation solution, but at cost that allows for multiple iterations to determine the final velocity. In one-way wave equation depth migration, the full wavefield is divided into a downgoing wavefield and an upgoing wavefield. These two wavefields are extrapolated

downward in depth rather than forwards and backwards in time as in RTM, thereby reducing the computer storage requirements to the solution the current and next depth level. The accuracy of the one-way wave equation depth migration falls between that of Kirchhoff depth migration and RTM. The one-way wave equation accounts for multiple paths, so long as they are going in the direction of wavefield extrapolation, and exhibits a lower sensitivity to velocity errors than RTM.

The key challenges of wave equation depth migration on land data include data regularization, amplitude preservation, and velocity model building. Seismic data from land surveys sometimes are not well sampled in different domains, with shot spacing often coarser than receiver group spacing. Prestack seismic gathers often exhibit “holes” due to surface “obstacles”, which add additional artifacts to the subsurface image. In our research, seismic data regularization is carefully handled before migration in the F-X domain (Spitz, 1991). In this paper, we mainly focus on amplitude preservation and depth-domain velocity model building.

Older, more indurated rocks outcropping at or near the surface in overthrust terrains may have significantly higher velocities than the underlying strata. Unless they have flat interfaces, waves propagating through these zones may be strongly refracted away from the deeper target, leading to irregular subsurface illumination, giving rise to lateral changes in amplitude. After correction for spherical spreading and surface consistent amplitude corrections, we follow Zhang et al. (2005) and add amplitude recovery terms to the one-way wave equation depth migration algorithm that compensate for the lateral variation of illumination in depth. Figure 8 shows the comparison of different depth migration methods on the synthetic data previously shown in Figure A.2. Low frequency artifacts creep into

the Kirchhoff depth migrated image indicated by yellow arrows in Figure A.8a, but are largely suppressed in the one-way wave equation image (Figure A.8b). The underlying reflectors are poorly imaged due to the overlying high velocity structures in the Kirchhoff migration (Figure A.8a), but are well imaged by the one-way wave equation migration, indicated by the red arrow (Figure A.8b). The amplitude-preserving algorithm (Figure A.8c) more accurately represents the correct amplitude, especially for the deep reflectors indicated by the green arrow.

Figure A.9 shows the prestack depth migration workflow in the overthrust belt, including the tomographic velocity updating procedure. Migration aperture plays an important role in depth migration, especially for the structures with steeply dipping reflectors and faults, such as overthrust structures. A much larger migration aperture is needed to image steep reflectors than flat reflectors. The larger migration aperture makes prestack depth migration more time-consuming. The migration aperture (14 km) used in the survey shown in Figure A.9 is much larger than the maximum source-receiver offset of 5.5 km, in order to image the steeply dipping structures. Figure A.10 compares images from three different prestack depth migration methods, including Kirchhoff (Figure A.10a), one-way wave equation (Figure A.10b), and amplitude-preserved one-way wave equation (Figure A.10c). The underlying faults are better imaged by the one-way wave equation migration (Figure A.10b, A.10c) indicated by the red circle and arrow. The amplitude-preserving algorithm further compensates the imaging energy of the deep reflectors.

Depth-domain velocity model building

Gray et al., (2001) report that if the velocity is correct and gives rise to ray bending, depth migration provides superior images than time migration. In contrast, if the velocity

model is inaccurate, time migration may provide a more focused (though laterally mispositioned) subsurface image.

For the Tuha Basin survey, the shallowest component of the velocity model uses the previously described co-kriging static correction to a floating datum. The reflection events are then used to construct the velocity model below the floating datum.

For the areas of the survey with relatively simple structures, no outcrops, and a high S/N ratio, an initial model based on layer-based coherency inversion (Yilmaz, 2001) works well. This initial model is then updated using tomography of the migrated gathers, iterating until the residual moveout approaches zero (i.e. the events are "flat"). The tomographic velocity updating workflow is included in Figure A.9. In this study, we use a layer-based tomography method. Figure A.11 shows the results of this workflow from the Gobi Desert area of the Tuha Basin survey. The shallower part of Figure A.11a shows the interpretation of a prestack time migrated result, exhibiting relatively simple structures and high data quality. The deeper part of Figure A.11a was computed using coherency inversion, focusing the area interpreted by the light blue horizon. This workflow provides a good initial velocity model with few artifacts. Figure A.11b shows the residual about the light blue layer horizon before tomography. After three iterations using the tomography method, the residual is better focused, converging towards zero, which is shown in Figure A.11c. In Figure A.12, we show the depth-domain common-image gathers located at x=14.0 km on Figure A.10. The reflections are overcorrected on the common-image gather without tomography, and there are obvious vertical residuals (Figure A.12a). After tomography iterations, the reflections are aligned along the offset axis on the common-image gather and the vertical residuals are almost zero (Figure A.12b).

There are plenty of faults and steeply dipping reflectors in our research survey, as shown in a representative geologic model in Figure A.13. The underlying structures (orange arrow) are important exploration targets in Tuha Basin. However, the imaging of these structures is difficult due to the overlying outcropped rocks with very high velocities. Depth-domain interval velocity model building is critical for the imaging of these structures. Due to the complexity in these areas, the workflow for velocity model building in Figure A.9 fails. The deeper part of Figure A.14a shows the coherency inversion result of one layer in the overlying outcropped area. It is chaotic, making it difficult to pick accurate initial velocities. The simpler conversion of RMS stacking velocities to interval velocities also fails. If the initial velocity model is too far from the correct velocity, the tomographic velocity updating workflow also fails.

Coherency inversion indicates three candidate velocity ranges. The lowest range is tightly clustered around 2000 m/s. We consider this velocity to be unreasonably low for the older rocks in the Tuha Basin. Figure A.14a shows the velocity model built with the middle range of velocities, without any geologic constraints. However, Figure A.14b shows that the corresponding depth migration is of poor quality with crossing events, even after several iterations of tomography. The overlying outcropped rocks in Figure A.13 were measured directly and found to exhibit a very high velocity around 5000 m/s. Based on this outcrop analysis, we choose the highest range of velocities to be the initial velocity model. After several tomographic iterations (Figure A.14c), we obtain an improved, better focused subsurface image (Figure A.14d). Black arrows indicate better illuminated shallow, steeply dipping reflectors. The green arrow indicates a suite of previously poorly illuminated horizontal reflectors. The blue arrow shows that the shallow high velocity part of the model

significantly changes the depth and structural orientation of the deeper anticlinal target.

With the workflow presented in this paper, we evaluate the prestack depth migration result in our research survey. Figure A.15 shows the comparison of prestack time and depth migration. The prestack time migration image (Figure A.15a) is displayed in time and the prestack depth migration image (Figure A.15b) in depth. Note the superior quality of depth-migrated (Figure A.15b) compared to time-migrated result (Figure A.15a). Specifically, depth migration (Figure A.15b) better images the faults and the steeply dipping strata more clearly than time migration. There are also fewer migration artifacts (unfocused ellipses) in the depth imaging result. Examining differences in the strata underneath the overthrust structure, the time migration shows them dipping up to the right (Figure A.15a), while the depth migration shows them dipping down to the right (Figure A.15b). This velocity pull-up pitfall is common in time imaging beneath high velocity overlying structures.

Conclusions

Imaging overthrust geologic structures is difficult for several reasons. First, overthrust terrains exhibit high lateral variations in velocity, requiring depth migration, and in turn an accurate velocity-depth model. Second, this lateral variation in geology occurs near the surface as well as at depth; the shallow section is often poorly illuminated, potentially resulting in erroneous estimates of the shallow velocity, thereby degrading all deeper images. In our example, we found that incorporating outcrop measurements provided a more accurate velocity-depth model and better subsurface images. Third, because older, more indurated rocks may lie near the surface, the seismic data may be contaminated by high amplitude headwaves and other linear noise. Cascaded linear noise attenuation performed first on common shot and then on common receiver gathers effectively

suppresses much of this noise but leaves aliased low velocity components in the filtered images. These aliased components have shallow apparent dip and will overprint the subsequent migrated image. Overthrust terrains can exhibit rugose topography. We find that tomographic statics solutions provide significantly improved images over simple elevation corrections and conventional refraction statics solutions in the mountain area. Finally, tomographic velocity updating provides improved images over simpler residual velocity analysis techniques. The numerical tests on the synthetic overthrust model data and the field data in Tuha Basin indicate that this paper's method could provide high-quality seismic images for the overthrust structures.

In summary, there is no simple solution to imaging overthrust geology. Appropriate modification and significant care at each step of the processing and imaging workflow to account for these particularly challenging imaging problem is necessary.

Acknowledgements

The authors would thank the sponsors of the Attribute-Assisted Seismic Processing and Interpretation (AASPI) consortium in the University of Oklahoma. We would thank PetroChina Research Institute of Petroleum Exploration & Development-Northwest (NWGI) for permission to publish these results and their commercial licenses of Paradigm's GeoDepth and WesternGeco Omega processing softwares. We would also thank the three reviewers whose comments helped improve and clarify this paper.

References

Alfonso, H., and Guevara S., 2004, Imaging over complex structures-Colombian Andes Case. 74th Annual International Meeting, SEG, Expanded Abstracts, 486-489.

Alfonso, H., 2001. Seismic imaging and analysis over Colombian foothills, ACIPET.

Baysal, E., D. D. Kosloff, and J. W. C. Sherwood, 1983, Reverse-time migration: Geophysics, 48, 1514-1524.

Bell, M. L., Lara, R., and Gray, W. C., 1994, Application of turning-ray tomography to the offshore Mississippi delta: 64th Annual International Meeting, SEG, Expanded Abstracts, 1509-1512.

Bleistein, N., 1987, On the imaging of reflectors in the earth: Geophysics, 52, 931-942.

Claerbout, J., 1971, Toward a unified theory of reflector mapping: Geophysics, 36, 467-481.

Dix, C. H., 1955, Seismic velocities from surface measurements: Geophysics, 20, 68-86.

Etgen, J., S. H. Gray, and Y. Zhang, 2009, An overview of depth imaging in exploration geophysics: Geophysics, 74, no. 6, WCA5-WCA17.

Etgen, J., 1988, Velocity analysis using prestack depth migration: linear theory. 58th Annual International Meeting, SEG, Expanded Abstracts, 909-912.

Fagin, S., 1996, The fault shadow problem: Its nature and elimination: The Leading Edge, 15, 1005-1013.

Gray, S. H., J. Etgen, J. Dellinger, and D. Whitmore, 2001, Seismic migration problems and solutions: Geophysics, 66, 1622-1640.

Gray S. H., and Marfurt K. J., 1995, Migration from topography: Improving the near-surface image: Can. J. Expl. Geophysics, 31, 18-24.

Hémon, C., 1978, Equations d'onde et modèles, Geophysical Prospecting, 26, 790-821.

Jiao J., Trickett S., and Link B., 2004, Wave equation Migration of Land Data: CSEG national convention.

Marfurt, K. J., and Duquet, B., 1999, Mapping prestack depth migrated coherent signal and noise events back to the original time gathers using Fermat's principle: Geophysics, 64, 934-941.

McMechan, G. A., 1983, Migration by extrapolation of time-dependent boundary values: Geophysical Prospecting, 31, 413-420.

Osypov, K., 1998, A comparative study between 3-D diving-wave tomography and head-wave refraction methods: 68th Annual International Meeting, SEG, Expanded Abstracts, 1222-1225.

Ritchie, W., M. Popovici, M. Fleidner, and C. Saxon, 2005, Challenges and Opportunities in Pre-Stack Depth Imaging of Legacy Seismic Data: an Overthrust Belt Case Study, 75th Annual International Meeting, SEG, Expanded Abstracts, 400-404.

Reshef M., 1991, Depth migration from irregular surfaces with depth extrapolation methods: Geophysics, 56, 119-122.

Ristow, D., and T. Ruhl, 1994, Fourier finite-difference migration: Geophysics, 59, 1882-1893.

Shan, G., L. Zhang, Y. Wang, T. Nemeth, and W. Liu, 2008, Velocity Sensitivity of Reverse-time Migration: 78th Annual International Meeting, SEG, Expanded Abstracts, 2321-2325.

Schneider, W. A., 1978, Integral formulation for migration in two and three dimensions: Geophysics, 43, 49-76.

Schneider, W. A., and Kuo, S., 1985, Refraction modeling for static corrections: 55th Annual International Meeting, SEG, Expanded Abstracts, 295-299.

Shragge J., 2005, Wave equation migration from topography: Imaging Husky: Stanford Exploration Project, Report 123, 49-56.

Spitz, S., 1991, Seismic trace interpolation in the F-X domain: Geophysics, 56, 785-794.

Stoffa, P. L., J. T. Fokkema, R. M. de Luna Freire, and W. P. Kessinger, 1990, Split-step Fourier migration: Geophysics, 55, 410-421.

Stork, C., 1992, Reflection tomography in the postmigrated domain: Geophysics, 57, 680-692.

Taner, M. T., Wagner, D. E., Baysal, E., and Lu, L., 1998, A unified method for 2-D and 3-D refraction statics: Geophysics, 63, 260-274.

Taner, M. T., Koehler, F., and Alhilali, K. A., 1974, Estimation in correction of near-surface time anomaly: Geophysics, 39, 441-463.

Vermeer, G., 1991, Symmetric sampling: The Leading Edge, 10(11), 21-27.

Wang, X., Y. Wang, X. Wang, W. Liu, Q. Su, B. Lyu, Y. Tian, 2012, Methods and Application for Relative Fidelity Processing of Seismic Data: Petroleum Industry Express (in Chinese).

Whitmore, D. N., 1983, Iterative depth imaging by back time propagation: 53rd Annual International Meeting, SEG, Expanded Abstracts, 382-386.

Yilmaz, O., 1987, Seismic data processing: Society Exploration Geophysics.

Yilmaz, O., 2001, Seismic Data Analysis: Society Exploration Geophysics, Tulsa.

Zhang, Y., G. Zhang, and N. Bleistein, 2005, Theory of true amplitude one-way wave equations and true amplitude common-shot migration: Geophysics, 70, no. 4, E1-10.

Zhou, B., and S. A. Greenhalgh, 1994, Wave-equation extrapolation-based multiple attenuation: 2-D filtering in the f-k domain: Geophysics, 59, 1377–1391.

Zhu, X., D. P. Sixta, and B. G. Angstman, 1992, Tomostatics: Turning-ray tomography + static correction: The Leading Edge, 11, 15-23.

Appendix chapter figures

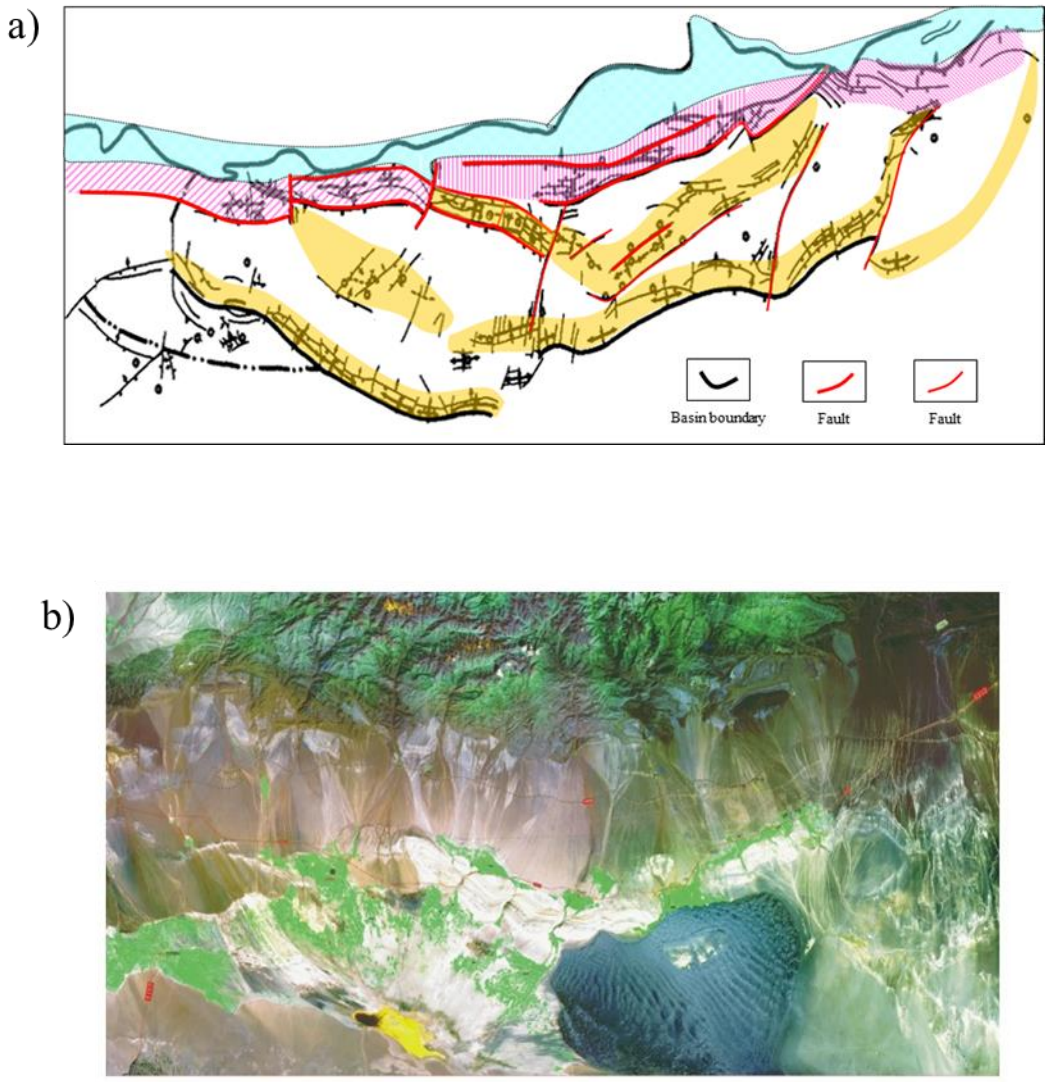

Figure A.1. The geology map (a) and surface condition (b) of our research survey in the overthrust belt of Tuha Basin, China. (after Wang et al., 2012).

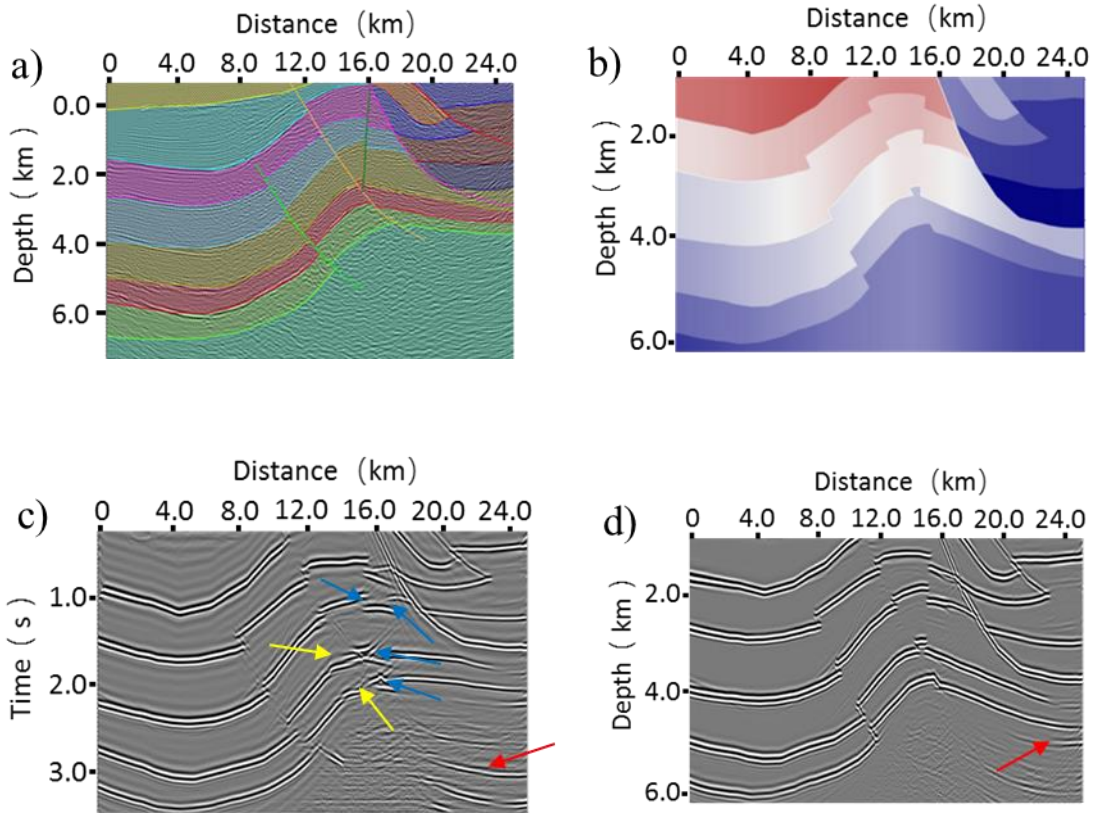

Figure A.2. A synthetic model built from the image of Tuha Basin to quantify any limits in imaging the overthrust structures. (a) Depth-domain structural interpretation of a typical line of our research survey. (b) Velocity-depth model used to generate acoustic wave equation synthetic shot gathers using a finite-difference algorithm. Resulting images from (c) prestack time migration, and (d) prestack depth migration. Note the strong fault shadow effects on the deepest two reflectors (yellow arrows) on the prestack time migration. Prestack depth migration could image these fault zones much better. The fault-plane reflection is also mispositioned with prestack time migration (blue arrows). There are less migration artifacts in depth imaging, and the pull-up pitfall is also removed in depth imaging. In contrast, the multiples are more coherent, but easier to identify as being multiples on the prestack time-migrated volume. While the multiples are weaker, but may be misidentified as being structures on the prestack depth-migrated data volume (red arrows).

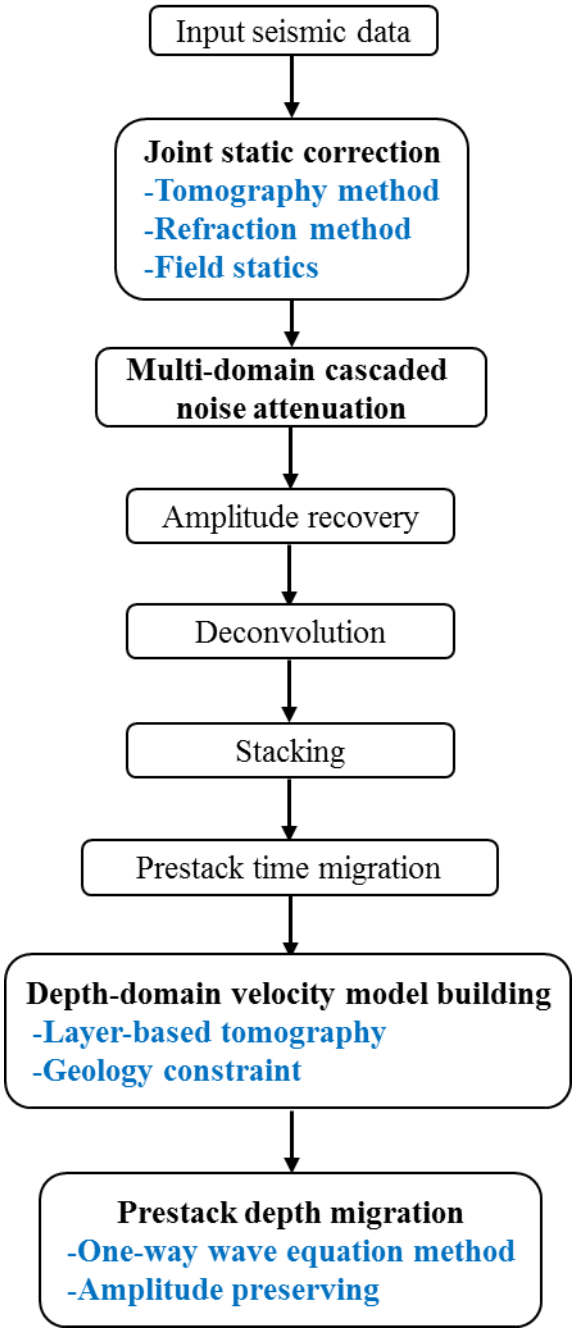

Figure A.3. The seismic processing workflow in the overthrust belt indicate the four key steps for seismic imaging in the overthrust belt, including static correction, noise attenuation, prestack depth migration algorithm, and depth-domain velocity model building.

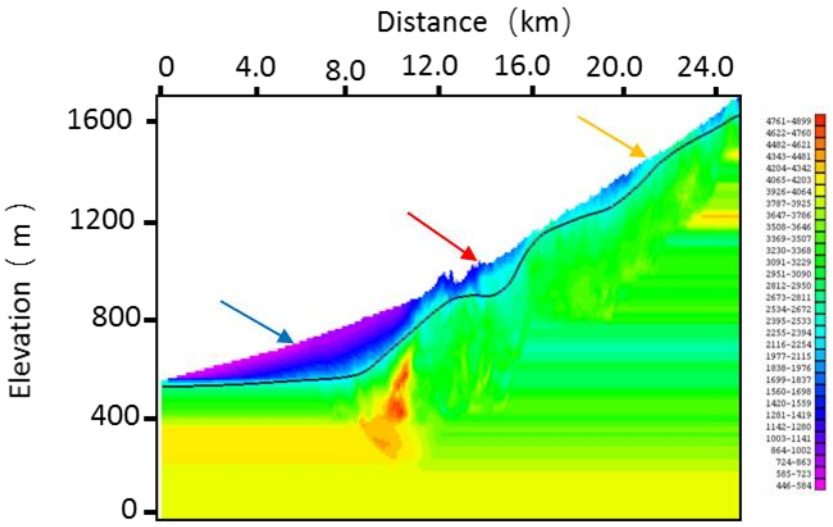

Figure A.4. The near surface model built with tomography method shows that the elevations vary from 500 m to 1700 m above sea level. The Gobi Desert (blue arrow) is relatively flat with small elevation variations. In the mountain front transition zone (red arrow), the elevation variation become larger, but there is still stable refraction layer. However, the mountain outcrop area (orange arrow) exhibits serious lateral variations, and there are not stable refraction layers.

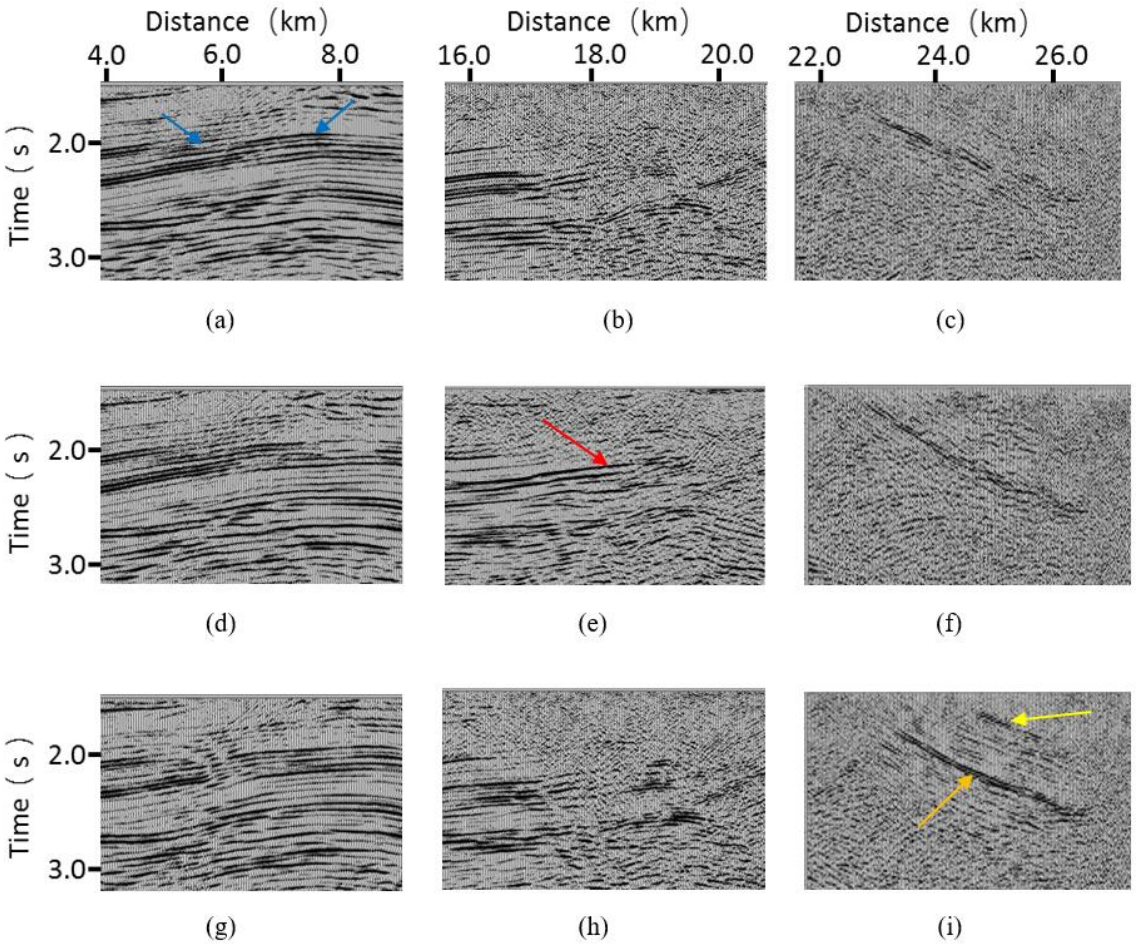

Figure A.5. The effect of alternative statics solutions on the final depth-migrated images for the overthrust belt, Gobi Desert, and mountain front field data examples. Tomographic statics provides a more continuous shallow reflector (yellow arrow) and higher resolution deeper reflector (orange arrow) than the other two solutions for the overthrust belt. Refraction statics provides a more continuous reflector at depth for the mountain front example (red arrow). In contrast, field statics provides more continuous reflectors in the Gobi Desert example (blue arrow).

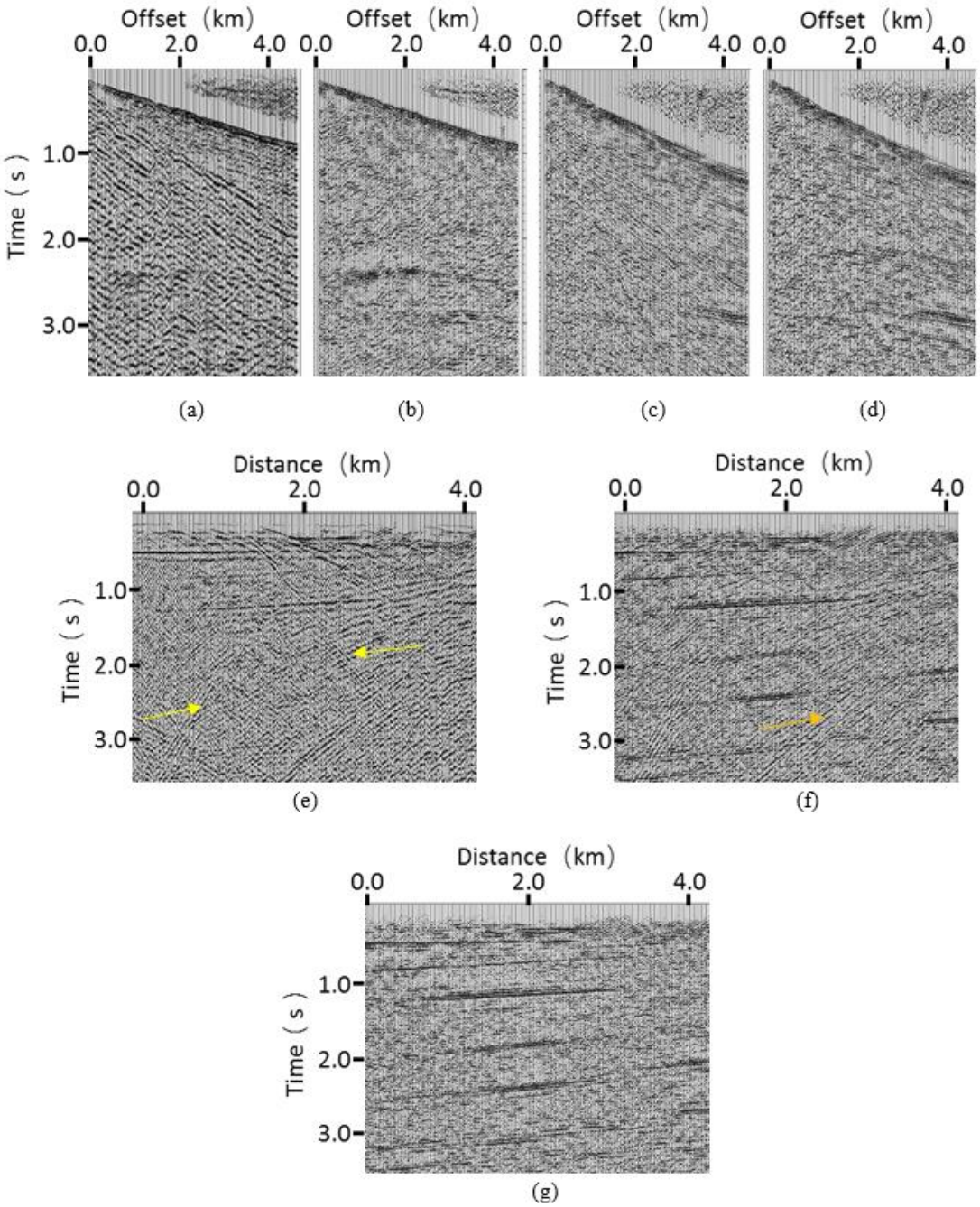

Figure A.6. The results of multi-dimensional suppression of linear noise in the overthrust example. A representative common shot gather (a) before and (b) after linear noise attenuation. (c) The rejected linear noise reappears when sorting the previously filtered data into common receiver gathers. (d) The same common receiver gathers shown in (c) after a second pass of linear noise attenuation on common receiver gathers. Stacked images of (e) the original unfiltered data, (f) after linear noise suppression only in the common shot domain, and (g) after linear noise suppression in both the common shot and common receiver domain. Note the linear noise in both directions leaks through the stack array (yellow arrows). While it is suppressed, linear noise still leaks through after filtering common shot gathers (orange arrow). Sequential filtering of common shot followed by common receiver gathers significantly reduces the noise in the stack shown in (g).

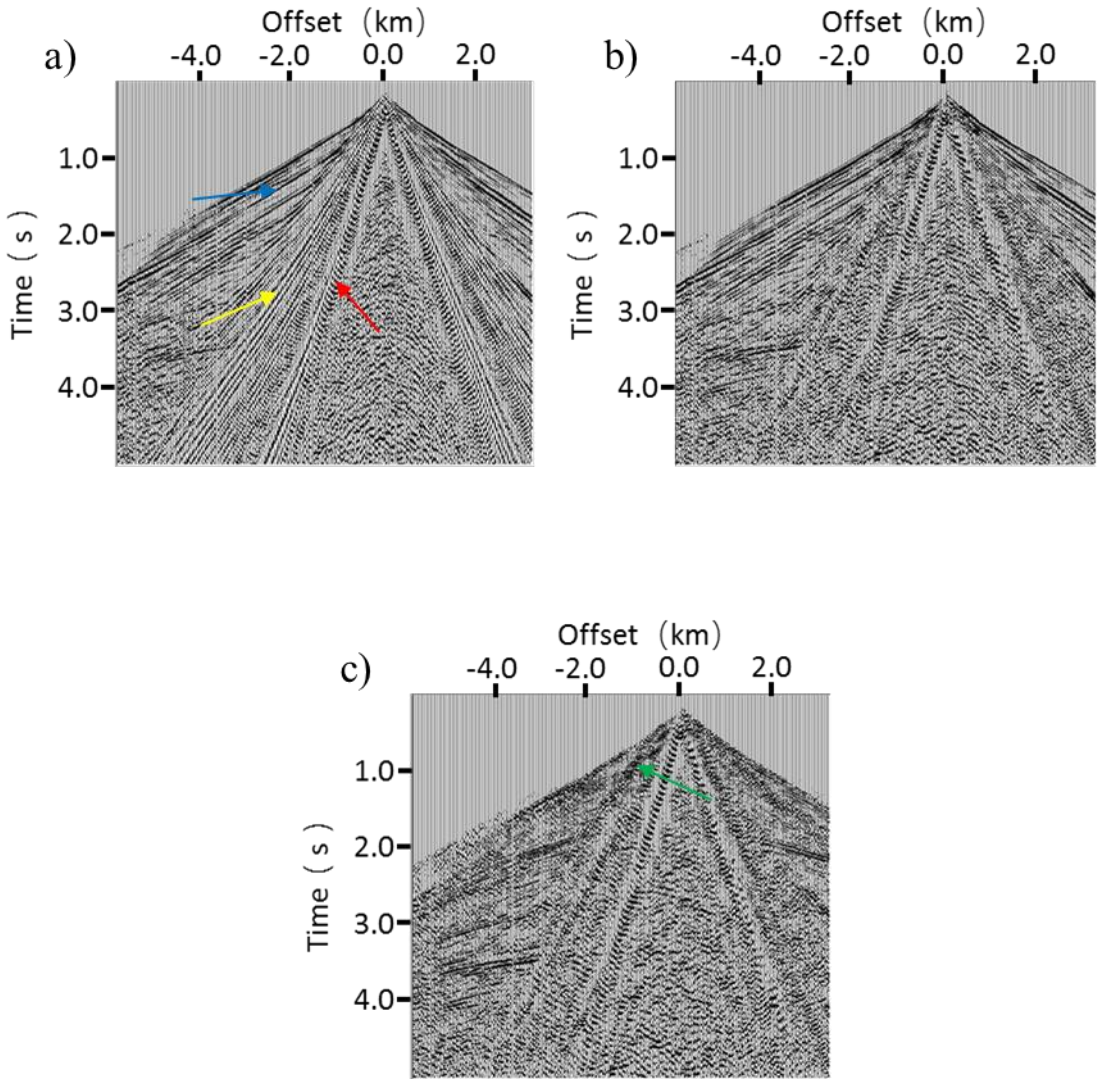

Figure A.7. Multi-step linear noise attenuation for the overthrust belt example. (a) A representative common shot gather exhibiting high velocity noise (blue arrows), low velocity noise (yellow arrows) and ground roll (red arrows). The same gather after linear noise suppression of the (b) the low velocity linear events and (c) low and high velocity linear events. While the high velocity linear events are effectively suppressed, aliased components of the lower velocity events, including ground roll, have leaked through the filter. The shallow apparent dips (green arrow) of these events will be migrated as "signal" into the final image, damaging the overall signal-to-noise ratio and interpretability of the section.

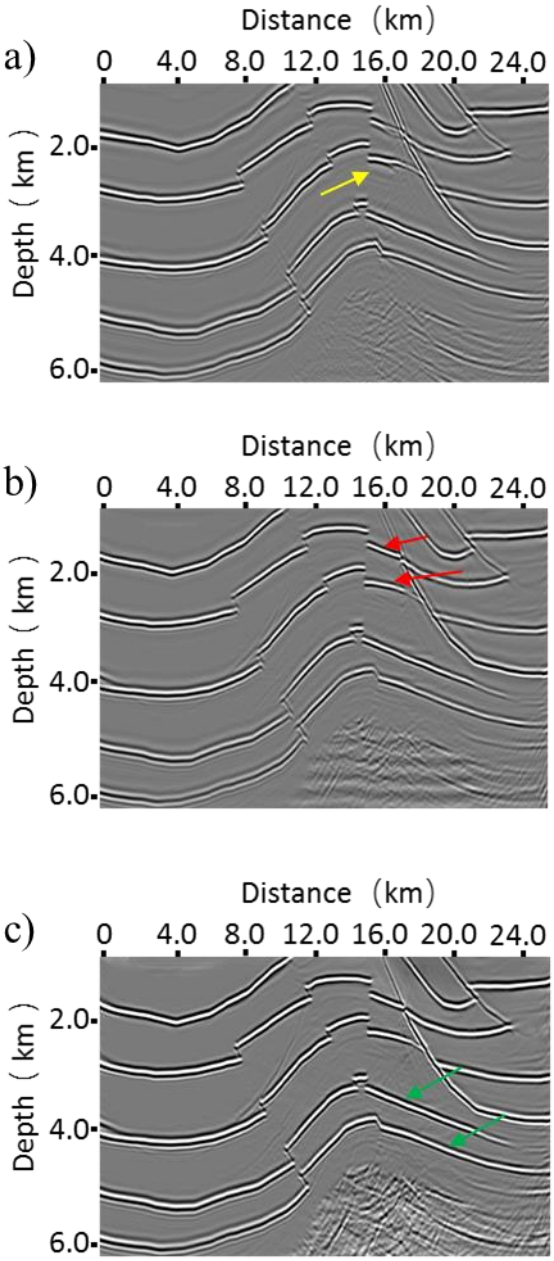

Figure A.8. Comparison of different depth migration methods on the overthrust synthetic data of Figure A.2. (a) Kirchhoff depth migration, (b) conventional one-way wave equation depth migration, (c) amplitude-preserved one-way wave equation depth migration. Low frequency artifacts creep into the Kirchhoff depth migrated image indicated by yellow arrows, but are largely suppressed in the one-way wave equation image. The underlying reflectors have poor images due to the overlying high velocity structures in the Kirchhoff migration, but are effectively improved by the one-way wave equation migration indicated by the red arrow. The amplitude-preserving algorithm more accurately represents the correct amplitude, especially for the deep reflectors indicated by the green arrow.

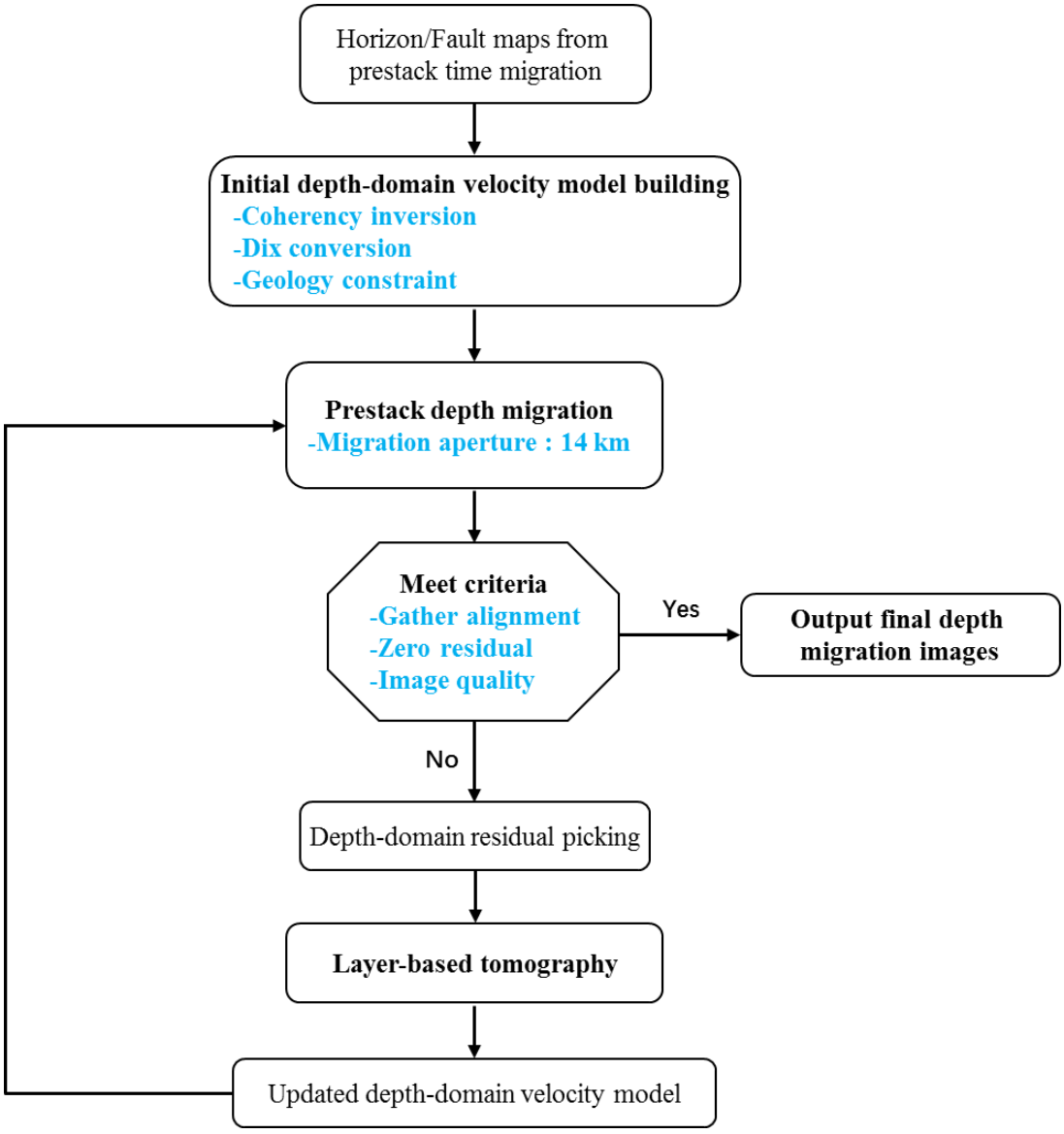

Figure A.9. The prestack depth migration workflow in the overthrust belt, including the tomographic velocity updating procedure. Note that large migration aperture is needed to image the steeply dipping reflectors and faults in overthrust belt.

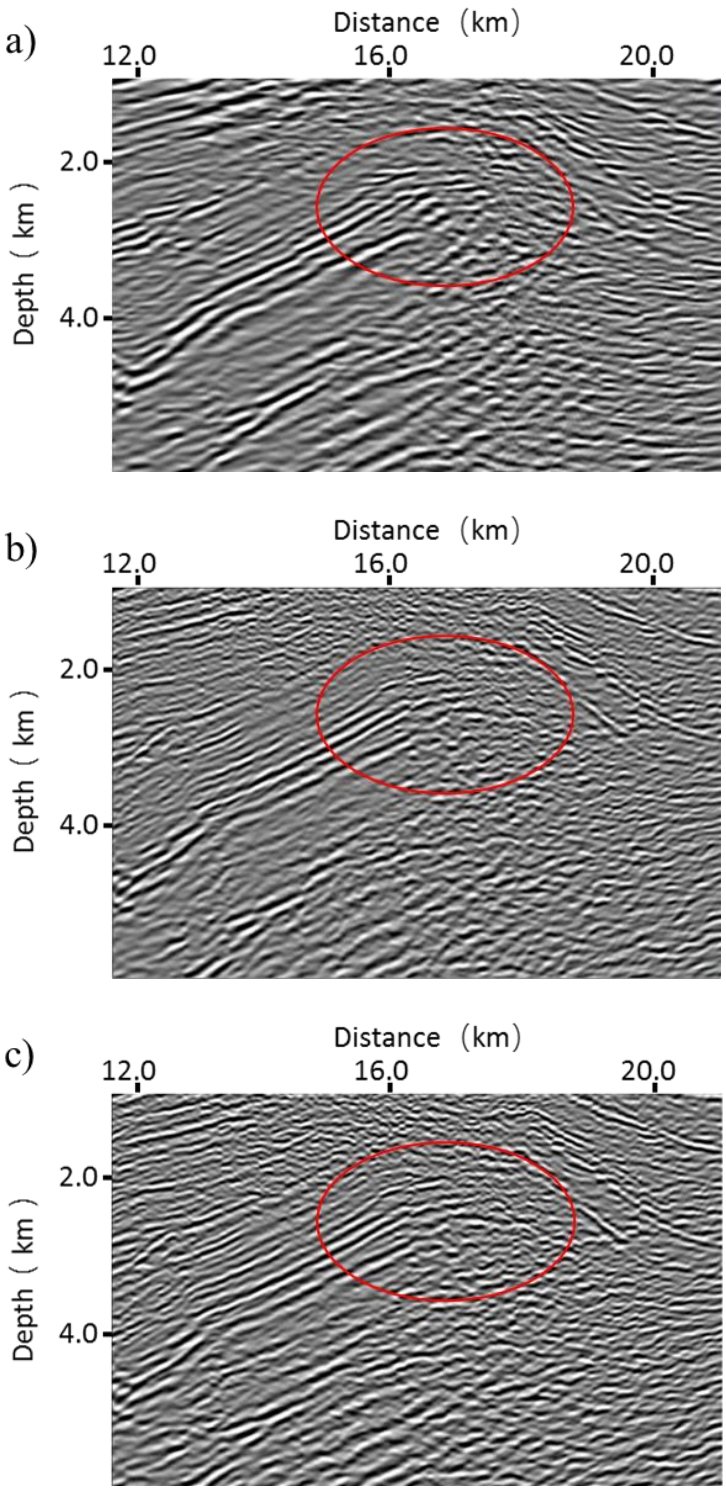

Figure A.10. Comparison of different depth migration methods on the field data with overthrust structures. (a) Kirchhoff depth migration, (b) conventional one-way wave equation depth migration, (c) amplitude-preserved one-way wave equation depth migration. The underlying faults are better imaged by the one-way wave equation depth migration (red circle). The amplitude-preserving algorithm further compensates the imaging energy of the underlying reflectors.

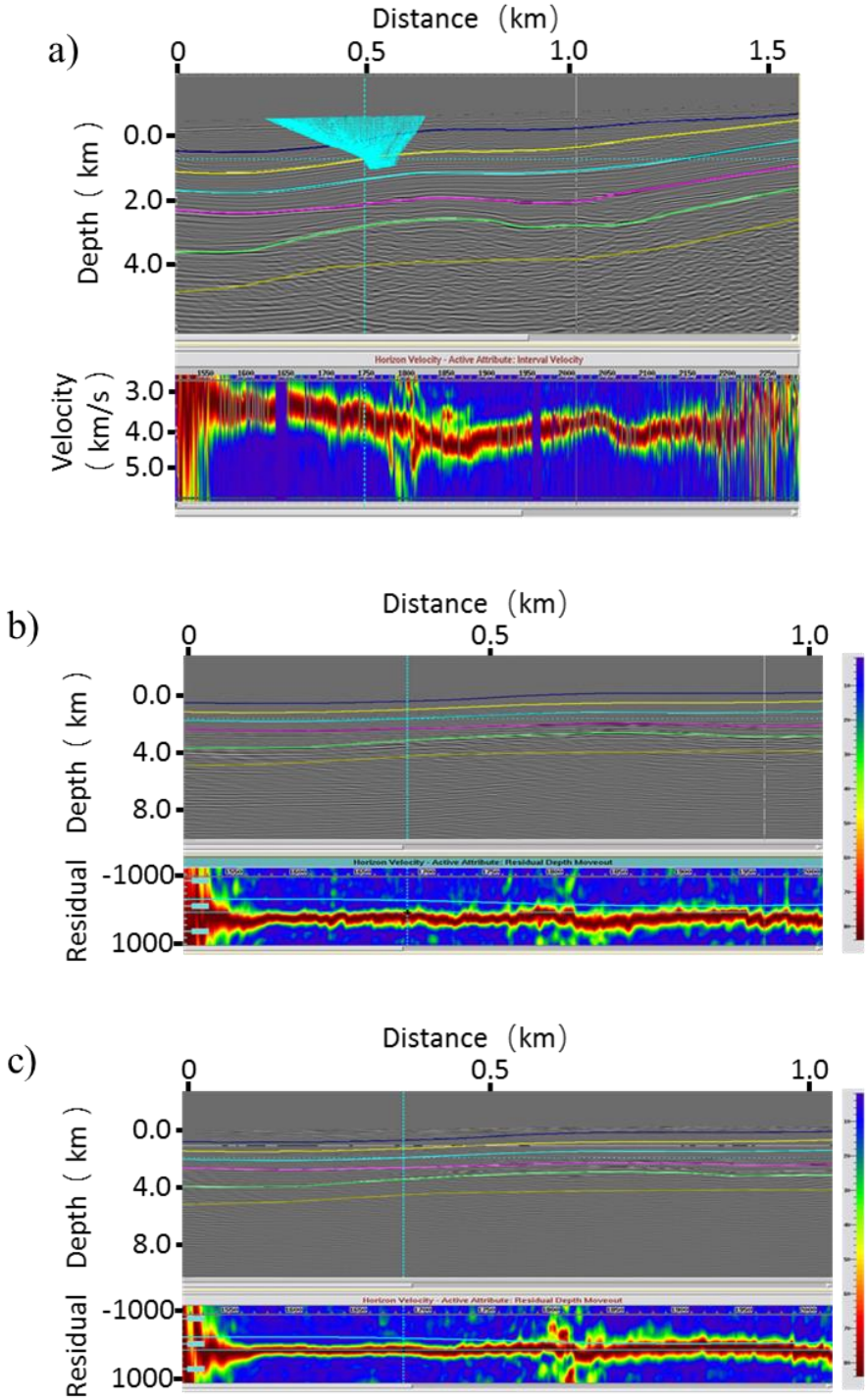

Figure A.11. A comparison of alternative depth-domain velocity model building methods as measured by computing semblance scans across the migration gathers. For accurately migrated data, the gathers should be flat, showing a misalignment of 0. In contrast, areas that are overcorrected will have negative residual moveout while those that are undercorrected will have positive residual moveout. Residual moveout computed from seismic images migrated using (a) Yilmaz's coherent event conversion result and (b) before and (c) after tomographic residual velocity correction.

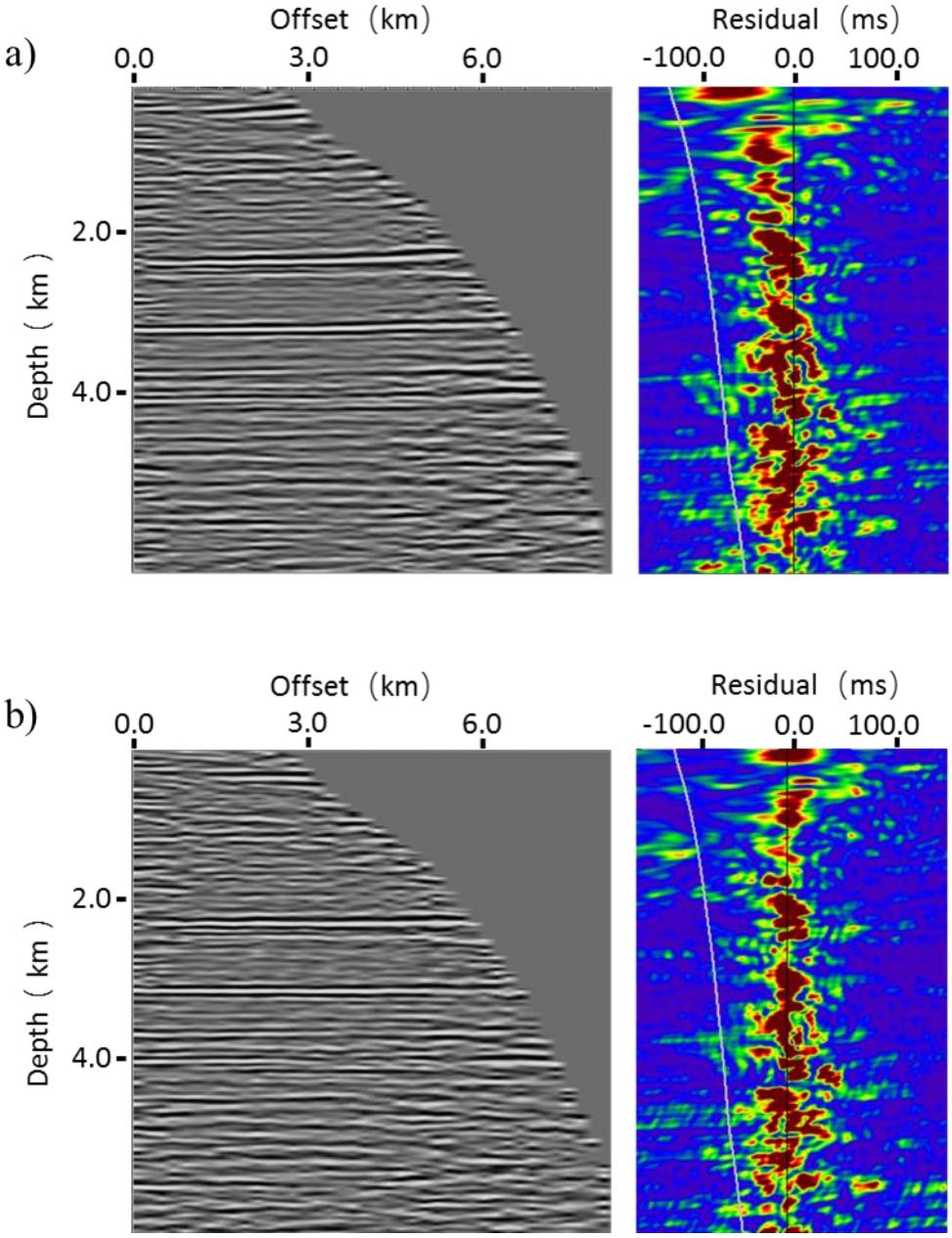

Figure A.12. Comparison of common-image gathers located at lateral distance 14.0 km of Figure 10 (a) before and (b) after tomography. Note that the reflections behave upward with residuals before tomography, and they are aligned after tomography.

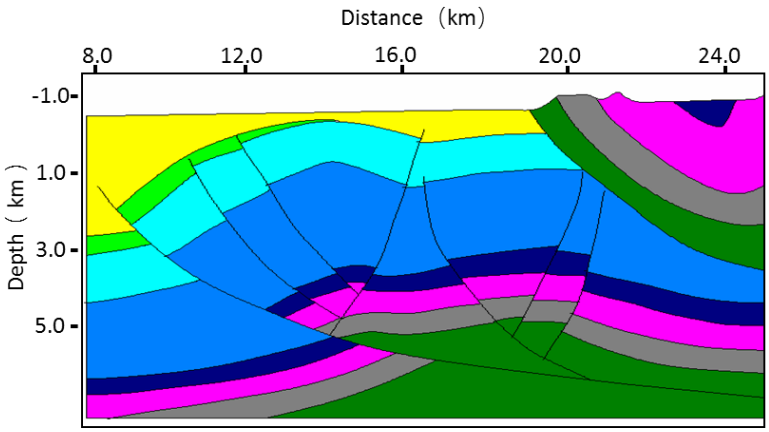

Figure A.13. A typical geologic model in our research survey. The overlying outcropped rocks behave very high velocities.

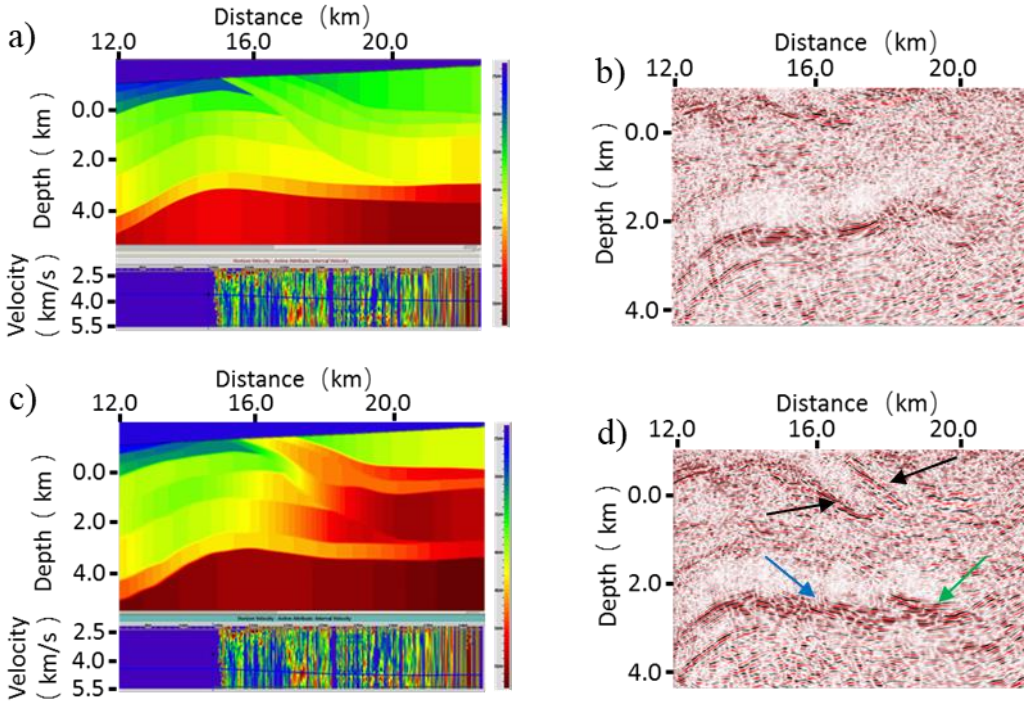

Figure A.14. The importance of adding geologic constraints in building the velocity depth model for the overthrust example. (a) Velocity-depth model and (b) corresponding seismic image built using the seismic data alone. Seismically derived velocities are more accurate for intermediate depths where the fold (more accurately, the number of illuminating ray paths) is high. Considering the geologic model in Figure A.13, the overlying outcropped rocks behave very high velocity. The range of velocities that we choose are too low, and make the initial velocity model far from the correct one, so it is difficult for the tomography algorithm to converge. Incorporating this geologic information into the (c) update velocity depth model generates (d) an improved, better focuses subsurface image. Black arrows indicate better illuminated shallow steeping dipping reflectors, the green arrow a suite or previously poorly illuminated horizontal reflectors, while the blue arrow shows that the higher shallow velocity significantly changes the depth and structural orientation of the deeper anticlinal target.

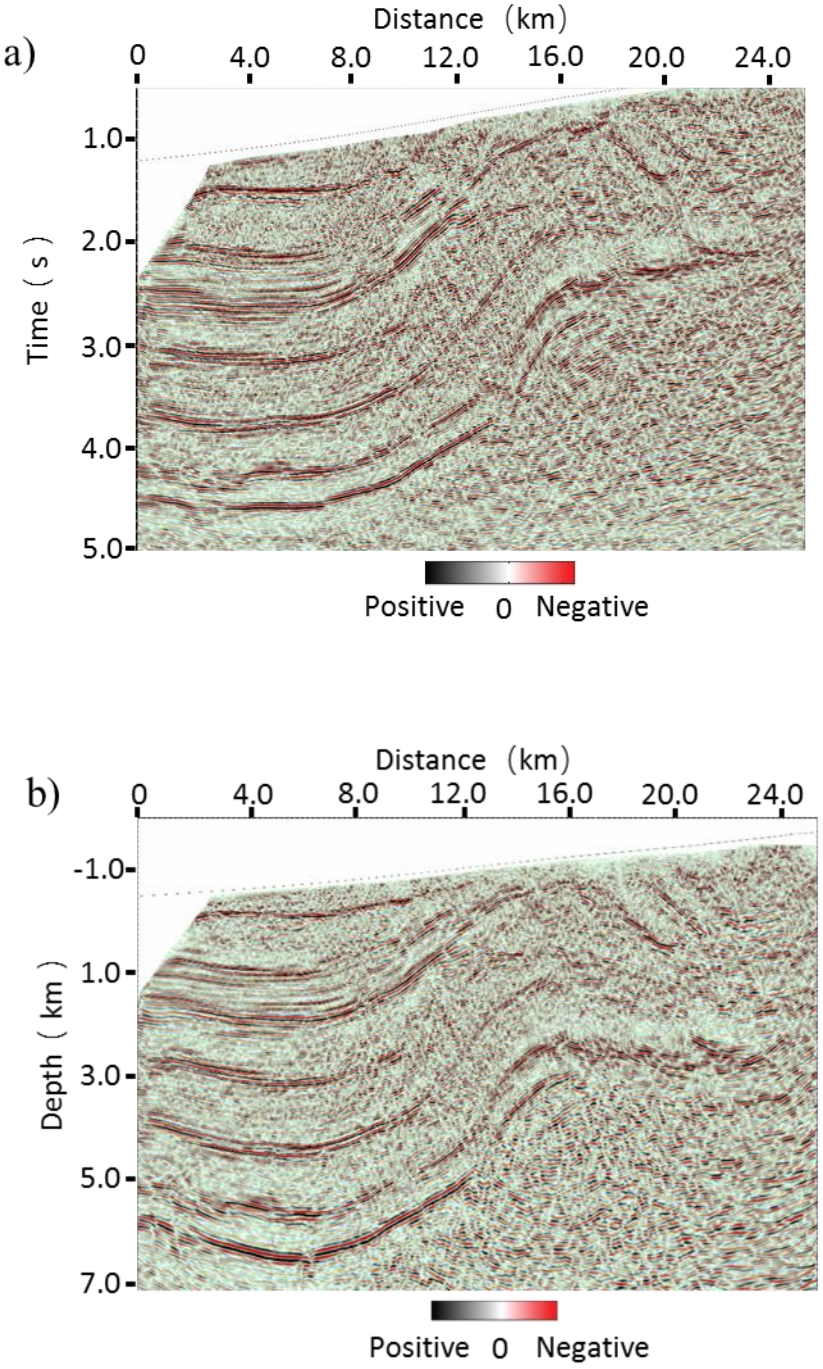

Figure A.15. Comparison between prestack (a) time and (b) depth migration of the land survey with overthrust structures. Note the superior quality of the depth-migrated image compared to the time-migrated result. Specifically, the depth migration better images the faults and the steep dipping strata more clearly than time migration. There are also fewer migration artifacts (unfocused ellipses) in the depth imaging result. Examining differences in the strata underneath the overthrust structure, the time migration shows them dipping up to the right, while the depth migration shows them dipping down to the right, to avoid the velocity pull-up pitfall in time migration.